Airflow in Interior Spaces:
Implications on Comfort and Health

by

Johnathan J. Kongoletos

Bachelor of Science, Engineering
Massachusetts Institute of Technology, 2014

Master of Science, Architecture: Building Technology
Massachusetts Institute of Technology, 2018

Submitted to the Department of Architecture
In Partial Fulfillment of the Requirements for the Degree of

Doctor of Philosophy in Architecture: Building Technology

at the

Massachusetts Institute of Technology

May 2022

Signature of Author……
Department of Architecture
May 11, 2022

Certified by……
Leon Glicksman
Professor of Building Technology and Mechanical Engineering
Thesis Supervisor

Accepted by……...
Leslie K. Norford
Professor of Building Technology
Chair, Department Committee on Graduate Students

Dissertation Committee:

Leon R. Glicksman, PhD
Professor of Building Technology & Mechanical Engineering
Massachusetts Institute of Technology
Thesis Supervisor

Leslie K. Norford, PhD
Professor of Building Technology
Massachusetts Institute of Technology
Thesis Reader

John H. Lienhard V, PhD
Abdul Latif Jameel Professor of Water and Mechanical Engineering
Massachusetts Institute of Technology
Thesis Reader

Robert J. Stoner, PhD
Deputy Director for Science and Technology of MIT Energy Initiative
Director of the Tata Center for Technology and Design
Massachusetts Institute of Technology
Thesis Reader

Abstract

The International Energy Agency projects that rising income and greater access to air conditioning equipment in many developing countries will increase CO_2-equivalent emissions, energy consumption, and urban heat island effects. India exhibits these traits, where new building trends, hot climatic conditions, increasing social aspirations, and rapid population growth is likely to spread the adoption of air conditioning. Within India, while air-conditioners are attainable, the financial cost of acquisition and operation preclude their usage by the population's most vulnerable. To reduce the need for air conditioning and increase available building options, low cost and socially-acceptable options are necessary to reduce productivity losses and excess mortality.

This work presents the results of long-term temperature monitoring within four occupied homes, builds a model for understanding the influence of material choice, and evaluates that model on the basis of a reduction in peak indoor air temperature and energy savings as compared to an equivalent air conditioner. Results from the occupied homes show a peak reduction in inside air temperature of 8.2 °C during the summer months relative to informal housing in the same community. Further, using scale models and input from the Ramdev Nagar community in Bhuj, the impacts of operational airflow changes are quantified with a focus on next-day thermal comfort. Applicable outside of India, the techniques can be used concurrently with active cooling systems to reduce energy consumption or extend capacity. Targeting near-term implementation in India, this work focuses on tangible improvements spanning construction and operation.

Shifting towards offices using chilled beams, this work presents data on the impact of ceiling fans on chilled beam performance both in steady-state and in transient situations to address discomfort in conference room settings where rapid changes in cooling performance are required or capacities exceeded. This work extends on that theme to propose improved thermostat placement targeting the reliability of the thermostat readings to serve as a proxy for thermal comfort.

Finally, this work looks at dispersion of bioaerosols within a classroom environment. Via simulations, this work contributes through the quantification of different ventilation approaches and generalizable recommendations for contaminant control at the breathing zone.

Thesis Supervisor: Leon Glicksman

Title: Professor of Building Technology and Mechanical Engineering

Acknowledgments

This research was largely sponsored by the MIT Tata Center for Technology and Design. I am grateful to the Tata Center and its leadership for their continued support of this research and for facilitating a supportive environment to pursue the application of academic research to current widespread challenges. I especially appreciate their guidance in framing arguments from a multitude of perspectives. Even the best technical answer is meaningless if it is in a vacuum with respect to social, cultural, economic, and regulatory perspectives.

I would like to thank Professor Leon Glicksman for his encouragement, sage advice, judicious planning, and expert guidance. Without his mentorship, none of this work would have been possible. Of the many things that I will miss from these past years include his ability to reframe topics to provide mental growth opportunities. I will also miss our weekly meetings and discussions that allow me to maintain a broad awareness of the world around me. I began working with Leon in early 2013 and have cherished his advice and input with many decisions, large and small.

I would also like to thank my committee: Les Norford, John Lienhard, and Rob Stoner, for their guidance, encouragement, and thoughts on improvement. Their contributions allowed this work to develop and their backgrounds allowed the work to remain targeted towards applications. I appreciate their patience as this work took shape and embodied the central premise of Murphy's Law.

To all within the Hunnarshala Foundation, working alongside you has been a rewarding experience on both the professional and personal levels. With your enthusiasm and willingness to test both new ideas and revisit old ones, this work has been able to include a vital social feedback component with long-term testing, allowing the research to stand by itself.

To my friends, both near and far, and to Molly, you have been there to ensure I am more than my work and have picked me up when I've fallen down. This journey has been possible because I have never walked it alone.

To my paternal grandparents, who fled persecution and sought a better life, instilling an appreciation of education and hard work. And to my maternal grandparents, who faced the horrors of war and ensured that they were defined not by their past, but by their present. Let us retain those values and the memories of where we came from, so that we can pursue a better tomorrow.

To my parents, I am especially grateful for your continued love, support, and supply of tsoureki. To my brothers and sister, you too had a role in giving me the skills and confidence to push boundaries and make this work possible. Along with my extended family, my gratitude and love extend far beyond the scope of the written word.

Table of Contents

List of Figures

List of Tables

1 Introduction

1.1 Problem

Global mean temperatures are expected to increase [1], leading to an increase in the intensity of heat waves [2, 3]. Currently, around 30% of the world's population is exposed to potentially deadly heat stress for at least 20 days a year. By 2100, this is projected to increase to 48% of the world's population if greenhouse gas emissions are drastically reduced, and 74% if greenhouse gas emissions grow [4]. The largest effect will be felt in the developing regions, such as India, either through increased mortality rates or work productivity loss [5, 6]. These effects are particularly concentrated among low income populations, infants, the sick, the elderly, and heavy laborers [7, 8].

Heat-induced mortality is relative to a baseline, sometimes referred to as a Minimum Mortality Temperature or Optimum Temperature Value. This baseline varies by publication and dataset, and increases along a 'V' or 'U'-like relationship from the baseline. For the case of the Indian subcontinent, heat waves are the dominant concern. During heat waves, overall mortality rises above a baseline rate and will then typically fall below said baseline rate for a number of weeks post-heat wave. This compensatory effect principally affects those who are already at significant risk or are compromised, and, while gloomy, their deaths may not be counted in some datasets since there in no significant reduction in overall lifetime [9, 10]. The academic literature therefore seeks to filter out the contribution of deaths attributable to excess mortality, or those who would statistically have survived had the heat wave not occurred. Aside from author and dataset, variations among the temperature baselines can be attributable to geography, culture, and socio-economic status. For South Asia, Hashizume, et al. [11] concludes that every 1°C increase above 31°C correlates with a 3.2 percentage point increase in mortality.

All told, heat waves in the city of Ahmedabad, the capital of Gujarat state, claimed one of every 4,192 residents in 2010 [12, 13] and one of every 3,981 in 2015 [14, 15]. As of the time of this writing (May 2022), India's western state of Maharastra has registered the most deaths from heat stroke in April in the last five years, a grim milestone in the wake of the warmest March in over a century [16]. Worsening these conditions, local outdoor temperatures within informal communities are roughly 2.0 °C greater than formal communities [17], attributable to a denser built environment (roof surface areas) in informal communities relative to formal communities.

Heat-related impacts are not confined solely to mortality. High temperatures are affiliated with increased rate of occupational injuries [18], and heat stress is estimated to reduce work productivity by 30% independent of the work being indoor or outdoor. For every degree above 26 °C, self-reported productivity purportedly decreases by 7.1% [19]. These economic losses as a proportion of GDP are larger for low- and middle-income countries in warmer climates [20], and are principally born by the working classes, who are estimated to lose 1.2 work hours per heat-wave day in India [21]. Further, workers in heat waves forego an additional 0.46 hours of family time, highlighting a non-productivity, non-mortality related impact.

To combat these heat waves, air conditioners are the go-to choice for many. During April 2022, Indian households bought double the amount of air conditioners than during April 2021, and are on track to exceed yearly sales expectations from only six months ago [22, 23]. This growth is due to a variety of

factors, including the relative abandonment of vernacular housing techniques, the urban heat island, increasing affluence and living standards, and increased building thermal gains, among others [24]. This growth will come with large costs and environmental implications exacerbated of which air-conditioning usage will exacerbate [25]. Official state and urban policies within India do not include heatproofing for new or retrofit housing [26], which adds another barrier for those reliant on government funded housing and those who not be able to afford the electricity to power an air-conditioning unit [27].

Complicating this further, 74% of India's electricity production is from coal [28], and 50-60% of New Delhi's electricity supply is for air-conditioning alone [29]. These two factors help New Delhi to become the world's most polluted capital city [30] and subtly allude to how thermal comfort is intertwined with a reliable electrical supply network. Further, through the carbon emissions inherent to coal, these factors illustrate how air-conditioning use in coal power-reliant developing countries has implications on global climate change. Such a dependency on a developing energy grid also has implications for the current air-conditioning owners who are now more exposed to price shocks (i.e. coal supply shortages), natural disasters (long-term outages), and equipment downtime caused by electric supply challenges (voltage and waveform instability). To help alleviate these concerns and increase the resiliency of the Indian building stock, integrated building thermal solutions are needed to keep building occupants cool.

1.2 Past Work

Largely located within the tropics, many efforts to keep buildings cool in India have focused on reducing the solar heat gain of the roof. Either through external coatings, material choices, or shading [31, 32, 33], the roof is a natural choice due to the persistent solar exposure, relative ease of modifications, and compound effect on both the roof temperature and local air temperature, which has community benefits. For the building occupants, the roof contributes up to 60% of the total heat in warmer climate zones [34].

Many of the at-risk demographics combine within Bhuj, India, where several former MIT students have looked to improve thermal comfort and reduce heat-associated risks [35, 36, 37]. Bhuj is notable as the ASHRAE-reported annual peak dry-bulb temperature is 43.1 °C [38], and existing informal housing options can exceed ambient temperatures [39, 26]. Academic literature is abounding on the role construction and operation of the built environment have on the need for air-conditioning. Within the context of this work, literature is specifically available on cool roofs, and increasing awareness of vernacular methods [40, 41]. These approaches assist designers in adding climate resiliency to the building portfolio.

This research will make modest use of cool roof approaches, but rely more on above sheathing ventilation, also referred to as double-layer roofing. Starting on the topic of cool roofing, an assessment by Garg, et al. evaluated the impact of a change of roof absorptivity from 0.8 to 0.4 for a 15 cm cement roof slab building without additional conditioning equipment and found that cool roofs are associated with an average reduction in indoor air temperatures of 2.1 °C and peak air temperature reduction by 5.0 °C [42]. Further, citywide application of cool roofs is reported to contribution to a maximum 3.0 °C reduction of the city center daytime temperatures [43].

While the cool roof efforts can apply to both flat slab and pitched roofing, Within the small city, low-income Indian housing context, pitched roofing using is more common in the Bhuj area. Primarily, these homes use Mangalore tile roofs, which are well-established in the Indian vernacular and have a

social affiliation with the permanence of government institutions that low-income residents can associate with the concept of home. Utilizing this existing social infrastructure, Madeline Gradillas conceptualized a double-layer roofing system constructed of the Managalore tile, a radiant barrier, an air gap, and mudroll inner layer [36]. While other double-skin proposals do not maintain a constant separation [44, 45], the above-sheathing ventilation concept has been experimentally studied by Miller, Herman, and Graves in varying configurations for application to the North American climate. Notable conclusions from Miller, Herman, and Graves concluded that a roof fitted with a 4 cm air gap between layers had the potential for an almost-black exterior layer to still have the seasonal cooling load of a 75% solar absorptive single layer metal roof and that a 2 cm air gap had the potential to reduce the solar absorptivity 15 percentage points from a 90% absorptive base [46]. Those conclusions built upon the work of Miller, Wilson, and Karagiozis, who attributed the double-layer roofing system to a 30% reduction in heat flow through the roof layer [47].

Other research points to the implications of using ventilation cavities below tile roofing [48], but inherently assumes a classic barrel tile geometry that significantly reduces the active ventilation area below a tile roof system. However, D'Orazio, et al. do present an offset tile case and collect field data to conclude that the natural ventilation of the roofing system reduces the heat flux from a mean of 4 W/m^2 (tiles in direct contact to sheathing) to 1-2 W/m^2 (tiles offset from sheathing) [49]. Tile roofing was also investigated through a computational lens by Bottarelli, et al., who modeled and experimentally investigated the air permeability of Mangalore tile (also known as the Marseillaise, or Marseille tile) [50], and the impact of wind conditions on permeability through the tile layer.

To build on this research within India, the research team at the Massachusetts Institute of Technology ("MIT") has collaborated with The Hunnarshala Foundation ("Hunnarshala"), based in Bhuj, Gujarat, India. Bhuj is a challenging city to design for thermal comfort due to the dangerous heat waves that frequently exceed 45°C [36]. The state of Gujarat has a higher than average urban population percentage (43%) and 6.5% of the population live in slums [51]. In partial response to a recent earthquake in 2001, the local, state, and national governments have been working under the "Housing for All by 2022" program to subsidize the construction of housing in the region. Providing a financial grants or interest subsidies up to 230,000 Indian rupees ($3,375) per household, the government has been crucial in helping to spurn development of housing targeted towards those earning less than 200,000 Indian rupees ($2,935) per year [52, 35].

Hunnarshala began this collaboration and initial research with former MIT student Gradillas, who laid the groundwork in understanding social, cultural, and economic factors, building material selection, and undertook the initial efforts in measurement and establishment of baseline thermal performance [36]. Emma Nelson then continued the research through the development of energy modeling software to look at the performance and configuration of radiant barriers [35].

The low-income residential housing is Bhuj is largely single- or two-story dwellings of roughly 30 m^2 with electricity within the community, household water cisterns, and indoor plumbing. Within the constraints offered by these homes, Gradillas offered a series of suggestions for future work, refining the design, and continuing the co-design process. Notably, Gradillas acknowledged that there are no silver bullets to improve thermal comfort, and recommended the incorporation a double-layer roof with a radiant barrier as one contribution towards an amalgamation of strategies. Nelson then continued the work

through the construction and initial measurement of test cells built in Bhuj, along with an economic aspect to understand the affordability of proposed roof designs to remain within the desired price points of the target audience and Housing for All participants. Among others, Nelson recommended an assessment of airflow patterns on both short- and long-term comfort, and the reduction of solar absorptivity of the rooftop surface.

The author's previous work built on this to focus on testing and verification of strategies across three different scales, production of experimental results of local materials for surface radiative properties, and applications of the work to both Bhuj, India, and traditional Nepali housing [39]. Testing within full-scale test chambers in Bhuj also tested the influence of tin roofing, wall color, interior mud plaster, and ventilation options. That testing provided a set of conclusions that varied from those of Gradillas and Nelson, particularly that low absorptivity wall paint led to a reduction of the peak air temperature by 1.5 to 2.5 °C relative to an unpainted baseline and that increasing night ventilation helped reduce the next-day peak air temperatures by roughly 1.0 °C while increasing nighttime air temperatures by 1 to 5 °C compared to the concurrent outside air temperatures.

While the author's previous work did include long-term monitoring of the occupied housing in Bhuj, it stopped short of providing recommendations for the implementation of the concepts. Notably, the work failed to improve upon the roofing style originally presented by Gradillas and scale tested by Nelson.

1.3 Opportunities

For application to India, the system proposed and evaluated by Miller, et al. uses materials and construction techniques not commonly available in India and the system from D'Orazio investigates the system on the basis of net heat flux, implying that the space below is conditioned. Neither of these is true in India, where the material cost dominates construction costs and spaces are not universally conditioned, especially when unoccupied. This is especially the case of the aforementioned cool roofing literature, which used a polymer-acrylic blended ceramic coating in lieu of commonly available paint or whitewash.

This work seeks to provide insight into the system proposed by Gradillas and later evaluated on a test-cell level by Nelson. This work goes beyond that of Nelson to construct four homes with long-term occupancy and monitoring, evaluating the roofing typologies on the basis of the relative influence on the air temperature of the space inside. Further, the inclusion and quantification of the role of a radiant barrier remains absent from the academic literature as applied to the context of the double-layer roofing and when used outside of a conditioned environment. This work seeks to fill those literature gaps.

Where Nelson had recommended a reduction of the solar absorptivity of the rooftop surface, this work provides an assessment of the possibilities of reducing the solar absorptivity of the slab and the implications that change has on the slab temperature throughout the next day. Differentiating this work from other literature in the field is the inclusion of homeowner input on the usability of the rooftop with the various proposed modifications and the recognition that the proposed materials are available in the local market and do not represent a large modification to the roofing slab system.

Gradillas had advocated for the inclusion of night flush ventilation as a means to reduce peak day temperatures within the homes and this theme was extended by Nelson to warn of the pitfalls of enhancing heat transfer from hot surfaces in the absence of sufficient ventilation. Continuing the trend of

homeowner-conscious options, a detailed investigation of the possibility of forced air cooling of the interior of the ceiling slabs is included within this work to provide an operational change for homeowners to implement. Above and beyond a generalized air change argument for ventilation, this work helps quantify the significance of that ventilation through a ceiling-average convective heat transfer coefficient and model the impact on subsequent peak slab temperatures.

2 Bhuj Pitched Roof Housing

Section 2 is organized starting with a Background section (2.1) to set up the rationale, materials, and sample available literature. Section 2.2 brings in a societal perspective. Section 2.3 describes the impact of powered ventilation of the air cavity. Section 2.4 then takes an opposite perspective and describes the impact of removing ventilation within the air cavity, and Section 2.5 defines a modeling approach to compare to the physical testing. Section 2.6 wraps up the main takeaways and recommendations based on the research.

2.1 Background

Within the vernacular row-home-like structures common in Bhuj, most solar energy is incident upon the roof. This makes the roof a natural choice to target for improvements to reduce the thermal heat transmittance. To date, the existing work (Gradillas, Nelson, 2018) largely focused on pitched-roof style housing and opportunities to reduce indoor air temperatures using double-layer roofing, or above-sheathing ventilation strategies. Four such homes were constructed in cooperation with a local NGO, of which three are shown in Figure 1.

Figure 1: Pitched roof second floor structures

In these homes, the primary difference is in the construction of the roofing structure. All of the experimental roofs constructed are double-layered (also known as double-skin or above-sheathing ventilation), meaning that there is an exterior layer that is the primary waterproofing, a continuous open-ended air cavity separating the two physical layers, and an air-impermeable interior layer. Figure 2 provides an example of the system, as illustrated by Gradillas [36].

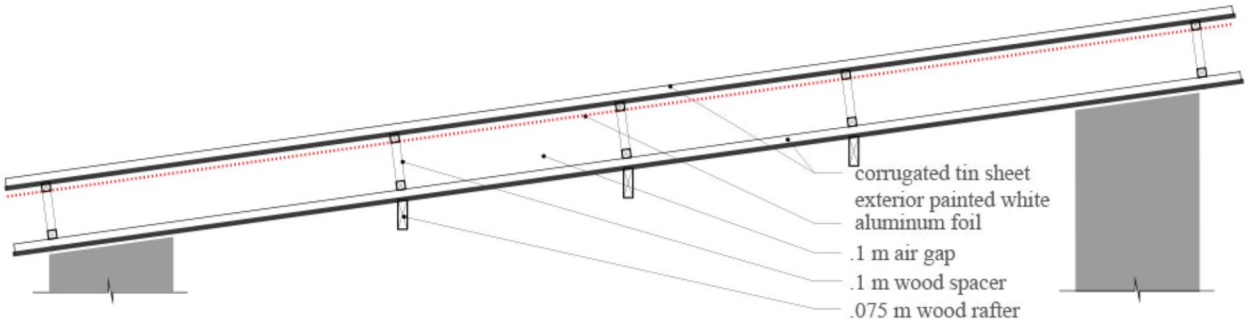

Figure 2: Section view of low mass double layer roofing system, illustration from [36]

Double-layer roofing is a passive roofing system that have been studied primarily to reduce the heat gain into the interior. However, few parts of this body of research have physically applied the technique to physical applications and fewer still that have used the technique for developing economies. The developing economy aspect is particularly important in this aspect, as the existing literature on energy savings is less significant as compared to thermal comfort and passive building improvements. Gradillas noted this lack of research and used scale models to experimentally show that adaptive thermal comfort can be achieved through most of the operating hours with double-layer roofing. [36]

Tracing the history of the literature in this field, beginning in 1942, Elenbaas [53] used an experimental approach to build relations for natural convection between isothermal parallel plates, ultimately defining a heat transfer coefficient based on geometry. Elenbaas then continued to define an optimal width for buoyancy driven thermal transfers, but while adjusting for radiation leaving the open side of the experiment, did not account for changes to the radiative properties of the surfaces. Azevedo and Sparrow [54] then returned to the same question as Elenbaas in 1985, for fixed inclination angles, but particularly arrived at a different conclusion on the significance of the channel width towards the heat transfer. Interest into the question of the effective heat transfer picked up again with the 1997 publication of Fracastoro et al., who presented a steady-state approach for the quantification of the reduction of heat gain through under-roof cavities through a combined energy and pressure drop approach, ultimately concluding that the solar heat transmittance could be reduced to 5% of the solar heat load with a modest conductive thermal resistance [55]. Similar to Elenbaas though, Fracastoro assumed a gray body approximation for the interior surfaces and did not investigate the impact of changes to the thermal radiation properties.

The literature of double-layer roofing systems finally began to include a radiant barrier system in 2003 with the work of Miranville [56], who also introduced a multi-zone model and discretization approach. Miller then added to the literature with experimental results and arrived at a conclusion that a 70% reduction of the heat flow was possible with double-layer roofing and low-solar absorptivity tiles [57]. Biwole [58] then used both simulation and experimental setups to investigate the influence of various material and physical characteristics on the heat transfer. Of importance, Biwole notes the greatest

significance of the overall heat transfer is the internal emissivity of the surfaces, followed by the outer layer's outer surface's emissivity, the conductive thermal resistivity, and the thickness of the cavity, in decreasing order.

Sponsored by MIT's Tata Center, the current work applied the double layer system to low-income housing to demonstrate its performance while using local materials and designs that met local acceptability. Several prototype homes were designed and instrumented in cooperation with a local NGO.

These homes are two-story dwellings incorporated within the community and area a four-room design split across two stories, with the kitchen and bath facilities on the ground floor. Total area for the entire home, excluding the wash room and water closet, is 49 m^2 (527.4 $ft.^2$), split between the ground floor (26 m^2) and the first floor (23 m^2). An early architectural plan is shown in Figure 3.

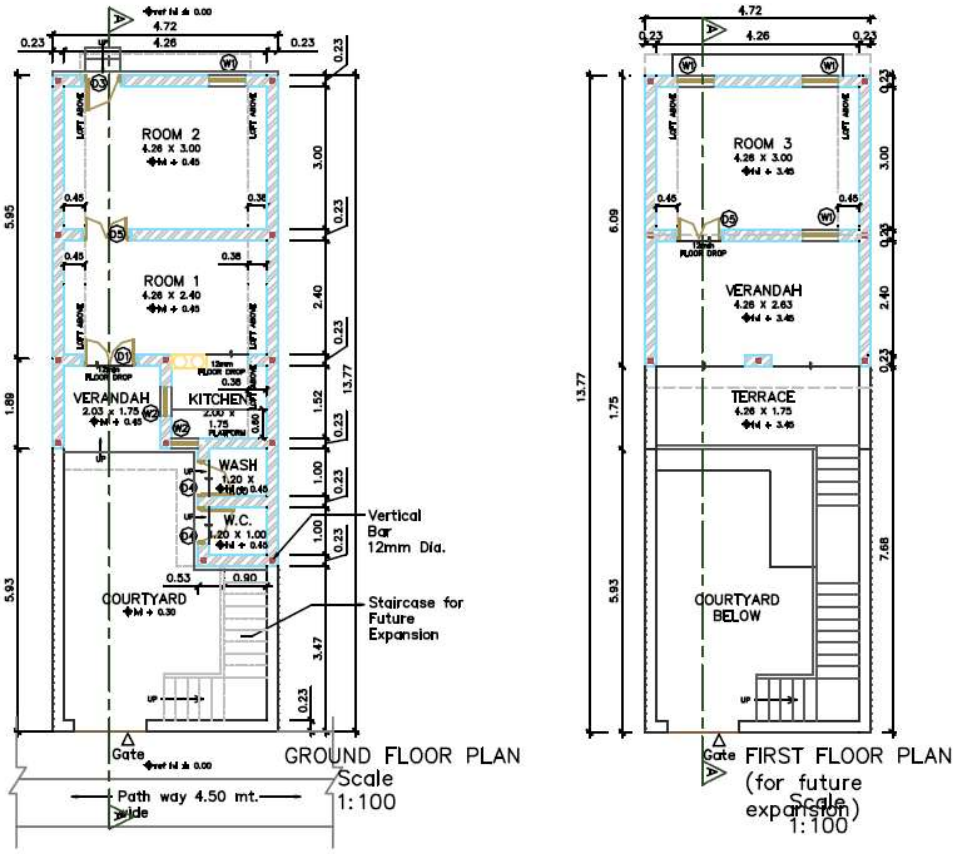

Figure 3: Early Architectural Plans for Two-Story Homes. Note that the 'First Floor Verandah' was enclosed to create 'Room 4' when constructed; (Courtesy Hunnarshala)

Physically building on previous research of Gradillas [36] and Nelson [35], who performed scale testing and started construction activities, two of the homes in Bhuj have an exterior water-shedding layer constructed of an interlocking Mangalore clay tile with a natural finish (also known as a French or Marseilles tile), while the other two homes have a pre-painted galvanized sheet exterior layer. Remaining aware of seismic considerations, the roof was intended to remain lightweight, and the interior layers were made of either a thin layer of sheet steel and aluminized bubble wrap, wooden slats, or a mudroll

assembly. Note that all of these materials are locally available in the marketplace and were chosen to remain cost-conscious.

The mudroll, made from mud applied to a layer of burlap and wrapped around a small wooden dowel, was intended to provide a measure of thermal mass in the interior roof assembly while remaining cognizant that seismic risk is exacerbated by higher mass roofing.

Figure 4: Mudroll cross section, with quarter for scale

The first home, referred to as the 'Tin-Bubble' was made of an outer tin sheet with radiant barrier underside, air gap, and aluminized bubble wrap supported by another tin-sheet layer. The second home, referred to as the 'Tin-Wood' replaced the aluminized bubble wrap/tin sheet combo with a wooden underlayer.

Figure 5: Tin-Bubble (Top) and Tin-Wood (Bottom)

The first home, referred to as the 'Tile-Wood was made of an outer Mangalore Tile layer with radiant barrier underside, air gap, and wooden underlayer. The second home, referred to as the 'Tile-Mudroll' replaced the wooden underlayer with a mudroll underlayer.

Figure 6: Tile-Wood (Top) and Tile-Mudroll (Bottom)

To collect date over the monitoring period, an Onset Computer Corporation HOBO UX120-006M analog temperature logger was coupled with four two-meter thermocouples (TMC6-HD). Shown in Figure 7, the four thermocouples measured the black globe temperature, air temperature at roughly 2m

elevation, a south-wall temperature, and a ceiling temperature. For simplicity, many of the following charts will make use of the air temperature sensor alone.

Figure 7: Long-term temperature monitoring in Bhuj, India

Using the collected data, these assemblies are also shown inset in Figure 8, which also shows an 'average day' for the homes in the months of April and May 2018. In this context, an 'average day' is the average of the time-based temperature data at the same hour of the day throughout the dataset.

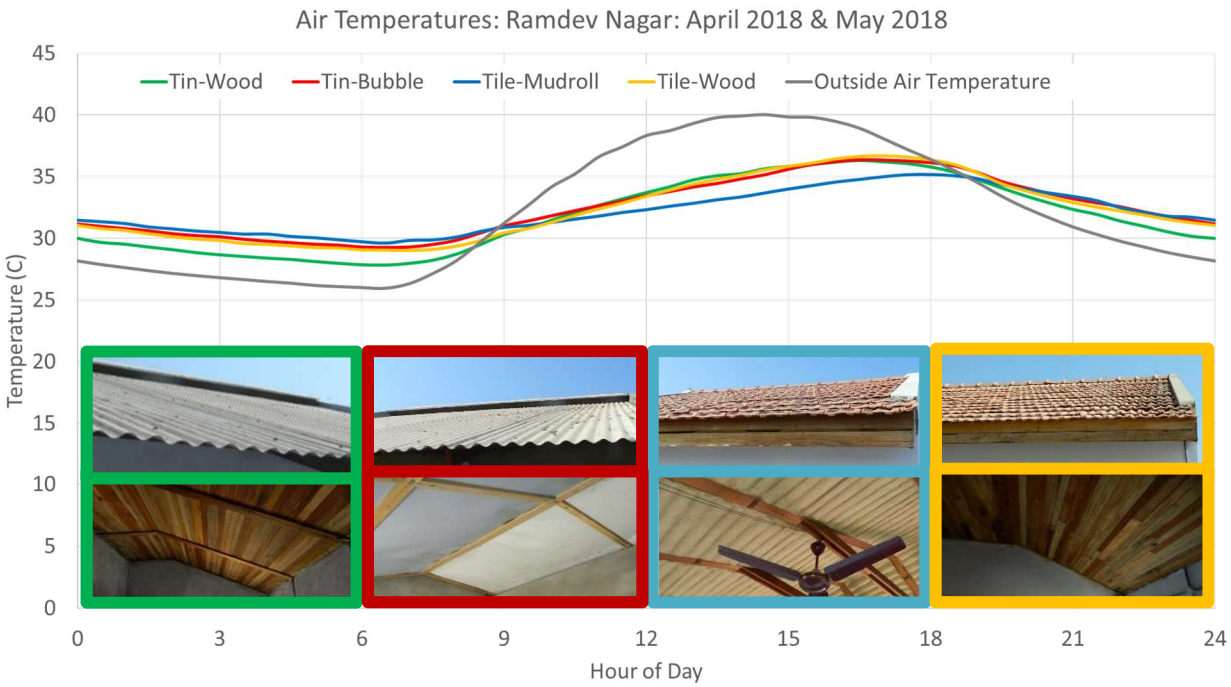

Figure 8: Average daily temperatures for four occupied double layer pitched roof structures (Ramdev Nagar, Bhuj, India)

Figure 8 shows the measured interior air temperatures, averaged over two months, for the occupied pitched roof structures shown in Figure 1. Within this plot of the indoor air temperatures of the structures and the corresponding outdoor air temperatures, three (Tin-Wood, Tin-Bubble, Clay-Wood) of the structures show similar thermal performance. These structures remain ~5°C cooler than the outside air temperature throughout the warmest part of the day, but also retain heat through the duration of the night. Of these three, the ~1.5°C cooler nighttime temperatures of the Tin-Wood structure are possibly due to the window shutters remaining open throughout the night. This reduction of nighttime temperature helps illuminate further opportunities for improving thermal comfort in the subsequent day. The major outlier throughout the day is the Tile-Mudroll structure, shown in blue, which remains ~1.5°C cooler during the warmest part of the day primarily through the added thermal mass of the mudroll.

In addition to the four constructed homes, the 2018 work installed temperature monitoring equipment in an informal housing unit within a hundred yards of the formally-built homes. This home, shown in Figure 9, was monitored in parallel with the other homes for a short period of time to provide a baseline comparison for the temperature results.

Figure 9: Informal homes in the same community as those in Figure 1

For this informal structure, the roof of the home is comprised of several tarpaulin layers, and a decorative sheet on the inside. The only major ventilation through the home is through the front door, and the door is left open throughout the day to cool off the space. The informal home is shown in purple in Figure 10. In this graph, the horizontal axis are the hours of a 'typical day' whereas the vertical axis is either the indoor air temperatures for the housing or the outdoor air temperature. Confirming the observations of Mahadevia, et al., the indoor air temperature of the informal housing is greater than the outdoor air temperature [26] and peaks near solar noon. The comparison of the informal and formal housing shows a maximum 8.2 °C reduction in indoor air temperature, but thermally similar performance at night. This latter conclusion is to be expected with nighttime ventilation in use.

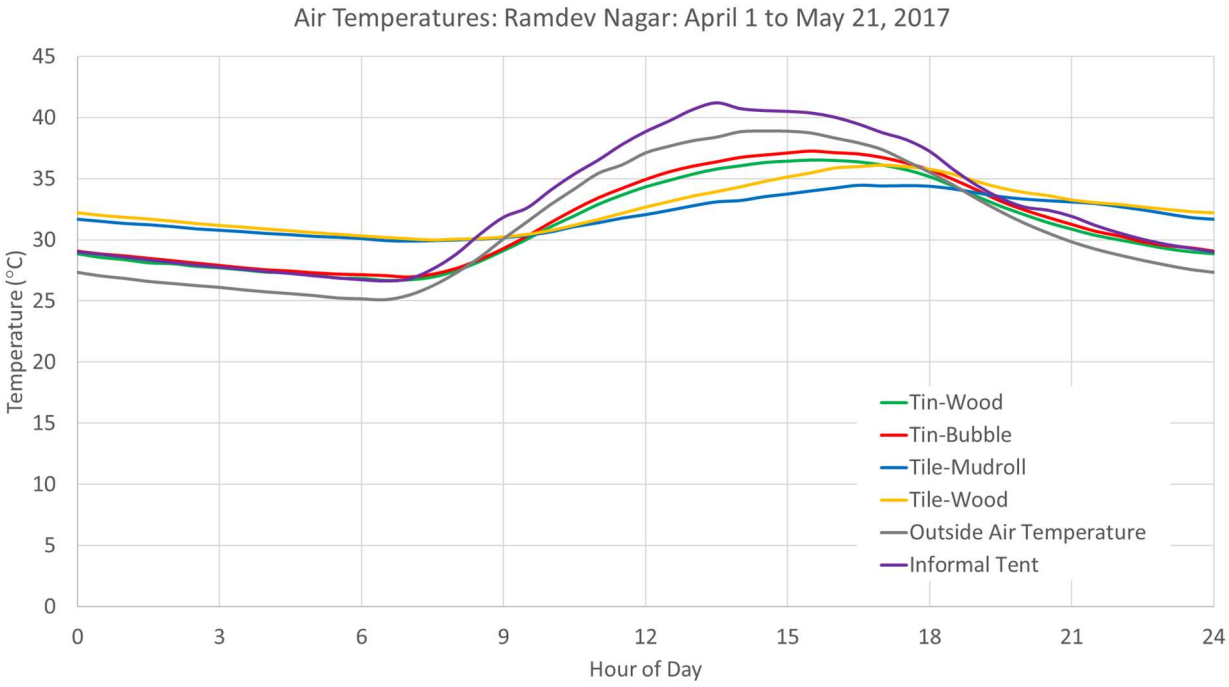

Figure 10: Interior Air Temperature of Informal Home as compared to the double layer roof homes of Figure 1

Expanding on this, Figure 11 highlights the hottest three-day timeframe during the measurement period. Note that the scale has been shifted relative to Figure 10. In Figure 11, the ordering of the roofing approaches remains constant, although the spread maximum air temperature difference between the informal tent and the Tile-Mudroll structure raises to 10.9 °C. This is encouraging to note that even as temperatures rise, the relative performance against the informal tent home increases.

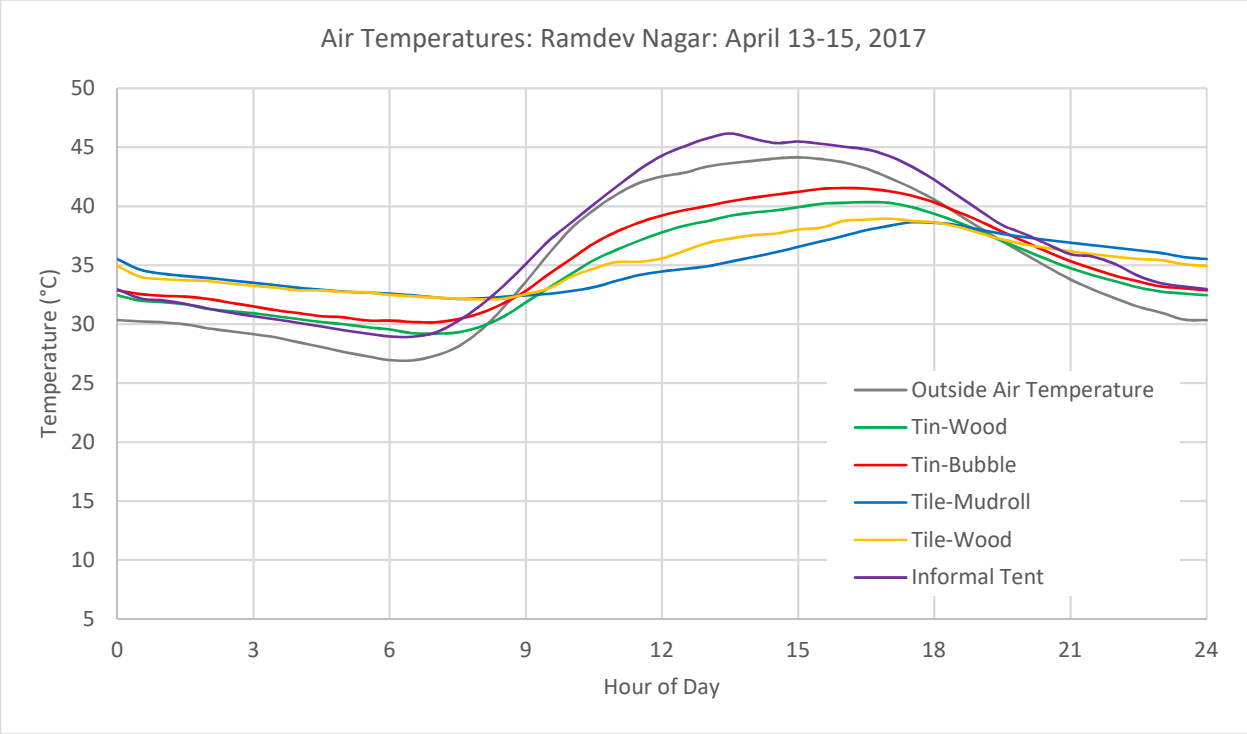

Figure 11: Interior Air Temperature of Informal Home as compared to the double layer roof homes of Figure 1

2.2 Clay tile roofing: a societal point of view

Much of this work will mention the inclusion of Mangalore tile ("tile") roofing, also known as French interlocking clay tile [59]. For the geographic area and target population to which this work will benefit, tile roofing is both an established form and resilient building material that is socially preferred. From the aesthetic point of view, part of this preference may be due to the social aspirational qualities that accompany this roof styles, where clay tiles are associated with the identity of a home that is enduring through time via the usage on government facilities [60, 61]. Further, these tiles were provided on many permanent structures due to the numerous production facilities in the Mangalore area throughout the post-World War II era to the 1990s, having replaced thatch since their introduction in 1864 [62] and cementing their establishment as the roofing of choice for structures that may continue to this day.

A shift in government encouragement is also a potential candidate for a reason why the tiles have fallen out of favor for some, where asbestos or synthetic roofing may be encouraged over the tiles, [61] despite the established risk of asbestos in housing [63, 64, 65] and the suitability of heavier materials for monsoon rains. To a casual observer, these partially handmade tiles may indicate a lack of standardization of material form, but the physical properties (dimensions, tolerances, weight, tie down hole, water absorption, strength, system-wide water shedding) are all detailed and standardized [66].

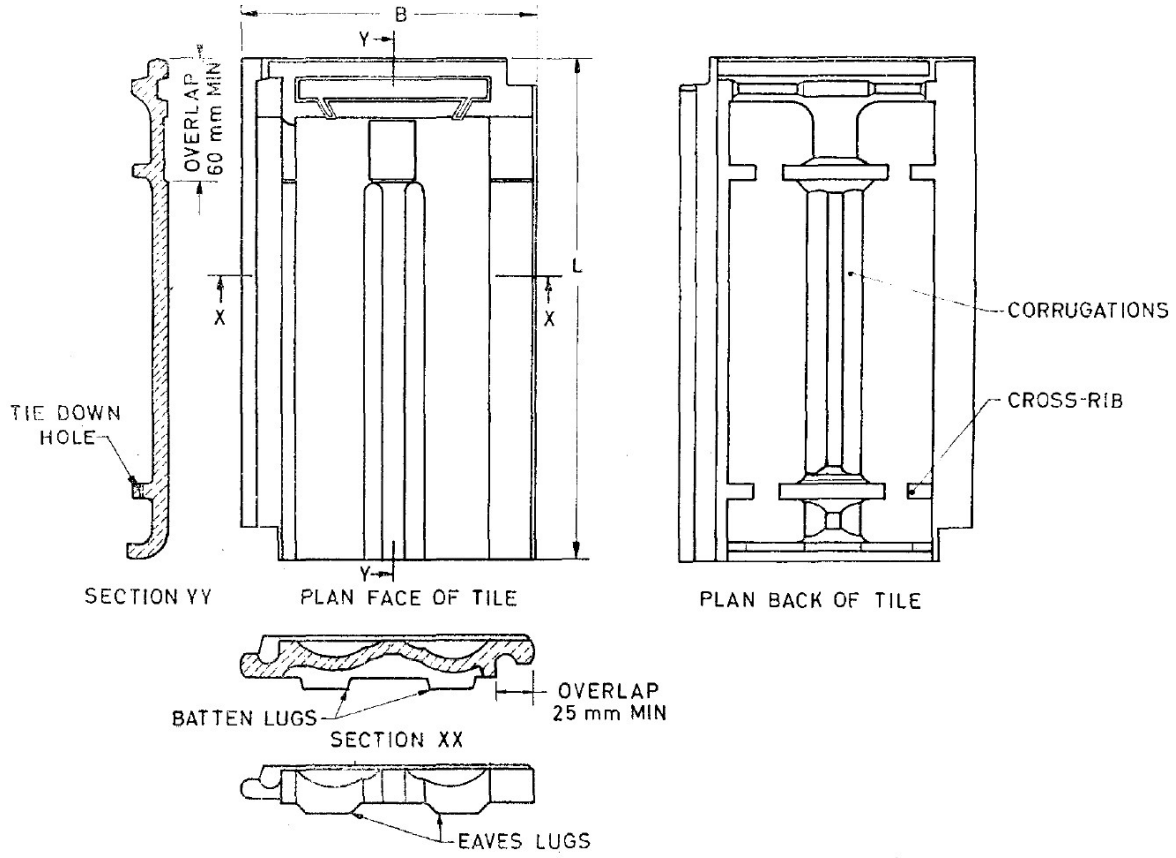

Figure 12: Mangalore Tile Schematic (Fig. 1 from [66])

From the physical point of view, the tiles are naturally fire-resistant, eco-conscious, and sturdy [67]. From a social architectural point of view, the indigenous nature of the roofing literally resembles the earth from which the homes are made, represents a community's role in building a home (via the engrained human-machine coproduction that is the nature of the tiles), and engrains both tradition and heritage into the building fabric. [68] In regards to the thermal performance of these tiles, natural variations resulting from the latter stages of the forming and firing process of these tiles may be beneficial in that it allows for an exchange of air through the external roofing layer. A visualization of this is provided below, in Figure 13.

Figure 13: Potentially Thermally Advantageous Porosity of Mangalore Tile Roofing

2.3 Ventilation of the cavity

Gradillas, Nelson, and the author's previous work all stated the importance of nighttime ventilation towards improving thermal comfort in the subsequent day. Figure 10 shows that the most significant system towards maintaining a lower daytime air temperature is the Tile-Mudroll system. Yet, this system is also tied with the Tile-Wood system for remaining the warmest throughout the night. A classical nighttime ventilation approach would ventilate the interior of the structure through a gradual increase in the total volumetric air change rate. However, this approach fails to consider the impact on the occupants during this time. Notably, with such high air change rates and the associated wind chill, the occupants feel cold. [35] If the air change rate for the interior of the structure is limited, the next step is to work to control the air within the air cavity, the first of which is to increase the ventilation of the cavity at the same times that nighttime ventilation would classically be used.

To evaluate the potential for ventilation of the cavity, an Onset Computer Corporation HOBO UX120-006M 4-channel analog logger was used with four TMC6-HD thermocouples arranged as in Figure 14. Using a test chamber in Bhuj, the roof of the test chamber was natural divided into four

sections by the rafters. Two adjacent sections were left in their natural state while the other sections were supplemented with the addition of a Havells i-Cool 175mm diameter fan, one per section.

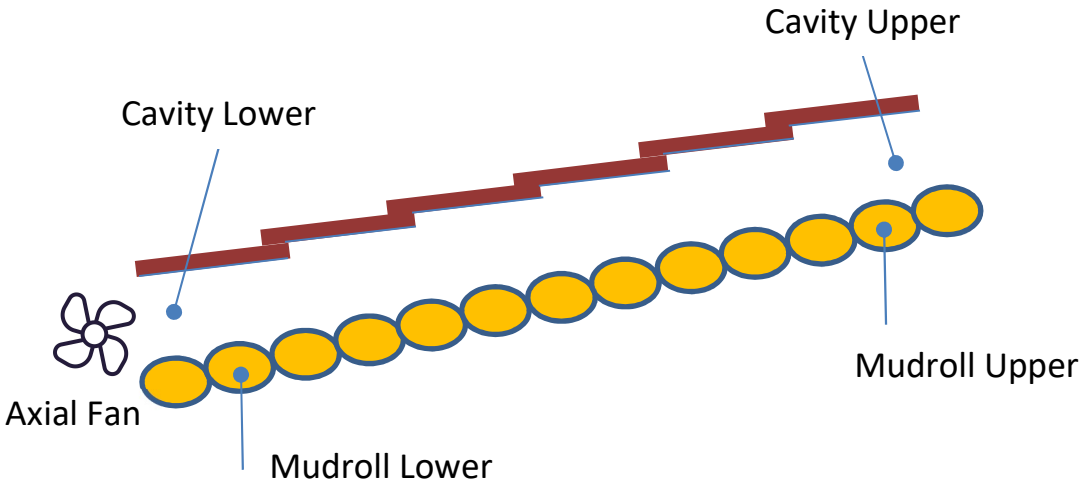

Figure 14: Location of thermocouples for cavity ventilation testing

These fans were selected based on local availability and selected based on their overall diameter being able to fill the available horizontal space, as well as the highest measured air speed of the available options in the local marketplace. To assess the available options, a Pacer DA30 vane anemometer was used to measure the air speeds at 1 diameter downstream and area averaged to provide an educated guess on the volumetric flowrate. At speeds of ranging from 3.5 to 5.0 m/s, the fan was believed to have a volumetric flow rate of 6.5 m^3/min (40 m^3/min rating [69]), which for a cavity volume of roughly 0.13 m^3 for each of the four sections in the test chamber, would have a theoretical upper limit of 2,770 air changes per hour assuming no resistance through the length of the cavity. This is likely a poor assumption due to the geometry of the fan placement and construction of the cavity, but establishes an upper limit. These airflow numbers have extremely low accuracy and should not be used for any rigorous analysis. The fans were installed as in Figure 15.

Figure 15: Fans Installed on Half of the Roof of the Structure (Bhuj, India)

The fans were manually turned on from 8 PM to 8 AM local time between May 30th and June 4th, 2019, inclusive. An Onset Computer Corporate HOBO UX90-004 Motor Logger was also installed to ensure the accuracy of the start and stop times. The collected data was then compiled into an 'average day' and is shown in Figure 16.

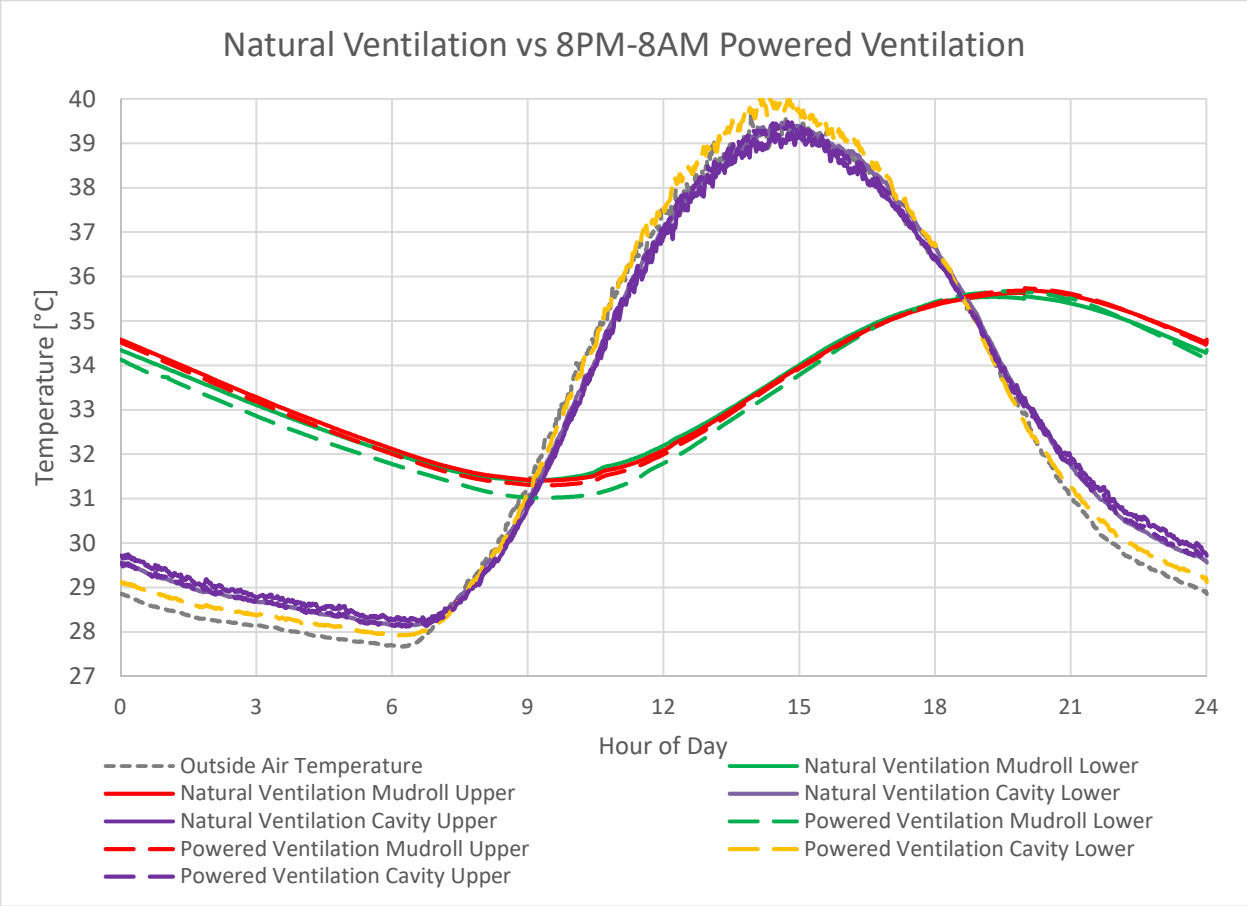

Figure 16: Natural Ventilation vs Power Ventilation Experimental Results

In Figure 16, the horizontal axis is the hour of the day, the vertical axis is the recorded temperature, and the individual plots are color-coded to each other. The Natural Ventilation options are shown in solid lines, where the Powered Ventilation options are shown in dashed lines. Based on the data, there is a marginal improvement between the temperatures recorded on the natural ventilation side of the test chamber, and those recorded on the powered ventilation side of the test chamber. The lower area of the mudroll (Green lines) are roughly 0.4 °C lower than that of the naturally ventilated side. The upper section of the mudroll (Red lines) is effectively unchanged from the naturally ventilated side.

A similar takeaway is present from the cavity air temperatures, where the difference is present for the lower elevation values, but not for the upper elevation values. This suggests that, while the idea has merit, the powered ventilation option is not substantially driving the performance of the system. This could be due to (a) the fans being undersized to have a significant impact on the convective heat transfer coefficient of the system as a whole (b) a porous outside surface, thereby diminishing the driving pressure of the fan, or (c) other factors, such as wind, dominating the performance of the system.

Nonetheless, while the test may seem to be fruitless, it does show the relation between the cavity air temperature and the outside air temperature. For the late morning and early afternoon hours, the lower cavity air temperature closely follows that of the outside air temperature, but the upper cavity air temperature lags by about 0.5 °C until around noon. This is important to note since it implies that heat is being absorbed by the mudroll as the air passes through the length of the cavity. Since the air leaving the

cavity is cooler than that entering the cavity, it means that the system has potential improvements to be had from restraining the airflow throughout the early part of the daylit day.

It also means that the positively buoyant forces from the upper hot tile dominate the airflow despite the negatively buoyant forces from the lower cooler mudroll, opening up the possibility of non-unidirectional air flow within the cavity.

2.4 Closing off the cavity

A second iteration of the test was conducted then with the addition of a shutter to constrain the airflow. This test, from June 5th to June 7th, 2019 inclusive, maintained the same times when the fan was energized, but the lower section of the roof at the eave was packed to restrict airflow from 8 AM to 1 PM.

Since this experiment was a very short run and there is a heightened amount of volatility in the outdoor air temperature data, it is improper to present it in an 'averaged day' style. This is shown in Figure 17.

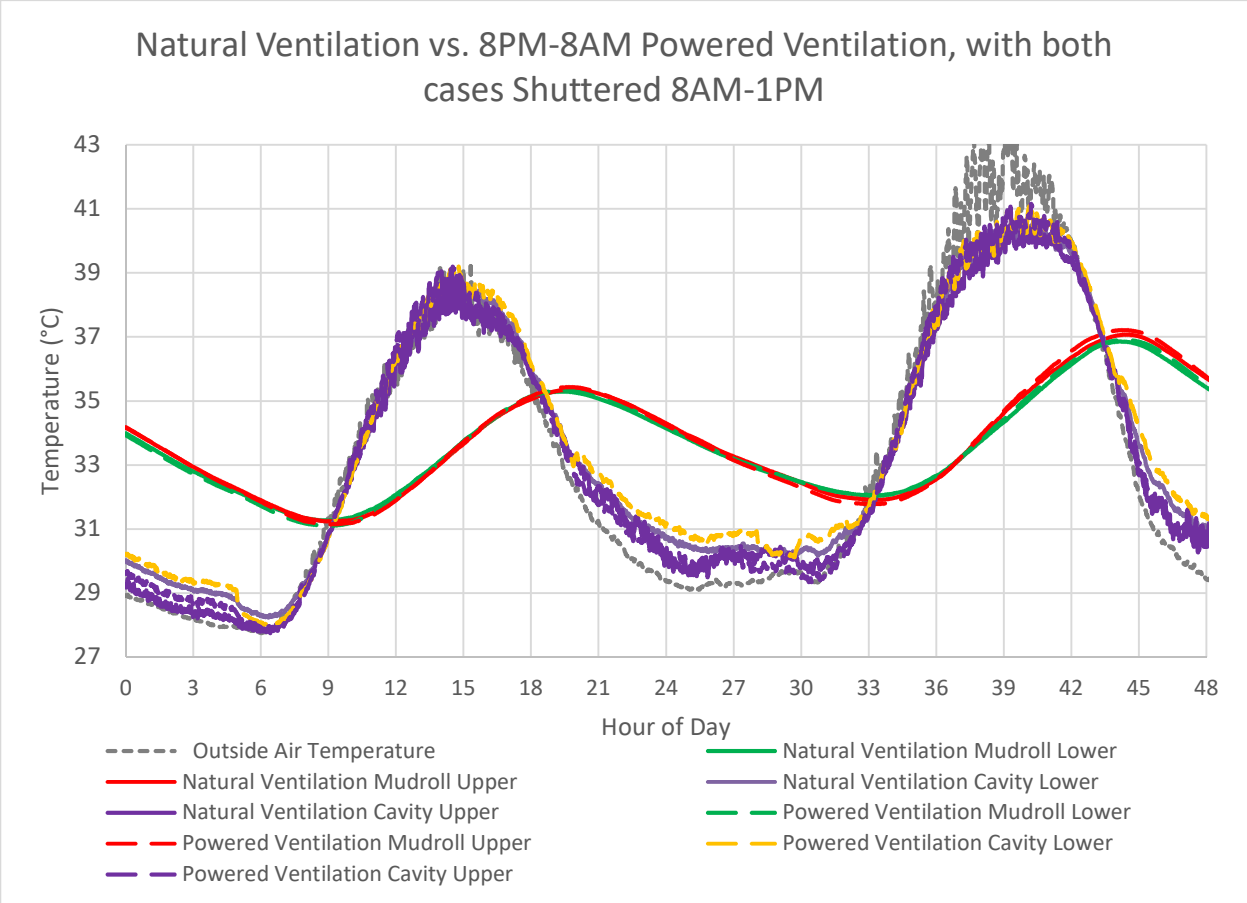

Figure 17: Two-day test of Natural Ventilation vs Powered Ventilation, including shutters

With the inclusion of the shuttering on the lower side of the cavity, the lower cavity temperature no longer leads the upper cavity temperature through the early morning hours. Instead, the values trend together. Aside from that, it is difficult to make conclusions from this dataset alone. As such, this is an area worthy of future investigation.

2.5 Modeling Theoretical Performance to Understand Significant Factors of Above Sheathing Ventilation

Whereas a bulk of the previous experimental work in the 2018 update and presented thus far is experimental based, the existing work failed to directly establish a principles-based model to understand the importance of thermal massing, roof color, air gap spacing, roof inclination angle, seasonality, or location. To better understand how to improve on this performance, this work includes the development of a lumped capacity assumption and hourly data both from an experimental chamber in Bhuj and EnergyPlus Weather (EPW) files.

Using first principles and material properties, this model uses an assumed one-dimensional model of heat flow normal to length of the roof, and is an energy balance approach using a first order difference model with fifteen-minute timesteps. A heat flow representation of the model is shown in Figure 18. Key assumptions are:

- both upper (tile) and lower (mudroll) layers are modeled as lumped thermal masses and considered uniform in both depth (thickness) and length (height along roof);
- the upper layer (tile) temperature is based on an energy balance including a mixed (forced & natural) convection over a flat plate (wind), solar infrared radiation on the top surface, infrared radiation at the lower surface, and natural convection from the lower surface;
- the lower layer (mudroll) temperature is based on an energy balance including natural convection from the cavity and infrared radiation from the upper layer (tile), with the lower surface of the lower layer (mudroll) being adiabatic;
- changes of air or material properties due to humidity are neglected;
- the cavity itself is of uniform spacing; and
- there are no impediments to free air flow at the eave or ridge.

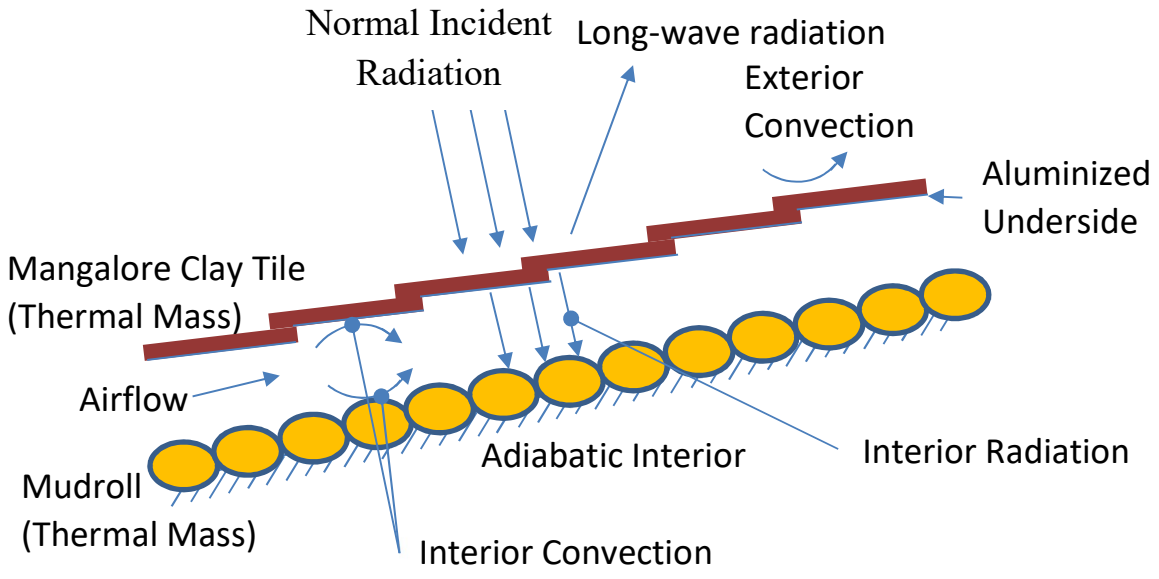

Figure 18: Model of double layer roof system using Mangalore tiles and a mud roll interior layer

To model the performance of the system using the EPW files for Bhuj, India, the first step taken was to linearly interpolate the inter-hour data to fill 15-minute increments. A 15-minute increment was chosen so as to remain cognizant of the available computing power, and could easily be reduced should more resolution be needed. Building up the physical relations, the sky temperature will be needed to determine long-wave radiation exchange, and thus the fictious sky emissivity was derived from Clark & Allen [70, 71] (Equation (1)) and Walton [72, 71] (Equation (2)).

$$\varepsilon_{sky,clear} = 0.787 + 0.7964 * \ln(\frac{T_{dp}}{273}) \quad (1)$$

where $\varepsilon_{sky,clear}$ is the clear sky emissivity and T_{dp} is the dewpoint temperature, in Kelvin.

$$\varepsilon_{sky} = \varepsilon_{sky,clear}(1 + 0.0244N - 0.0035N^2 + 0.00028N^3) \quad (2)$$

where ε_{sky} is the sky emissivity, and N is the opaque sky cover, in tenths.

Sky temperature was then approximated through an intermediate Horizontal Infrared Radiation Intensity nested inside the Energy-Plus Sky Temperature calculation, the result of which is Equation (3) [71].

$$T_{sky} = T_{db} \sqrt[4]{\varepsilon_{sky}} \quad (3)$$

where T_{sky} is the temperature of the sky, in Kelvin, T_{db} is the drybulb temperature, in Kelvin, and ε_{sky} is the sky emissivity from Equation (2).

Combining Equation (2) and Equation (3) and evaluating for the Bhuj EPW-based data, the sky temperature scales linearly with the dry bulb temperature, such that the linear correlation between the two can be approximated as in Equation (4) with an R^2 coefficient of 0.97.

$$T_{sky} = 1.12 * T_{db} - 48.12 \quad (4)$$

Assuming that the roof is in a sufficiently rural area such that view between the roof and the sky is unimpeded, the amount of long-wave radiation heat flux per unit area from the roof to the sky ($\dot{q}_{LW\ radiation}$, in watts) can be written as in Equation (5). In line with the illustration of Figure 18, a positive number is defined as a heat outflow from the system.

$$\dot{q}_{LW\ radiation} = \varepsilon_{rooftop,outer}\sigma(T_{rooftop}^4 - T_{sky}^4) \quad (5)$$

where σ is the Stefan-Boltzmann constant, $T_{rooftop}$ is the temperature of the rooftop as a lumped mass, labeled as 'Mangalore Clay Tile' in Figure 18 and evaluated in Kelvin, and $\varepsilon_{rooftop,outer}$ is the long wave emissivity of the outer surface of the rooftop (clay tile) layer.

Shortwave radiation flux per unit area is accounted for by the multiplication of the Normal Solar Incident Radiation, $\dot{q}_{incident\ solar}$, and the rooftop's solar absorptivity, $\alpha_{rooftop}$. This is then combined

with the long-wave radiation in Equation (5) to produce Equation (6) for net radiation exchange, $\dot{q}_{net\ radiation\ gain}$.

$$\dot{q}_{net\ radiation\ gain} = \dot{q}_{incident\ solar}\alpha_{rooftop} - \dot{q}_{LW\ radiation} \quad (6)$$

The heat loss rate per unit area due to exterior convection, $\dot{q}_{exterior\ convection}$, was modeled based on the correlation from McAdams [73] for turbulent flow over a flat plate, shown in Equation (7).

$$\dot{q}_{exterior\ convection} = (5.7 + 3.8v)(T_{rooftop} - T_{outside\ air}) \quad (7)$$

where v is the direction-independent velocity of the ambient wind, in m/s, and $T_{outside\ air}$ is the outside air temperature, in Kelvin.

Interior convection between the two individual plates and the air within the cavity was modeled for the geometry (2.24 m long, 0.58 m wide, 0.1 m deep) of the Bhuj experimental setup (Figure 19, page 41, for the experimental data) or housing (for the full-scale impacts), using Azevedo and Sparrow's [54] inclination-adjusted global correlation, applicable to the cases of either or both of the external and internal layers being warmer than the air temperature. This correlation is reproduced in Equation (8) and is evaluated independently for each surface, the upper tile or the lower mudroll.

$$Nu_s = \frac{h_{c,i}S}{k_{air}} = 0.673[\left(\frac{S}{L}\right)Ra_s cos\theta]^{0.25} \quad (8)$$

where
Nu_s is the Nusselt number dependent on S,
$h_{c,i}$ is the convection coefficient for the wall surface i,
S is the interplane spacing (thickness of the channel, 4 inches (~0.1 m) for these cases),
k_{air} is the thermal conductivity of the fluid (air),
L is the channel length (3.87 m for the full scale housing or 2.24 m for the experimental setup),
Ra_s is the Rayleigh number ($Ra_s = [g\beta(T_{wall} - T_{outside\ air})S^3/\nu^2]Pr$),
g is the acceleration due to gravity (assumed constant at 9.806 m/s^2),
β is the coefficient of thermal expansion ($1/T_{outside\ air}$),
T_{wall} is the temperature of the either the upper ($T_{rooftop}$) or lower ($T_{mudroll}$) layer,
$T_{mudroll}$ is the temperature of the lower surface of the cavity (labeled as "Mudroll" in Figure 18),
ν is the kinematic viscosity,
Pr is the Prandtl number, and
θ is the inclination angle (27°).

It should be noted that this approach is inherently limited since the Azevedo and Sparrow correlation is a function of the ratio of the height of the air cavity to the length of the cavity and does not account for either the inherent variations of the boundary layer between different geometries (S/L ratios) or the change in temperature as a function of length inside the naturally ventilated cavity, both of which may change the correlation for very long cavity lengths. Further, the conclusions of Azevedo and Sparrow were not explicitly evaluated for cases where surfaces may be cooled relative to the air within the cavity. These factors are important to note since smoke tracing within the cavity confirms that local wind

conditions dominate the direction of airflow within the cavity, and this Azevedo and Sparrow convection model assumes no wind is present. Due to the lumped approximation for the physical surfaces, the McAdams exterior convection values use the same air temperature and surface temperature inputs as the Azevedo and Sparrow correlation uses for interior convection values, and, on average, the McAdams-based exterior convection heat transfer is roughly seven times that of the Azevedo and Sparrow-based interior convection heat transfer. The model assumes that the interior surface of the lower surface of the mudroll is adiabatic and is an approximate model. Yet, it can be useful to help illustrate the relative importance of system inputs. A pictorial illustration is provided in Figure 18.

The thermal-fluid properties of air are based on a dataset using an assumed 10^5 Pascal absolute pressure (0.9869 atm) [74, 75], with the thermal conductivity of air, k_{air}, based on a combined dataset including the 1.00 bar datapoints of Stephan and Laesecke [76]. These thermal-fluid properties were then linearized based on temperature across the range of 0 °C to 100 °C, with the linear regression and R^2 coefficient (n=11) based on published data listed in the table below.

Property, symbol [units]	Linear Regression (T = temperature [°C])	R^2 coefficient	Value at 20 °C
Density ρ [kg/m^3]	-0.0034 T + 1.2585	0.9924	1.1905
Isobaric Specific heat, c_p [J/kg·K]	0.0555 T + 1005.3	0.9606	1006.41
Thermal Conductivity, k_{air} [W/m·K]	(0.0703 T + 24.295) ·10^{-3}	0.9983	0.0257
Dynamic viscosity, μ [kg/m·sec]	(0.0047 T + 1.7306) ·10^{-5}	0.9997	1.83 ·10^{-5}
Kinematic viscosity, ν [m^2/sec]	(0.01 T + 1.3366) ·10^{-5}	0.9991	1.54 ·10^{-5}
Prandtl, Pr [unitless]	(-4 ·10^{-6} T) + 0.7135	0.8560	0.7134

Table 1: Thermal-Fluid Properties of Air at 10^5 Pa (0.9869 atm)

With these values, Equation (8) is then rearranged to determine the value of $h_{c,i}$ for both the upper and lower surfaces to arrive at $\dot{Q}_{cavity\ convection,rooftop}$, the heat flow due to convection from the upper layer (tile) into the air cavity, and $\dot{Q}_{cavity\ convection,mudroll}$, the heat flow due to convection from the lower layer (mudroll) into the air cavity. A is the area term associated with the plane exposed to the cavity, which is assumed to be an equal value for both the upper and lower layers. For the initial step of the model, the rooftop and mudroll temperatures are assumed to be equal to the outside air temperature at the first time step.

$$\dot{Q}_{cavity\ convection,rooftop} = A\dot{q}_{cavity\ convection,rooftop} = h_{c,rooftop}A(T_{rooftop} - T_{outside\ air}) \quad (9)$$

$$\dot{Q}_{cavity\ convection,mudroll} = A\dot{q}_{cavity\ convection,mudroll} = h_{c,mudroll}A(T_{mudroll} - T_{outside\ air}) \quad (10)$$

The sum of these two values then becomes a total cavity convection value, $\dot{Q}_{cavity\ convection}$, which is the total heat removed from the system through the convection in the cavity.

$$\dot{Q}_{cavity\ convection} = \dot{Q}_{cavity\ convection,rooftop} + \dot{Q}_{cavity\ convection,mudroll} \quad (11)$$

Inter-surface, across the cavity thermal radiation, $\dot{q}_{cavity\ radiation}$, assumes that the cavity is sufficiently long such that the decrements to the view factor are marginal. In practice, the view factor from one surface to both open ends of the cavity is 0.037 in the test chamber, and 0.022 in the full-size home (based on [77]). Equation (12) describes this radiation heat transfer.

$$\dot{q}_{cavity\ radiation} = \varepsilon_{rooftop,inner}\varepsilon_{mudroll}\sigma(T^4_{rooftop} - T^4_{mudroll}) \quad (12)$$

where $\varepsilon_{rooftop,inner}$ is the long-wave emissivity of the inner surface of the rooftop (clay tile) layer and ε_{mudro} is the long-wave emissivity of the mudroll.

Building on the implicit assumption of a constant emissivity or absorptivity property, the surface radiative properties of the various material options can be summarized in Table 2. All material options are evaluated later with the exception of White Plaster, which is provided for reader reference.

Material	Short-wave (solar) absorptivity	Long-wave (thermal) emissivity	Sources
Clay tile, natural color	0.53-0.56	0.86-0.88	[78, 79]
Clay tile, white paint	0.27	0.89	[79]
Clay tile, weathered	0.60-0.63	0.86-0.88	[79]
Clay tile, weathered white paint	0.66-0.69	0.89	[79]
White paint (0.017 in.) on aluminum	0.20	0.91	[80, 81]
White plaster	0.07	0.91	[80, 81]
Aluminum foil, new	0.15	0.04	[82, 83, 80, 81]
Aluminum, weathered (75S-T6, 20,000 hr on DC-6 aircraft)	0.54	0.16	[82, 83]
Mudroll ("dry sand")	0.82	0.90	[80, 81]
Tin sheet	0.32	0.14	[39]
Wood	--	0.90	[82]
Cotton, white	0.29-0.55	0.77	[84, 85, 86, 87, 88]
Polyester, white	0.60	0.77	[84]

Table 2: Radiation surface properties of selected materials

Note that while the pictorial illustration (Figure 18) shows the mudrolls as a collection of circles in section, the concavity between the rolls is filled with a mud-based mortar applied by hand during installation of the mudroll. The remaining concavity is estimated to reduce the total mass of the mudroll by 2.4% and this is not included in spreadsheet model. For inputs into the model, the radiative properties of the outer tile were assumed to be in line with that of dried clay and the radiative properties of the mudroll were assumed to be in line with that of Adobe. Physical properties of the clay tile were assumed to be in line with fired clay brick [80], and physical mudroll properties were obtained by those published

by Abanto, et al. and Wang, et al. [89, 90]. The density of the mudroll used in practice was based on field measurements of a mudroll assumed to be a perfect cylinder (1,472.5 kg/m^3). As expected, this is lighter than that of pure adobe and can be used to conclude that the mudroll system can be approximated as clay with 13.6% air content.

As noted above, this model was evaluated on a quarter-hour basis. Each timepoint was evaluated for both the temperature of the tile and the temperature of the mudroll, then using the above equations to determine the net heat flow ($\dot{q}_{net\ heat\ flow}$) for each time step following the conventions illustrated in Figure 18. This is shown below in Equations (13) and (14).

$$\begin{aligned}\dot{q}_{net\ heat\ flow,upper\ thermal\ mass} \\ = \dot{q}_{net\ radiation\ gain} - \dot{q}_{exterior\ convection} \\ - \dot{q}_{cavity\ convection,upper\ thermal\ mass} - \dot{q}_{cavity\ radiation}\end{aligned} \quad (13)$$

$$\dot{q}_{net\ heat\ flow,lower\ thermal\ mass} = \dot{q}_{cavity\ radiation} - \dot{q}_{cavity\ convection,lower\ thermal\ mass} \quad (14)$$

Since the time steps were large enough that the approximation could become unstable due to heat flows being evaluated at set time points and evaluated for larger time spans, some amount of data smoothing was required to remove instabilities in the approximation. The simplest means to do this was to use a basic exponential smoothing approach by equally weighting the net heat flow of the previous timestep and the timestep being evaluated. Using this approach, the net heat flow is multiplied but the time increment, Δt, and divided by the applicable thermal mass' (clay tile, mudroll) physical properties. This value is then added to the previous time step to determine the temperature (T_t). This is shown in Equation (15). Physical properties of core materials are then shown in Table 3.

$$T_t = \frac{(\dot{q}_{net\ heat\ flow,t} + \dot{q}_{net\ heat\ flow,t-1})\Delta t}{2t_{thermal\ mass}\rho_{thermal\ mass}c_{p,thermal\ mass}} + T_{t-1} \quad (15)$$

where
$t_{thermal\ mass}$ is the thickness of the thermal mass (clay tile or mudroll);
$\rho_{thermal\ mass}$ is the density of the thermal mass;
$c_{p,therm\quad mass}$ is the specific heat of the thermal mass; and
T_t is the temperature of the thermal mass at the current time step.

Material	Thickness [m]	Density [kg/m^3]	Specific Heat [J/kg*K]	Source(s)
Clay Tile	0.02	1600	920	[91, 92]
Mudroll	0.1	1,472.5	750	[89, 90]
Tin Sheet	0.005	7,304	226	[35, 80, 93]
Wood (1" pine)	0.0254	497	2,805	[80, 93]

Table 3: Physical Properties of Selected Roofing Materials

2.5.1 Evaluating the Lumped Capacity Above-Sheathing Ventilation Model

Even without considering the interior of the structure in the lumped approximation, using this spreadsheet-based approach yields an acceptable level of error (Root Mean Square Error = 0.66°C, n=24, shown in Figure 23) when compared against data from a field experiment run in Bhuj during the summer of 2018. In the experimental setup, a test chamber with 9 m^2 of floor area and a south-facing roof with a 27° inclination was constructed with a double layer roofing setup (similar to Figure 2) using the Mangalore tile exterior with aluminized underside. The exterior of structure was made of white-painted sandstone block and the windows remained closed. Further, a boundary wall was immediately adjacent to the chamber on the northwest and northeast sides of the structure. Low-height trees were present on the exterior of the property's boundary wall to the northeast. Figure 19 shows this setup as well as a view up into the air cavity from the eave.

Figure 19: Test Chamber

Prior to evaluating the system as a whole, it should be noted that field measurements taken in May of 2019 with a Pacer DA30 vane anemometer which recorded values of 0.5-0.7 m/s within the cavity on a calm day. However, with modest wind or gusts, the air velocity within the cavity is governed by the wind instead. One set of readings at 15 second increments for five minutes suggested an average air cavity air velocity of 1.7 m/s were possible when ambient wind component parallel to the major axis of the air cavity were recorded near 1.9 m/s at a local weather station during that time period ([39] p. 111). Due to possibilities of setup and timestamp error, this last comparison should not be used for complete validation of approach, but only to confirm the wind-dominated ventilation within the cavity.

The data presented below is based on an 'average day' approach, whereby the temperature of the hours of the day are defined by the average corresponding hours within the time period of interest. In the following example, the data of interest is 2-April-2018 to 9-April-2018, inclusive. The experimental results presented in Figure 22 are those taken from the Bhuj chamber (Figure 19) and the lumped approximation values are those derived from the lumped approximation. For this case, the weather data used to define the lumped approximation were based on the nearby weather station and assumed a clear sky. This clear sky assumption was confirmed using the 'Daily Observations' field of the historical weather feature of Weather Underground for the Bhuj Airport Station. [94] Further, the wind was

assumed to be direction agnostic, meaning that despite the potential for the wind to be in the direction of the downslope of the roof and therefore implying that a roof section was on the leeward side of the wind, no accounting for this effect was included. For the occupied homes, the roof structure was an 'A' in shape and has two nearly equal roof sections of equal nominal pitch. The test cell only had a single pitch roof.

For the single pitch roofing of the test cell, local observations with a smoke pencil confirmed suspicion that incident wind can dominate the buoyancy effect and reverse flow direction.

The weather station data was collected with an Onset HOBO® Micro Station (H21-USB) data logger matched with sensors for wind speed (S-WSB-M003), wind direction (S-WDA-M003), solar radiation (S-LIB-M003), and temperature/relative humidity (S-THB-M002). These were installed 3.4 kilometers northeast by east of the experimental site and maintained with lithium batteries on a six-month rotation. The wind direction is aligned with magnetic north, as determined by a recreational compass (Suunto A-10), and thus has a higher degree of uncertainty than desired. The weather station installation is shown in Figure 20.

Figure 20: Bhuj, India weather station. From left to right: Solar radiation sensor, Temperature/RH sensor in solar shield, wind direction sensor, and wind speed sensor.

The mudroll data collection utilized a HOBO UX 120-006M datalogger with two TMC6-HD and two TMC20-HD air temperature sensors. Three of these thermocouple sensors were placed within the air cavity, with the remaining thermocouple sensor placed into the center of the mudroll.

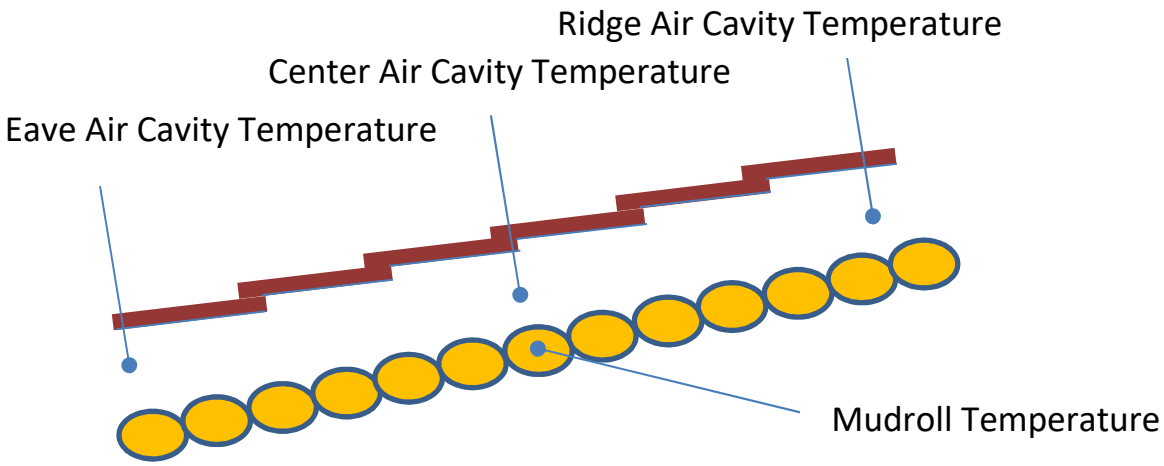

Figure 21: Double Layer Roofing Instrumentation Locations

During the period of interest, the average outdoor air temperature was 29.6 °C, peaking at 37.9 °C around 3 pm local time. Comparatively, the ceiling (mudroll) temperature averaged 30.8 °C with a peak of 34.2 °C around 5:30 PM. A comparison of the double layer experimental results can be seen in Figure 22, as referenced against the outdoor air temperature (OAT) at that time.

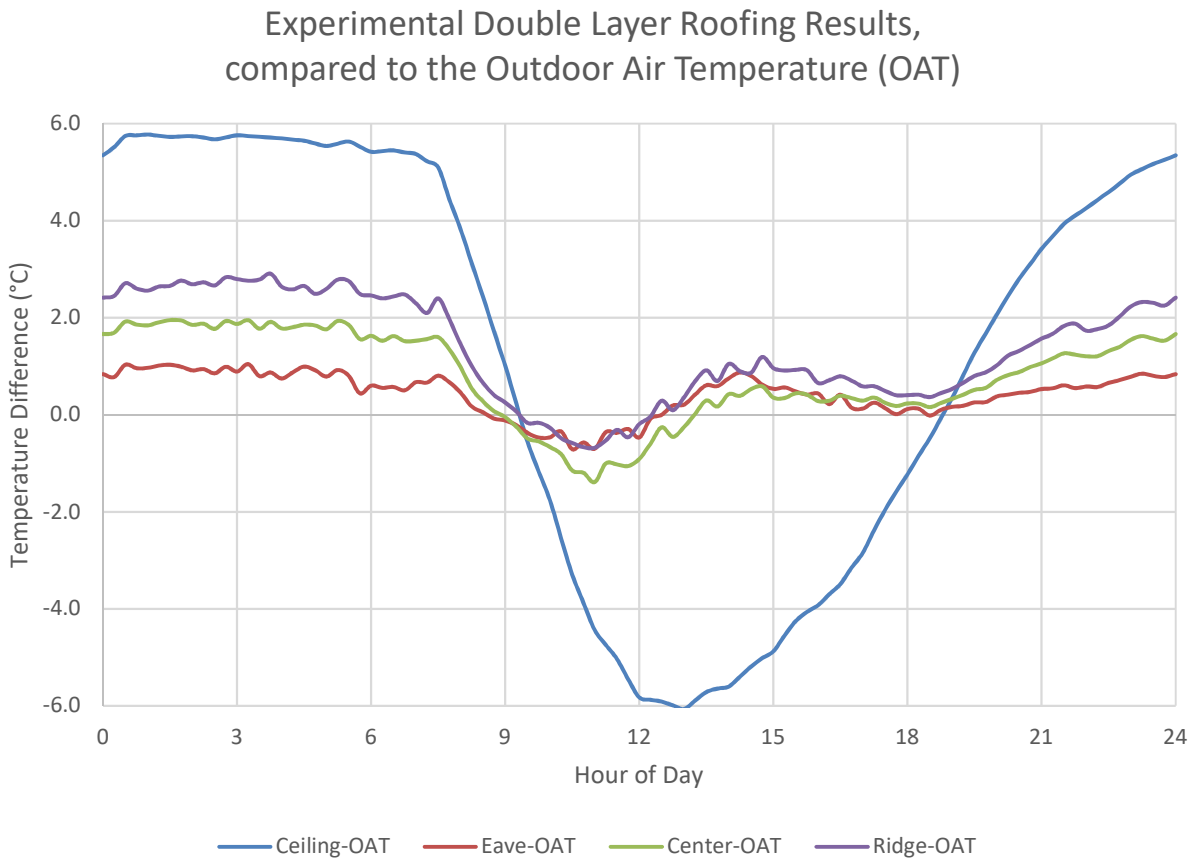

Figure 22: Experimental Double Layer Roofing Results, compared to the Outdoor Air Temperature (OAT)

During the morning hours, the ceiling remained considerably warmer (~5.75 °C) than the prevailing outdoor air temperature. Note that this experimental run was completed with doors and windows closed at all times, so this curve should not illustrate the best possible thermal improvements. Shortly after noon, the system reaches peak performance compared to the outdoor air temperature, holding 6 °C cooler than the outdoor air temperature. Within the air cavity, the temperature rise from eave to ridge is roughly 2.0 °C over the 2.25 m cavity length throughout the nighttime hours, and is unclear throughout the day. This is most likely due to diminishing prevailing winds at night, allowing the stack effect to dominate. For comparison, in the lumped approximation, the temperature rise from the ambient environment to the ridge is roughly 1.3 °C in the evening hours.

With a Root Mean Square Error of 0.66 °C based on the 24-hour sample, the lumped approximation compares favorably with experimental results. Daily high temperatures were approximated at 34.7 °C compared to an experimentally recorded 34.1 °C, but the approximation was delayed about an hour as compared to the experimental case. Daily low temperatures were approximated at 27.3 °C compared to a recorded 28.1 °C, without a time delay. The shift in the maximum temperatures is likely the result of the evening sun hitting the unshaded western wall of the chamber, which is not accounted for in the lumped approximation approach.

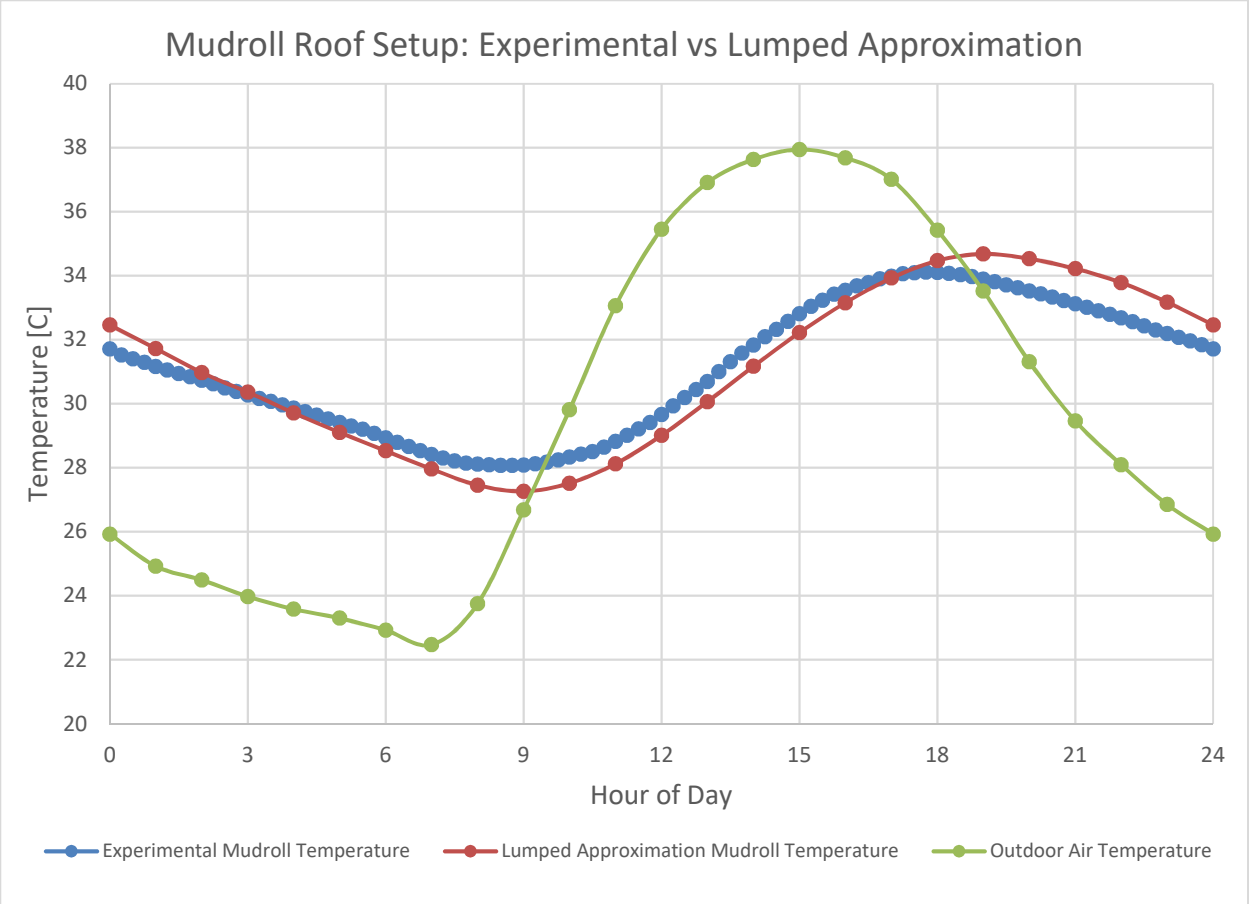

Figure 23: Lumped Approximation vs Measured Values from Bhuj-based Test Chamber

2.5.2 Applications of the Lumped Capacity Above-Sheathing Ventilation Model

Whereas Figure 23 is shown for an April time period using recorded data and the roof geometry of the test chamber, Figure 24 shows the same approach using many of the same assumptions and lumped approximation, using weather file data sourced from the US Department of Energy EPW file for the month of May in Bhuj, India and the geometry of the housing in the Ramdev Nagar community. Combined with various surface (Table 2) and material properties (Table 3), the impact of material selection, cleanliness, and weathering can be seen. Most importantly, the importance of the aluminized undercoating in limiting the net heat transfer from the upper surface to the mudroll is shown in Figure 24. Note that the approximation is solar position and orientation agnostic, but depends on the length of the cavity.

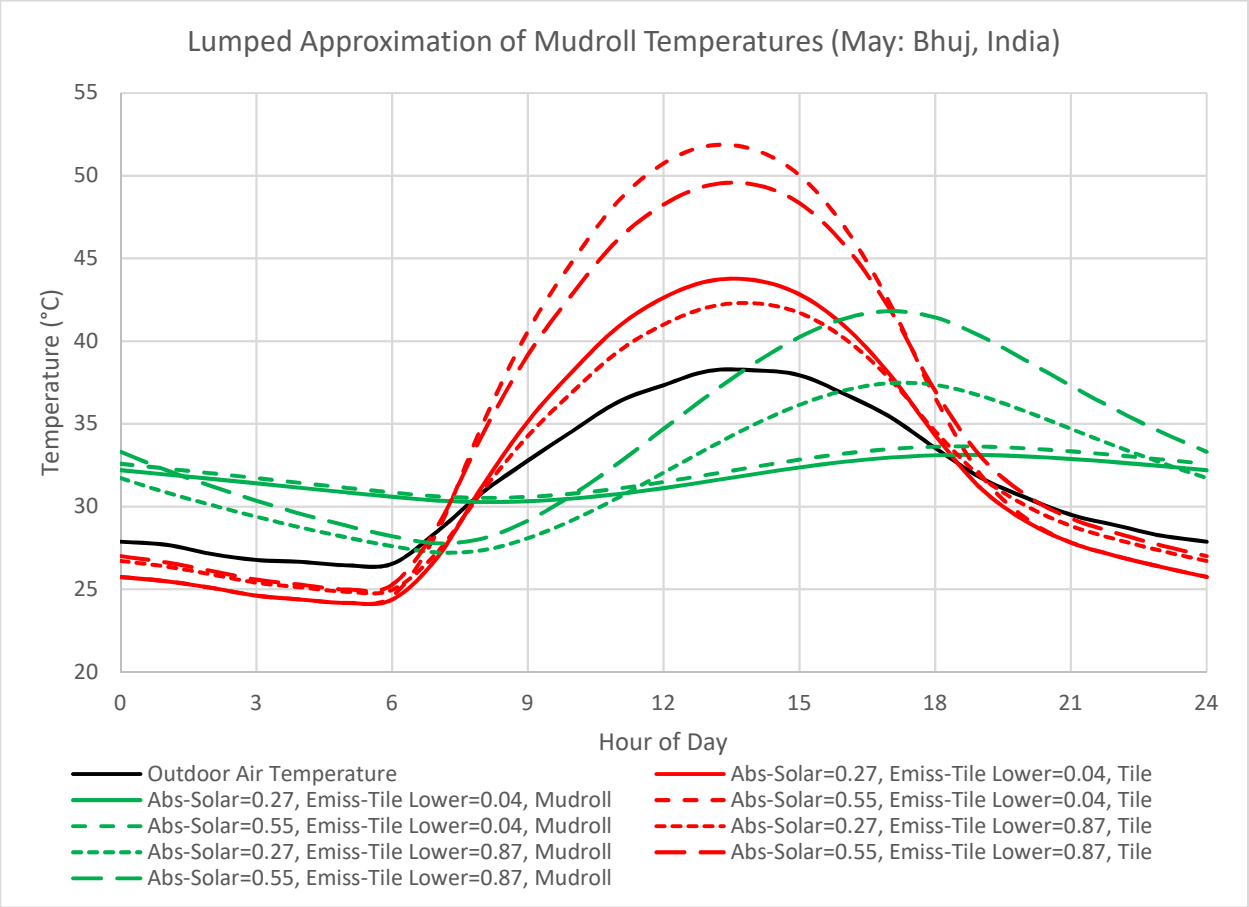

Figure 24: Lumped Approximation Mudroll System Temperatures: Exterior Tile (red) and Interior Mudroll (green) for varying surface emissivity values

Within the plot, 'Abs-Solar' refers to the solar absorptivity of the exterior surface, with values of 0.55 representing fired clay and 0.27 representing the surface of a white tile as a stand in for un-weathered white clay tiles. 'Emiss_Tile Lower' refers to the thermal emissivities of the underside of the exterior layer, with 0.04 representing an un-weathered aluminized surface and 0.87 representing the emissivity of fired clay. All four of these values are based on values published by D'Orazio, et al. [78] and Paolini, et al. [79]

The black line through the center of the plot represents the dry bulb outside air temperature, where the red lines are the temperature of the exterior tile layer, and green the temperature of the internal mudroll. For interior comfort considerations, the temperature of the mudroll is the most appropriate to look at. Based on this approximation and noting the limits of the assumptions, the most significant (8.3 °C) driver to the mudroll temperature is the presence of the aluminized underside on the exterior layer. After that, the change of the exterior surface from the natural clay color to a white surface only decreases the mudroll temperature by another 0.5°C.

If the other route is taken and the exterior surface color change is targeted first, the color change (leaving the underside untouched) results in a 4.4 °C temperature reduction of the mudroll, versus the 8.3 °C reduction if starting with the aluminized undercoating.

For a comparison to literature, Biwole [58] physically tested a double-layer roof with a large interplane spacing to cavity length ratio, and reported a 52% drop in the total heat flux when changing one inside surface of the cavity from an emissivity of 0.8 to 0.15. If those values were used for the thermal emissivity of the lower surface of the clay tile layer, this model predicts a 66% drop over the same conditions.

This conclusion of diminishing returns is corroborated by a test run in 2018 in which the topside of the Mangalore tile roofing of a test structure was varied between a natural clay (Figure 19) and a week later when the roof was painted white. In this setup, interior air temperature was recorded from a test chamber in Bhuj for a duration of two one-week periods. The roof construction was a single-slope, south-facing double skin with reflective underside, made of a Mangalore tile exterior layer, an aluminized underside, an airgap, and a mudroll interior layer. The first week had an unpainted exterior and aluminized interior of the Mangalore tile, and the interior air temperature is shown in relation to the outdoor air temperature as a red line in Figure 25. This was followed in the subsequent week by the exterior of the roof being painted white, all else remaining the same. The interior air temperature's relation to the outdoor air temperature of the second week is shown as a green line in Figure 25. For comparison purposes, cloud cover was marginal during this period and wind velocities were similar.

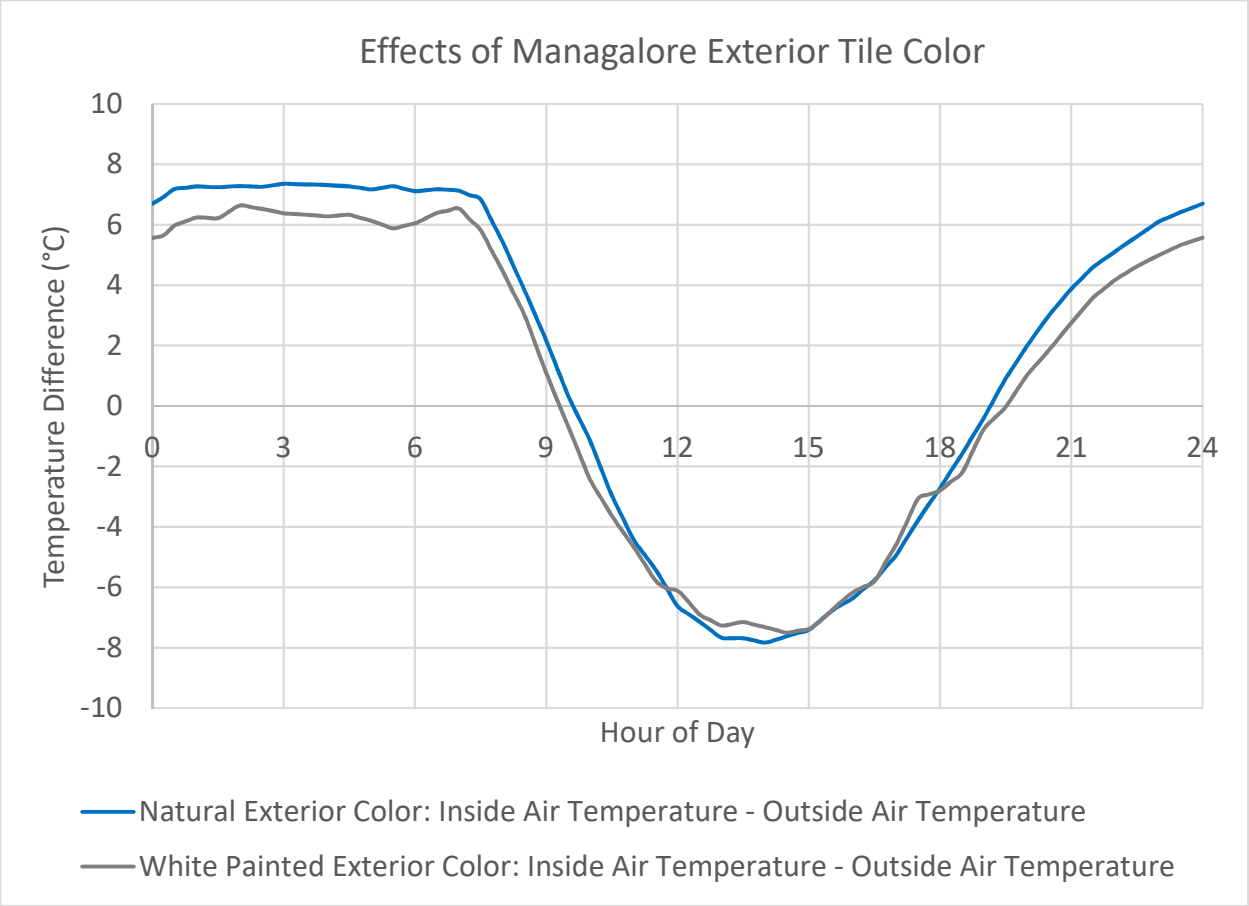

Figure 25: Experimental Test Chamber Results of the Impact of Exterior Color on the Double Layer Roofing with Mangalore Tile and Mudroll. Natural Tile is assumed to have solar absorptivity of 0.55, and White Paint 0.27.

From this field test, the low emissive surface exposed to the air cavity drives the performance of the roofing system. However, while the white painted exterior color was anticipated to produce better results, another way to understand this data is through a difference between the prior-assumed emissivity and the emissivity in practice. Based on lookups to similar materials, it was assumed that the absorptivity of the white paint would be close to 0.2, but literature available after the experiment suggest that the appropriate values should have been closer to 0.27. When the white tile approaches a weathered state, the solar absorptivity jumps significantly to ~0.68, similar to the natural exterior color. Incomplete painting of the tile would also presumably have a similar impact as the weathering of the white paint. The tests were performed remotely, so the assumptions are difficult to assess.

As a means to better understand the impact of these various factors, Table 4 and Table 6 show the maximum and minimum temperatures (in °C) of various roofing configurations based on the lumped approximation model and the assumptions outlined in Table 2 and Table 3. The upper section of the table assumes the Mangalore Clay Tile exterior, while the lower section assumes a low-cost Tin Roof exterior. The clay tile section is further broken down to the mudroll interior layer and a 1" pine interior layer. Further, to evaluate the impact of time, weathered data is included based on available literature.

		Simulated Variation Upper Material / Radiant Barrier / Lower Material	Upper Layer (°C)		Lower Layer (°C)	
			Max	Min	Max	Min
		Outside Air Temperature	38.2	26.5	38.2	26.5
Mangalore Clay Tile Exterior	Mudroll Interior	Baseline Natural Clay Tile / Bare (Nothing) / Mudroll	49.5	25.0	41.8	27.8
		Weathered Baseline Weathered Clay Tile / Bare / Mudroll	51.2	25.0	42.9	27.9
		Radiant Barrier Natural Clay Tile / Aluminum (AL) Foil / Mudroll	51.8	24.2	33.6	30.5
		Radiant Barrier - Weathered Weathered Clay Tile / Weathered AL Foil / Mudroll	53.3	24.4	36.1	30.5
		White Painted Upper Layer White Tile / Bare / Mudroll	42.2	24.8	37.4	27.2
		White Painted Upper Layer - Weathered Weathered White Tile / Bare / Mudroll	45.6	24.9	39.4	27.5
		White Painted Upper Layer – Radiant Barrier White Tile / AL Foil / Mudroll	43.6	24.1	33.1	30.3
		Radiant Barrier on White Painted Upper - Weathered Weathered White Tile / Weathered AL Foil / Mudroll	54.5	24.4	36.3	30.6
		Weathered Aluminized Outer Surface of Tile with Radiant Barrier Interior Weathered AL Tile / Weathered AL Foil / Mudroll	56.1	26.3	37.0	31.2
	Wooden Interior	Baseline Natural Clay Tile / Bare (Nothing) / Wood	50.6	24.4	46.8	25.1
		Radiant Barrier Natural Clay Tile / Aluminum Foil / Wood	51.8	24.2	35.8	28.6
		Radiant Barrier - Weathered Weathered Clay Tile / Weathered AL Foil / Wood	53.3	24.3	39.8	27.6
		White Painted Upper Layer White Tile / Bare / Wood	43.5	24.3	41.6	25.1
		White Painted Upper Layer - Weathered Weathered White Tile / Bare / Wood	46.5	24.3	43.7	25.1
		Radiant Barrier on White Painted Upper Layer - Weathered Weathered White Tile / Weathered AL Foil /Wood	47.0	24.2	37.9	27.5
Tin Sheet	Mudroll Interior	Corrugated Metal Sheet Exterior Layer Tin Sheet / Bare / Mudroll	47.2	26.0	33.7	31.9
		Corrugated White Metal Sheet Exterior Layer White Painted Tin Sheet / Bare / Mudroll	36.3	22.8	32.3	30.7
		Corrugated Metal Sheet Exterior Layer with Radiant Barrier White Painted Tin Sheet / Aluminum Foil / Mudroll	37.1	22.8	32.1	30.9

Table 4: Minimum and Maximum Values of Roof Materials using Lumped Capacitance Thermal Mode

As seen in Table 4, a myriad of options is available with minor changes to the surfaces or the layers. Starting within the confines of the Mangalore Clay Tile exterior, the first step of including a radiant barrier on the underside of the tile can lower the maximum mudroll temperature by 8.2 °C, but has a tradeoff in raising the minimum temperature by 2.7 °C. The downside risk of adding an aluminum radiant barrier remains the same as the roof weathers, with the minimum temperature remaining roughly constant while the maximum temperature reduction decreases to a 6.8 °C improvement.

Painting the tiles white has a benefit for both the maximum and minimum temperatures, but to achieve this performance, it may need to have a glazed finish instead of a painted finish. Even in the weathered case, the white paint provides a 3.5 °C reduction in the maximum temperature relative to the weathered baseline. Targeting the lowest long-term maximum temperature, the best option among the Clay Tile-Mudroll category is the white painted tile interior radiant barrier.

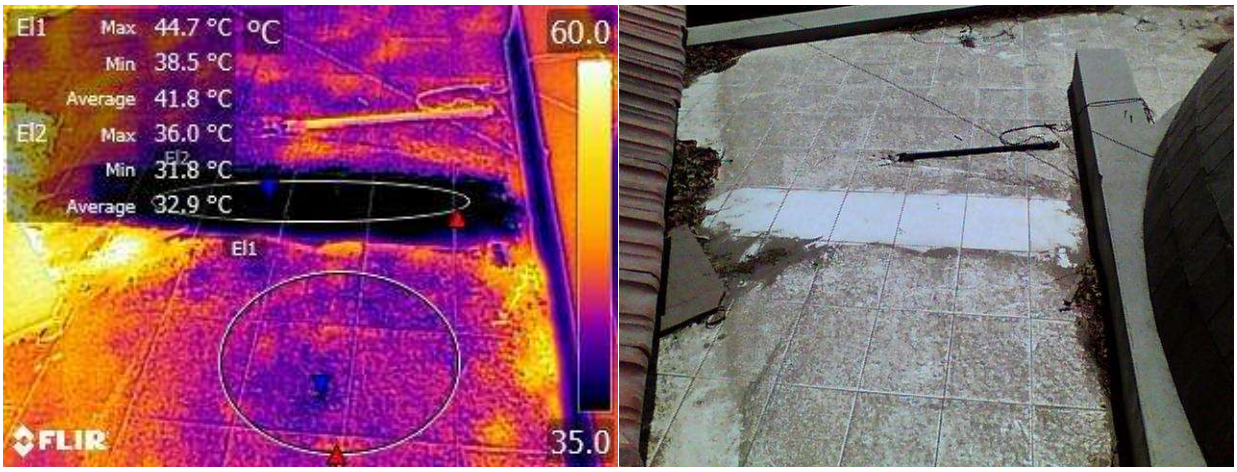

Figure 26: Degradation of Tile Performance with Accumulation of Dust on Horizontal Roof (Bhuj, May 2019. Assumed Emissivity=0.89, Assumed Reflected Temp = 42.0 °C

The same story holds true based on a short-term demonstration in Bhuj, where dust had accumulated on the white-tiled roof of a commercial building. In this example, a ~25cm stripe of white tile was brushed off to remove accumulated dust and a thermal image was taken at noon the next day from the top. As Figure 26 shows, the infrared image suggests that the clean white tile averages 32.9 °C, while the dusty ("weathered") white tile has a surface temperature in the neighborhood of 41.8°C. This then compares to the exposed structural cement on the right-hand side, which has an average surface temperature of 46.2°C. This supports the previous paragraph's statement that even a weathered case of a low-absorptivity surface can be thermally better than the baseline high-absorptivity surface. While Figure 26 is shown on a flat roof structure, less accumulation of dust is likely to occur with an inclined roof [95]. Further, one should note that these observations contrast the assumptions of solar absorptivity and thermal emissivity outlined in Table 2, where weathered white paint has a higher absorptivity than weathered natural clay tile. As such, it should be noted that the assumptions leading into Table 2 are likely to vary based on location (weather), material choices, coating types, and dust composition.

The model suggests that the lack of thermal mass (via the tin sheet exterior) will increase the maximum temperature of the inner layer by roughly 5 °C compared to the Tile-Mudroll baseline. The

minimum temperature does drop by 2.7 °C though and may be more appropriate for occupational patterns that are evening oriented (i.e., when heat stress reduction is available elsewhere during the day). Within the wooden interior options, the presence of the aluminum radiant barrier maintains significance as it is able to reduce the maximum temperature by 5.8 °C compared to the weathered case, or 9.0°C in the fresh-installed case.

These data suggest that further iterations of the design may seek to reduce the presence of the exterior thermal mass to reduce cost. The tin sheet exterior may also allow for more uniform application of high albedo coating that may also be washed during rain storms. However, it would be remiss not to include the homeowners' preferences in this discussion: the residents of Ramdev Nagar generally stated a preference towards the clay tile roof over a tin sheet roof from the aesthetic and acoustic (monsoon rain) perspectives.

The underlying assumptions for the tin sheet have a low long-wave emissivity, and thus serve as an excellent demonstrator of the possibilities of coupling a lightweight thermal mass with the double layer roofing system. In this scenario, the high reflectivity of the tin sheet combined with the low emissivity allow the mudroll to have a very small range of temperatures throughout the day, on the order of 1.8 °C. Reducing the solar absorptivity also reduces the maximum and minimum temperatures by about 1.3 °C together, whereas adding the radiant barrier further reduces the thermal connection between the two layers, and the inner mudroll layer is closer to the average temperature of the entire day.

As introduced in Section 2, previous testing in Bhuj, India had documented the low-mass roof case via the Tin-Wood roof assembly as compared to the Tile-Wood roof assembly. Notably, Figure 8 shows the average daily temperatures through the four occupied double layer pitched roof structures, and illustrates that the maximum temperature of the tin roof structure is marginally warmer than that of the tile-wood structure. The most notable difference between these two roofing typologies is that the tin-wood roof structure is considerably cooler than the tile-wood roof structure at night. This was presumably due to the massing of the outer tile. These conclusions differ from the results shown in Table 4, which suggest that the Tin-Mudroll structure is 8.1 °C cooler than that of the Natural Clay Tile-Mudroll configuration, and may seem to invalidate the model.

It is imperative to mention that the comparison is not equivalent. Most importantly, the former comparison assumes a lightweight wooden roof assembly, as compared to the mudroll assembly. This reduction of mass is partly the cause of the reduced performance when looking at the maximum temperatures. Further, the time-dependent data of Figure 8 suggest this role is roughly 2.5 °C throughout the heat of the day, and not just the ~1.5°C difference of maximum observed air temperatures. Secondly, Table 4 is referencing the temperature of the mudroll, and not the inside air temperature as referenced by Figure 8.

While discussing these types of nuanced changes of terms, the validity of the ceiling temperature as a proxy for air temperature must be established. Using the data collected from the G+1 level of the Bhuj homes outlined in Figure 3 and previously described in the 2018 work [39], this can be seen in Figure 27.

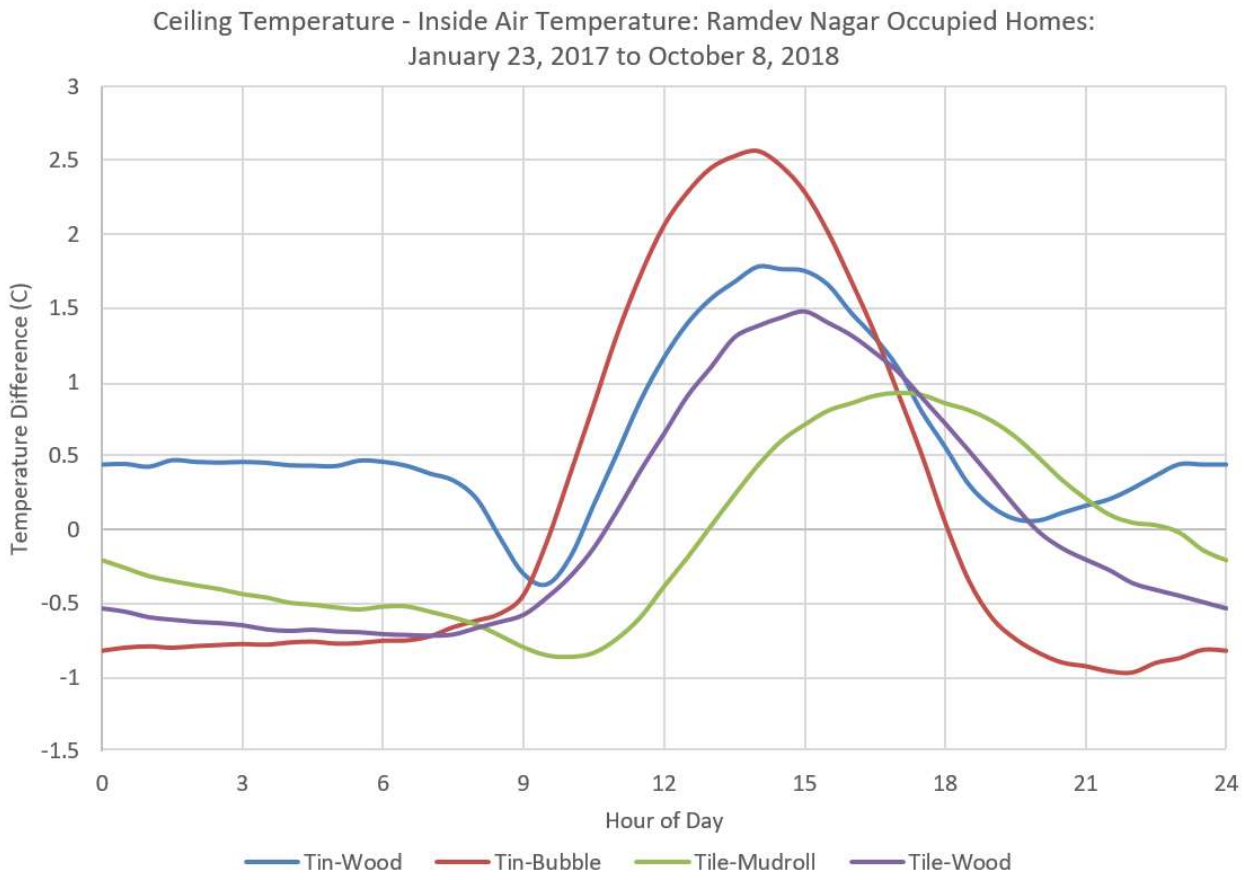

Figure 27: Difference between Ceiling Temperature and Inside Air Temperature (Ramdev Nagar, Bhuj, India, 2017-23-1 to 2018-8-10)

Figure 27 illustrates the temperature difference between the ceiling and inside air temperature as a function of the hour of the day, averaged across more than a year and a half. There are two major conclusions. First, the super lightweight Tin Sheet-Aluminized Bubble Wrap roof had a strong digression towards 2 pm local time, around the same time as the maximum outdoor air temperature. This precedes the maximum ceiling temperature of the Tin-Bubble assembly by an hour and a half. Second, the larger mass Tile-Mudroll system stays within a 1°C variation of the inside air temperature, peaking at 5 pm local time. This is roughly in line with the peak of the individual Ceiling and Air Temperatures and suggests that, while the ceiling temperature does not provide an exact supplement to the indoor air temperature, it can favorably be used for comparisons of the mudroll roofing. In terms of the contribution to uncertainty, the individual ceiling temperatures within the lumped assumption crest and trough at the same time as the data from Ramdev Nagar, suggesting that the maximum inside air temperature is roughly 1 °C less than the maximum ceiling temperature. Conversely, the minimum air temperature is roughly 0.8 °C greater than that suggested by the lumped approximation.

2.5.3 Double Layer, Double-Stacked

Gradillas had proposed using a double layer of mudroll assemblies of the roof, achieving a near doubling of the thickness of the mudroll without changing the dimensions of the air cavity. To understand the impact of thermal massing of the interior layer, that geometry configuration was also evaluated in Table 6 using the same input as Table 4, except that the thickness of the mudroll has been increased to 7.46 inches (0.189 m, 1.866x that of a single layer). An illustration of this packing arrangement is shown in Figure 28.

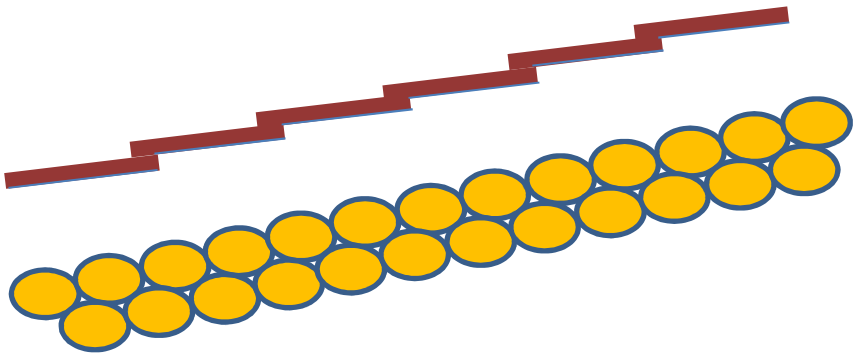

Figure 28: Double layer roofing, using a stacked mudroll geometry proposed by Gradillas [36]

Due to the doubling of the thickness, a quantification of the Biot number is necessary to understand how if the underlying lumped capacity assumption is still valid. The Biot number is a dimensionless quantity that compares the thermal resistances at the surface of the mudroll to the interior of the mudoll. If this number is much less than 1, convection resistances dominate and the lumped approximation is valid. If the Biot number is much greater than 1, internal resistances dominate and the lumped approximation is invalid. For values around 1, convection and conduction resistances are similar.

The Biot number requires the evaluation of the total heat transfer coefficient, $\bar{h}$, at the surface of the mudroll, which varies by the construction dimensions and material choices. The total heat transfer coefficient includes both the convective and radiative components and is possible to determine based on the model already established, including the convective heat transfer coefficient of at the mudroll-cavity interface, $h_{c,mudroll}$, from Equation (8), and the cavity radiation, $\dot{q}_{cavity\ radiation}$, from Equation (12). This new term is defined in Equation (16).

$$\bar{h} = h_{c,mudroll} + \frac{\dot{q}_{cavity\ radiation}}{T_{rooftop} - T_{mudroll}} \tag{16}$$

In line with the unidimensional model, the Biot number is defined such that the internal resistance is evaluated at half the thickness of the mudroll, $t_{therm\quad mass}/2$.

$$Bi = \frac{\bar{h} t_{thermal\ mass}}{2k_{thermal\ mass}} \tag{17}$$

where

$t_{thermal\ mass}$ is the thickness of the thermal mass
(~0.102 m for the single mudroll layer, ~0.189 m for the double layer);

$k_{thermal\ mass}$ is the thermal conductivity of the thermal mass (0.304 W/m·K for adobe [89]); and

$\bar{h}$ is the total heat transfer coefficient (Equation (16)).

While the heat transfer rate varies as a function of time, a simple average of all the overall heat transfer coefficients of the mudroll skews too high (8.02 W/(m^2·K)) as compared to the bulk of the data. Therefore, the 50th percentile of the data is more akin to represent the performance of the system. For the single mudroll layer with the unpainted tile and radiative barrier, the 50th percentile of the total heat transfer coefficient is 2.25 W/(m^2·K), meaning a Biot number of 0.38 for that situation. Therefore, the Biot value of the double layer mudroll is 0.74. Although the double layer is only 87% thicker than that of the single layer, this doubling of the Biot number is due to the 50th percentile of the total heat transfer rising to 2.39 W/(m^2·K) combined with the length component of the Biot number.

A Biot number of 0.74 is encouraging since it implies that there is still some validity to the lumped thermal model even in the double layer mudroll case. For an insight on variation of the Biot due to varying factors, see Table 5. Note that these changes are independent of one another and are based on a single mudroll layer, unless otherwise noted. The experimental dataset was used instead of the Bhuj EPW file.

Parameter, change of parameter Interpretation of Change	50th Percentile overall heat transfer coefficient from the mudroll to the cavity	Biot number at 50th percentile
Baseline	2.25	0.38
Double-stacked mudroll	2.39	0.74
Solar absorptivity, 0.55 to 0.27 White painted tile case	1.62	0.27
Radiant barrier emissivity, 0.04 to 0.16 Weathered foil case	2.29	0.38
Overall length of cavity, 2 to 4 m Larger roofing case	2.00	0.33
Lower angle of inclination, 27 to 15	2.08	0.35
Higher angle of inclination, 27 to 45	2.39	0.40
Tile thickness, 0.01 to 0.02 m	1.96	0.33
Air cavity spacing, 0.1 to 0.2 m	2.29	0.38
Air cavity spacing, 0.1 to 005 m	2.27	0.38
Specific Heat, 750 to 837 J/(kg·K) Thermal Conductivity, 0.304 to 0.934 W/(m·K) Density, 1,472 to 2,307 kg/m^3 Mudroll replaced with concrete	2.34	0.13

Table 5: Impact of various parameters on Biot number

With the lumped approximation confirmed through the Biot number, it is possible to use the same methodologies as the single-stacked geometry, but with the double stacked geometry to understand the influence of the thermal mass. Figure 29 illustrates this change as a function of the hour of the day.

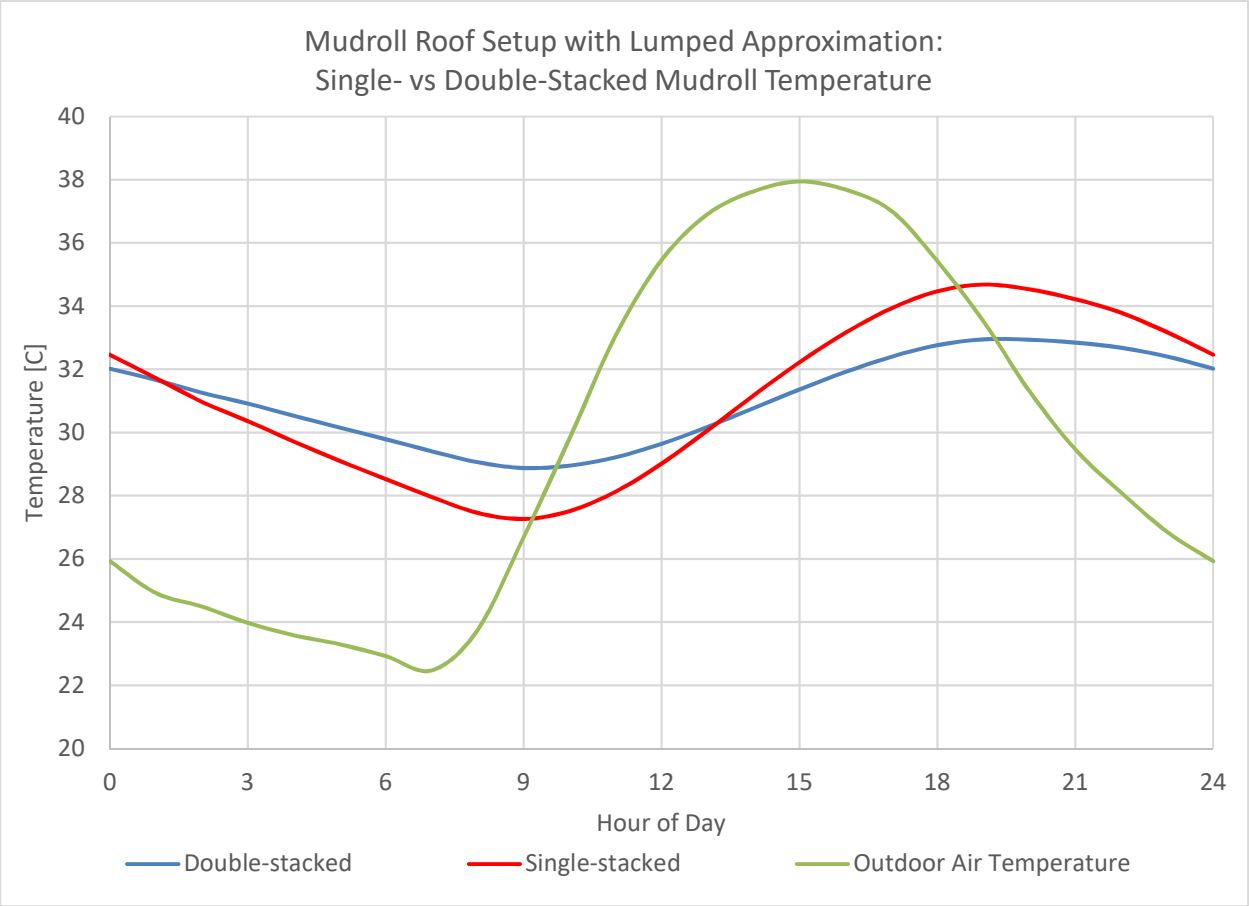

Figure 29: Mudroll Roof Setup: Lumped Approximation Influence of Single- vs Double-Stacked Mudroll on Mudroll Temperature

Figure 29 shows the single-stacked lumped capacity assumption in red, the double-stacked in blue, and the Outdoor Air Temperature in gray. The single-stacked assumption curve is the same that is shown in Figure 23. With the additional thermal mass of the double-stacked setup, the curve expectedly becomes damped out. The maximum temperature drops by 1.7 °C to 32.9 °C and the minimum temperature increases by 1.6 °C to 28.9 °C. Notably, the points at which the minimum and maximum occur do not substantially shift in time, and the total time where the double-stacked assembly has a greater temperature than the single-stacked assembly is twelve hours.

The figurative sum of the low Biot number determination and the reduction of the maximum temperature by 1.7 °C is encouraging to note as it is a conceptually easy way to reduce the thermal heat stress inside the home.

Using the Bhuj EPW file instead of the experimental data above, it is possible to repeat the investigation of the impacts of various factors using the same lumped capacity assumption. The results are shown in Table 6.

		Simulated Variation Upper Material / Radiant Barrier / Lower Material	Upper Layer (°C)		Lower Layer (°C)	
			Max	Min	Max	Min
		Outside Air Temperature	38.2	26.5	38.2	26.5
Mangalore Clay Tile Exterior	Double-Stacked Mudroll Interior	Baseline Natural Clay Tile / Bare (Nothing) / Mudroll	48.9	25.4	38.5	30.3
		Weathered Baseline Weathered Clay Tile / Bare / Mudroll	49.2	25.5	38.6	30.3
		Radiant Barrier Natural Clay Tile / Aluminum (AL) Foil / Mudroll	51.5	24.2	32.9	31.2
		Radiant Barrier - Weathered Weathered Clay Tile / Weathered AL Foil / Mudroll	53.3	24.4	34.7	31.7
		White Painted Upper Layer White Tile / Bare / Mudroll	42.0	25.1	35.1	29.1
		White Painted Upper Layer - Weathered Weathered White Tile / Bare / Mudroll	52.1	25.5	40.0	30.8
		Radiant Barrier on White Painted Upper Layer Weathered White Tile / AL Foil / Mudroll	43.6	24.1	33.1	30.3
		Radiant Barrier on White Painted Upper Layer - Weathered Weathered White Tile / Weathered AL Foil / Mudroll	47.0	24.4	33.6	31.0
		Weathered AL Outer Surface of Tile with Radiant Barrier Weathered Aluminized Tile / Weathered AL Foil / Mudroll	56.1	26.4	35.6	32.4

Table 6: Minimum and Maximum Values of Roof Materials using Lumped Capacitance Thermal Model, using a stacked mudroll geometry proposed by Gradillas

Comparing Table 6 and Table 4, the baseline double-stacked double-layer system reduces the maximum lower layer temperature by 3.3 °C as compared to the single-stacked option (0.3 °C greater than peak Outside Air Temperature as compared to 3.6 °C greater in the single stack case). Correspondingly, the minimum of the lower layer increases by 2.5 °C relative to the minimum of the single stack case.

With the weathering of the baseline case, the lower layer of the double stack interior shows much less response to the slight change in solar absorptivity (0.55 to 0.62) that accompanies the weathering of the outer clay tile. Whereas the maximum of the lower layer of single stack case rose by 1.1 °C when the outer layer “weathered”, the lower layer maximum of the double stack case only rose by 0.1 °C.

When including the radiant barrier on the interior surface, the results are similar, as the lower layer maximum of the double stack with the radiant barrier interior is 32.9 °C as compared to the single stack at 33.6 °C. In the weathered case, the maximum lower layer temperature is 1.4 °C lower with the double stack than the single stack, while only raising the minimum of the lower layer by 1.2 °C.

Representing the best option in a weathered state, double stacked white painted tile with an aluminum foil radiant barrier remains the best option to reduce daytime thermal exposure, keeping the

maximum temperature of the lower layer 3.6 °C cooler than the exterior. Additionally, the inclusion of the second layer of mudroll delays the maximum lower layer temperature roughly half an hour when using the Bhuj EPW weather file, meaning that the overall difference between peak outside air temperature and the coincident lower layer (mudroll) increases to 4.7 °C. The qualitative conclusion follows the initial precedents set by Gradillas [36] for the reduction of the surface absorptivity and inclusion of thermal massing. This work quantifies that impact.

2.5.4 Implications of geometry

As introduced in Table 5, different modifications to the structure have an impact on the 50th percentile of the overall heat transfer coefficients and the resulting Biot number at that point. More importantly, these modifications can alter the temperature profile and overall thermal performance of the system. As the implications of these modifications are not always intuitive, the lumped approximation model was used with the Bhuj EPW file to establish the variations of these changes.

The variations tested are listed as follows, build upon the baseline system, but are otherwise mutually exclusive changes. Where appropriate, the shorthand form is the associated label for Figure 30:

- Baseline system (Single-stacked mudroll, natural clay tile, radiant barrier), “Baseline (Single Layer)”;
- Double-stacked mudroll;
- White tile (Solar absorptivity changed from 0.55 to 0.27);
- White tile and Double-Stacked;
- Larger roofing case (Overall length of cavity increased) from 3.87 to 7.75 m;
- Lower angle of inclination, 27° to 15°;
- Higher angle of inclination, 27° to 45°;
- Tile thickness doubled, 0.01 to 0.02 m, “Tile double”;
- Air cavity spacing, 0.1 to 0.2 m ,“Air cavity double”;
- Air cavity spacing, 0.1 to 005 m, “Air cavity half”; and
- Mudroll replaced with concrete, “Concrete instead” (Specific Heat, 750 to 837 J/(kg·K), Thermal Conductivity, 0.304 to 0.934 W/(m·K), Density, 1,472 to 2,307 kg/m^3 [80]).

The impact of the changes in these variables on the temperature of the mudroll is shown in Figure 30, and the minimum and maximum values of each curve are extracted into Table 7.

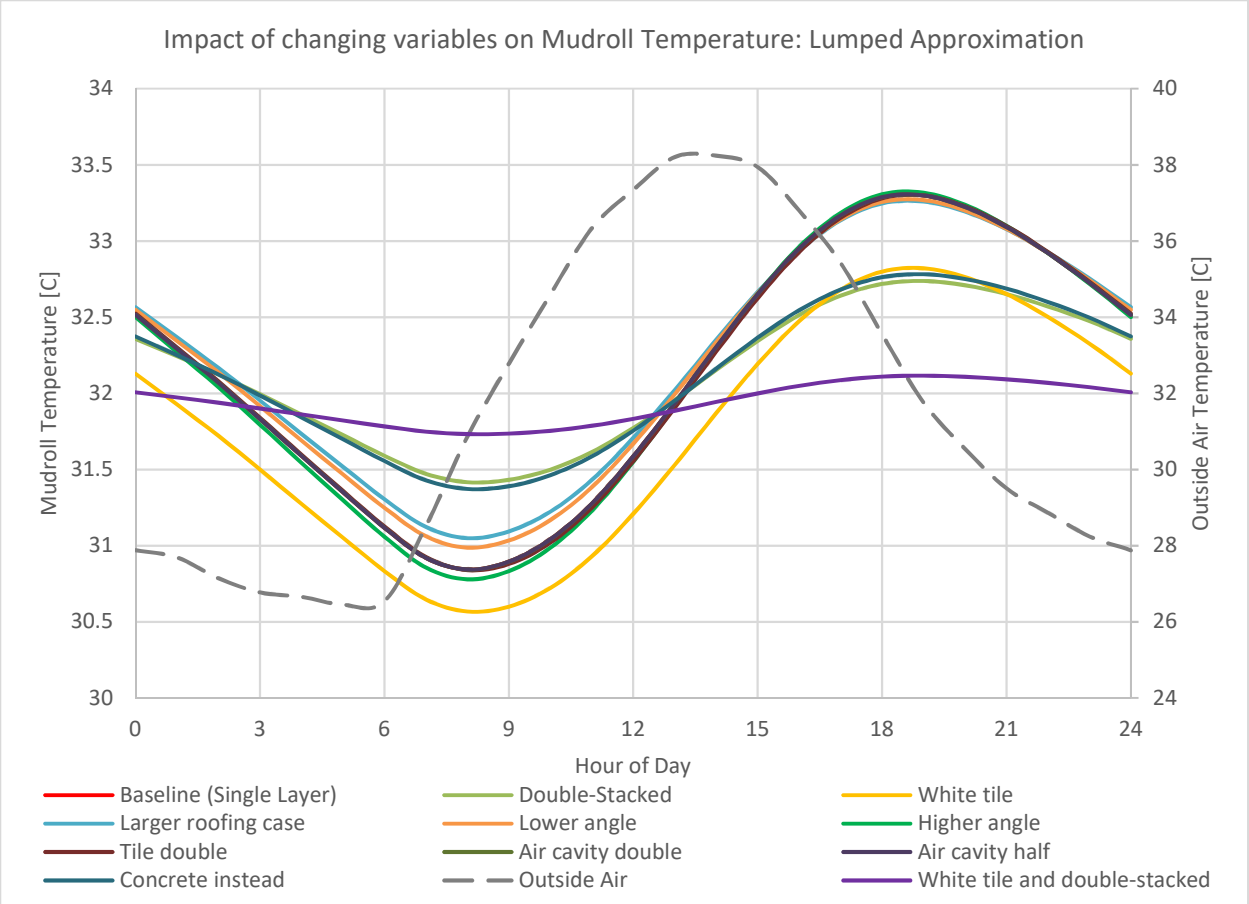

Figure 30: Graphical Impact of Various Modifications on Mudroll Temperature using Lumped Capacity Assumption and Bhuj EPW file dataset

	Tile Temperature (°C)		Mudroll Temperature (°C)	
	Min	Max	Min	Max
Outside Air	26.4	38.2	26.4	38.2
Baseline (Single Layer)	24.1	51.8	30.8	33.3
Double-Stacked	24.1	51.8	31.4	32.7
White tile	24.1	43.7	30.6	32.8
White tile and double-stacked	24.1	43.7	30.9	32.5
Larger roofing case	24.1	51.9	31.0	33.3
Lower angle	24.1	51.9	31.0	33.3
Higher angle	24.1	51.7	30.8	33.3
Tile doubled in thickness	24.1	51.7	30.8	33.3
Air cavity doubled in height	24.1	51.8	30.8	33.3
Air cavity halved in height	24.1	51.8	30.8	33.3
Mudroll replaced with concrete	24.1	51.8	31.4	32.8

Table 7: Minimum and Maximum Temperatures of Tile and Mudroll with Various Modifications (Lumped Approximation)

Figure 30 and Table 7 illustrate the impact of various modifications to the roofing structure using the lumped approximation model and the Bhuj EPW weather dataset. Critical amongst them are the two initially stated by Gradillas [36]. The first, reducing the solar absorption ('White Tile') is responsible for a vertical shift in the temperature profile of roughly 0.5 °C. The second, increasing the thermal mass (either 'Double-Stacked' or 'Concrete instead') is responsible for a dampening out of the thermal profile, resulting in a 0.6 °C reduction in maximum temperature and an equal increase in minimum temperature. Note that while the 'Concrete instead' is evaluated here for reference, it is only intended for reference, and physical implementation should be independently advised by a qualified structures engineer.

Nonetheless, the white tile and double-stacked mudroll combination suggests that a further reduction of the maximum temperature of 0.8 °C is possible on top of the gains from the air cavity with radiant barrier that already exists and represents a concept worthy of moving to a scale model (thermal chamber) phase.

2.5.5 Refugee and textile housing

Transitioning away from adding mass to a home, there are many for whom solid walls are a luxury. This is especially true for refugees [96, 97], nomadic populations [98], and members of armed forces [98, 99]. For these populations, tents are an intrinsic property of their current state, or of their identity [100]. Without the thermal mass of traditional walls, these structures have little ability to dampen out heat waves, and so add to the pressures these communities face. This was seen in practice when a IKEA flatpack shelter was assembled on MIT's campus in the summer of 2019. While the shelter was located in a shaded courtyard, it was partially exposed to the sun for around two hours. A single Onset Computer Corporation HOBO UX100-003 was hung from the support poles so that is was centrally located in the structure. In combination with a local weather station, the data was monitored for a period of 47 days.

During that time, the two hours or so that had the shelter exposed to the sun raised the internal temperature of the structure from roughly 2 °C below ambient temperature to 2 °C above ambient temperature. This rapid rise of temperature is especially worrying since the 'ventilation' openings were in the ajar position. With this worry noted, the same ventilated cavity/lumped model approach that has been used thus far can also be applied to a textile or tin-roof construction, so long as the air cavity is continuous and open to the environment. This application is possible since the Biot number becomes much less than zero, effectively to the point that one can ignore the thermal mass entirely.

Ultimately, once one ignores the thermal mass and also assumes that the textile is sufficiently small such that there is no thermal resistance due to conduction, it becomes much easier to find an equivalent solar absorptivity given a set of inputs. This equivalent solar absorptivity is the solar absorptivity value at which the mudroll temperature of the double-layer system is equal to the single layer temperature of a single-layer system. The equivalent solar absorptivity has application as a field metric to approximate a single layer steady-state system and also the effectiveness of the heat avoidance of a double-layer system.

The determine the equivalent solar absorptivity, Equations (13) and (14) are summed together to a total heat gain for the double-layer system ($\dot{q}_{net\ heat\ gain,double\ layer\ system}$, Equation (18)).

$$\begin{aligned}\dot{q}_{net\ heat\ gain,double\ layer\ system} &= \dot{q}_{net\ radiation\ gain} - \dot{q}_{exterior\ convection} \\ &- \dot{q}_{cavity\ convection,upper\ thermal\ mass} \\ &- \dot{q}_{cavity\ convection,lower\ thermal\ mass}\end{aligned} \tag{18}$$

To model the single-layer system, the cavity and lower layer components of the double-layer system (Equation (18)) are removed to approximate a single-layer system ($\dot{q}_{net\ heat\ gain,single\ layer\ system}$, Equation (19)).

$$\dot{q}_{net\ heat\ gain,single\ layer\ system} = \dot{q}_{net\ radiation\ gain} - \dot{q}_{exterior\ convection} \tag{19}$$

Equation (19)) is then evaluated such that the lower layer temperature of the double-layer system and the temperature of the single-layer system are equal. Further, at steady-state, the net heat gain terms are equal to zero, and so Equation (18) and (19) can be equated to solve directly. This is shown in Equation (20), where the left-hand side is the contribution from the double layer and the right-hand side is the contribution from the single layer, denoted accordingly.

$$\begin{aligned}(\dot{q}_{net\ radiation\ gain} - \dot{q}_{exterior\ convection} - \dot{q}_{cavity\ convection,upper\ thermal\ mass} \\ - \dot{q}_{cavity\ convection,lower\ thermal\ mass})_{double-layer} \\ = (\dot{q}_{net\ radiation\ gain} - \dot{q}_{exterior\ convection})_{single\ layer}\end{aligned} \tag{20}$$

Noting that the net radiation gains are defined as the contribution from both short-wave absorption and long-wave radiation exchange, the algebraic solution to Equation (20) for the system can be reproduced from previous equations.

Solving this using the framework developed for the lumped capacity first difference model, a damped iterative solver was coded to determine what the equivalent solar absorptivity for the system would be to produce the same temperature ("Equivalent temperature") previously mentioned. Given that the lower surface of the lower layer is assumed adiabatic and it is steady-state, this helps limit the complexity of the system.

Using these values, we can use a single set of weather conditions to evaluate what material choices would yield benefit to the thermal comfort of the occupants. This is detailed in Table 8.

Setup	#1	#2	#3	#4	#5	#6	#7
Upper layer, upper surface (Solar absorptivity, Thermal emissivity)	Tin sheet (0.32, 0.14)	White painted Aluminum (0.20, 0.91)			Polyester (0.60, 0.77)		
Upper layer, lower surface (Thermal emissivity)	Tin sheet (0.14)	White painted Aluminum (0.91)	Aluminum foil (0.04)	Weathered aluminum foil (0.16)	Polyester (0.77)	Aluminum foil (0.04)	Aluminum, weathered (0.16)
Lower layer, upper surface (Thermal emissivity)	Tin sheet (0.14)				Polyester (0.77)		
Equivalent temperature (°C)	36.5	34.8	31.1	32.5	47.6	33.8	39.17
Equivalent solar absorptivity	0.09	0.15	0.09	0.12	0.35	0.12	0.21

Table 8: Equivalent Solar Absorptivity of Textile Single Layer Roofing when using Double-Layer Roofing Construction. Assumptions: Outside Air Temperature = 30 °C, air speed = 1.5 m/s, dew point = 18 °C (50% RH), cloud cover = 0, Vertical Incident Solar Radiation = 1000 W/m^2, 27 degree incline, 0.5 m rafter spacing, 0.1m interplane spacing, 2.25 m length of cavity [97], Equivalent thermal emissivity of single layer = thermal emissivity of upper layer, upper surface.

Although this approach is highly limited in this context due to the neglected internal convection and radiation components, the equivalent solar absorptivity does provide an insight into the significance of the various surface types and the potential efficacy of the system. Further, the equivalent temperature is also listed, which is the temperature that a single layer system would have. This value would be necessary to then help inform the thermal comfort within the space. These two values are particularly important for advocacy for the double layer system as applied to the existing polyester case. Polyester is a common material used for camping tents and comprises up to 70% of the poly-cotton blend of the United Nations High Commissioner for Refugees family tents [101, 102]. The steady state approximation suggests that simply by doubling the layers of the roofing while providing an open-ended cavity drops the equivalent solar absorptivity by almost half the original value. Further, providing an aluminized cavity interior surface drops the equivalent solar absorptivity to 0.12, or to about one-fifth the original value. This has significant implications for providing residents relief from summer heatwaves by giving them a roof temperature more akin to the air temperature, rather than the 61.6 °C that a single-layer polyester sheet might produce.

For future work, the model can also be used to evaluate the system given setups prevalent in other regions of the world, such as the influence of solar panels offset from a roofing system and the subsequent coupling of solar panel efficiency and heat penetration.

2.5.6 Equivalent air conditioning sizing

As a coarse assumption, it is possible to use the Maximum Mudroll Temperature from Table 7, and assumptions of the heat transfer coefficient and geometry to estimate the effective equivalent air-conditioner sizing that the double-layer roofing provides over a single-layer tile roof baseline.

To establish the single-layer tile temperature, the lumped approximation using the approach described in Equation (19) is defined using the thermal mass and radiation properties of the clay tile. For comparison to Table 7, the maximum temperature is 46.3 °C, which is 8.1 °C over that of the peak outside air temperature.

The equivalent air-conditioning size, or the avoided heat transfer to the interior of the home ($\dot{q}_{avoided\ heat\ gain}$) is estimated at an assumed linearized radiative heat transfer coefficient (h_r) of 5 W/(m^2·K) and a convective heat transfer coefficient (h_c) of 2 W/(m^2·K). Reiterating an assumption from earlier that the mudroll temperature was indicative of the air temperature within the home, this can then be combined with the area of the roof (24.9 m^2), as shown in Equation (21).

$$\dot{q}_{avoided\ heat\ gain} = (h_r + h_c)A_{roof}(T_{single\ layer} - T_{double\ layer}) \quad (21)$$

Where Equation (21) provides a result in Watts of thermal energy, a conversion of 3.412 BTU/h can be applied to be among the same units as air-conditioner sizing. This yields the proposed equivalent air-conditioner sizing shown in Table 9.

Modification	Equivalent Air-Conditioner Sizing [BTU/h]
Single-Layer of Tile, no Mudroll	0
Tile and Single-stacked Mudroll	7,734
Tile and Double-stacked Mudroll	8,092
White tile and Double-Stacked Mudroll	8,211

Table 9: Equivalent Air-Conditioner Sizing

Table 9 suggests that, for the Bhuj climate and housing geometry, the double-layer roofing system has the effective performance akin to a 7,734 BTU/h air-conditioner. Yet, it does not consume any electricity and thus has no operational costs or carbon emissions, and remains resilient despite loss of power incidents.

2.6 Conclusions and Recommendations

Based on the work to date on ventilated, double layer roofing, the experimental results from the occupied structures in Bhuj suggest that the roofing helps contribute to an overall reduction in the peak air temperature of 5 °C throughout a majority of the day when heat risk is possible, rising to near 7 °C for the case of the tile and mudroll setup. Although further improvements to this setup were not evaluated for a multi-year period alongside the original setups, testing in scale models (test chambers) and modeling can provide insight into further steps. Largely in agreement with Gradillas and Nelson, the universal steps of

reducing solar heat absorption and adding thermal mass positively contribute to the goal of peak temperature reduction, in the range of an additional 0.5 °C to 1.3 °C reduction.

Nighttime ventilation of the cavity produces no noticeable change in the thermal performance, in part due to the constraints of the geometry in which to fit the fan. While there are further gains to be had from controlling or limiting the airflow within the cavity given the air cavity air temperature measurements compared to the outside air temperature, the experimental data was unable to isolate the impact of those actions. As the system can be modeled as a lumped model (Biot < 1), further work can be done to understand the implications of those actions.

The lumped model works well to approximate the performance of the system under natural ventilation conditions. While the theoretical reduction of the Biot number due to the proposed containment of the air within the cavity can limit the application of the lumped model in those situations, the overall heat transfer coefficients can be halved until the approximation begins to no longer be applicable. The lumped model can also be used to define the implication of various geometries, for which it may be cost prohibitive to try. Within the model, the relative size of the interplane spacing has little effect on the resulting thermal performance. However, a lower angle of inclination and a longer cavity result in higher minimum temperatures, but no significant impact on maximum temperatures.

Vital significance of the radiant barrier and air gap combination is shown with the steady-state approximation that takes the form of the textile housing. Where traditional temporary housing materials may be used, the system can reach an effective solar absorptivity of 0.12, resulting in a stiff reduction in solar heat absorbed, which drove excessive thermal gains with sample refugee housing installed locally.

Especially within the context of a locally-crafted, socially-desired material, the double layer roofing with a Mangalore tile-Mudroll combination is sufficient to provide a sizable reduction in thermal risk. The reduction in thermal risk is roughly equivalent to a 7,750 BTU/h air-conditioner serving the same space, despite having no operational carbon emissions. As such, the roofing methodology may be conceived as an air-conditioning avoidance measure as it enables homeowners to avoid the purchase of an air-conditioner of the same size.

Further work is necessary to push the system through the controlled ventilation opportunities, surface absorptivity options, and through a coupling of ventilation options with the interior of the structure.

3 Flat slab roofing

Within Bhuj, the housing built under Indian government's Housing for All program is predominantly flat slab roofing to allow occupants to further expand the structure vertically as their finances improve. As such, the roof layer is made of a single concrete slab and conventional methods to moderate the interior temperatures of these homes typically rely on controlling the solar absorption of the roof surface and use diurnal cooling with the thermal mass of the roof slab. Previous work has sought to apply these methods to ground-level row style housing with flat concrete-slab roofing in the community of Ramdev Nagar, which are the homes without second story (G+1) housing, similar to the ground floor of the houses with the upper level pitched roofing shown in Figure 1. However, within the social context of Bhuj, changing the surface radiation property is at direct odds with the way the space is used as part of the home.

The image below (Figure 31) shows a short test run in Bhuj in which an attempt was made to quantify the change in interior temperature from low-cost modifications to the roof. The mylar sheets, both in direct contact and offset from the roof represented one of the lowest cost options, and the white tiles were available in the local market and are already in use in middle-income housing.

However, the homeowners in the community noted complaints of glare and visual discomfort when occupying the roof space during the day with these solutions. This roof space is used periodically throughout the day as a place of recreation, social gathering, and to take a break from manual work. Through the night, it is also used as a sleeping platform. Due to the social feedback against these possibilities, other options are needed.

As such, the avenues to reduce solar thermal gains are limited. The following research is focused on improving the use of cool night air to cool the underside of the concrete roof slab, thereby using the thermal mass to help moderate the interior temperature during the day. The challenge is to find an efficient way to direct the incoming air over the ceiling area without creating uncomfortable drafts for the occupants within the space.

Figure 31: Field Experiment of Different Roofing Treatments for Horizontal Concrete Slab Roofing

3.1 Ceiling heat removal

In field experiments conducted in Bhuj, a small test chamber with a low slope corrugated sheet roof was outfitted with a ceiling fan and the associated window shutter were operated under a night flush strategy. Based on observations and inquiries of occupant behavior, any ceiling fans in the residences were more likely to be operated during the day. Unfortunately, for homes that use a low-thermal mass roof, the operation of the fan during peak solar irradiation hours provided short-term relief and increased their long-term discomfort. [35] The field experiment showed that the operation of the fan decreased the thermal stratification within the house and increased the air and operative temperatures within the occupied zone by roughly 2 °C, while decreasing the ceiling temperature by 4 °C. Overall, the ceiling fan had the possibility of making the living space more uncomfortable and the work concluded through the recommendation of using a pedestal fan instead of a ceiling fan. At nighttime the ceiling fan would create an uncomfortable draft on the occupants.

While this field work was significant in being able to quantify the possible negative impact of the usage of a ceiling fan in the structures of developing economies, it did not assess the possibility of integrating the thermal mass of the roofing slab through an operational approach. One example of this approach would be the integration of a window ventilation fan angled towards the ceiling at night when the air temperatures are lowest, to maximize the difference of temperature between the surface of the roof slab and the air passing over it. An ad-hoc test of this type was run in Bhuj in May of 2019 in an occupied home, using a pedestal fan located near the window plane and aimed towards the ceiling.

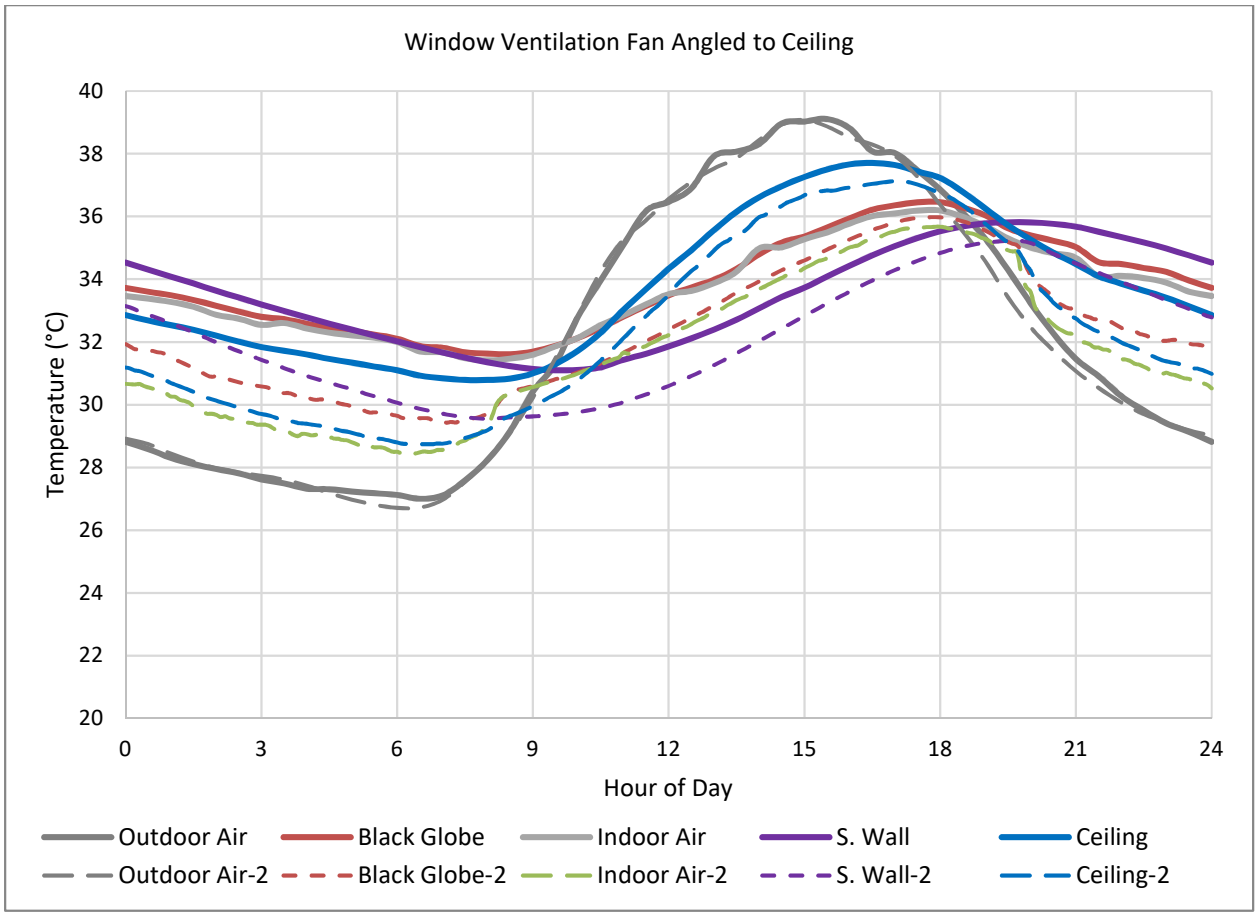

Figure 32: Experimental Results for the Addition of a Window Ventilation Fan Angled Towards the Ceiling (Solid Line: Baseline, No Fan. Dashed Line: With Fan)

Here, the horizontal axis is the hour of the day and the vertical axis is the temperature, in °C. The data shown in dashed lines with the "-2" suffix, are those that are have a pedestal fan in the window angled to the ceiling. The data shown in solid lines are the baseline case with window shutters on a nighttime ventilation schedule (closed 8am-8pm, open 8pm-8am). Based on only four days of running the setup in similar weather conditions, the angled approach of the fan was able to maintain a reduction in both the ceiling and indoor air temperature throughout the next day by roughly 1 °C as compared to the absence of the fan. As a reference point, previous work for these structures in this climate had suggested that a simple window fan installation with horizontal air flow utilizing nighttime operation did not produce significant differences in temperatures either during operation or during the subsequent day when compared to the same operation using only the available winds and open shutters. This 1°C threshold of the difference in the indoor air temperature remained until the roughly 4 PM local time, when it continued to narrow until the ventilation fan turned on at 7 PM.

During this test, the roof had a low thermal mass and provided limited parallels to the Housing for All homes that are in Bhuj. Therefore, in an attempt to understand the potential for heat removal from the roofing slab due to spreading out the jet airflow on the underside alone, we utilized an analytical model based on a lumped capacity assumption of a concrete slab with a thickness of 10 cm and lateral distance of 3 m over an eight-hour time frame.

As a means to evaluate the impact of various air speeds on cooling the ceiling slab assuming that the upper surface is adiabatic, a one term solution for unsteady conduction was used, as published by Glicksman and Lienhard [103]. A prerequisite for this approach is that the Fourier number must be greater than 0.4. The Fourier number (Fo, Equation (22)) is the dimensionless time for heat to diffuse a length L through the material. Evaluated through the thermal diffusivity, α, the value for concrete is in the range of 5.94-11.6 $\cdot 10^{-7}$ m^2/s as reported by Howlander, et al. [104] and Owczarek [105], and checked against Carman and Nelson [106] . For added intuition, the thermal diffusivity is defined as the thermal conductivity (k) divided by multiple of density (ρ) and specific heat (c_p). [107] For the sake of assigning a value at this abstracted phase, the average value of those presented by [104], 8.7 $\cdot 10^{-7}$ m^2/s will be used when evaluated. This corresponds to a concrete of roughly 2,050 kg/m^3 density and 2.15 W/m·K thermal conductivity. The slab thickness is also assumed to be 0.1 m.

$$Fo = \frac{\alpha t}{L^2} = \frac{\frac{k}{\rho c_p} t}{L^2} \tag{22}$$

For an eight-hour timeframe (28,800 seconds) and the above assumptions, the Fourier number is 2.51. Since the Fourier number greatly exceeds 0.4, the one-term solution can then be represented by Equation (23) with an error less than 0.1%, far below that induced by the upper surface adiabatic assumption.

$$\bar{\theta} = 1 - \phi = D_1 \exp(-\lambda_1^2 Fo) \tag{23}$$

where

$\bar{\theta}$ is an effective normalized value of the amount of heat that has yet to be removed, and is equal to $((\bar{T} - T_\infty)/(T_0 - T_\infty))$;

$\bar{T}$ is the spatially averaged temperature of the slab;

T_∞ is the temperature of the environment;

T_0 is the initial temperature of the slab;

ϕ is an effective normalized value of the heat that has been removed ($(T_0 - \bar{T})/(T_0 - T_\infty)$); and

D_1 and λ_1 are approximate equations for parameters of the one-term solutions [108].

Another way to describe ϕ is through Equation (24), which relates ϕ to the normalized total heat transfer ($Q(t)$) from the initial state through time to a time, t.

$$\phi = \frac{\int_0^t Q(t)\, dt}{\int_0^\infty Q(t)\, dt} \approx 1 - D_1 \exp(-\lambda_1^2 Fo) \tag{24}$$

λ_1 (Equation (25)) and D_1 (Equation (26)) are approximate equations for parameters of the one-term solutions as applied to a slab and are sourced from Ostrogorsky. [108]

$$\lambda_1 = \frac{\pi/2}{(1 + \frac{2.62}{Bi^{1.07}})^{0.468}} \tag{25}$$

$$D_1 = 1 - \frac{0.189}{(1 + \frac{3.8}{Bi^{1.116}})^{1.62}} \tag{26}$$

Each equation is a function of the Biot number, which is written in terms of the total heat transfer coefficient h, thickness of the slab L, and thermal conductivity of the slab k.

$$Bi = \frac{hL}{k} \tag{27}$$

Assuming that the heat transfer coefficient is comprised solely of the contribution from convection, the convective heat transfer coefficient can be approximated by the velocity of airflow over the surface of the ceiling. Using a correlation from Žukauskas and Slanciauskas, applicable for Prandtl numbers up to 85, Equation (28) was proposed [109]. The correlation is reported to be roughly a 15-25% overprediction of the heat transfer coefficient for air [110]. Note that, unlike the Biot number, the Nusselt number is computed based on the characteristic length of the airflow and the thermal conductivity of the fluid, not the solid. The heat transfer coefficient remains the same.

$$Nu = \frac{hL}{k} = 0.032\, Re_L^{0.8}\, \mathrm{Pr}^{0.43} \tag{28}$$

The analytical model also used a constant thermal conductivity for air, at 0.026 W/(m·K) [76], a constant Prandtl number of 0.707, and assumes a constant air supply temperature. For comparison purposes, air passing over the ceiling with a velocity of 1 m/s would produce a convective heat transfer coefficient of roughly 4.16 W/(m^2·K). Further, the model assumes that the entire width of the jet flow has the same velocity, but that velocity is reduced to satisfy a constant initial flow rate and is assumed to be universally perpendicular to the wall where the inlet is located. Areas of the ceiling that are not exposed to the jet are assumed to have a convective coefficient in line with a velocity of 0.001 m/s, and as such, the values in Figure 33 are a weighted average by area.

Note that this approach is inherently conservative in comparison to reality, since the upper surface was assumed adiabatic.

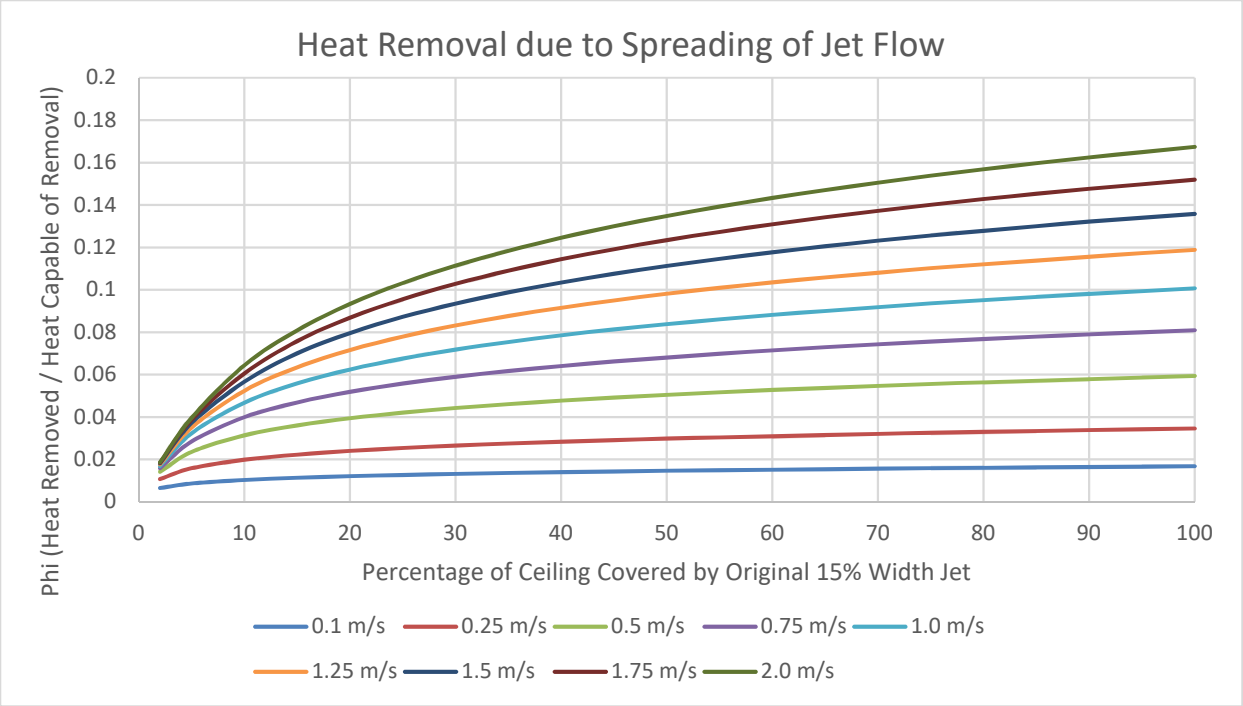

Figure 33: Impact of Spreading out a Jet's Flow on the total heat removed, starting from a 15% width of the roof slab

In the figure above, the horizontal axis is the amount of spread that a nominal amount of flow is constrained or expanded to, based on an initial jet being 15% the width of the entire ceiling. This would be akin to having a narrowly-defined window through which air was forced via a fan and diffused across a ceiling. The vertical axis (phi, ϕ) is a measure of how much heat can be removed by the airflow of the jet alone as compared to the total heat that can be removed (based on the mass, specific heat, and temperature difference between the original value and the ambient value). The takeaways of this figure are (1) increasing the initial velocity (and thus the mass flow) of the jet along the ceiling increases the total heat removal from the roofing slab, (2) at low initial velocities, there is a modest (48% increase in Phi for 0.1 m/s from 15% width to 100% width) benefit to be gained by spreading out the initial jet flow, and (3) for higher velocities, there is a substantial (107% increase in Phi for 2 m/s from 15% width to 100% width) benefit to spreading out the initial jet flow.

As compared to a natural convection only scenario for a heated plate facing down [111] for the same time period, that would yield a value for phi of 0.0001, roughly the same for a marginal-velocity jet focused on a small portion of the ceiling. For scale, each 0.04 increment of phi would roughly correlate to a 1 °C change in the slab temperature. These values apply to a room which has a length from air entry to exit of 3 m, and larger spaces would produce lower values of phi, as the air stream has a finite capacity of heat that it can absorb from the concrete slab roof.

While these improvements may not seem to have a significant variation due to the small numerical differences in phi, note that this is only the contribution of the convection from the internal surface; it does not include the radiation on either face, as well as the convective effects from the external face. This importance becomes more significant at low values of phi, which would show that the convective heat transfer from the inside surface does not significantly contribute to the overall

temperature change. Nonetheless, the jet does compare favorably to the generalized air change rate-induced heat transfer through change in the value of phi by about three orders of magnitude.

With both the ambient inside and outside ambient air approximated at a constant 20 °C and including heat loss from the top surface, the change variation in the slab temperature between a modest forced convection on the interior face and natural convection on the interior face becomes more pronounced.

Based on a lumped capacitance model using both interior and exterior convective correlations published in [111] and a conservative radiation estimate of the ambient environment at the same temperature as the air, a modest amount of airflow produces a significant drop in the slab temperature over an eight-hour time frame. The initial introduction of the forced convection above that of natural convection drops the slab temperature by 2.8 °C, whereas the subsequent change to a higher velocity continues to decrease the slab temperature by another 2.0 °C, showing some diminishing returns with higher velocity airflows. Note that this includes a critical assumption underlying this approximation, that (1) the convective coefficient is constant across the entirety of the roof slab, (2) the outside convection is due to still-air natural convection alone, and (3) that the interior air remains a constant 20 °C, which is not always the case. All told, this could help reduce the subsequent inside air temperature by 2 °C throughout the peak of the day.

3.2 Ceiling Heat Transfer Coefficient Experimental setup

To assess the possibilities of the impact of redirection of the inlet air on increasing the convective heat transfer coefficient, it became clear that an experimental setup was needed. Due to COVID-related travel restrictions, that testing was performed at scale instead of in India.

Whereas the pitched roofing focuses on a construction-oriented approach, this testing was intended to help determine the next-day temperature reduction through the operational lens. Such an operational lens might be more meaningful to occupants of housing with a thermally massive roof slab, either in the single-story dwellings in Bhuj, or multistory apartment-style dwellings where structural changes are difficult or modifications must be reversible.

3.2.1 Scale models

Moving towards a scale model to allow for rapid testing within a controlled setting, a linearly scaled mockup of the Bhuj ground floor housing was constructed on MIT's campus. As a whole, the mockup was constructed largely of insulation foam boards cut to shape, with an aluminum ceiling and a series of heat mats to provide a stand-in for the heat absorption that would occur with the flat-slab roofing in Bhuj.

3.2.1.1 Physical Test Cell: Location and Conditions

The mockup (test cell) is located within another controlled environment space that was designed for airflow and occupant comfort studies. This chamber is an insulated room of 5.3 m (208 inches) length, 3.6 m (144 inches) width, and 2.2 m (86 inches) height. The anterior of this chamber is conditioned via a

Mitsubishi heat pump cartridge unit set to 68 °F on auto mode, static vanes, and high fan. Air was circulated through the chamber with combination of the built-in ventilation systems (four duct fans running through two independent HVAC systems with the intakes physically blocked off), and the anterior space with a Lasko 20" box fan. Using this setup, the air space within the testing chamber was kept within 11.6 °C to 23.7 °C, with ninety percent of that time spent between 14.8 and 22.1 °C. At those same times, the outside air temperatures varied between -15.6 °C and 26.0 °C with ninety percent between -10.2 °C and 13.2°C. Note that this variation also impacts the supply temperature to the test cell, but that the temperature is noted where applicable. Earlier experimental iterations had a reduced temperature range of within 1.6 °C, but conditioning-equipment failures required a fallback plan with less temperature control.

Testing took place during January to March of 2022 when outside dew point ranged from -24.7 to 15.0 °C with ninety percent between -18.0 and 9.1°C. Dehumidification of the anterior space was taken care of via a standalone dehumidifier, set to 35% relative humidity, and checked and drained daily. Spot measurements (n=42) during the testing period with a Vaisala MI70 indicator coupled with a HMP75 temperature and relative humidity sensor recorded relative humidity values ranging from 8 % RH (21.8 °C inside air temperature, -12.5 °C dew point) to 32 % RH (18.4 °C inside air temperature, 1.4 °C dew point) (n=42). At these temperatures and humilities, the Vaisala sensor is estimated to have an accuracy of ±1% Relative Humidity [112].

3.2.1.2 Physical Test Cell: Construction and Material Properties

The chamber itself was largely constructed of Owens Corning Foamular 250 extruded polystyrene (XPS) and constructed with a removable bottom to facilitate taking infrared thermograms (thermal photographs). The walls were constructed of a core one-inch XPS layer surrounded by an additional two inches XPS layer with a layer of aluminum foil on the interior surface. The floor was a one inch XPS sheet with an aluminum foil inner layer. The ceiling, starting at the inside, was constructed of a 1/8" sheet of aluminum faced with a single layer of 3M ScotchBlue painter's tape, a layer of resistive heaters (Ohuhu Seedling Heating Pad), two inches of foil-faced Polyisocyanurate (Polyiso) foam board (foil face down), three inches of Owens Corning Foamular 250 XPS (Two ½" sheets and two 1" sheets), and two sheets of medium density fiberboard (pegboard) with offset peg holes (combined thickness of 0.9 cm, finished side facing up).

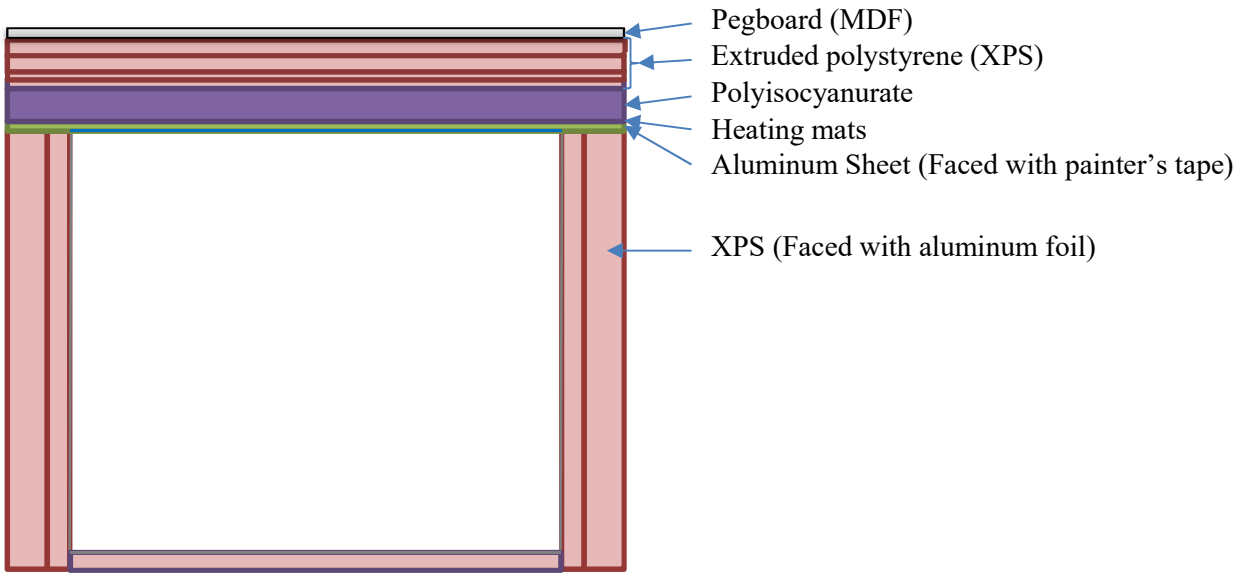

Figure 34: Test cell construction layering

In regards to rationale behind the ceiling construction, the heat mats have a nominal rating of 18 W each, but measured near 20 W each, or around 214.5 W/m^2. The XPS insulation board has a maximum service temperature of 74 °C [113], whereas the Polyiso has an upper service temperature of 121 °C [114]. Based on a simple analysis, it was believed that the aluminum sheet and heat mats could reach an upper limit of near 95 °C localized near the resistance wires inside the heating mats, far above the service limit of the XPS insulation. To prevent health and fire risks, the Polyiso was added to the configuration.

The horizontally offset pegboard is part of the system purely for its displaced weight, serving to keep the insulation boards in contact with the boards below, and the heating mats in contact with the aluminum sheet. Thermally the pegboard was an unknown in terms of conductivity as an assembly for two main reasons. First, it was an unknown what the presence of the ¼" diameter peg holes on a one-inch square grid would do to the overall thermal conductivity, and second, it is difficult to quantify the contact resistance between the unfinished lower side of one board, and the finished upper surface of the next board. To quantify this, a one-dimensional thermal conductivity test was performed on two 12" x 12" samples of the pegboard.

Using a Netzsch Heat Flux Meter (HFM) 436/3/1 Lambda v3.04, the sample was placed between plates of two different temperatures and held until a constant heat flow is detected. The HFM 436 series is advertised to measure Thermal resistances between 0.05 and 8.0 m²K/W with ±1% to 3% accuracy, and 0.25% repeatability [115]. Inside the Netzsch HFM 436/3/1, the machine has an integrated Peltier system to establish the thermal temperature gradient, and a thickness gauge to determine the thickness of the sample. The system also has integrated heat flux transducers to determine when steady state conditions have been met, and when a reading can be taken for the representative thermal conductivity. It is important to note that the HFM can only sample in a single dimension, and so all the materials tested had uniform construction through the central area of interest, defined by the 10cm x 10cm center of the 30cm x 30cm sample area. An illustration and schematic of the system is shown below, in Figure 35

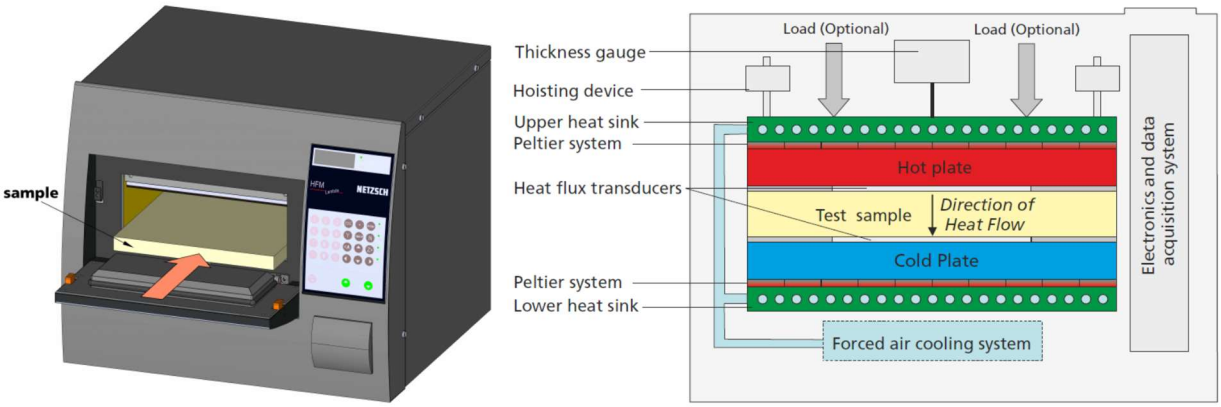

Figure 35: NETZSCH HFM 436/3/1 Lambda illustration and schematic [116]

Before starting testing, the machine was calibrated against a piece of insulation from the National Institute of Standards and Technology (NIST). This piece of insulation is made from one-inch thick Standard Reference Material 1450d, Fibrous Glass Board, and has an accepted thermal conductivity of 0.031 W/(m·K) at 280 K [117]. The thermal conductivity of the sample increases linearly at an approximate rate of 0.0011 W/(m·K) per each 10 K increase in temperature, and the thermal conductivity does not have significant variance with bulk density values within the 115 to 122 kg/m³ range [118]. Based on NIST Special Publication 260-173 [118], these values are about equal to the thermal conductivity values of 0.0317 W/(m·K) and 0.0348 W/(m·K) at the as-tested temperatures, without including the stated accuracy range.

To further ensure that the calibration sample remained constant throughout the duration of testing, the sample has been maintained with marginal thickness plastic wrap to maintain the as-tested humidity values within the sample. The sample has then been stored away from sources of physical damage. However, possible sources of the difference between the NIST values and the as-tested values may be related to the quantity of physical samples (NIST utilized 450 testing panels where only one panel was tested with this work), or to the variance in the HFM machine itself. Nonetheless, the values are within the acceptability range given the instrument.

The HFM measured a single layer of pegboard at 0.49 cm with an average Thermal Conductivity of 0.085 W/(m·K) (n=20) at an average mean measured temperature of 26.03 °C. The change in thermal conductivity as a function of the mean measured temperature was small in absolute terms (0.011 W/(m·K)) within the 15.8-38.5°C range of measured temperatures.

For a double layer (thickness of 0.91 cm), the thermal conductivity rose slightly to an average of 0.106 W/(m·K) (n=20) at an average mean measured temperature of 25.65 °C. The change in thermal conductivity as a function of the mean measured temperature was small in absolute terms (0.013 W/(m·K)) within the 15.1-39.6 °C range of measured temperatures. While there was no significant difference in the thermal conductivity as a function of the direction of the net heat flow (bottom plate or top plate, 0.002 W/(m·K)), the alignment of the peg holes had a marginal impact on the thermal conductivity when measured with a lower plate being heated (0.004 W/(m·K)).

The as-tested thermal conductivity of the double layer 0.113 W/(m·K) (n=10, average 25.74 °C) compares favorably to the 0.09 W/(m·K) reported by [119] and [120], and 0.101-0.117 W/(m·K) range

reported by [121]. Yet, it contrasts with the 0.2-0.25 W/(m·K) range reported by [122]. This contrast may be due to a variation of density, resin, or fibers, among others. [123] Note that the thickness of the double layer is less than double the thickness of the single layer. This is believed to be from non-uniformity of the surface. Determining the cause of this non-uniformity and isolating the uncertainty around the thermal conductivity of the MDF is outside the scope of this work.

Of much larger significance, the Owens Corning Foamular 250 XPS makes up a majority of the test cell construction. Two nominally thick 2" samples were tested to compare the thermal conductivity. Based on a total of 22 data points, the average thermal conductivity was 0.032 W/(m·K) at an average mean measured temperature of 28.11 °C. This compares favorably against the manufacturer-stated initial and long-term thermal conductivity of the material of 0.027 W/(m·K) at 24.4 °C. Further, inversion of the thermal gradient had no significant impact on the thermal conductivity.

The Polyisocyanurate (Polyiso) was made by Johns Manville and was of the AP Foil-Faced product line. At a nominal 2" thickness, it has an advertised U.S. R-Value of 13 °F·ft^2·h/BTU, or a converted thermal conductivity of 0.022 W/(m·K). Due to the author's apprehension with cutting this material, it was left in the 4' x 4' form and was not tested with the HFM.

The interior dimensions of the test cell were 34 inches (0.86 m) in width, 34 inches (0.86 m) in length, and 17.5 inches (0.45 m) in height, scaled linearly from the dimensions of a ground floor living space in Bhuj. Initially dominated by the length constraint of a piece of aluminum, this is roughly a 5.55:1 linear scaling from living space to scaled test cell. The inner layer of physical insulation boards making up the walls are affixed to each other via three #10 x 3 ½" coarse sheetrock screws at each corner, with an additional four screws locking in the 2" XPS outer walls.

The following tables illustrate the assumed material thicknesses, thermal conductivities, emissivities, and sources for those data for later computations.

Material	Thickness [cm]	Thermal Conductivity [W/(m·K)]	Source
Medium density fibreboard (Pegboard)	0.91	0.113	HFM testing
Extruded Polystyrene (XPS)	7.62 (3 inches), 2.54 (1 inch)	0.032	HFM testing
Polyisocyanurate (Polyiso)	5.08	0.022	[114]
Aluminum Sheet	0.32	0.237	[107]

Table 10: Summary of Material Thickness and Thermal Conductivity

Surface Material	Long-wave Emissivity	Source
3M ScotchBlue painters' tape	0.877	[124]
Aluminum Foil	0.04	[82, 111]

Table 11: Summary of Material Emissivities

3.2.1.3 Physical Test Cell: Window Locations

Noting that the building plans shown previously are not the as-built drawings, images taken from the Bhuj field site in 2019 were used to establish the size of the open window area. To do so, the image was flattened with Adobe Photoshop's Perspective Warp to remove the perspective, and the open window area was determined from the scaling of the window rough opening through the wall compared to the pre-construction documentation. These measurements were then confirmed via scaling to onsite measurements of the wall as a whole. Note that a flattened image of Figure 36 (not shown) suggests that the open window area is roughly 22.6 % of the rough window opening, or 2.0% of the entire wall. Within the context of the community, the rear door, one of which is shown open in Figure 36 due to the author's recent passage, is typically left closed at all times for security reasons.

Figure 36: Rear view of the as-built Bhuj housing. Window areas have been color-enhanced to highlight open window area. Red box on left outlines the limited open area through the entire rough window opening. Similar open area on the right has been covered with cloth as a means to seal off the window.

In line with the linear scaling, the scaled dimension the open window area for the test cell is roughly a circular hole of four-inch diameter. Thus, a circular air inlet was cut through one wall with a four inches diameter centrally located on width of the wall and one inch below the top of the wall. Later, for a second round of testing, this location was moved down to correspond to the scaled location along the wall (four inches from the ceiling).

Figure 37: Front view of the as-built Bhuj housing (Kitchen windows highlighted in red)

For the air outlet, the kitchen windows are highlighted in red in Figure 37 and the entirety of the highlighted area opens for ventilation. Although a gross-oversimplification of the system, for ease of construction and general applicability, it was assumed that the air outlet would be at the same position and of the same size as the air inlet.

The inlet air was provided via two inline four-inch duct blowers (Suncourt Inductor DB204C) rated for 65 Free Air cubic feet per minute (0.03 m^3/s, 265 air changes per hour) and 80 Boosted cubic feet per minute (0.038 m^3/s, 326 air changes per hour) [125]. This air was supplied through a four-inch flexible duct run 6 feet horizontally and roughly four feet vertically, and then connected to a 24” rigid duct oriented normal to the wall. Figure 38 shows the as-built construction from the exterior.

Figure 38: Test Chamber, as-built

To accommodate the thermal camera located below the chamber, the chamber was elevated on concrete bricks. This also allowed for easier removal of the lower panel to allow for thermal photographs. The field of view for the FLIR E8 series thermal camera is 45° x 34° [126], meaning that to capture the entirety of the ceiling with the camera, the camera lens must be located 56" (1.42 m) away from the ceiling. With the frame of the camera 5.5" (14 cm) thick and accommodating for the dimensions of the test cell, the ceiling was nominally placed 62" (1.57 m) above the plane of the floor. Further, as seen in Figure 38, small pieces of 1/8" cardboard was used for leveling of the ceiling layer and to occupy variations in the floor. Final leveling of the ceiling was measured at less than 0.2° from horizontal using a M-D SmartTool Gen2 electronic level (Accuracy ±0.1°) [127].

3.2.1.4 Physical Test Cell: Electrical Setup

Through the use of electric resistive mats, the total heat output varies as the square of the voltage. Thus, even a relatively small 5% variation in voltage could swing the total heating power by 10%. During October of 2018, the wall voltage at the setup varied throughout the day by roughly 5.8 volts AC (alternating current, 4.8% of nominal voltage) around an average value of 122.8 volts AC, well within the electrical code guidelines of a 5% maximum voltage drop from feeder and branch circuits, or the more conservative 3% drop from branch circuits alone [128]. Throughout the day, the voltage supply typically exhibited a localized higher than average wall voltage around 6 to 7 am, a generalized low from 11 am to 3 pm, and a generalized high in the evening hours. Since this fluctuation would provide an added layer of uncertainty when evaluating results later on, an online (double conversion) pure sine wave power supply was created to supply power within a narrower voltage band.

To create this system, the wall power supply, through a ground-fault circuit interrupter (Tower 30439005), was connected to a personal computer-targeted power supply (Dell L275AM-00) with the requisite "power-on" static load on the 5-volt DC (direct current) channel assumed by an incandescent

automotive headlight lamp (Phillips H11, 12362PRB2). Note that while this lamp is designed for roughly a 14-volt DC operating regime, the 5-volt DC supply was helpful to extend the lifespan of the filament in this application. The power supply is rated to provide 20 amps of continuous power at 12 volts (240 watts) and the total steady-state load of the downstream system at full power is 233 watts. The 12-volt DC output channels were then joined and connected to a 500W-rated pure sine wave inverter (Bestek MRZ5011BU [129]) This combination reduced the overall time-dependent variance of supply voltage to 0.2 volts AC (0.25% of nominal voltage) around an average voltage of 116.1 volts AC. As the voltage output of the power supply-inverter setup is load dependent, these readings were taken with the heaters and fans in their final operational setup, as outlined in Figure 39.

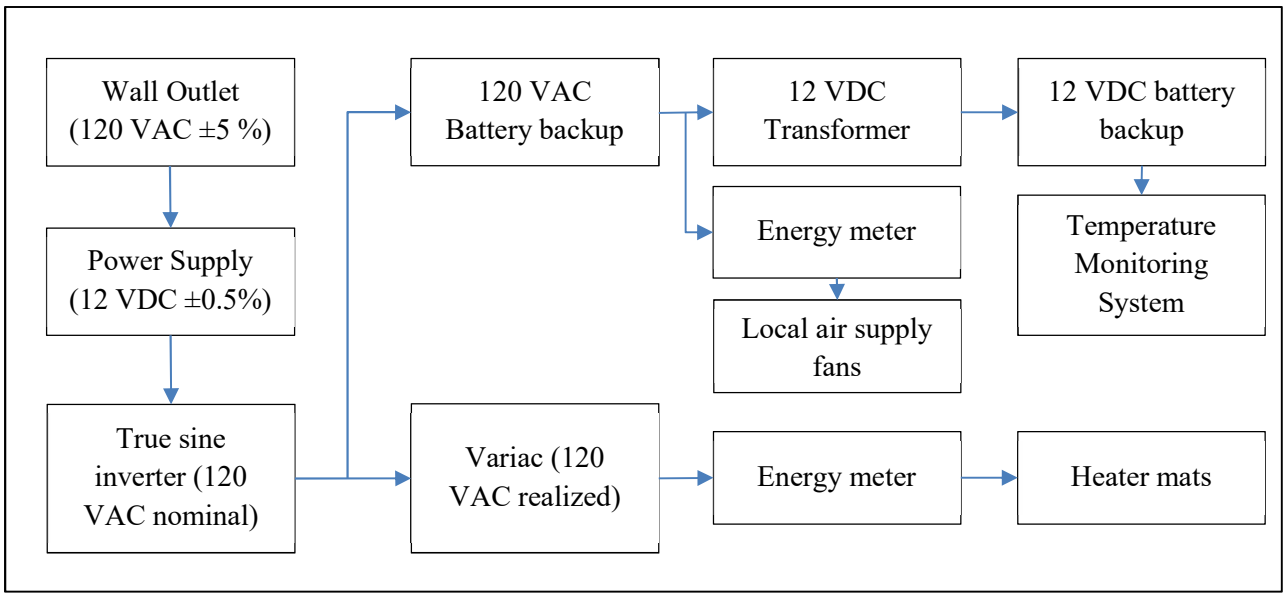

Figure 39: Electrical Supply System

This post-inverter power was then split between two legs. The first leg was then sent to an off the shelf battery backup system (APC Back-UPS LS 500, Yuasa Genesis NP7-12) to provide a safe cool down feature should the wall power be lost. From the battery backup system, the power and energy flow were monitored using an energy meter (WattsUp Pro 99333) feeding two 4" inline duct blowers (Suncourt Inductor DB204C) ducted in series to provide air into the heated part of the climate chamber. The battery backup system also provided power to the temperature monitoring system (Campbell Sci CR10X) through a nominal 12-volt DC transformer (Campbell Sci PN 9591) and an additional 12-volt power backup (Campbell Sci PS100, Yuasa Genesis NP7-12). From the CampbellSci data logger, the voltage at the logger was 13.38 ±0.03 volts DC.

To provide power to the resistance heat mats, the second leg took the post-inverter power and stepped it up to an average value of 120.2 volts AC using a Variac (Staco Energy Products 3PN1010) that produced a final variance in the voltage supplied to the heaters under load of up to 0.3 volts AC (0.25% of nominal voltage). As a final check, the waveform was spot-checked with the with an oscilloscope to qualitatively ensure that (a) the pure sine wave advertising of the inverter was correct, (b) the electronics of the secondary battery backup and transformer were not altering the waveform, and (c) the waveform did not change when under load for several days of use. Further, the energy meters were set to record

power factor for the initial shakedown run and recorded a power factor of one during that time, indicating a low-harmonic content and absolving concerns about adjustments to the power use.

3.2.1.5 Physical Test Cell: Anemometer Selection and Cross-Comparison

To ensure calibration of the anemometer used in this testing, a benchtop setup was used to compare against a known value. The test setup was comprised of a horizontally-orientated 1 ¾ inch (45 mm) internal diameter pipe roughly 6 feet in length (1.84 m) in length, plugged at one end except for a compressed nitrogen gas inlet line, and open to the ambient environment at the other. A slot was milled into the open end of the tube for the instruments to be inserted through. At this slot, the readings were taken roughly 40 diameters downstream of the nitrogen injection. A baseline test was run against the established hot wire anemometer setup.

This hot wire anemometer setup used a cylindrical hot film sensor, a Hewlett Packard 6632A power supply, and a Vernier LabPro coupled with Vernier Voltage Probe (VP-BTA). With this setup, a correlation was pre-determined by the lab instructor based on pitot tube measurements and is shown in equation (29), where C_0 is 8.06 ± 0.21 V^2 and C_1 is 7.19 ± 0.10 $V^2 \cdot (m/s)^{-1/2}$ [130]. This was tested across gas velocities from 0 to 10.75 m/s, the high side of which is well above the values that are measured in physical chamber testing.

$$velocity_{nitrogen} = \left(\frac{Voltage_{anemometer} - C_0}{C_1}\right)^2 \tag{29}$$

In addition to the existing anemometer, the nitrogen flow was controlled with a two-stage regulator and measured prior to the 6-foot tube via a flowmeter (Omega FMA-A2322), that was referenced for nitrogen gas at 70°F and 29.92” Hg. During testing, this flowmeter was referenced for consistency of air flow throughout the individual testing.

Six available sensors were selected due to availability and tested against the values in this nitrogen gas setup. The sensors, stated accuracies, and stated ranges are listed in Table 12. All sensors were tested with fresh batteries or a power adapter, if applicable. Note that the Onset Computer Corporation (“Onset”) equipment was coupled with Onset S-FS-CVIA Analog Module & H22-001 Energy Logger for data recording. Due to oversight when testing, all readings are taken in actual velocity and thus do not compensate for any drop in the fluid temperature throughout each experimental run.

Make / Model	Stated Accuracy	Range [m/s]	Source(s)
Testo 425	5% of reading + 0.03 m/s	0 – 20	[131]
Solomat MPM500e	3% of reading ± 0.1 m/s	0.01 – 12	
TSI Velocicalc 8345	Greater of 3% of reading or 0.015 m/s	0 – 30	[132]
Onset T-DCI-F350-W5A3 (Degree Controls Inc. F350-5A30)	1% of reading ± 0.05 m/s	0.15 – 1.0	[133, 134]
Onset T-DCI-F350-W5B3 (Degree Controls Inc. F350-5B30)	4% of reading ± 0.1 m/s	0.5 – 10	[133, 134]

Table 12: Anemometer sensors, stated accuracies, and stated ranges

For each trial run, the flow was controlled by the regulator pressure setpoint and measured with the pre-existing anemometer setpoint. Targeting airflows in the 0.4-1.0 m/s range, that yields Reynolds numbers in the 1,200 to 3,000 range, suggesting that the flow was laminar up until 0.77 m/s (Re_D <2300), and turbulent beyond 0.975 m/s (Re_D >2900). During each trial run, the velocity was measured by the pre-existing setpoint for a two-minute period, each individual sensor was run for a two-minute period using the averaging function, and the pre-existing setup was then reset to ensure consistency with the initial reading. Results are shown in Table 13.

	Run 1	Run 2	Run 3
Target Velocity	0.4	0.5	1.0
Reynolds number (flow regime)	1,189 (laminar)	1,487 (laminar)	2,973 (turbulent)
Make / Model			
Hot Wire Setup (Pre)	0.39 ± 0.01	0.46 ± 0.04	1.00 ± 0.05
Testo 425	0.39	0.73	1.29
Solomat MPM500e	0.30	0.81	1.54
TSI Velocicalc 8345	0.52	1.15	1.76
Onset T-DCI-F350-W5A3	0.54	n/a (max reading)	n/a (max reading)
Onset T-DCI-F350-W5B3	n/a (below min threshold)	1.38	1.90
Hot Wire Setup (Post)	0.41 ± 0.01	0.52 ± 0.05	1.02 ± 0.08

Table 13: Comparison of available anemometer results in controlled flow setup [actual m/s]

Assessing the results of Table 13, the variation in the hot wire setup may be due to omission of a temperature reading to correct values to standard velocity. Especially for Run 3, a drop in the output temperature by 6 °C across the total run time of the test is plausible and can explain the difference. Note though that this only accounts for a 2% experimental error, which is an order of magnitude less than the error exhibited by the other anemometers.

In determining the selection of anemometer, none of the options met the manufacturer stated accuracies across the three velocity choices. However, the Testo 425 was the best choice of the available

options due to the consistency and smallest error. In implementation, the Testo 425 has been used as a point of comparison, and the volumetric airflow is derived from a heat balance spreadsheet approach outlined in section 0.

3.2.1.6 Physical Test Cell: Thermocouples and data collection

To collect air and mass temperatures, thermocouples were used along with a data logger. Due to the relatively high amount of data points to collect, the thermocouples of the setup are based on a roll of T-type special limit thermocouple duplex extension wire (Omega EXPP-T-20-SLE-200). These were cut to size, stripped of insulation, twisted together, trimmed to match end lengths, and welded to join the wires, forming a small (~2 mm) thermocouple bead. Measured from end to end, the wires range in length from five feet to 13 feet, well within the 500-foot lead length threshold for lead length compensation [135]. Using a Campbell Scientific AM25T Thermocouple Multiplexer and a Campbell Scientific CR10X (accuracy: ±0.05%), the thermocouples were wired according to manufacturer instruction and the CR10X code was written in Edlog using the baseline setup within the AM25T documentation [135] combined with the CR10X documentation [136] and consultation with technical support [137]. The Edlog programming uses a 10 second measurement interval, averaged across a single minute and reported as such. For convenience, the code is included in Appendix A: Campbell Scientific CR10X/AM25T temperature measurement program.

To assess precision, these thermocouples were bundled together and placed in a heated water bath (VWR 89032-218). With an average ambient air temperature of 23.5 °C, the temperature control on the heated bath was set to 29.7 °C and the bath was let to sit for 12 hours. During this time, the Edlog code was temporarily rewritten to record and report every 2 seconds. Based on this, the simple average of all data points for all 19 channels was 29.66 °C (n=425,144) with the variations between thermocouples having a maximum difference at any one point in time of 0.35 °C and an average difference of 0.15 °C. These differences are well within the published error criteria of the greater of 0.5 °C or 0.4% [138]. Looking purely at the averages of the individual thermocouples, the highest thermocouple had an average of 0.08 °C higher than the mean of the group, and the lowest thermocouple had an average 0.05 °C lower than the mean of the group. The thermocouples had standard deviations ranging from 0.016 °C to 0.048 °C, with the average of the standard deviations of the individual thermocouples at 0.033 °C.

To assess accuracy, a sample of Gallium (Alfa Aesar 100g, 99.999%, packaged in poylethylene [sic] bottle) was added to the heated bath at the start of the 12-hour period with an assumed melting point of 29.7646 °C [139]. The temperature of the bath was then set 0.1°C higher to 29.8°C and the bath let to sit. Periodically throughout that time, the sample of Gallium was removed to check for a two-phase consistency. Data was collected from the logger once melting was qualitatively observed. At this data point, the simple average of the thermocouples was 29.77 °C (n=19) with the individual thermocouples reading from 26.73 °C (0.04 °C lower than mean) to 29.82 °C (0.05 °C higher than mean).

Based on these two tests, the thermocouples are well within the experimental limits set by the vendor and the readings exhibit good agreement with the accepted value. Assuming the reference standard for Gallium is the accepted value, the root mean square error of the thermocouples is ±0.12 °C.

3.2.1.7 *Physical Test Cell: Infrared Camera Accuracy and Uniformity*

As mentioned earlier in Section 3.2.1.3, the ceiling was 62" (1.57 m) above the floor on which the thermal camera was located. This was primarily based on the limiting angle of the field of view (34°). On the physical aspect of taking the reading, the aluminum sheet alone would be more prone to thermal reflections and would lead to a high uncertainty with the result. Accordingly, the aluminum sheet was covered with a single layer of 3M ScotchBlue painters' tape and pressed with a small painting roller to ensure contact. Air bubbles were relieved with a scalpel. For the thermal photographs, Gustavsen and Berdahl [124] reported Fourier Transform Infrared Reflectance (FTIR) spectroscopy results to determine the normal emissivity for masking tape as a pre-requisite for their testing. Of these, Scotch 231 3-712 masking tape was determined to have a normal emissivity of 0.877, while Red Permacel P-34 masking tape and Tartan 5140 masking tape were measured at 0.870 and 0.861, respectively. Higher values for masking tape emissivity values are conventionally within the 0.90-0.95 range, but are typically assumed [140, 141, 142, 143] and not measured [144].

Building on the thermocouple validation in Section 3.2.1.6, assessment of the validity of the 0.877 emissivity assumption for the masking tape was established using a thermocouple applied under a small piece of tape. In this setup, the heating mats were provided a limited amount of power, the inlet and outlet capped, and the bottom closed. Figure 40 shows the thermal image and the crosshairs (Sp1) where the thermocouple was located.

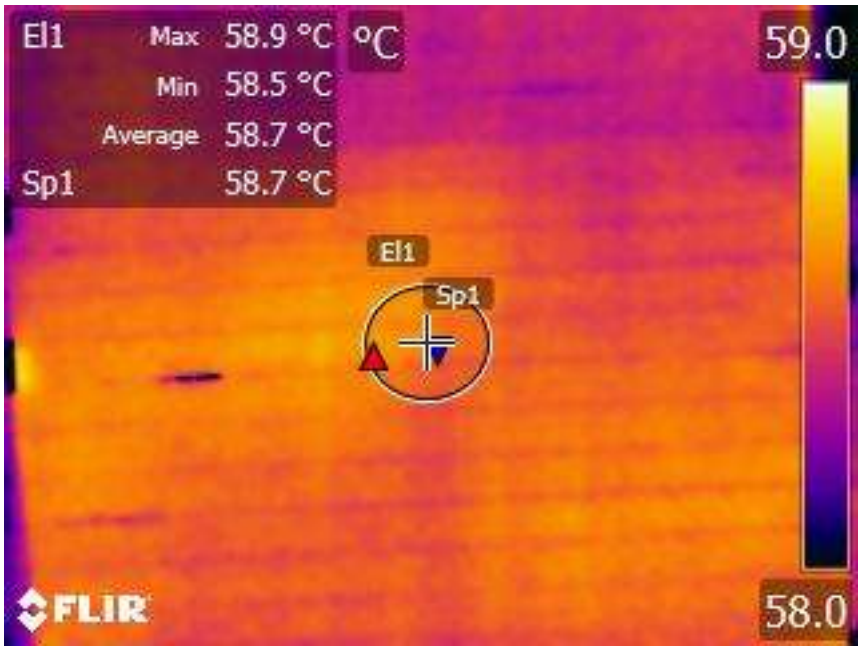

Figure 40: Thermocouple-infrared agreement (Emissivity 0.877, Reflected, Atmospheric & Exterior Optics Temperature 20.4 °C, 1.4 m Distance, Relative Humidity = 35%). Thermocouple measurement was 58.9 °C

Other inputs into the thermal image are include the atmospheric and exterior optics temperature, distance to object, and relative humidity. While these values have a smaller influence on the reading of the thermal camera since the distance to object is low, they were still included in the analysis of the thermal images. The atmospheric and exterior optics temperature inputs were derived from the average of the two inlet air thermocouple readings. The distance to object was kept at 1.4 m, and the relative

humidity assumed to be 35% (upper limit due to dehumidifier in space). The more important input, that of the reflected temperature, was also assumed to be equal to the inlet air temperature within the space. These assumptions remained in place throughout all of the thermograms seen in this paper.

Using the 0.877 emissivity value obtained from [124], as well as temperature data recorded from ambient thermocouples in the space and an assumed relative humidity, the thermogram provides exceptional agreement (58.7 °C) with the thermocouple (58.9 °C) that was previously located at that location. While the stated error of ±2% or 2 °C of the thermal camera far exceeds this error, the error is more in line with the sum of the thermal sensitivity (0.06 °C) of the camera and the error of the thermocouples. Given this agreement, it is assumed that the published value of 0.877 for the emissivity of the blue painter's tape is appropriate when the other factors associated with thermography are accounted for. For completeness, those other factors are reflected temperature, distance, atmospheric temperature, exterior optics temperature, exterior optics transmissivity, and relative humidity. Further, before taking infrared photographs, the camera was powered on for roughly ten minutes prior so as to finish the initial self-calibration steps that are frequent within the first three minutes.

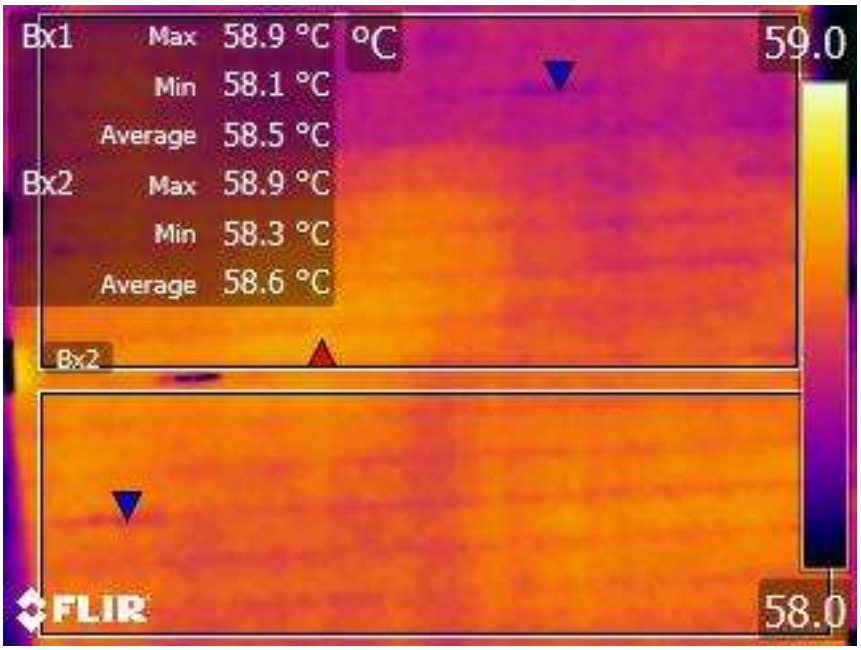

Figure 41: Heater uniformity (Emissivity 0.877, Reflected, Atmospheric & Exterior Optics Temperature 20.4 °C, 1.4 m Distance, Relative Humidity = 35%).

There are eight individual heating pads within the test cell, leaving an opportunity for a resistance variation between the pads to manifest itself within the thermal image. As seen in Figure 41, the overall variation in temperature of the bottom of the aluminum sheet is in the range of 0.8 °C, correlating to a variation in total power through the heating mats of an estimated 1.5%, assuming that the overall heat transfer coefficient is uniform across the ceiling. Note that, at high degrees of power turn-down, such as the roughly 65% that would correspond to the above case, voltage metering is not possible on the downstream leg of the Variac since the voltage is below the threshold for the WattsUp energy meters. An electric reading upstream of the Variac would give a false sense of scale due to both the static state and load/voltage conditions on the Variac at that time.

3.2.1.8 Physical Test Cell: Summary of Data Collection Process and Variability

The physical instrumentation of the test cell is as important as the process of collecting the data, especially since the test cell at steady-state has a lower floor that needs to be removed for the thermogram. While the thermocouple and energy meter data can be downloaded without impacting the operating conditions of the test cell, the thermogram cannot. To assess a variation in the temperature of the aluminum sheet as a function of time, it can be analytically approached using the time constant, τ.

To use the time constant in this application, the upper surface of the aluminum is assumed to be adiabatic, especially so in the short term. As such, using an approximated Biot value with an assumed total heat transfer coefficient of 7 $m^2 \cdot K/W$ and the thickness (0.32 cm) and thermal conductivity (0.237 $W/(m \cdot K)$) of aluminum from Table 11, arrives at a Biot number of roughly 0.1. Since the Biot number is much less than unity, convection resistance dominates and the lumped approximation is valid. Even in a case where the total heat transfer coefficient is half of the suggested value of 7 $m^2 \cdot K/W$, the Biot number is still roughly 0.2, and much less than unity.

Given this, the time constant for a slab can be evaluated through Equation (30), from Glicksman and Lienhard. [103] As the Biot number is much less than unity and the exterior convection dominates, the thickness L is evaluated at half the plate thickness.

$$\tau = \frac{\rho c_p L}{\bar{h}} \tag{30}$$

Using values from [111], aluminum alloy 1100 has a specific heat of 896 $J/(kg \cdot K)$, and a density of 2,740 kg/m^3. Retaining the 7 $m^2 \cdot K/W$ assumption from before, this yields a thermal time constant of 561 seconds, or 9.4 minutes. As three times the time constant is the rough time for a slab to warm/cool 95% of the way from the starting temperature to the final temperature, readings taken shortly (less than a minute) after removing the floor of the chamber are taken on face value and support a premise that the reported values are conservative estimates of the subsequent convective heat transfer coefficient. Using the prior assumptions is also an aggressive approach, since the change in the total heat transfer coefficient is assumed to be only the change of the radiative heat transfer component in the short term. This assumption can be made since the primary airflow over the surface of the ceiling remains unchanged with or without the test cell lower panel.

During the data collection process, all thermograms were taken from below within a one-minute time frame of the floor of the test cell being removed. The first readings, or the thermograms that constitute the reported values, are largely within the first 15 seconds of removing the test cell floor, and thus well within the 561 seconds of a single time constant. All first readings were recorded within 30 seconds of removing the floor of the test cell. Nonetheless, to understand the implication of time in collecting the thermal images, thermograms from below the test cell are shown below for the ten-second, one-minute, and three-minute time frames after removal of the floor of the test cell, all taken with a FLIR E8 thermal camera.

In this setup, there is a moderate (0.5 m/s) jet flow from the bottom of the image, ambient environment temperature is 19.3 °C, test cell exit air temperature is 35.9 °C, and the uppermost thermocouple temperature is 37.6 °C.

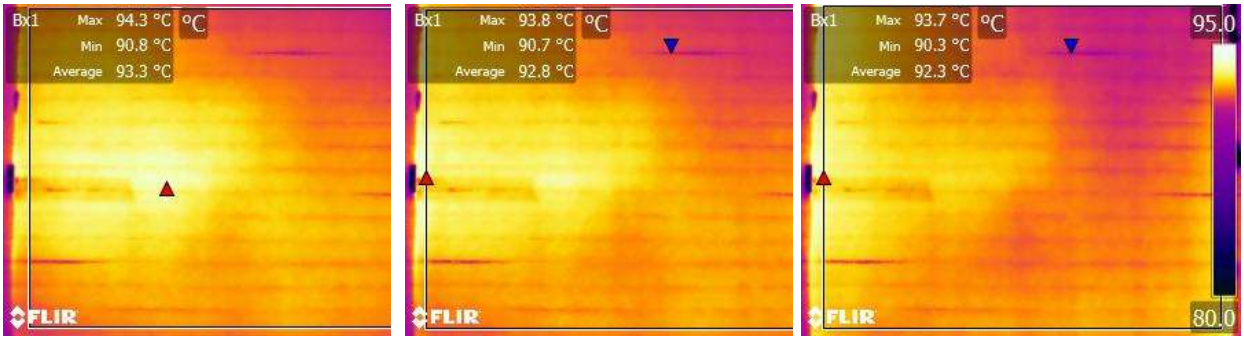

Figure 42: Comparison of thermal camera readings as a function of time. Left: 10 seconds after removal of test cell floor, Center: 1 minute, Right: 3 minutes. The test setup included jet flow into the cell from the bottom of the photograph. (Assumed Emissivity=0.877, Reflected, Atmospheric & Exterior Optics Temperature: 19.3 °C)

The variation of temperature across the photographs (1.0 °C) is meaningful in that it confirms the hypothesis from the thermal time constant approach listed above. Within the first three minutes, there is a change to the overall temperature of the ceiling, underscoring the importance of timing of the thermogram. During the collection phase, the thermograms were taken within the first ten seconds after removing the floor of the cell. Prior to this, the thermal camera was powered on for about ten minutes to ensure that it had effectively warmed-up, which is more than three times the three-minute period in which the thermal camera self-calibrates often.

A keen observer will note that, despite best efforts, the thermograms do not encompass the entirety of the ceiling. This suggests that the effective field of view may be smaller than that published by the manufacturer. Nonetheless, a workaround to this is to take a series of thermograms. In this case, four thermograms were taken for each test. One is directly normal to the surface of the ceiling, the second is angled towards the outlet, the third towards the inlet, and the fourth back to normal. The fourth thermogram was taken as a control to look at the surface temperature change during the thermography period, and as a backup in case the first thermogram was corrupted or had errors. The fourth thermogram is also useful in the sequencing of tests in that it requires the frame of reference to be re-centered, allowing the first thermogram of the next test sequence to be aligned and meet the ten second threshold.

The thermal camera itself is intended as a field-use instrument, and so the thermograms were taken through remote (wired) viewing to a laptop running FLIR Tools v6.4. Without this remote viewing, it is difficult to assess the framing and readiness of the camera given that the screen is adjacent to the floor. However, utilizing the remote viewing under the data stream does remove the visual component of the image, prohibiting the multi-spectral dynamic imaging feature which may be meaningful for interpretation of non-planar surfaces. At the time of writing, FLIR Tools has been discontinued and the functionality should now be within the FLIR Thermal Studio Suite.

3.2.1.9 Physical Test Cell: Data Collection Points

With the thermocouples and thermal camera data assessed, the thermocouples were placed to get estimates of heat flow through the insulation layers and via the airflow. Critical to these estimates is an assumption that the surfaces can be treated as unidimensional objects, and so ignore any variation with the temperature with respect to position along the wall. Within the test cell, two thermocouples were allocated to the roof, one at the XPS-Polyiso junction and one at the XPS-MDF junction. A thermocouple

was not placed at the Aluminum-Polyiso junction due to concerns over exceeding the maximum temperature of the polyvinyl insulation on the thermocouples [145].

Two thermocouples were allocated to each of the four walls, located at the center point of the wall, with one thermocouple between the aluminum foil and the inner XPS sheet, and one between the inner and outer XPS sheets. Two thermocouples were also to the center point of the floor, with one located between the XPS and the aluminum, and one taped to the bottom of the floor with black Gorilla brand tape.

Understanding the significance of the incoming air, two thermocouples were allocated to this. One was located in the center of the duct immediately before penetrating the XPS wall, and one was located at the point where the flexible 4" diameter duct meets the rigid duct. A single thermocouple was allocated to the outlet air, centered in the orifice, and one was left outside the test cell to measure the ambient air. This ambient air thermocouple was located away from any significance heat source or suspected thermal plumes.

Finally, the thermal camera was located beneath the chamber, as mentioned in section 3.2.1.7. Figure 43 shows these locations graphically.

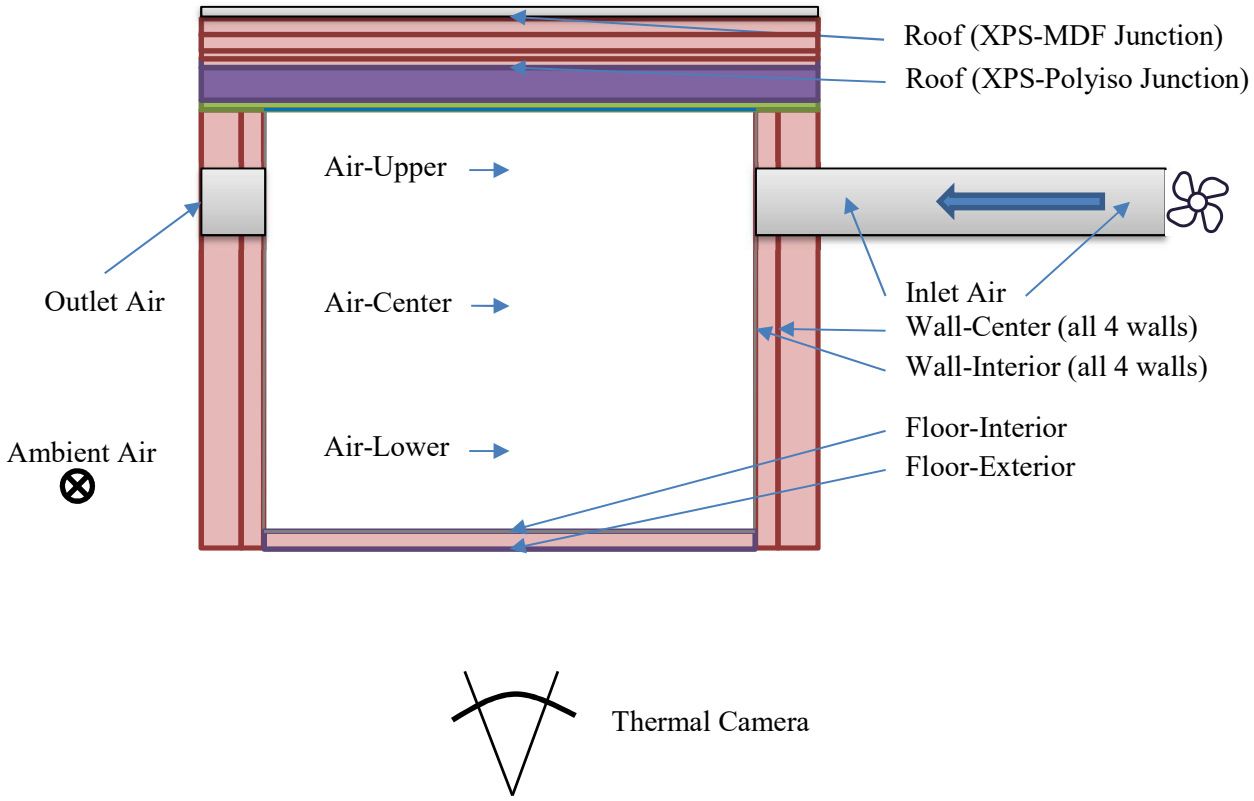

Figure 43: Summary of 18 thermocouple locations

Energy data was logged via WattsUp? Pro power meters (Model 99333) on a 5-second logging interval to record watts, volts, amps, power factor, duty cycle, frequency, and volt-amps. This data was time-synchronized with the laptop clock upon recovery. Some of these logged fields may seem

superfluous, but all have a role. Principally for the later assessment of the heat transfer, watts remained the most useful. Volts were logged to assess any changes in the performance of the double-conversion power supply setup and variac. Amps were logged for a more granular view of the heating mats, as the resistive component of the heating mats varies as a function of temperature and final assessment of electrical stability would be logged in this field. Power factor, duty cycle, frequency, and volt-amps were recorded to quantitatively assess any possible phase and electrical waveform concerns. Overall accuracy of the WattsUp Pro models for the electrical loads of interest is ±3% [146]. For repeatability of these results, it is recommended that future researchers use a currently-supported model, some of which publish accuracies near 0.5% [147].

3.2.1.10 Physical Test Cell: Louvers

Within the test cell, the louvers were placed directly against the inlet orifice of the chamber. In the 1” offset case, the louver was slid into position and held by the weight of the roof. In the 4.2” offset case, the louver was screwed into position through the inlet orifice which connected to the inlet plenum. The latter design (4.2” offset) was designed to have a louver depth of three times that of the anticipated lower bound of turbulent intensity (the turbulent length scale of fully developed flow) [148].

Figure 44: Inlet Louvers. 1" Offset (Left) and 4.2" Offset (Right)

For the 1” offset cases, the louvers were a coarse setup 50 mm in depth normal to the wall and centered along the inlet of the orifice. For the horizontal spread cases, the individual louvers are 1 mm in thickness and have a 14 mm vertical gap along the inlet. Assuming the incoming flow was fully-developed turbulent flow, 50 mm corresponds to roughly seven times the turbulent length scale [148]. For the vertically redirected cases, four fins were spaced 25 mm on center, with the second from top fin located along the centerline of the orifice. This density was chosen so that there was no normal linear path through the diffuser at 20° incline.

The 4.2” offset cases limited the depth of the louver setups to be more in line with reasonable expectations for the scaling in a home setting. At a 15 mm depth normal to the wall, the depth is roughly twice that of the turbulent length scale. The overall assembly covers the entirety of the four-inch diameter orifice and mates flush with the wall. Maintaining the 1 mm thick louvers, an example of the case of the 60° inclination angle with 10° spread is shown in Figure 45. Note that for angles smaller than 50°, the density of the louvers was doubled to ensure that the air flow was influenced. 0° cases, including jet flow, did not have louvers for that direction. Further, the inclination angle defined in this flat slab roofing section is pertaining to the direct of the airflow, not the angle of the roof slab from Section 2: Bhuj Pitched Roof Housing.

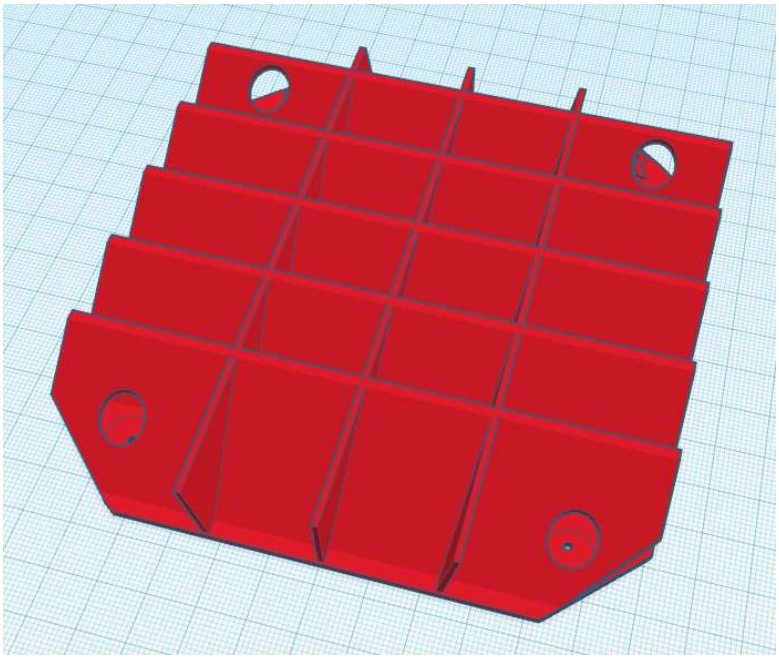

Figure 45: Inlet Louvers. 4.2" Offset case of 60°inclinations angle with 10°horizontal spread. Background is 1 mm minor grid and 1 cm major grid. Four corner holes are exterior to the main region of the airflow.

3.2.1.11 Physical Test Cell: Initial Model and Expectations

Previous sections reference an initial model that was used to determine what ranges of temperatures might be expected at various points within the test cell. This model was developed to check the impact of various heat transfer coefficients, power (heating mat) inputs, and air flow rates. Further, it was used to understand what temperatures might be expected and then assess how those temperatures related to the limitations of the materials (i.e. working limits of insulation materials). The core assumptions of this model are that:

- it is well-mixed;
- it is at steady-state;
- no radiation exchange through the inlet and outlet; and
- interior radiation can be approximated by a standard gray body model without reflections.

Structurally, the model uses the geometry of the inside of the test cell as the source of the area terms. This has the implication of remaining ignorant of edge effects, which would imply that the model is conservative in terms of the conductive heat loss. Given that the structure is made entirely of XPS insulation though, this contribution was considered minor. The resistive heating mat heat input is also expressed in terms of what would be read by the WattsUp energy meters, and so ignores any energy that is used by the status lights on the two power strips used in practice, as well as electrical resistive losses downstream of the meter. The unloaded state of the power strips with status lights illuminated was not registered on the energy meters (assumed less than 0.1 W), and the electrical resistive losses of the power cords are estimated to be negligible given the low current and conductor sizing of the cords.

Conductive resistance was evaluated using a basic first-principles approach by turning the thickness and thermal conductivity of the layers into thermal resistance. Thermal conductivities are established previously in Table 10. Convection was initially assumed to be an input based on an assumption that the convective coefficient was between 4 and 8 W/(m^2·K), but later enhanced based on the convective coefficients for vertical and horizontal plates outlined in 2017 ASHRAE Fundamentals [111].

The iterations were guided by individual energy balances for each of the surfaces (ceiling/roof, wall, floor) that originated with the assumed temperature at the ambient environmental temperature, and then readjusted the temperature of the surface based on the heat balance. Structurally, this was accomplished by evaluating the inside and outside heat flows based on the temperature value, looking for the net difference between those values, and, if the difference was greater than 1,000, dividing the heat balance number by 1,000 and adding it to the temperature values. While inconsistent with units, this approach proved effective, easy to implement, and quick to iterate.

Radiation was based on assumed long-wave emissivity for the surface (Table 11) with addition of the polystyrene insulation as published by Raznjevic (emissivity=0.9) [149], along with a view factor correlation for finite aligned parallel rectangles obtained from Incropera, et al. [107], and cataloged by Howell [150]. For the geometry of the test cell, the view factor from the ceiling to the floor was roughly 0.41, leaving the remaining view factor to the walls at 0.59.

While it may seem counterintuitive to have both a convection assumption and then evaluate the correlation value, the model uses an iterative solver for each surface to achieve the steady-state approximation since the surface temperature is an input into the Grashof number and a seed value is needed.

The convection coefficient values from 2017 ASHRAE are reproduced below, and are based on the Grashof (Gr), Rayleigh (Ra), and Prandtl (Pr) numbers. While the Prandtl is based on the correlation from Table 1, Grashof (Equation (31)) and Rayleigh (Equation (32)) are reproduced below.

$$Gr = \frac{g\,\beta\rho^2|\Delta T|L^3}{\mu^2} \tag{31}$$

where
g is the acceleration due to gravity;
β is coefficient of thermal expansion;
ρ is the density of air (via Table 1);
$|\Delta T|$is the absolute value of the difference between the surface temperature and the bulk fluid temperature;
L is the characteristic length; and
μ is the dynamic viscosity of the air (via Table 1).

$$Ra = Gr \cdot Pr \tag{32}$$

For an assumed constant heat flux through the surface of a wall with a characteristic length L of height, with the the coefficient of thermal expansion assessed at the bulk fluid temperature, the Nusselt

number correlation is shown below in Equation (32), and is applicable to Rayleigh numbers between 10^{-1} and 10^{12}. For the test cell, Rayleigh numbers for the walls were in the 10^{7} range.

$$Nu = \left\{0.825 + \frac{0.387\ Ra^{1/6}}{[1 + (0.437/\mathrm{Pr})^{9/16}]^{8/27}}\right\}^{2} \qquad (33)$$

For a downward-facing heated plate (ceiling when no ventilation is present) and an upward-facing cooled (floor) horizontal plate, the correlation is identical within the Rayleigh numbers between 10^{5} and 10^{10}. In this scenario, the characteristic length L is the area of the plate divided by the perimeter of the plate. For the test cell, Rayleigh numbers for the floor are in the 10^{6} range. Note that the applicability of this correlation should be checked on a case-by-case basis for higher emissivity floor materials, as the floor may be radiatively heated thereby be an upward-facing heated plate [111].

$$Nu = 0.27\ Ra^{0.25} \qquad (34)$$

This same correlation (Equation (34)) is also applicable to the exterior surface of the test cell floor, which has a Rayleigh number in the 10^{6} range.

For an upward-facing heated plate, where characteristic length L is the area of the plate divided by the perimeter of the plate, is applicable to the exterior of the ceiling assembly. The correlation presented below (Equation (35)) is applicable to Rayleigh numbers between $8 \cdot 10^{6}$ and $1.5 \cdot 10^{9}$. The test cell value was in the neighborhood of $1.2 \cdot 10^{9}$.

$$Nu = 0.15\ Ra^{1/3} \qquad (35)$$

The three previous equations ((33), (34), & (35)) are listed in terms of the Nusselt number, which is previously defined as part of Equation (28).

With governing conduction, convection, and radiation correlations established, the list below illustrates the inputs (left) and estimates (outputs, right) based on the model.

Inputs	Outputs (Estimates)
Ambient (environment) temperature	Surface convective coefficients
Interior dimensions	Interior surface temperatures
Electrical (heat) input	Exterior surface temperatures
Material thicknesses	Heating mat temperature
Material thermal conductivities	Heat Flow through surfaces
Material surface emissivities	Heat Removal via Airflow
Air thermo-physical properties (Table 1)	Air outlet temperature
Air flow rate	Inside air temperature
Ceiling Convective Coefficient	Interior view factors
Interior Wall Convective Coefficient (if applicable)	Air change rate

Using this model, it is possible to vary one input and predict the change on the outputs. While many of the directions of the outputs are intuitive, the scale may not be. As applied to the physical testing, the influence of the ceiling convection coefficient on the indoor air temperature and the overall heat removal via airflow is illustrated in the figure below (Figure 46). Along with assumptions of geometry and material characteristics, the ambient temperature (20.0 °C), electrical input power (160.0 W), airflow rate (0.93 m/s, 0.0075 m^3/s), and interior wall convection coefficient (4 $W/(m^2K)$) were held constant, only varying the ceiling convection coefficient. For reference, the evaluation of Equation (34), a downward facing heated plate assumed to be the state where there is no airflow enhancing the convection, suggests a ceiling convective coefficient of 2.6 $W/(m^2K)$ when holding the interior wall convection coefficient at 4 $W/(m^2K)$. The ceiling convection coefficient remains the same (2.6 $W/(m^2K)$) when the interior wall convection coefficient is evaluated via Equation (33) at 1.5 $W/(m^2K)$.

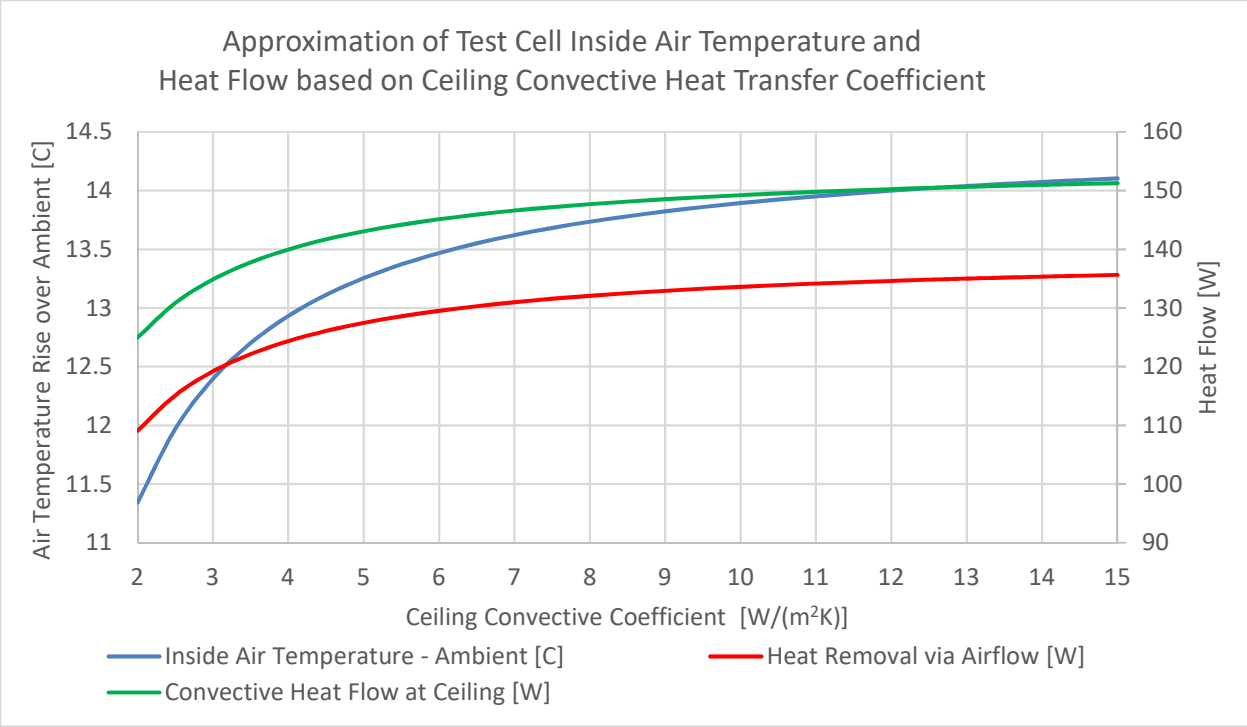

Figure 46: Approximation of Test Cell Inside Air Temperature and Heat Flow based on Assumed Ceiling Convective Heat Transfer Coefficient Assuming a Constant Airflow Rate

As Figure 46 illustrates, the model illustrates a diminishing change in the air temperature, heat flow at the ceiling due to convection, and overall heat removal due to airflow with increasing ceiling convection coefficients. However, most importantly, it illustrates that above ceiling heat transfer coefficients around 11 W/(m^{2}K) or so, the increase of the net heat removal via airflow diminishes substantially, suggesting that airflow rates would need to be increased to remove this heat from the ceiling, rather than simply moving the heat from the ceiling to the interior of the space as the increasing temperature illustrates.

A more appropriate way to look at this data would be to link the concepts of airflow and ceiling convective coefficients together, as Spitler, Pedersen, and Fisher did [151]. Using their correlation for the convective coefficient of a ceiling given a side wall inlet yields a ceiling convective coefficient of 3.1 W/(m^{2}K) and a side wall convective coefficient of 5.4 W/(m^{2}K). While the underlying coefficients are at the limit of the stated applicability ranges for the jet momentum and Archimedes number, it is entirely possible that these two limits do not capture the scaling of the test cell to an occupied house.

3.2.2 Physical Testing: Analysis Method

Whereas Section 3.2.1 described the setup and Section 3.2.1.11 described a well-mixed simplified model meant to build a cursory understanding of the impacts of the heat transfer coefficient on the expected temperatures, it did not describe a way to take the experimental data and use that to determine the heat flows, thereby decreasing the amount of assumptions and providing a better parallel to Indian housing.

The structure of the analysis method is the same as the simplified model previously described, but the analysis method is able to drop parts of the well-mixed assumption. An important distinction is made here in that there is only a single thermocouple assigned to the surfaces, but that the convective coefficient is a function of the adjacent air temperature, and not solely the mean or well-mixed air temperature.

Using the data from the thermocouples from Figure 43, a single dimensional approach using the overall thermal resistivity allows for an approximation of the net heat transfer leaving the test cell through the six surfaces. Note that heat flow is only evaluated between the two points where the thermocouples are placed, so it is critical to assess either the heat removed from the test cell via airflow or the heat transfer through the aluminum sheet. The net heat flows are best described in equation form. Equation (36) describes how the input of power into the test cell via the heating mats ($\dot{Q}_{heatingmats}$) is constrained to either being removed by conduction through one of the six sides ($\dot{Q}_{conduction,i}$), or via the airflow through the space ($\dot{Q}_{airflow}$).

$$\dot{Q}_{heatingmats} = \dot{Q}_{airflow} + \dot{Q}_{conduction,i} \qquad (36)$$

Equation (37) then suggests an alternate (smaller) control volume where the heat input into the heating mats either goes through the insulation on top of test cell ($\dot{Q}_{rooftop\ conduction}$) or through the aluminum into the test cell airspace ($\dot{Q}_{aluminum\ conductio}$).

$$\dot{Q}_{heatingmats} = \dot{Q}_{rooftop\ conduction} + \dot{Q}_{aluminum\ conduction} \qquad (37)$$

Equation (38) expands on Equation (36) to define the temperature of the heating mats ($T_{heatingmat}$) as a function of the assumed or collected values.

$$\dot{Q}_{heatingmats} = \frac{k_{XPS} A_{ceiling} (T_{XPS-PolyISO} - T_{XPS-Pegboard})}{t_{XP}} + \frac{k_{aluminum} A (T_{heatingmats} - T_{ceiling})}{t_{aluminum}} \qquad (38)$$

where
k_{XPS} is the thermal conductivity of the extruded polystyrene (Table 10);
t_{XPS} is the thickness of the extruded polystyrene (Table 10);
$T_{XPS-PolyISO}$ is the temperature at the XPS-PolyISO interface;
$T_{XPS-Pegboard}$ is the temperature at the XPS-Pegboard interface;

$A_{ceiling}$ is the area of the ceiling;
$k_{aluminum}$ is the thermal conductivity of the aluminium sheet (Table 10);
$t_{aluminum}$ is the thickness of the aluminium sheet (Table 10);
$T_{heatingmats}$ is the inferred temperature of the heating mats; and
$T_{ceiling}$ is the measured temperature of the ceiling via the thermal camera (Section 3.2.1.7).

With the conduction constraints defined, evaluating the convection heat transfer first requires the definition of an assumed radiative heat transfer. The view factor from the ceiling of the test cell to the floor of the test cell was defined at 0.41, leaving the remaining view factor to the walls at 0.59. Thus, the view factor from the ceiling to any single of the four walls is roughly 0.15. Using a gray-body approximation without reflections yields an assumed radiative heat transfer. For the test cell radiation heat transfer component, the walls were assumed to be isothermal with the temperature for each wall matching that of the recorded value from the thermocouple.

Equation (39) defines the two modes of heat transfer from the ceiling into the test cell.

$$\dot{Q}_{aluminum\ conduction} = \dot{Q}_{convection,ceiling\ to\ air} + \dot{Q}_{radiation,ceiling\ to\ other\ surfaces} \quad (39)$$

Equation (40) defines the radiation heat transfer from the ceiling to each of the five surfaces inside the test cell.

$$\dot{Q}_{radiation,ceiling\ to\ other\ surfaces} = \sum_{i=1}^{5} \varepsilon_{ceiling}\alpha_{surface,i}\sigma A_{ceiling}\mathcal{F}_{ceiling,surface\ i}(T_{ceiling}^4 - T_{surface,i}^4) \quad (40)$$

where
$\varepsilon_{ceiling}$ is the long-wave emissivity of the ceiling (assumed to be 0.877);
$\varepsilon_{surface,i}$ is the long-wave absorptivity of the five internal surfaces (assumed to be equal to the long-wave emissivity and 0.04 for aluminum foil);
$\mathcal{F}_{ceiling,surface\ i}$ is the view factor from the ceiling to surface i (assumed to be 0.41 to the floor, and 0.15 to each of the four walls); and
$T_{surface,i}$ is the absolute temperature of the non-ceiling surfaces (assumed to be isothermal and equal to the thermocouple values).

From Equation (39), it is then possible to define a convection coefficient based on an assumed reference temperature ($T_{reference}$), where $T_{reference}$ can be either the inlet air temperature (T_{inlet}), the thermocouple nearest the ceiling ($T_{adjacent}$, akin to an adjacent air temperature), or the average of the three inside air temperatures ($T_{average}$, akin to an average air temperature). Each of these reference temperatures are used in various pieces of literature and have significance to difference audiences.

$$\dot{Q}_{convection,ceiling\ to\ air} = h_{convection}A(T_{ceiling} - T_{reference}) \quad (41)$$

3.3 Experimental Results

The test cell allowed a series of louvers to be installed to evaluate the impact of diameter-based Reynolds number and airflow direction angle on the convective heat transfer. These variations encompassed two different inlet locations (1" from ceiling and 4.2" from ceiling), Reynolds numbers between 3,950 and 45,710, and inclination angles between 0° and 60° towards the ceiling. In addition, a handful of cases combined the inclination with a broadening out of the airflow. In total, 44 cases were tried.

Within the 1" offset inlet location tests, Reynolds numbers were limited in scope, ranging from 6,650 (0.86 m/s) to 7,450 (0.96 m/s). The testing variations ranged from normal to the inlet wall to (0° towards ceiling) to 20° towards the ceiling. Further, horizontal spread ranged from 0° to 20° in combination with, and independent of, the vertical variation.

Within the 4.2" offset inlet location tests, the Reynolds numbers were broader, ranging from 3,950 (0.5 m/s) to 45,710 (5.7 m/s). These Reynolds numbers were chosen to be on the same scale as what one would expect to find in the Bhuj homes (window hydraulic diameter of 0.56 m, pedestal fan diameter 0.45 m) with an air velocity of 0.24 m/s. This is the same air velocity that was recorded from a locally-acquired Bajaj Tornado-II pedestal fan set on low, as recorded with a Pacer DA30 anemometer one foot downstream of the fan blade. High speed settings were recorded around 0.76 m/s (Reynolds ~ 23,000). Within the scope of airflow, the laminar to turbulent transition is likely within the 2,300 to 4,000 range, with lower numbers within the laminar regime and higher numbers in the turbulent regime. As all testing was with Reynolds numbers above 3,950 and with the presence of the louvers, air flow can be considered turbulent. The 4.2" offset cases also varied the angle of inclination from 0° to 60°, with some cases expanding the horizontal spread by 20°. No testing was done for either case was done with the angle of the jet directed towards the floor, or with a nozzle to constraint the flow or modify the mass flow rate or velocity.

As the ultimate takeaway from this testing was the impact on the convective coefficient, the following are a collection of the thermograms taken during testing. On the left-hand side is the thermogram itself, adjusted for an emissivity of 0.877, a distance of 1.4 m, exterior optics transmissivity of 1.0, relative humidity of 35%, and a reflected temperature, atmospheric temperature, and exterior optics temperature at the recorded ambient value. On the right-hand side are the inlet temperature (T_{inlet}), the uppermost thermocouple temperature ($T_{Upper\ T/C}$), the difference between the ceiling and in the inlet air temperature ($\Delta T_{ceiling}$), the difference between the outlet air temperature and inlet air temperature ($\Delta T_{inside\ air}$), the estimated conductive heat flow through the ceiling ($\dot{Q}_{cond}$), the Reynolds number of the airflow through the inlet orifice (Re_{inlet}), the convective heat transfer coefficient based on the inlet temperature (h_{inlet}), and the convective heat transfer coefficient based on the uppermost thermocouple temperature ($h_{upper\ T/C}$).

For these steps $T_{inside\ air}$ is defined via the air exiting the test cell. In practice, as compared to the average of the three thermocouples within the space, these values were within 0.3 °C of each other and deviated by an average of 0.1 °C.

$$\Delta T_{ceiling} = T_{ceiling} - T_{inlet} \tag{42}$$

$$\Delta T_{inside\ air} = T_{outlet} - T_{inlet} \tag{43}$$

$$h_{inlet} = \frac{\dot{Q}_{convection,ceiling\ to\ air}}{A\ \Delta T_{ceiling}} \tag{44}$$

$$h_{upper\ T/C} = \frac{\dot{Q}_{convection,ceiling\ to\ air}}{A(T_{ceiling} - T_{upper\ T/C})} \tag{45}$$

A selected few cases are shown below, notably showing the distribution patterns for the 1" offset jet, showing the increase in convective heat transfer coefficient when moving from a 0° to a 20° incline case., and then the impact of horizontally spreading the flow by 20°. Further, the impact of relocating the inlet to 4.2" off the ceiling (scaled to match the Bhuj housing) is shown with a 0° rise and 30° rise.

Note that not all thermograms are illustrated on the same axis, as varying levels of heating mat power inputs were used to ensure that the working limits of the materials were not exceeded, especially the XPS. A full inventory of the testing results is attached in Appendix B: Catalog of Thermogram Results. For all of the thermograms, the image is taken looking up from the floor level, with the air inlet located on the bottom of the image.

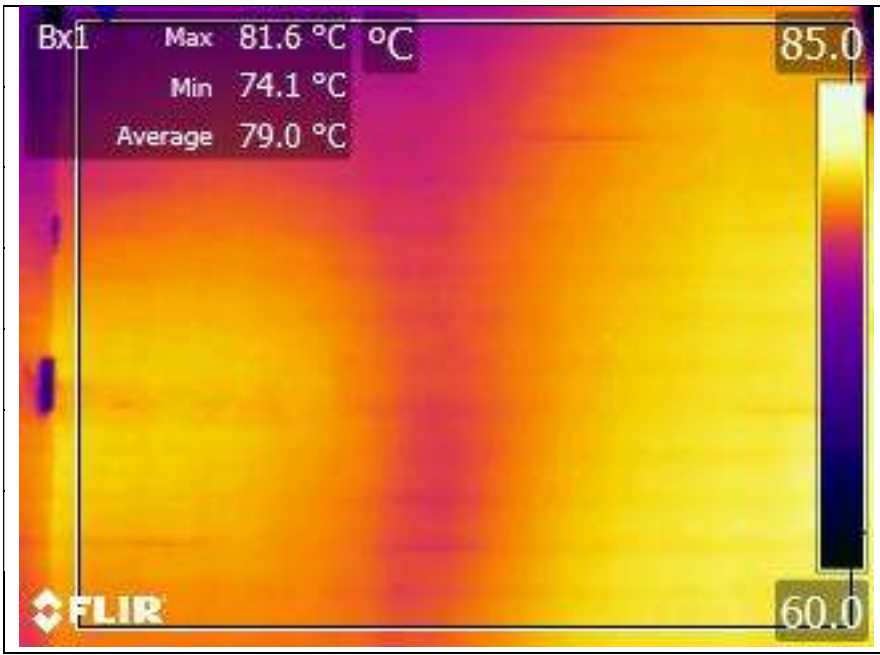

T_{inlet}	22.2 °C
$T_{Upper\ T/C}$	38.4 °C
$\Delta T_{ceiling}$	56.8 °C
$\Delta T_{inside\ air}$	13.6 °C
$\dot{Q}_{cond}$	152.4 W
Re_{inlet}	7,019
h_{inlet}	2.2 W/(m^2·K)
$h_{upper\ T/C}$	3.1 W/(m^2·K)

Figure 47: Thermogram from 1" offset jet, 0.91 m/s jet from bottom of image

Figure 47 shows a 0.91 m/s jet parallel to the surface of the ceiling from an inlet along the bottom of the image. The cooler section running vertically through the center of the image shows a trace of the jet that is running along the ceiling. The broadening of the cooler section near the back wall (top of image) suggests that the jet is splashing against the far wall and still has untapped potential to cool the ceiling surface. In this case, h_{inlet}, derived for the entirety of the ceiling, is evaluated at 2.2 W/(m^2·K). In comparing this to literature, the boundary layer Reynolds number evaluates to 46,200 based on flow for a flat ceiling surface assuming uniform velocity over the entire surface. This Reynolds number is within the laminar regime and, using the geometry of the test cell, would yield a local heat transfer coefficient of 2.0 W/(m^2·K) and an average heat transfer coefficient of 4.0 W/(m^2·K) [111]. While this is not a perfect comparison due to (a) the flow likely retaining turbulent characteristics from the inlet, (b) the flow not directly being in contact with the plate from the onset, (c) the difference between reference temperatures, and (d) the difference between local and average heat transfer coefficients, it does help to illustrate that the experimental approach is within the realm of the published values.

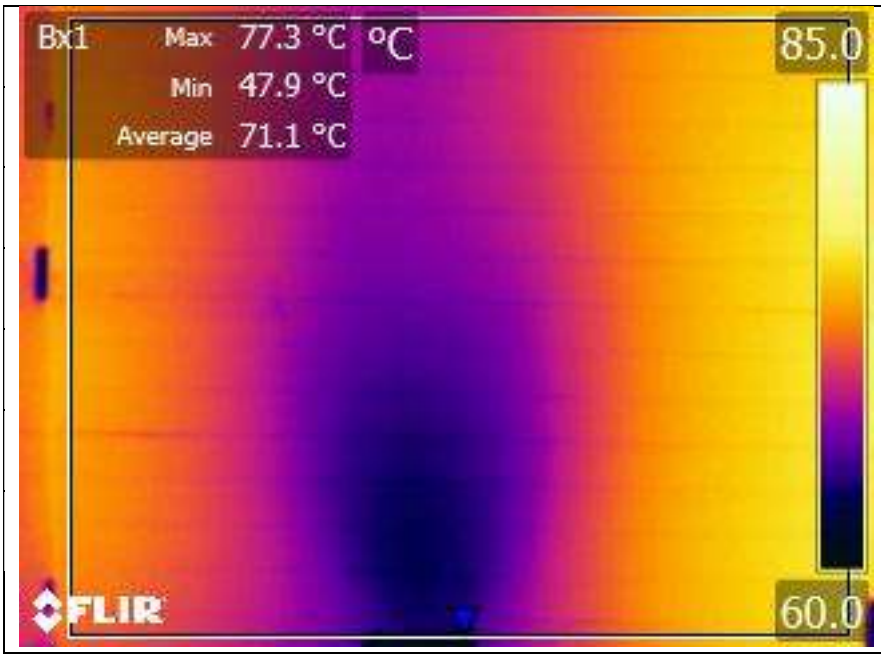

T_{inlet}	22.3 °C
$T_{Upper\ T/C}$	44.0 °C
$\Delta T_{ceiling}$	48.8 °C
$\Delta T_{inside\ air}$	12.9 °C
$\dot{Q}_{cond}$	154.0 W
Re_{inlet}	7,011
h_{inlet}	3.0 W/(m^2·K)
$h_{upper\ T/C}$	5.5 W/(m^2·K)

Figure 48: Thermogram from 1" offset jet, 0.91 m/s jet from bottom of image angled 20 degrees towards ceiling

Figure 48 contrasts Figure 47 in that, with the jet redirected towards the ceiling, the jet spreads out across the ceiling and extracts more heat. This is most pronounced with the variation in the minimum temperature, which is roughly half the difference (25.6 °C vs. 51.9 °C) seen in Figure 47.

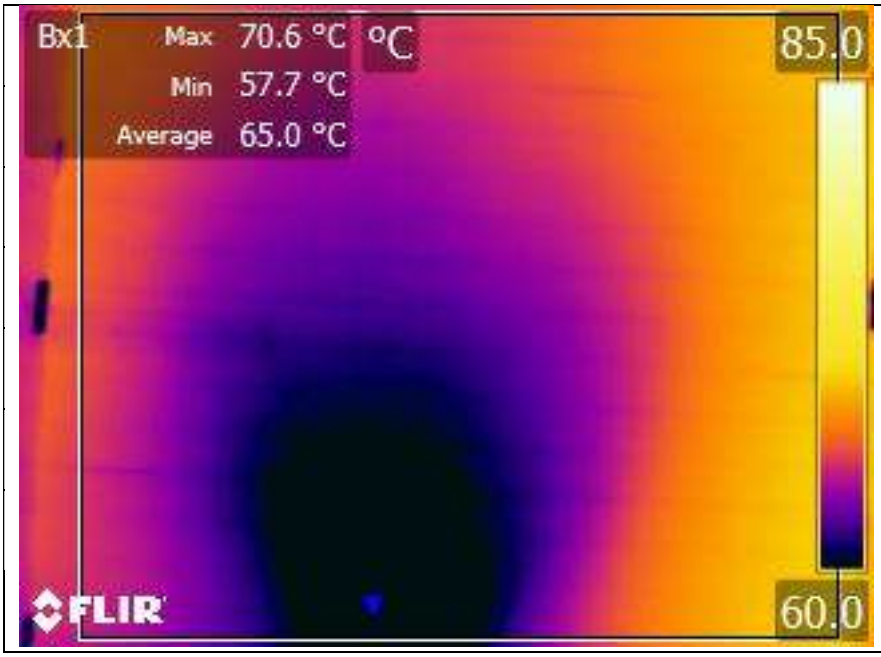

T_{inlet}	22.0 °C
$T_{Upper\ T/C}$	36.9 °C
$\Delta T_{ceiling}$	42.9 °C
$\Delta T_{inside\ air}$	14.4 °C
$\dot{Q}_{cond}$	154.3 W
Re_{inlet}	7,028
h_{inlet}	3.7 W/(m^2·K)
$h_{upper\ T/C}$	5.6 W/(m^2·K)

Figure 49: Thermogram from 1" offset jet, 0.91 m/s jet from bottom of image angled both 20 degrees towards ceiling and 20 degrees horizontal spread

Figure 49 then sought to expand on the improvements of Figure 48 with a horizontal spread of the inlet jet by adding horizontal dispersion of the jet to the initial upward redirection of the jet. As compared to Figure 48, Figure 49 shows a reduction of the ceiling temperature with only a minor increase in the inside air temperature. The spread of the initial jet (Figure 49) yields a further benefit in that the ceiling

temperature reduces to 42.9 °C over the inlet air temperature and that the spread between minimum and average ceiling temperature decreases, suggesting a larger impact on the mean radiant temperature that occupants would be exposed to at that time.

T_{inlet}	21.7 °C
$T_{Upper\ T/C}$	29.8 °C
$\Delta T_{ceiling}$	64.8 °C
$\Delta T_{inside\ air}$	12.3 °C
$\dot{Q}_{cond}$	151.4 W
Re_{inlet}	7,052
h_{inlet}	1.7 W/(m^2·K)
$h_{upper\ T/C}$	1.9 W/(m^2·K)

Figure 50: Thermogram from 4.2" offset jet, 0.91 m/s jet normal to wall

Relocating the inlet location to the scaled location of 4.2" offset from the ceiling, a similar jet flow scenario that was present in Figure 47 is shown in Figure 50. However, in this case, there is no discernable influence of the jet flow directly on the ceiling temperature. This is critically important as it sets a baseline condition for the housing in Bhuj, and suggests that there are intermediate steps to improve the efficacy of nighttime fan use for next day comfort. Some influence of the jet splashing onto the far wall (top of image) is shown in the thermogram, but does little to impact the ceiling slab.

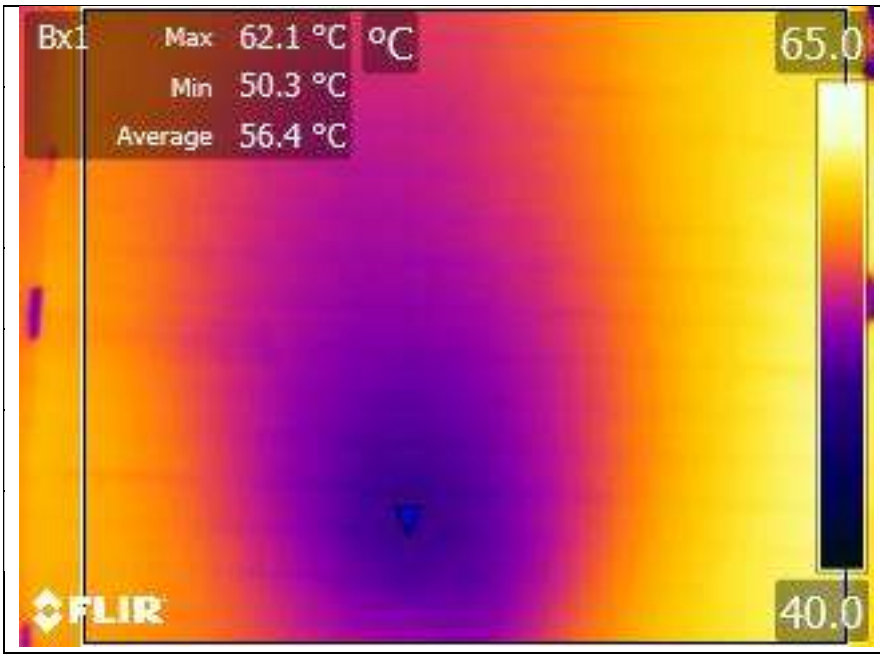

T_{inlet}	21.5 °C
$T_{Upper\ T/C}$	38.6 °C
$\Delta T_{ceiling}$	34.9 °C
$\Delta T_{inside\ air}$	11.6 °C
$\dot{Q}_{cond}$	155.6 W
Re_{inlet}	7,060
h_{inlet}	5.0 W/(m^2·K)
$h_{upper\ T/C}$	9.8 W/(m^2·K)

Figure 51: Thermogram from 4.2" offset jet, 0.91 m/s jet from bottom of image angled 30 degrees towards ceiling

Figure 51 shows a redirected flow of Figure 50 30° towards the ceiling. Note that the scale of the thermogram has changed, as the ceiling is roughly 30°C cooler than it was in the prior case. Compared to the 1" offset case with both 20° rise and 20° horizontal spread, the offset case with 30° rise gives a better performance of the entirety of the ceiling, as represented by an interior convection coefficient ranging from 5-10 W/(m^2·K), roughly 2.5-5 times that of the baseline 4.2" offset case.

Figure 47 - Figure 51 illustrate the varying degrees of improvements through the change in air distribution patterns alone. On the low side, Figure 50 (4.2" offset, jet flow) is emblematic of a simple well-mixed approximation that sees convective heat transfer coefficients within the 1.5-2 W/(m^2·K) range and whose daily heat balance is increasingly dominated by radiative and wind driven convective heat transfer. Shifting the window location closer to the ceiling (Figure 47), the convective heat transfer shifts upwards to the 2-3 W/(m^2·K). At the high end, increasing the inclination of the jet in the higher offset (scaled) case, Figure 51 demonstrates that heat transfer is now dominated by the interior convection (5-10 W/(m^2·K)). While the temperature of the ceiling has dropped substantially (~12.5 °C), the higher air change rate (~75 air changes per hour) allows the added heat in the space to be removed without increasing the average air temperature.

3.3.1 Physical Testing: Analysis and Observations

Across the 44 cases, the principle metric of interest has been the convective heat transfer coefficient across the ceiling, but the relative temperature over the ambient temperature must also be considered. In the charts that follow, the convective heat transfer based off inlet temperatures are shown as a solid line and those based off the uppermost thermocouple (Adjacent Air) temperature are shown in dashed lines. For charts referencing the air temperature rise over ambient temperatures, the solid lines refer to the air temperature rise over ambient, and the dashed lines the ceiling temperature rise over ambient. Further, the charts list the Reynolds number for each of the flow regimes. Given the constant size of the inlet orifice

and the small variation in the inlet temperature (impacting the viscosity), the relationship can be linearized. For convenience, the relationship is shown in Table 14.

Reynolds Number	Air Velocity [m/s]
3,900	0.50
4,450	0.57
7,100	0.91
7,875	1.01
44,450	5.70

Table 14: Relationship between Reynolds number and air flow for 4" diameter duct around 21 °C

For purposes of comparison, the values of the convective coefficient of a downward-facing heated plate, which may be considered a baseline for the Bhuj housing in the absence of significant ventilation, is 0.66 W/(m^2·K) based on an assumed temperature difference of 20 °C between the ceiling surface and the ambient air, and a correlation from 2017 ASHRAE Fundamentals [111]. Starting with Figure 52 based on the 4.2" offset case, it can be seen that the baseline case with the lower speed ventilation of the space is roughly 0.82 W/(m^2·K), close to that of the published approximation.

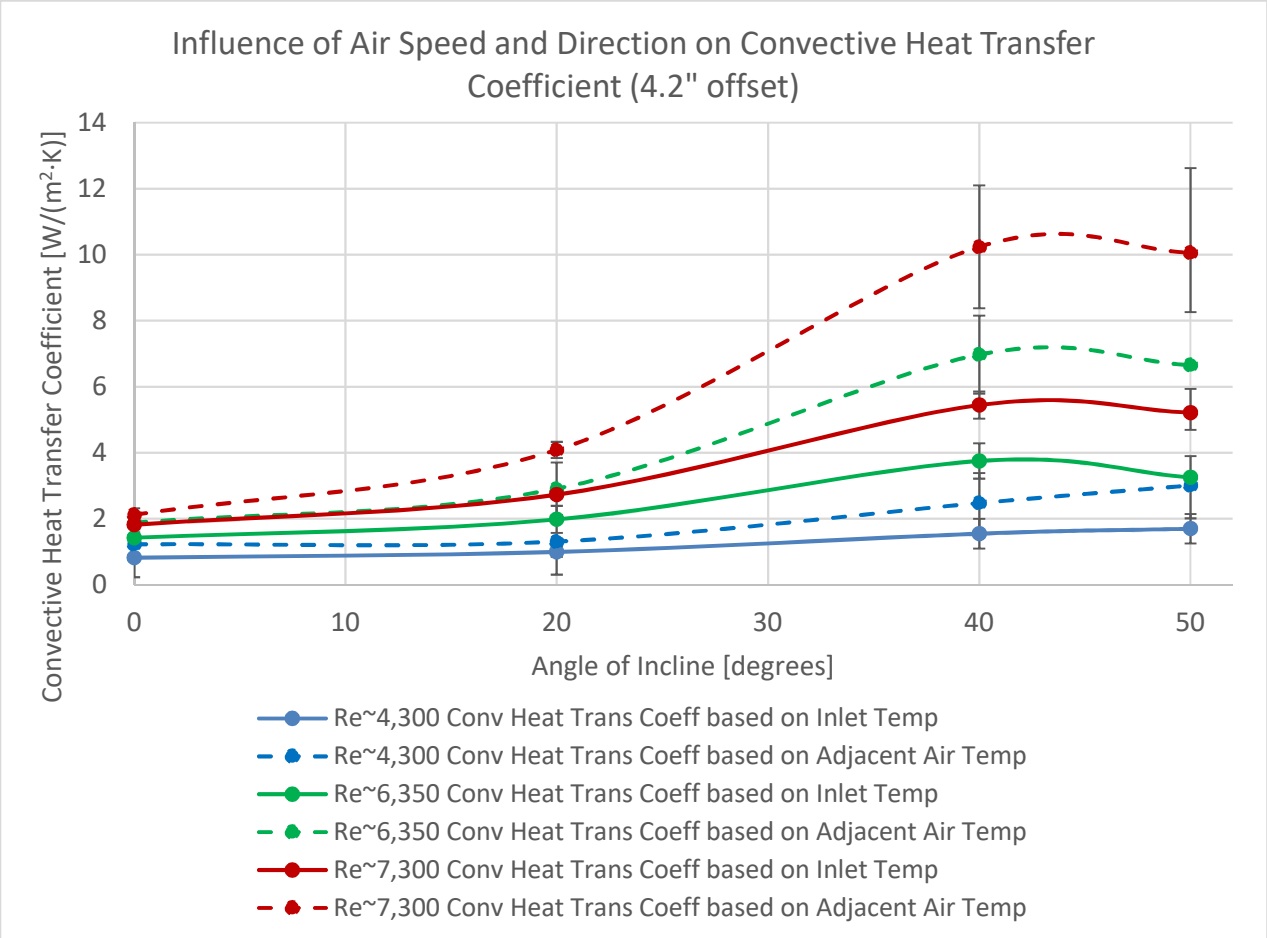

Figure 52: Influence of Air Speed and Direction on Convective Heat Transfer Coefficient, 4.2" offset

Starting at the lower velocities, the influence of air velocity and angle of incline follows a qualitatively intuitive relationship and is shown in Figure 52. At the jet flow (0° incline) cases, increasing

the Reynolds number (velocity) increases the convective heat transfer coefficient greater than the proportional increase of the Reynolds number alone, in contrast with the established correlations for turbulent boundary layers over a flat plate [111], where the heat transfer coefficient scales with the 0.5 power of velocity.

Nonetheless, it is evident that increasing the inclination of the jet towards the ceiling has a much higher impact on the convective heat transfer coefficient than moderate increases in the speed of the air itself. Further, Figure 52 suggests that there is an intrinsic limit to the maximum convective heat transfer coefficient when viewed for the ceiling as a whole at moderate flows, which is intrinsic when taking the average ceiling temperature value from the thermogram.

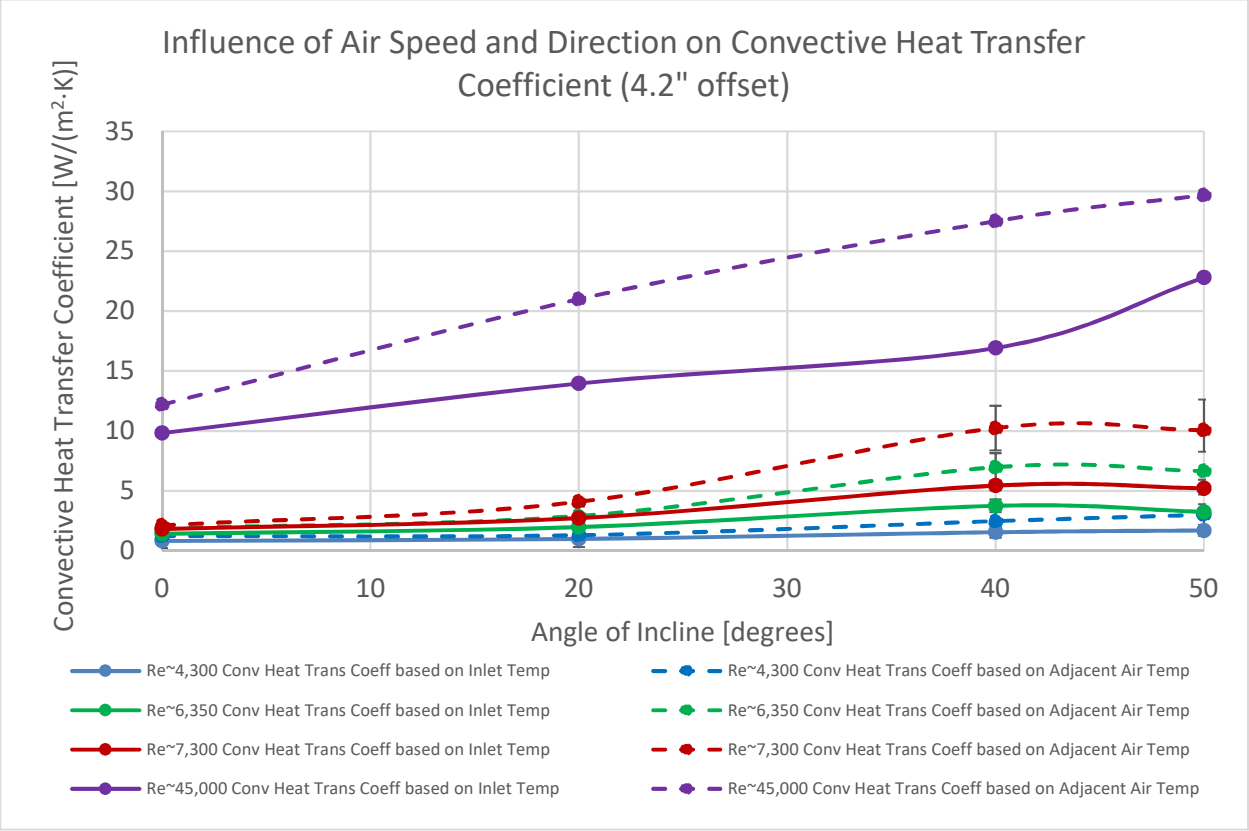

Figure 53: Influence of Air Speed and Direction on Convective Heat Transfer Coefficient, 4.2" offset

Figure 53 extends on Figure 52 to show the influence of a drastically higher air flow rate on the convective heat transfer coefficient. Note that the vertical scale has changed significantly. With the 5.7 m/s flow (Reynolds~45,000), the jet flow (0° incline) produces a 20% higher convective heat transfer coefficient as the 0.95 m/s (Reynolds~7,300) case with 40° incline, when using the adjacent air temperature as the baseline. Contrasting the moderate flows, the convective heat transfer coefficient continues to rise up to 50° incline in the 5.7 m/s flow cases.

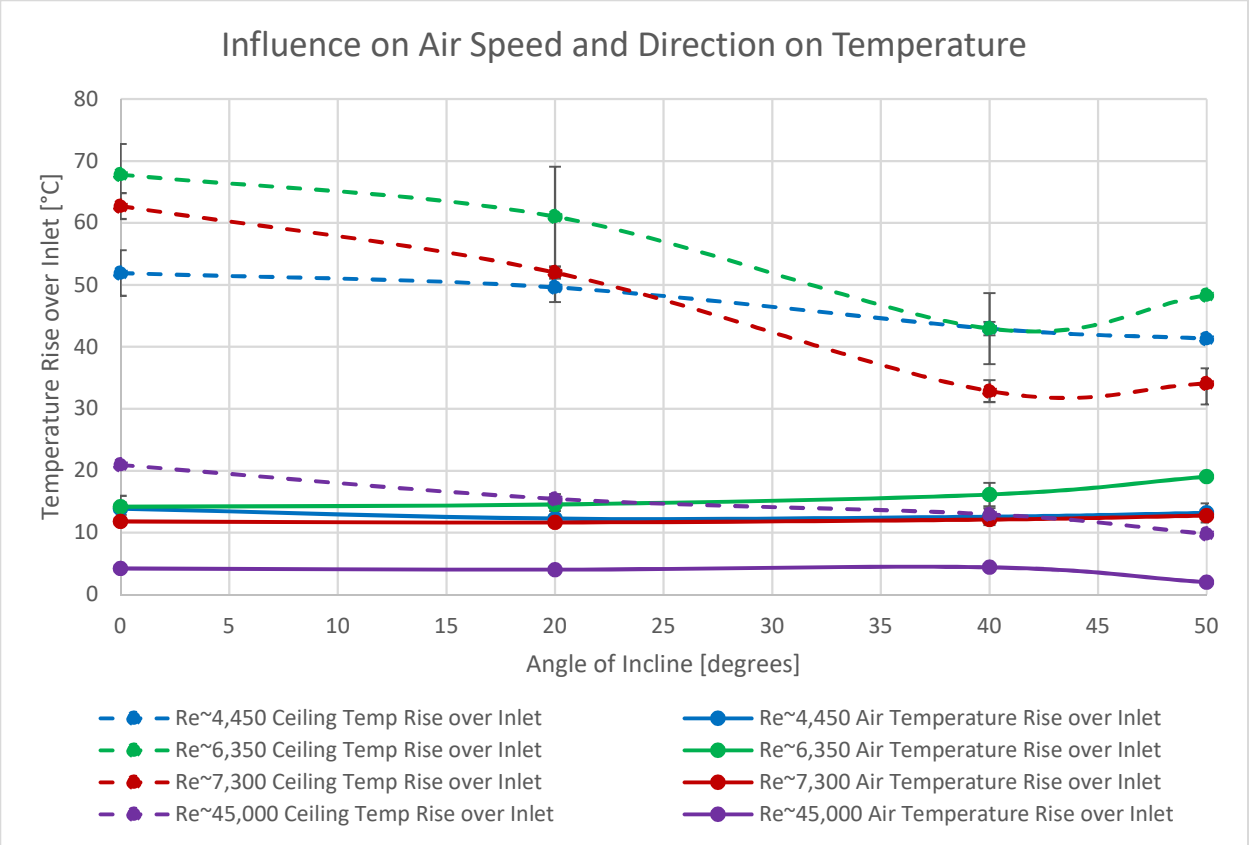

Figure 54: Influence of Air Speed and Direction on Temperature, 4.2" offset

Figure 54 shows the temperature rise across the varying velocities and angles of inclination, where Air Temperature is the average of the three centerline thermocouples within the test cell. It is encouraging in that it suggests that increasing the inclination of the jet towards the ceiling from 0° to 40°is able to decrease the temperature of the ceiling (higher convective heat transfer coefficient) while not having a significant impact on the air temperature throughout the space. This is attributable to the high air change rate (69 ACH) within the space. Unfortunately, this does not explain the 6,350 Reynolds number air temperature rise present.

At significantly higher velocities (5.7 m/s, Reynolds ~45,000), the air temperature inside the test cell begins to approach that of the inlet temperature. At this extreme air change rate (433 ACH), it is intuitive that the air temperature rise over the inlet would be small, but the relatively constant 4 °C offset is helpful to establish a tangible lower limit. While the electrical input into the heating mats for the 5.7 m/s case was increased by 10% relative to the other cases to maintain resolution in the thermal image, the ceiling temperature rise relative to the inlet temperature also establishes that the directionality of the flow retains significance even at flow rates where the well-mixed approximation for indoor air may be considered valid.

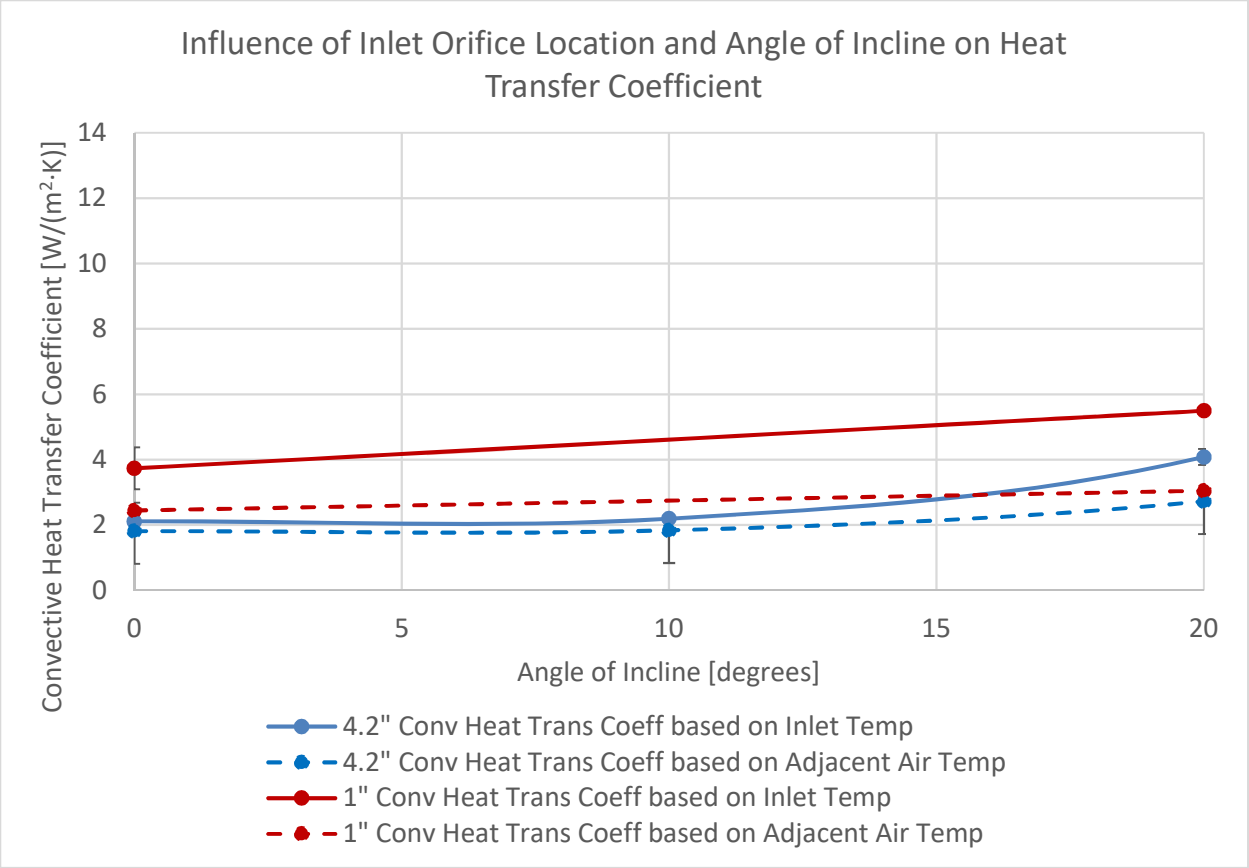

Figure 55: Influence of Inlet Orifice Location and Direction on Convective Heat Transfer Coefficient

Figure 57 shows the influence of location on the convective heat transfer coefficient. Note that the horizontal scale is different from previous plots. The scaled (4.2”) offset case shows an initially lower average convective heat transfer coefficient than the orifice location nearer to the ceiling, but this difference decreases with modest increases in the inclination angle. In this scenario, the 20° inclination angle suggests that the heat transfer coefficient based on the adjacent air temperature has no significant variation, but that the variation is still present for the heat transfer coefficient based on inlet air temperature. This contrast is best explained through the greater difference between ceiling temperature and inlet temperature present in the 4.2” offset case, or that the offset case is less effective at removing heat at low inclination angles.

While it is infeasible to plot all of the results in terms of the variations, the results can be found in Table 15 and continued in Table 16. Note that the Reynolds number varies due to the change in kinematic viscosity, which is referenced off of the inlet temperature. The air velocity readings are also listed.

Offset / Incline / Horizontal Spread	Air Vel.	T_{inlet}	$T_{Upper\ T/C}$	$\Delta T_{ceiling}$	$\Delta T_{inside\ air}$	$\dot{Q}_{cond}$	Re_{inlet}	h_{inlet}	$h_{upper\ T/C}$
1" / 0 / 0	0.91	22.2	38.4	56.8	13.6	152	7019	2.2	3.1
1" / 0 / 10	0.91	22.1	32.0	56.9	13.8	152	7027	2.2	2.7
1" / 0 / 20	0.91	21.4	32.4	55.8	13.7	152	7067	2.3	2.8
1" / 20 / 0	0.91	22.6	44.2	48.5	12.8	154	6994	3.1	5.5
1" / 20 / 20	0.91	22.1	36.9	42.9	14.4	154	7027	3.7	5.6
4.2" / 0 / 0	0.50	19.7	34.7	48.2	12.9	73	3948	0.7	1.1
4.2" / 20 / 0	0.50	19.2	33.5	47.2	11.0	73	3967	0.8	1.2
4.2" / 40 / 0	0.50	19.9	33.1	44.0	11.2	74	3941	1.1	1.6
4.2" / 50 / 0	0.50	20.0	37.3	42.1	11.7	74	3936	1.3	2.1
4.2" / 60 / 0	0.50	19.9	36.9	40.9	12.0	74	3941	1.3	2.3
4.2" / 0 / 0	0.57	20.6	40.0	55.6	14.9	94	4461	0.9	1.4
4.2" / 20 / 0	0.57	20.7	30.4	54.3	13.5	95	4457	1.0	1.2
4.2" / 40 / 0	0.57	20.5	37.6	41.9	14.0	96	4465	2.0	3.4
4.2" / 50 / 0	0.57	20.5	38.8	40.6	14.7	96	4465	2.1	3.9
4.2" / 0 / 0	0.85	20.5	31.9	62.9	12.4	141	6657	1.6	1.9
4.2" / 20 / 0	0.85	20.5	39.3	53.0	12.9	144	6658	2.4	3.7
4.2" / 40 / 0	0.85	20.6	38.2	37.2	14.3	146	6654	4.3	8.2
4.2" / 0 / 0	0.88	21.3	43.9	72.7	16.0	151	6845	1.3	1.8
4.2" / 20 / 0	0.88	18.1	36.0	69.1	16.2	152	7051	1.6	2.1
4.2" / 40 / 0	0.88	17.9	39.6	48.7	18.1	156	7064	3.2	5.8
4.2" / 50 / 0	0.88	17.2	41.9	48.3	19.0	156	7115	3.2	6.7
4.2" / 0 / 0	0.91	21.7	29.8	64.8	12.3	151	7052	1.7	1.9
4.2" / 10 / 0	0.91	21.4	31.7	62.6	12.0	152	7068	1.8	2.2
4.2" / 20 / 0	0.91	21.5	37.9	53.0	11.5	154	7061	2.7	3.8
4.2" / 30 / 0	0.91	21.5	38.6	34.9	11.6	156	7060	5.0	9.8
4.2" / 30 / 20	0.91	21.7	37.9	35.0	11.2	157	7052	5.0	9.4
4.2" / 40 / 0	0.91	21.6	37.7	31.1	12.0	156	7056	5.9	12.1
4.2" / 40 / 20	0.91	21.3	38.3	30.2	12.0	156	7078	6.1	13.9
4.2" / 40 / 40	0.91	21.3	36.1	30.0	13.0	156	7079	6.1	12.0
4.2" / 50 / 0	0.91	21.5	37.8	30.7	12.6	156	7063	5.9	12.6
4.2" / 50 / 20	0.91	21.6	35.2	34.4	13.6	156	7055	5.1	9.8
4.2" / 60 / 0	0.91	19.7	36.2	32.6	13.6	156	7186	5.5	11.1
4.2" / 60 / 20	0.91	20.8	35.9	35.0	14.1	156	7111	4.9	8.7
4.2" / 0 / 0	1.01	22.2	31.6	60.6	11.3	153	7791	2.0	2.3
4.2" / 20 / 0	1.01	22.3	40.2	51.0	11.8	155	7784	2.8	4.3
4.2" / 40 / 0	1.01	22.0	35.8	34.6	12.3	157	7806	5.0	8.4
4.2" / 50 / 0	1.01	22.6	38.7	35.0	13.1	157	7757	5.0	9.3

Table 15: Testing Results

Offset / Incline / Horizontal Spread	Air Vel.	T_{inlet}	$T_{Upper\ T/C}$	$\Delta T_{ceiling}$	$\Delta T_{inside\ air}$	$\dot{Q}_{cond}$	Re_{inlet}	h_{inlet}	$h_{upper\ T/C}$
4.2" / 0 / 0	5.70	20.2	24.2	20.9	4.2	170	44801	9.8	12.2
4.2" / 20 / 0	5.70	19.3	24.5	15.5	4.0	171	45148	14.0	21.0
4.2" / 40 / 0	5.70	18.0	23.0	13.0	4.4	172	45710	16.9	27.5
4.2" / 50 / 0	5.70	21.7	24.0	9.8	2.0	176	44170	22.8	29.7

Table 16: Testing Results, continued

From these results, the highest convective coefficients can be found in 40° incline cases, with higher inclinations reducing the convective heat transfer coefficients. Matching intuition, increasing the velocity increases the convective heat transfer coefficient. Note that values such as the 5.7 m/s (Re_{inlet} ~ 45,000) found in Table 16 are tested merely to establish an extreme case, as 433 air changes per hour is impractical and uncomfortable for building occupants.

3.4 Physical Testing: Translation to Impact

3.4.1 Impact: Heat Transfer Coefficient

While the convective heat transfer coefficients (h_{inlet} and $h_{upper\ T/C}$) are insightful, they fail to give meaning to homeowners and policy makers. To remedy this, the impact of the interior convective heat transfer coefficient can be modeled through a lumped approximation similar to the one shown in Figure 33. Equation (46) estimates the lumped temperature of the slab T as a function of time t and other physical properties.

$$\frac{T - T_\infty}{T_o - T_\infty} = \exp(-\frac{t}{\rho L c_p R_{eq}}) \tag{46}$$

where
T is the lumped temperature of the slab at time t;
T_∞ is the temperature of the environment (assumed to the 20 °C);
T_o is the initial temperature of the slab (40 °C);
t is the elapsed time (eight hours = 28,800 seconds);
ρ is the density of the concrete;
c_p is the specific heat of the concrete;
L is the thickness of the slab (0.1m for this case); and
R_{eq} is the equivalent resistance between the center of the thermal mass and the ambient environment.

The equivalent resistance listed in Equation (47) neglects the contribution of the internal resistance of the concrete. This is valid for cases up to roughly those with an interior convection coefficient of 15 W/(m^2·K) or so, when the Biot number is 0.52. As such, evaluation of the term suggests cooler temperatures than are likely for values larger than 15 W/(m^2·K). Further, Equation (47) neglects the contribution from interior radiation, which is assumed to be small given similar surface temperatures. The approach makes an implicit assumption that the inside air temperature of the space and of the inlet air

remains constant through time, which is not the case in practice. Nonetheless, the method does provide a way to provide a link from the experimental results and give meaning to the convective values.

$$R_{eq} = \left(\frac{1}{h_{convection,interior}} + \frac{1}{h_{convection,exterior}} + \frac{1}{4\sigma\varepsilon_{concrete}\varepsilon_{sky}(T_{m,top}^3)} \right)^{-1} \quad (47)$$

where

$h_{convection,interior}$ in the interior convection coefficient, as evaluated from $h_{convection}$ of Equation (41);

$h_{convection,exterior}$ is the exterior convective coefficient, assumed to be equivalent to a horizontal heated plate facing up, with characteristic length of 2.4 m, fluid properties at 30 °C, and a temperature difference of 20 °C, which suggests a value of 2.21 W/(m^2·K) [111];

$\varepsilon_{concrete}$ is the emissivity of the concrete, assumed to be 0.88 for concrete [65];

ε_{sky} is the equivalent emissivity of the sky based on the simple average of the evaluation of Equation (2) for night-time hours using the Bhuj EPW dataset, or 0.86; and

$T_{m,top}$ is the mean of the slab temperature and the sky temperature (Equation (3)), assumed to be constant at the average of the starting temperature (313.15 K) and the average night-time sky temperature (289.29 K).

Evaluating Equation (46) using the assumptions listed and plotting the resulting slab temperature values after an eight-hour timeframe allows for a means to transition the interior convective coefficient values found from the experimental testing towards a relatable value. Figure 56 illustrates this relation across the interior convective heat transfer coefficient values of 0.5 to 20. As a basis for comparison, the heat transfer coefficient for a horizontal surface with the heated side facing down, referenced to a characteristic length of 2.4m, fluid properties evaluated at 30 °C, and a temperature difference of 20 °C, is 0.66 W/(m^2·K) based on 2017 ASHRAE Fundamentals [111]. Using Figure 56, this illustrates that the natural convection value results in a final temperature of 28.5 °C, but that a modest rise to a convective value of 5.0 W/(m^2·K) results in a drop to 25.1 °C at the end of the figurative night. At the extreme of high convection coefficients (20 and 30 W/(m^2·K)), final slab temperatures of 20.9 and 20.3 °C are possible, respectively.

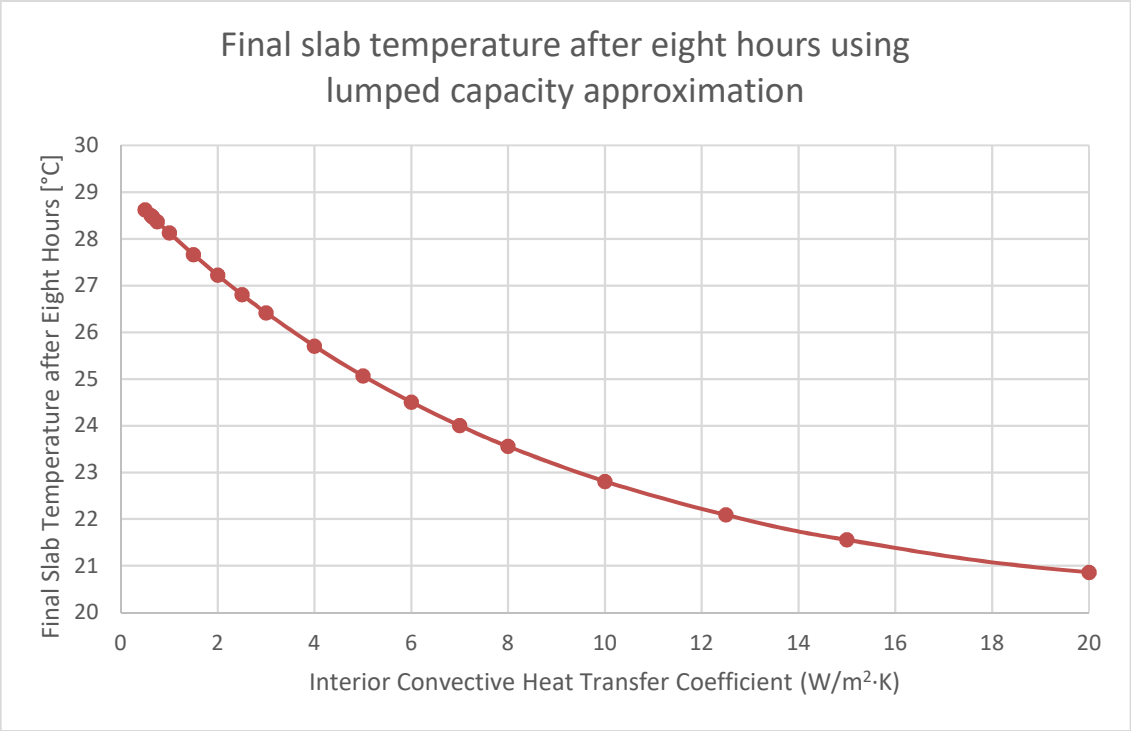

Figure 56: Final slab temperature after eight hours using lumped capacity approximation and based on varying the interior convective heat transfer coefficient

The final temperatures from Figure 56 can then be used as a starting temperature for a lumped capacity approximation run through for an eight-hour timeframe as a proxy for the daytime. Although overly simplified, an energy balance model can be useful to evaluate the next day's slab temperature. Using the ceiling slab's thermal properties, an assumed convective coefficient from the inside of 2 $W/(m^2 \cdot K)$ to a constant inside temperature of 20 °C, an outside convective coefficient of 5 $W/(m^2 \cdot K)$ to a constant outside temperature of 35 °C, a solar absorptivity of 0.55, and an incident solar rate based on a 24 hour sinusoid with a peak amplitude of 800 W/m^2, each starting temperature can be used to determine a possible peak temperature for the next day.

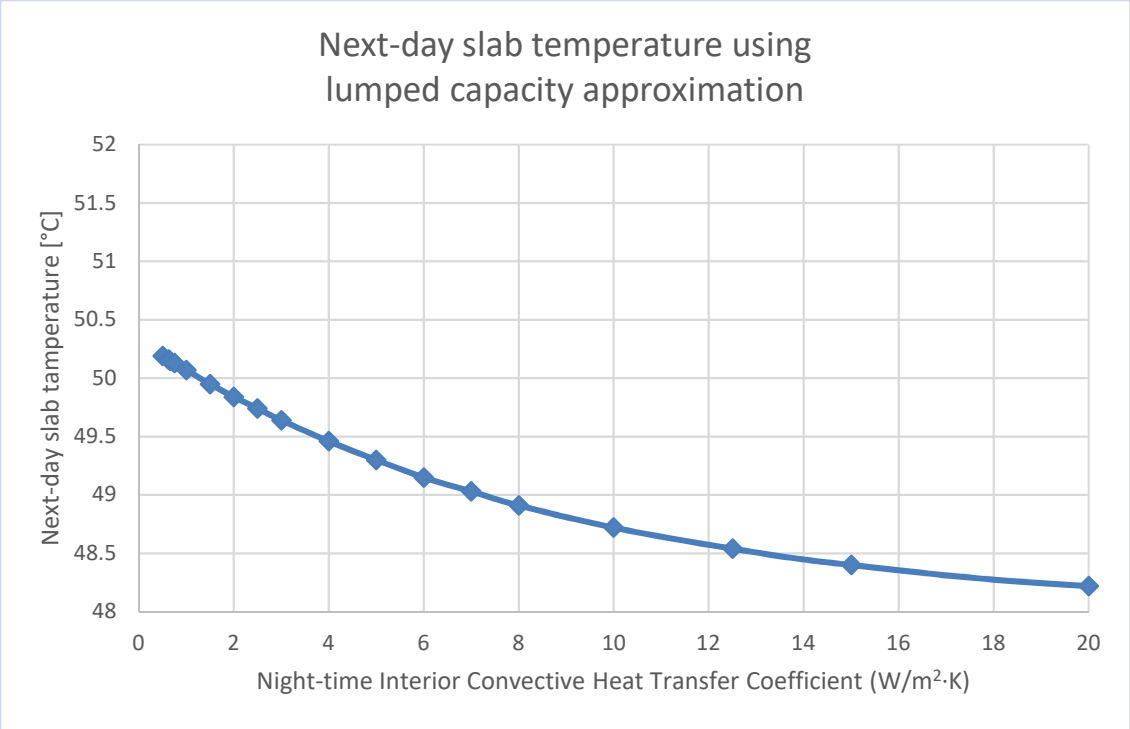

Figure 57: Next-day slab temperature after eight hours using lumped capacity approximation and based on varying the interior convective heat transfer coefficient

Figure 57 then illustrates that a change from the natural convection night-time setup (0.66 W/(m^2·K)) to a modest 5 W/(m^2·K) forced convection results in a decrease of the next-day slab temperature from 50.2 °C to 49.3 °C. These values are not outside of the realm of possibilities, as field measurements in May of 2019 suggested ceiling temperatures around 43°C around 11 AM, which is in line with the temperature at three hours (42.3 °C) using the same approach and based on the natural convection baseline.

At higher levels of the night-time interior convective heat transfer coefficient (10 -20 W/(m^2·K)), the peak daytime slab temperature improves further to 48.7 °C and 48.2 °C, respectively. Overall, a 2.0 °C reduction of the peak temperature of the slab throughout the day is a modest improvement, but represents a large change for the occupants of the home, who may not have another means to escape the heat of the day. Given that homeowners had noted concerns over the glare from the white glazed tiles run in the short-term roofing tests, the modest improvement above is considered an acceptable solution. Further, the applications extend to multi-story housing as well, as it lends itself towards amplifying the utilization of the thermal mass of the slab.

Using the night-time temperature values from Figure 56 and the 0.66 W/(m^2·K) natural convection baseline, the energy consumption can be defined based on the energy needed to drop the temperature of the slab as compared to the baseline. Extending this to a 23 m^2 home and an assumed air-conditioner coefficient of performance of 3, the energy savings ($(\Delta kWh\_elec)/year$) can then be derived as shown in Equation (48).

$$\frac{\Delta kWh_{elec}}{year} = \left[\left(\frac{(T_{FS} - T_{baseline})L\rho c_p A}{\frac{3600\ sec}{hr}\ \frac{1000\ W}{kW}\ CoP}\right) - \left(\frac{hrs_{op}P_{fan}}{\frac{1000\ W}{kW}}\right)\right]\frac{365.25\ days}{year} \quad (48)$$

where

T_{FS} is the final slab temperature for values above $h_{convection,interior}$=0.66 W/(m^2·K) (Figure 56);

$T_{baseline}$ is the temperature of the baseline, at $h_{convection,interior}$=0.66 W/(m^2·K) (Figure 56);

A is the area of the entire roof slab (23 m^2);

CoP is the coefficient of performance (assumed to be 3);

hrs_{op} is the duration that the fan runs each day (assumed to be 8 hours); and

P_{fan} is the power usage of the fan (assumed to be 90 W for the fan available in the Bhuj market [152]).

The evaluation of Equation (48) is shown below, in Figure 58. The baseline terms, that relating to the electrical energy consumption of the fan alone, are 375 kWh/year, or 29.60 US dollars per year.

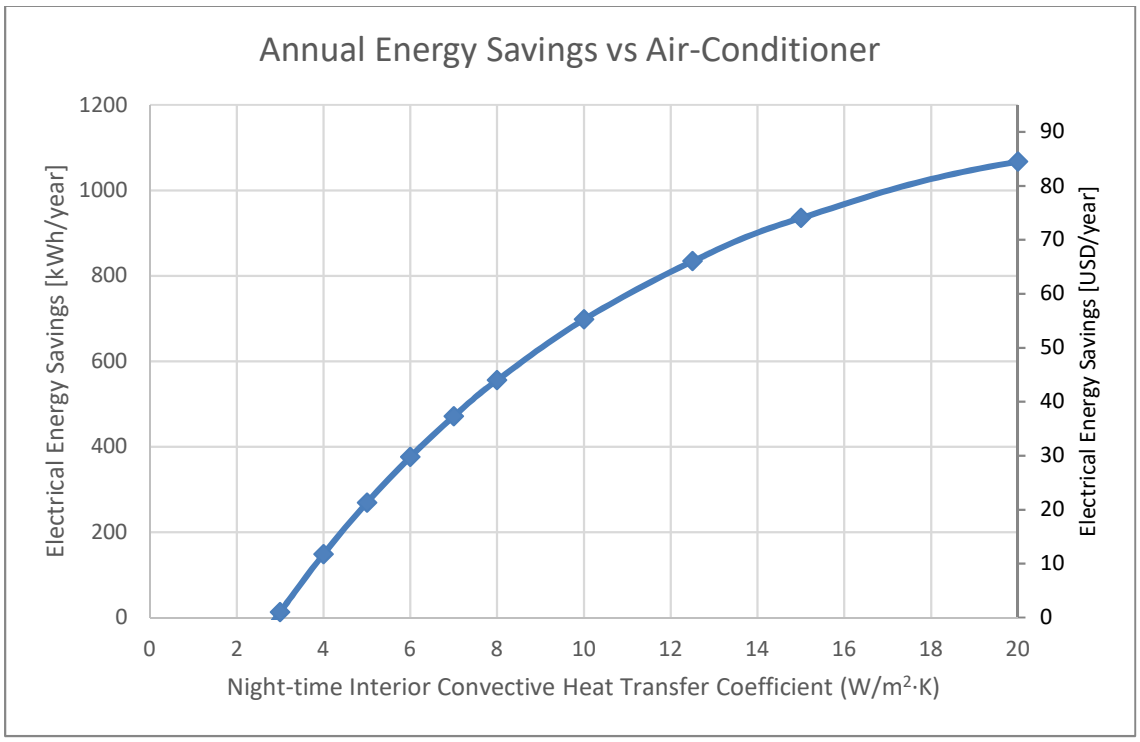

Figure 58: Annual Electrical Energy Savings vs Air-Conditioner as a function of Night-time Interior Convective Heat Transfer Coefficient

Figure 58 shows the electrical energy savings possible compared to an air-conditioner based on the interior convective heat transfer from the night before. The left-hand axis shows the electrical energy potential, whereas the right-hand side translates that number into monetary savings through household electrical pricing for September 2021 ($0.079/kWh [153]). This pricing data compares favorably with that proposed by the Gujarat Electricity Commission's Tariff proposal for 2021 and 2022 (5.89 ₹/kWh or $0.077/kWh at 100₹=1.31 USD). Note that using a fan to produce night-time interior convective heat

transfer coefficients less than 2.9 W/(m^2·K) are more energy (and carbon) intensive than the using an air-conditioner for those same night-time hours, omitting concerns of latent energy (moisture) within the air.

Within the context of carbon emissions, India has maintained a very carbon intensive electrical energy supply, only reducing its energy-based carbon intensity by 10% over the past 20 years [154]. The average carbon intensity is likely around 0.93 kg CO2/kWh$_e$ [155], although estimates cover the range from 0.675 to 0.96 kg CO2/kWh$_{elec}$ [156, 157, 158, 159]. Applying this lens to the data shown in Figure 58 suggests a total carbon savings reaching nearly 1,100 kg CO2 for the 20 W/(m^2·K) case. This data is plotted in Figure 59, which continues an observation from Figure 58 that even modest increases in the night-time interior convection coefficient (i.e. 4 W/(m^2·K)) have the potential for tangible savings (12 USD/year, 150 kWh/year, 140 kg CO2).

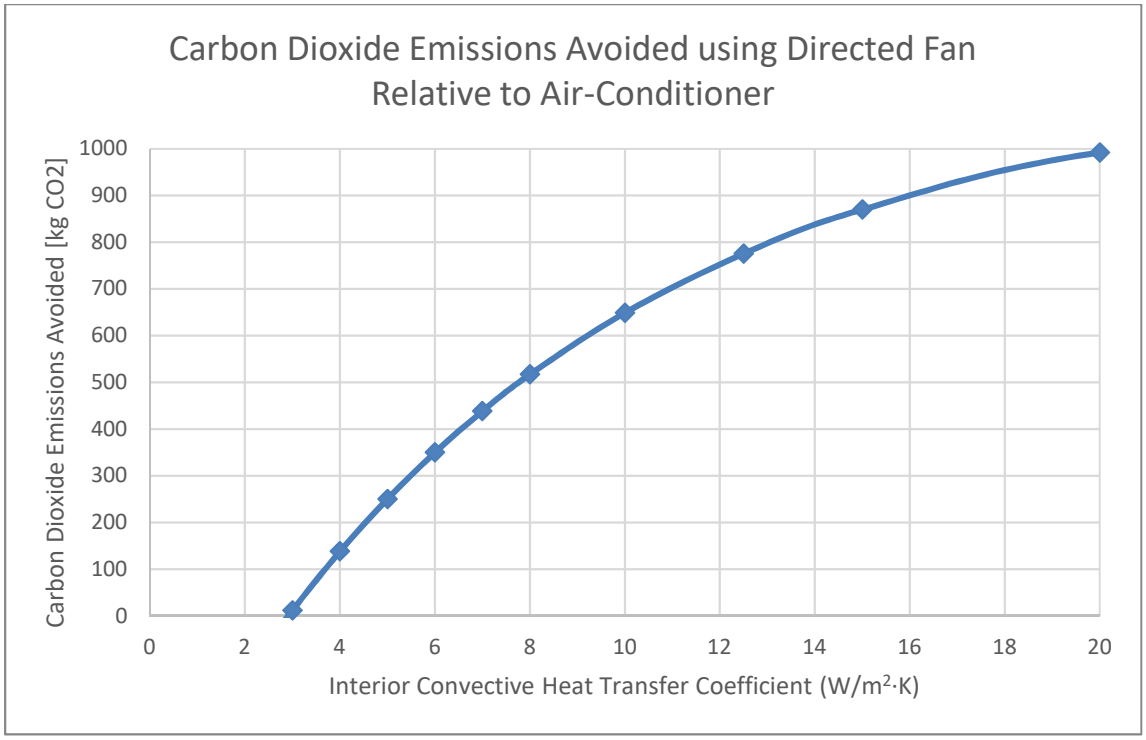

Figure 59: Carbon Dioxide Emissions Avoided vs Air-Conditioner as a function of Night-time Interior Convective Heat Transfer Coefficient

3.4.2 Impact: Heat Transfer Coefficient on Multi-Story Structures

The idea of applying this methodology to a multi-story structure was previously introduced as a possible application and extension of the work. To accomplish this, Equation (47) can be rewritten as Equation (49) where the external convective heat transfer coefficient is be replaced by the convective heat transfer coefficient from the floor slab to the upstairs living space, $h_{convection,floor}$. As the center floors of a multi-story dwelling with presumably have similar slab temperatures if subjected to the same conditions, the radiation component is also neglected.

For the convection coefficients, $h_{convection,ceiling}$ is evaluated from the experimental data, where $h_{convection,floor}$ is roughly 1.76 W/(m^{2}K) based on the geometry and orientation, as derived from an upward-facing heated plate without forced cooling as defined in 2017 ASHRAE Fundamentals [111].

$$R_{eq} = \left(\frac{1}{h_{convection,ceiling}} + \frac{1}{h_{convection,floor}} \right)^{-1} \quad (49)$$

Then, using Equation (46) over an eight-hour time period and many the same assumptions as Section 3.4.1, the final slab temperature can be plotted as shown in Figure 60. One additional modification between the two cases is that the multi-story case assumes a 10 °C differential of temperature for the floor convection, halving the associated Rayleigh number. Further, the initial temperature is varied between 40 °C (in line with previous assumptions) and 30 °C (more appropriate for an interior surface).

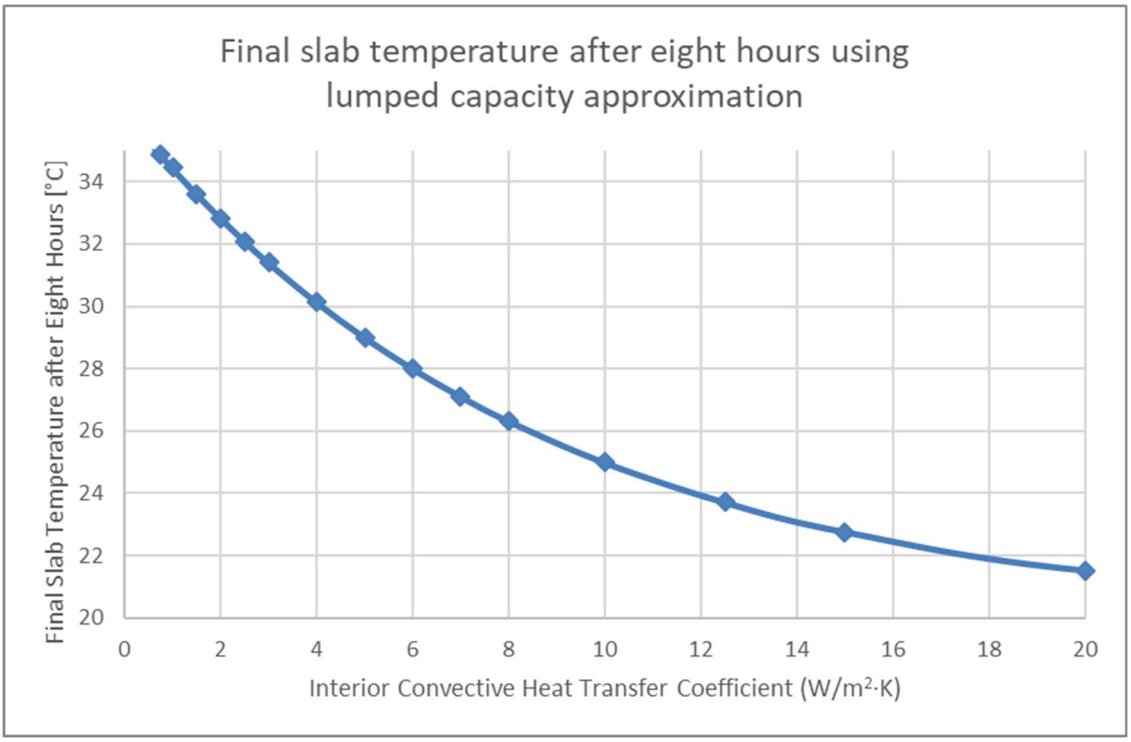

Figure 60: Final slab temperature after eight hours using lumped capacity approximation and based on varying the interior convective heat transfer coefficient for multi-story housing, starting temperature at 40 °C

Figure 60, shown with a different vertical axis than that used in Figure 56, illustrates how the absence of the radiative cooling increases the temperature of the slab as a whole. However, it does show how a strong relationship between the ceiling interior convective heat transfer coefficient (horizontal axis) and the final slab temperature can be meaningful to occupants. Moving from a baseline value of roughly 35.0 °C at an interior convective heat transfer coefficient of 0.66 W/(m^{2}K) to a slab temperature of 29.0 °C at 5 W/(m^{2}K) and 25.0 °C at 10 W/(m^{2}K) represents a substantial difference based on the interior convective heat transfer coefficient alone.

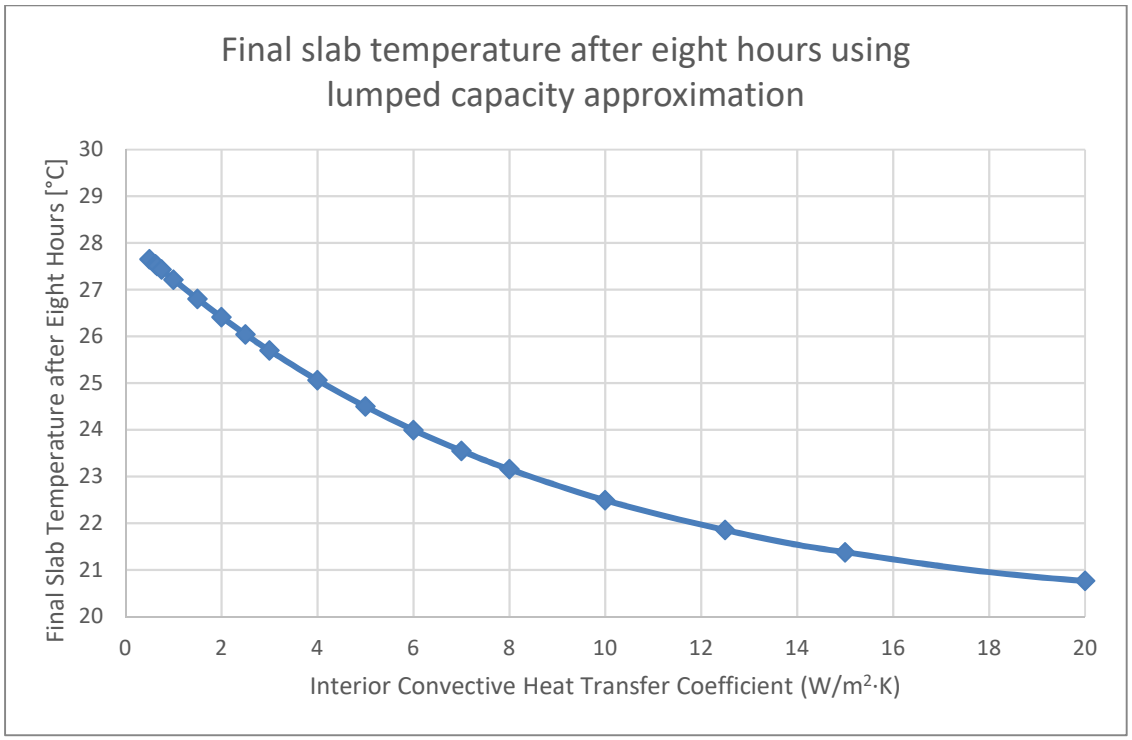

Figure 61: Final slab temperature after eight hours using lumped capacity approximation and based on varying the interior convective heat transfer coefficient for multi-story housing, starting temperature at 30 °C

Figure 61 varies the starting assumption of Figure 60 to a 30 °C starting temperature, as well as changes the vertical axis to match Figure 56. Figure 61 continues the conclusion that the interior convective heat transfer coefficient has a substantial impact on the slab temperature after an eight-hour time period and that it has the potential to reduce the slab by roughly 5.5 °C moving from a 0.66 W/(m^{2}K) baseline to a 10 W/(m^{2}K) data point.

Evaluating the next-day slab temperature in this scenario is heavily dependent on the façade characteristics and internal heat load, and those considerations are outside the scope of this research. Nonetheless, given the relative surface area differences between the ceiling slab and the wall, activating the thermal mass of the ceiling has strong benefits when coupled with heat rejection or insulation of the façade.

3.4.3 Impact: Airflow Rate and Heat Transfer Coefficient

The previous sections have discussed the implication of the variation in interior convective heat transfer coefficient on the subsequent day's temperature. However, previous sections have failed to discuss the importance of the volumetric air flow as a factor in those numbers. Under many of the previous cases, the flow rate was at 69 air changes per hour in the test cell (12.4 ACH in the full size), which is intentionally aggressive to keep the test cell well-ventilated. The importance of the flow rate can be related to the interior air temperature which influences the convection coefficient through a lumped approximation of the thermal mass of the ceiling slab.

The first equation, Equation (50), relates the rate of heat loss from the slab to the convection at the ceiling surface.

$$\rho_{concrete} c_{p,concrete} AL \frac{dT_{slab}}{dt} = \left(h_{conv,in} + h_{R,in}\right) A (T_{air} - T_{slab}) + \left(h_{conv,out} + h_{R,out}\right) A (T_{air} - T_{inlet}) \quad (50)$$

where
$\frac{dT_{slab}}{dt}$ is the change in slab temperature as a function of the change in time;
T_{slab} is the temperature of the slab;
A is the ceiling area, assumed to be 23 m^2;
T_{air} is the temperature of the air inside the home;
$h_{conv,in}$ is the overall ceiling convection heat transfer coefficient, based on inlet temperature;
$h_{R,in}$ is a radiation heat transfer coefficient, linearized as in [103] and assumed to be equal to 1 W/(m^{2}K);
$h_{conv,out} + h_{R,out}$ is the overall rooftop heat transfer coefficient, assumed to be equivalent to 5 W/(m^{2}K); and
T_{inlet} is the temperature of the air entering the room (the outside ambient temperature).

The second equation, Equation (51), relates the rate of heat extraction via the airflow to the convection heat loss assuming well-mixed air temperature inside the room.

$$\dot{m} c_{p,air} (T_{air} - T_{inlet}) = h_{conv,in} A (T_{slab} - T_{air}) \quad (51)$$

where
$\dot{m}$ is the mass flow rate of the air; and
T_{inlet} is the inlet temperature of the air.

Rewriting Equation (51) in terms of T_{air} yields Equation (52).

$$T_{air} = \frac{\dot{m} c_{p,air} T_{inlet} + h_{conv,in} A T_{slab}}{\dot{m} c_{p,air} + h_{conv,in} A} \quad (52)$$

Ultimately, substituting Equation (52) into Equation (50), yields a rate of change of the slab temperature as a function of the other constants, from which the time constant is of the form shown in Equation (53).

$$\tau = \frac{\rho_{concrete} c_{p,concrete} L (\dot{m} c_{p,air} + h_{conv,in} A)}{\left(h_{conv,in} + h_{R,in} + h_{conv,out} + h_{R,out}\right) \dot{m} c_{p,air} + (h_{conv,out} + h_{R,out}) h_{conv,in} A} \quad (53)$$

To which the time constant τ (in seconds) is shown that any individual change of the mass flow rate or the convective heat transfer coefficient produces an impact on the other, but that the two can also be set as inputs. On the whole, increasing either value decreases the value of the time constant.

To help with intuition, the mass flow rate of the air is displayed below in terms of the air change rate of the homes, $Air\ Change\ Rate$. This conversion is done through Equation (54). Note that the air

change rate is typically defined as air changes per hour, which is a units conversion from seconds^{-1} to hours^{-1}.

$$Air\ Change\ Rate = \frac{\dot{m}}{\rho_{air} AH} = \frac{A_{window} v_{window}}{AH} \tag{54}$$

where

ρ_{air} is the density of the air, assumed to be 1.19 kg/m^3;
H represents the height of the living space, 2.4 m;
A_{window} is the open area of the window through, 0.2 m^2; and
v_{window} is the velocity of the air through the window, evaluated from 0.4 m/s to 5.7 m/s.

From the time constant, a solution can be written using the temperature rise above ambient of the slab at the beginning of a theoretical night (assumed to be 20 °C above ambient), and an assumed steady ambient temperature (assumed to be 20 °C, the linear offset in the following equation). From that, the temperature of the slab can be written as a function of time, t in seconds, as shown in Equation (58).

$$T_{slab} = 20 \exp(-\tau t) + 20 \tag{55}$$

Equation (58) can then be evaluated for an eight hour (28,800 seconds), maintaining earlier assumptions of thickness (10 cm), concrete density (2,307 kg/m^3), and concrete specific heat (837 J/kg·K) and graphed as a function of the air change rate and the overall ceiling convective heat transfer coefficient. The results of that evaluation are shown in Figure 62.

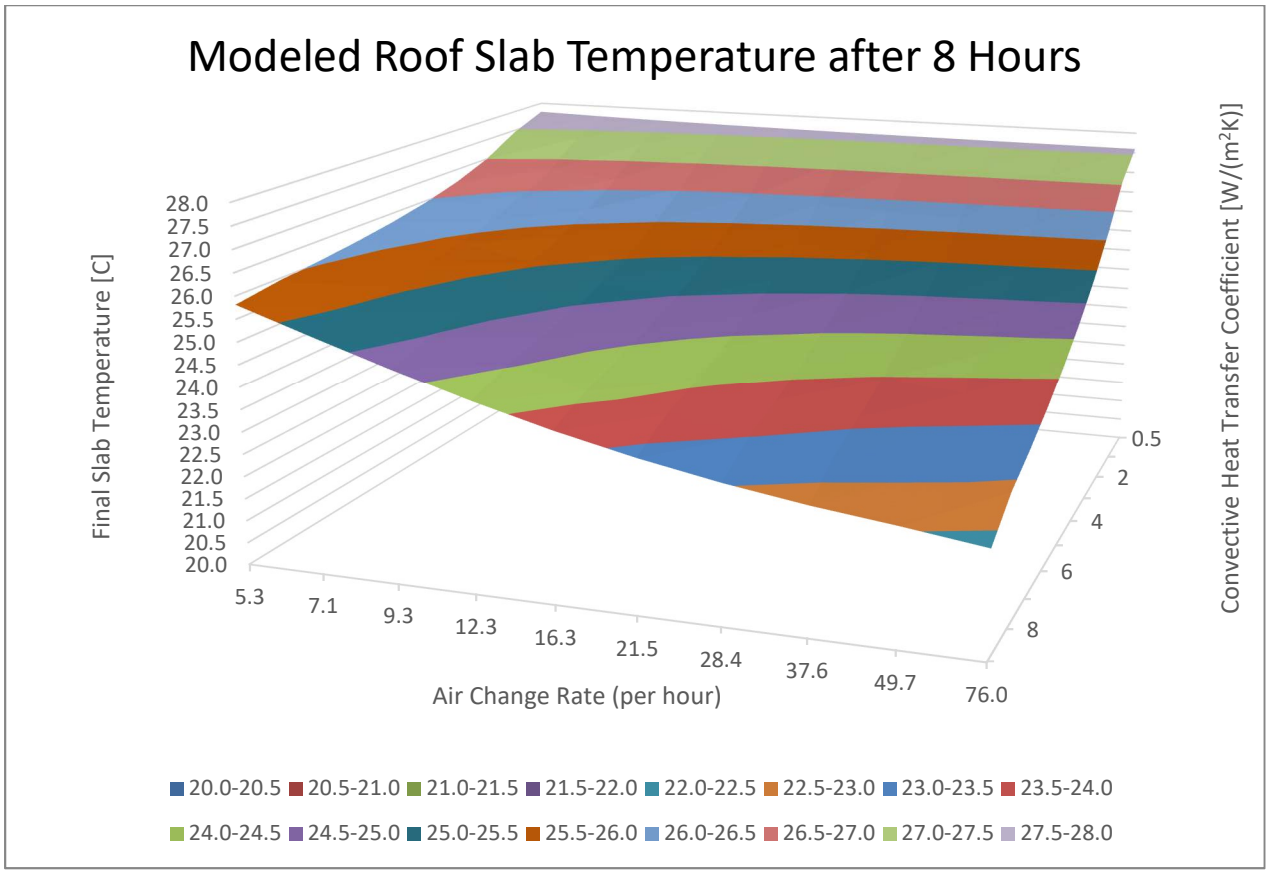

Figure 62: Modeled Roof Slab Temperature after 8 Hours

Figure 62 illustrates the final slab temperature is a function of both the air change rate (mass flow rate) and the convective heat transfer coefficient. Beginning in the background, at low air change rates (5.3 ACH) and low convective heat transfer coefficients (0.5 W/(m^{2}K)), the slab temperature after eight hours is 27.8 °C. As air change rates increase without a corresponding change in the convective heat transfer coefficient, only a very modest reduction in slab temperature is observable (27.6 °C at 76 ACH and 0.5 W/(m^{2}K)). Further, at low air change rates, the influence of a change in the convective heat transfer coefficient has a stronger influence (25.8 °C at 5.3 ACH and 10 W/(m^{2}K)) than simply increasing the mass flow rate. At more moderate air change rates, the influence of increasing the convective heat transfer coefficient can be seen in the shape of the final slab temperature bands, which begin to favor increasing the heat transfer coefficient rather than increases in mass flow rate for the purposes of reducing the final slab temperature. Overall, a meaningful reduction of the final slab temperature requires the combination of the two factors to be elevated above modest levels.

For next-day peak temperatures, the system used the same modeling approach as shown in 3.4, which based the next day peak temperature on the night-time interior convective heat transfer coefficients, the same values derived for the interior airflow cases. Using the same horizontal and depth axis as Figure 62, the next-day slab temperatures are shown in Figure 63.

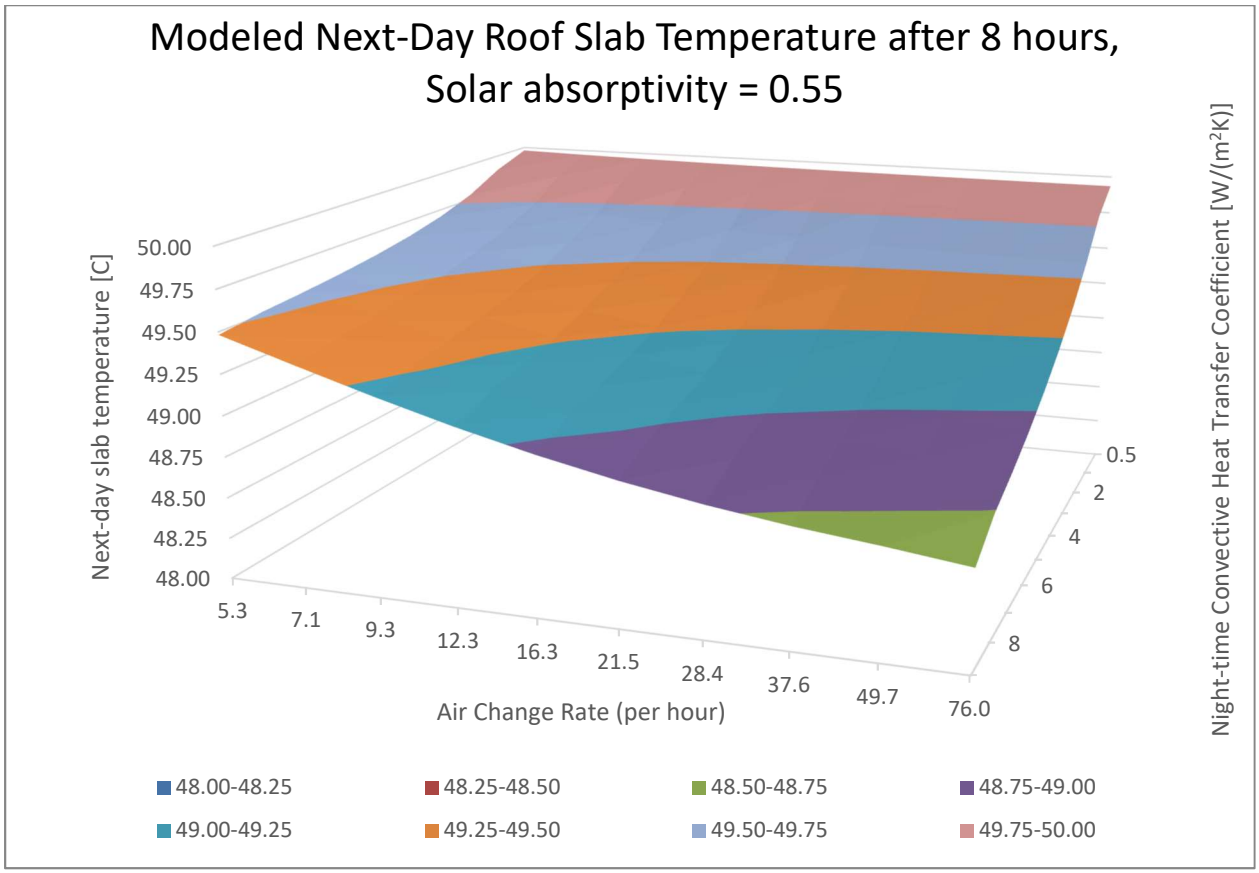

Figure 63: Next-day slab temperatures as a function of air change rate and night-time convective heat transfer coefficient, solar absorptivity: 0.55

Figure 63 confirms the previous conclusions that the temperature difference at the end of the night have diminishing magnitude, but maintain significance to the homeowners. In this setup, with a solar absorptivity of 0.55, the variations of air change rate and night-time convective heat transfer coefficients produce a 1.8 °C spread of next-day roof slab temperatures.

3.4.4 Impact: Rooftop Absorptivity

Whereas Figure 63 uses an assumed solar absorptivity of 0.55, that of a lightly colored cement, a solar absorptivity of 0.4 may also be possible using a whitewashing treatment and not produce the negative visual glare aspects noted with the glazed white tiles. The results of this change are shown in Figure 64.

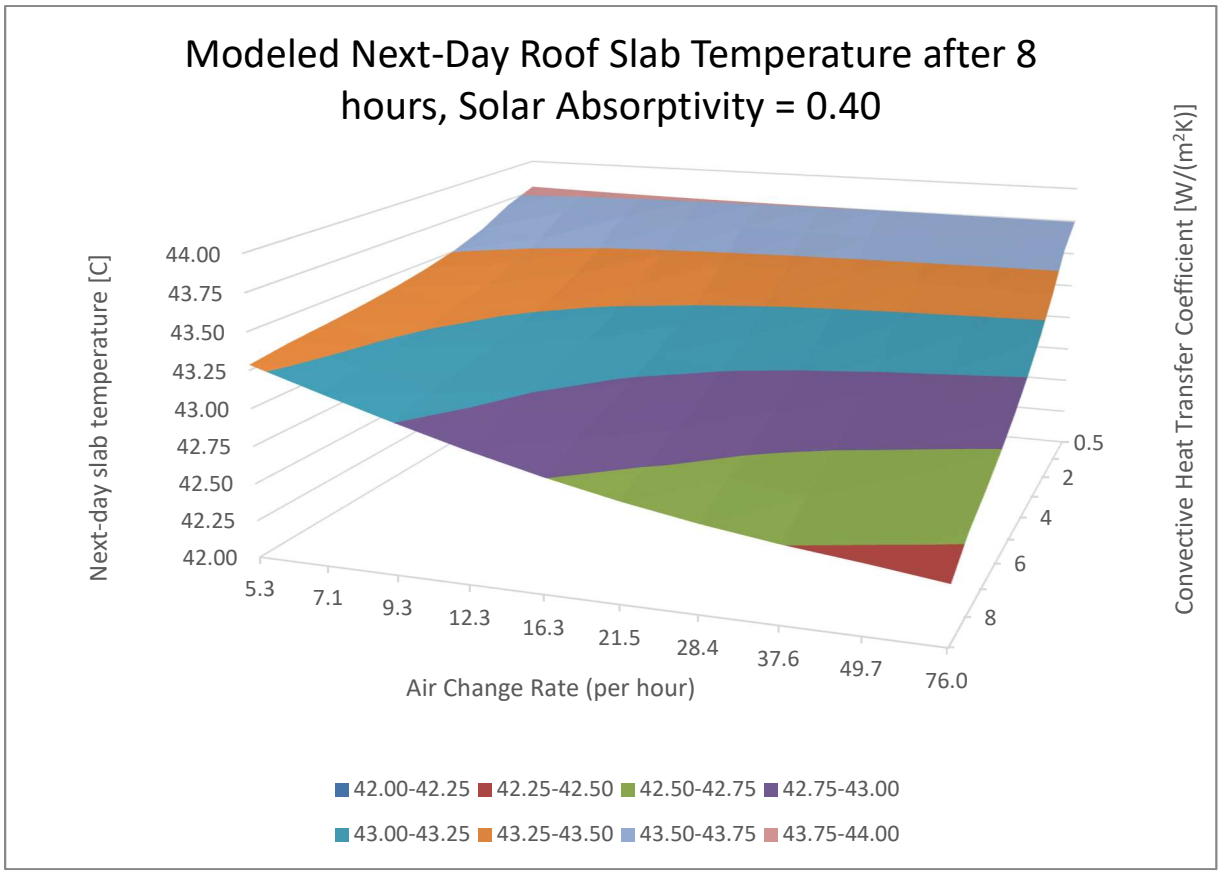

Figure 64: Next-day slab temperatures as a function of air change rate and night-time convective heat transfer coefficient, solar absorptivity: 0.40

At 1.4 °C, Figure 64 has a smaller spread of temperature values than Figure 63 and reinforces Gradillas' conclusion that multiple approaches are necessary to work together to improve thermal comfort. In this scenario, the change of modeled solar absorptivity from 0.55 to 0.40 produces roughly a near-universal reduction in the roof slab temperature of 6.2 °C, three times the magnitude of the impact of the ventilation at the moderate solar absorptivities.

3.4.5 Physical Testing: Conclusions

Existing solutions to use a window-mounted fan work to decrease the air temperature within the structure, but fail to decrease the temperature of the roof slab enough to provide a sufficient benefit to home occupants throughout the next day. Especially in the case of India, where the daytime home occupants are those traditionally considered at risk and who may not have access to other heat-relief areas (elderly, women, and children), the peak daytime temperatures represent the greatest detrimental impact to occupants.

The combination of increasing night-time airflow and the interior convective heat transfer coefficient has the potential to reduce the next-day slab temperatures on the order of 1.4-1.8 °C, depending on rooftop solar absorptivity. While this is a modest change, this has the potential to reduce the excess heat-induced mortality by 5.8 percentage points. Coupled with a small change reduction of the solar absorptivity through a process like whitewashing, this can reduce the next day slab temperature from a modeled baseline of 49.9 °C to 42.0 °C, a significant step towards reducing excess heat-related mortality (~25.3 percentage points) and improving thermal comfort.

Within the Bhuj housing and keeping air velocity within attainable bounds, increasing the angle of inclination to 30° is a significant step forwards and represents a full degree reduction of the next day peak slab temperature. A 40° angle of inclination can yield an additional half a degree, but more inclination does not provide benefits. While this half a degree may not seem substantial, combining the population size (200,000 as of 2020 [160]), 3.2 percentage points of excess mortality per degree of change, average death rate (5.9 deaths/year per100 people [161]) produces an average death rate of 32.3 individuals per day, to which the half degree shift over an arbitrary one week heat wave is 3.6 lives.

When cross-shopping these options against an air conditioner with a coefficient of performance of 3, breaking the 3 $W/(m^2 \cdot K)$ threshold for the night-time convective heat transfer coefficient is the financial simple payback break-even point. This can easily be achieved at medium velocities (0.85 m/s) at the 40° angle of inclination, and also at higher velocities (>0.91m/s) at 30° angle of inclination.

For homeowners and occupants, especially those who may find it too cold at night with a standard ceiling fan, they may find it beneficial to redirect the air towards the ceiling both as a means to reduce the local air velocity around their person and warm the space through cooling the ceiling. Ultimately, the combination of surface absorptivity changes, mass flow rate, and redirection of the airflow can help avoid the worst effects of the heat waves and represent a substantial improvement over the baseline conditions.

Further work to improve the convective heat transfer coefficient could include the addition of ribs to the ceiling, reducing the radiative emissivity of the ceiling to restrict daytime radiation transfer to the inside of the structure, and changing the inlet type from an axial fan to a centrifugal fan blowing directly across the ceiling. Additionally, this research suggests that there are benefits from coupling existing ceiling fans run on the updraft with simple window fans at 0° incline or even cross-draft ventilation, but the quantification of those two mechanisms and the energy implications are topics for future research and implementation in occupied housing.

4 Comfort

4.1 Chilled beam and ceiling fans

This section (4.1) was a combined effort with Nikhilesh Ghanta, and Leon Glicksman. It was published as part of the conference proceedings for the 2020 CIBSE-ASHRAE Technical Symposium in Glasgow [162].

4.1.1 Abstract

Active chilled beams are touted as an energy efficient option to provide cooling, primarily due to the higher temperature chilled water that the system requires when compared to a conventional air handler. This paper looks at the core arguments of chilled beam-associated thermal comfort and energy use through the means of sensor data collected from a standard commercial conference room located in Andover, Massachusetts. This work investigates the impact of ceiling fan and chilled beams through the air speeds and temperature distribution across the room. Although a few recent studies have been conducted on larger open plan office spaces, a typical conference room containing an external façade and window poses different scenarios and challenges. The results of this work show that the Standard Effective Temperature is lowered by 0.5 °C (0.9 °F) when the ceiling fan is in operation. This suggests a reduction of the cooling degree days by roughly 10% with the hybrid system, which may be used as a first-order indicator for the sensible cooling reduction that a chilled beam is loaded with. The results also show a decrease in the temperature distribution throughout the room by roughly half, showing that the quality of data collected by a building management system can be improved through a hybrid approach.

4.1.2 Introduction

As building heating and cooling consume 15% percent of total energy in the United States, the economic conditions are primed for the integration of mixed-mode space conditioning systems, or hybrid buildings. While proposals of mixed-mode approaches to space conditioning are abundant in the academic literature [163, 164, 165], there exists a void when integrating multiple low-energy systems while targeting an appropriate thermal comfort with minimal energy usage. Specifically, the integration of axial-type ceiling fans with chilled beams shows promise. Appropriately utilizing this hybrid approach allows for reduced cooling consumption while simultaneously improving system efficacy.

During the last decade, active chilled beams have gained acceptance as a popular air conditioning option primarily due to their energy saving potential. In particular, higher temperature chilled water leads to exergetic benefits. A considerable amount of research efforts has been spent within the last decade to assess the correct placement and operation of chilled beams [166, 167, 168, 169, 170, 171, 172]. Despite the published benefits of such a system, the literature does not adequately discuss how different systems can be used in conjunction with one another. One of the most basic solutions, the ceiling fan, is frequently omitted. Yet, it can play an important role in chilled beam applications, particularly in the presence of a sudden increase in heat loads, such as when a conference room is occupied.

4.1.3 Active Chilled Beam Method of Operation

Chilled beams are separated into two main categories, active and passive. The principle difference between the two is the presence or absence of a ducted air supply from a central air handler or Dedicated Outdoor Air Supply (DOAS). Within an active chilled beam, as was used in this paper, the air supply induces additional flow within the chilled beam through the venturi effect. The additional flow is drawn from the room through a heat exchanger and typically constitutes 67-89% of the eventual supply air [173]. The placement of the heat exchangers within individual active chilled beams allows a central air handler or DOAS system to take care of latent and ventilation loads, while the active chilled beam provides individualized sensible control throughout a space. In this way, the system can be more energy efficient in lieu of conventional variable air volume systems and can provide increased thermal comfort [174, 175].

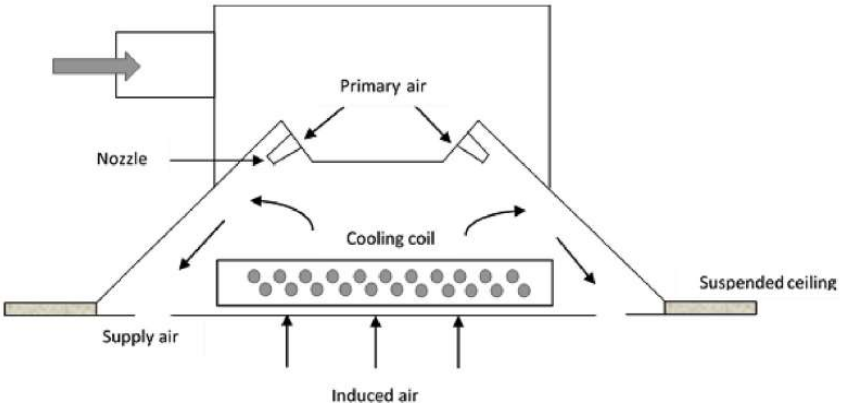

Figure 65: Active chilled beam cross section [175]

Of the key benefits of using an active chilled beam, one of the most touted is the ability to use temperate chilled water, which can reduce the size and upfront costs of the chilling equipment or allow for more energy efficient operation [176]. This also opens up the possibility of using heat recovery chillers and reusing energy within the building`.

4.1.4 Active Chilled Beam Airflow, Time Adaptation, and Test Setup

Active chilled beams make use of Coandă effect to maintain airflow across the ceiling. The Coandă effect, or the tendency for moving air to stay attached to a convex surface, helps reduce the airflow directed at occupants below. In this application, the convex surface is created by the angle between the suspended ceiling and the chilled beam housing. In most cases, the existing setup accomplishes the goals that the system was designed for. However, while chilled beams are an effective choice for nonuniform loads within a space, they may not be an effective choice for a space that experiences nonuniform loads through a day. For example, a conference room in an office building experiences rapid changes in occupancy and associated heat loads.

Combined with occupancy sensors and a temperature setback, a chilled beam may not provide enough cooling to drop the temperature of the space back into the comfort regime within a reasonable

amount of time. The Coandă effect, while normally beneficial to aide complete circulation of the air within the space, will now hinder the response time as this new wave of cold supply air will also absorb heat from the ceiling tiles instead of directly serving the occupants. To redirect this cold supply air down to the occupants and maintain thermal comfort, a ceiling fan is used within this study to look at the temperature implications at the seated positions. A ceiling fan helps also in moderating the temperature stratification in the room- both vertical (created by the chilled beam jet flow and buoyant plumes from heat loads) and horizontal (created by the solar irradiance through the external window).

To test the airflow conditions of an active chilled beam coupled with a ceiling fan, the team used a conference room located in Andover, Massachusetts with a north facing window. The room dimensions were 5.8 m long, 5.5 m wide, and 2.8 m high, and it was equipped with a 10-foot SEMCO IQHC Active Chilled Beam located parallel to the major axis of the room and offset toward the exterior window. The external window is 5 m long and 1.5 m high, located 0.8 m above the floor. The chilled beam is located 1 meter away from the external window (referred to in later sections also as Ext. Win.). The room was retrofitted during the study with an axial-type Hampton Bay 44-inch diameter Hawkins model fan (2.023 m^3/s, 4,286 cfm) located closer to the center of the room, above the conference table, and along the minor axis of the chilled beam. In this setup, no additional protections were needed to prevent personnel contact with the spinning blades. The room has a false-ceiling alongside the chilled beam ducts, rendering almost zero heat transfer through the top boundary of the room. The floor is concrete-based and is carpeted. The wall opposite the external window has a door with a considerable leakage area around its edges. The door is 0.8 m wide and 2.5 m high. The thermostat is located on the same wall as the door, away from it. Experiments were conducted in the month of June, when the outdoor temperatures were in the range of 23.0 °C- 26.0 °C.

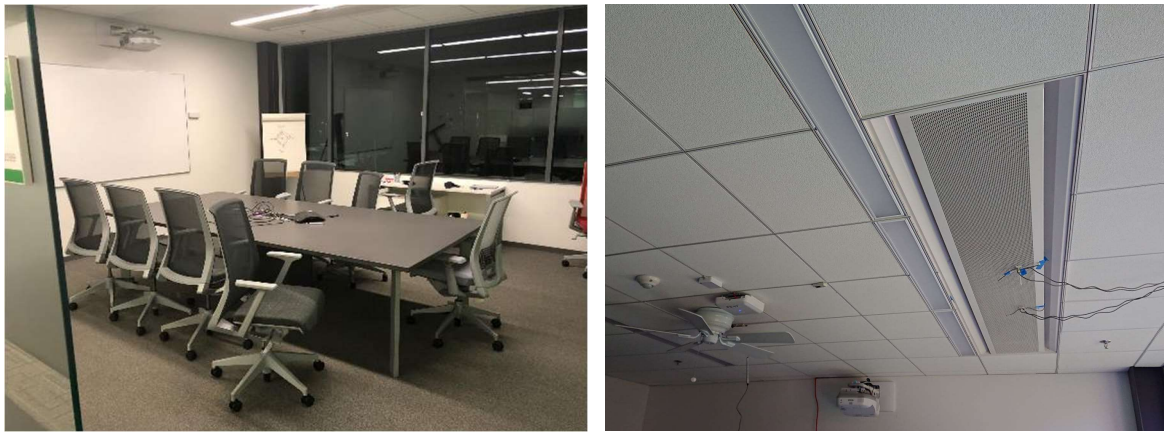

Figure 66: (Left) Conference room arrangement and (Right) ceiling arrangement showing fan and active chilled beam placement

For the velocity measurements at the ASHRAE 55 seated positions (0.1 m, 0.6 m, and 1.1 m), the team used a combination of hot wire anemometers suspended from the ceiling where the seats were to be located. The team used smoke tracing to confirm that the instruments were aligned appropriately with the net air movement. Prior to beginning both tests, without the fan in operation and with the fan in operation, the airflow patterns could stabilize for 20 minutes, a number determined from transient studies conducted in prior computational fluid dynamics (CFD) work [177]. To record the airflow values on the non-logging instruments, samples were taken at a time interval of 30 seconds for a 15-minute time period and written down manually.

The instruments used within this study, along with their stated accuracy, are listed in Table 17.

Data Point	Instrument	Range	Accuracy
0.1m air velocity	Solomat MPM 500e/129MS	0.01-12 m/s (2-2400 fpm)	±0.1 m/s ±3% of reading
0.1m air temperature	Onset Computer Corp. HOBO UX100-003	20° to 70°C (-4° to 158°F)	±0.21°C from 0° to 50°C (±0.38°F from 32° to 122°F)
0.6m air velocity	Onset Computer Corp. T-DCI-F350-W5A3 / HOBO H22 Energy Data Logger	0.15 to 1.0 m/s (30 to 200 fpm)	± (1% of reading + 0.05 m/s [10 fpm])
0.6m air temperature	Onset Computer Corp. T-DCI-F350-W5A3 / HOBO H22 Energy Data Logger	0°C to 60°C (32°F to 140°F)	±1°C ±1.8°F
1.1m air velocity	TSI VelociCalc 8345-M	0 to 30 m/s (0 to 6,000 ft/min)	±0.015 m/s (3 ft/min) or ±3.0% of reading
1.1m air temperature	Onset Computer Corp. HOBO UX100-003	20° to 70°C (-4° to 158°F)	±0.21°C from 0° to 50°C (±0.38°F from 32° to 122°F)
Surface temperatures	FLIR E8	–20°C to 250°C (–4°F to 482°F)	±2°C (±3.6°F) or ±2% of reading
Chilled beam return temperature	Onset Computer Corp. TMC20-HD / UX120-006M	-40° to 100°C (-40° to 212°F)	±0.15°C from 0° to 70°C (±0.27°F from 32° to 158°F)
Chilled beam supply temperature	Onset Computer Corp. TMC20-HD / UX120-006M	-40° to 100°C (-40° to 212°F)	±0.15°C from 0° to 70°C (±0.27°F from 32° to 158°F)
Ceiling air temperature	Onset Computer Corp. HOBO UX100-003	20° to 70°C (-4° to 158°F)	±0.21°C from 0° to 50°C (±0.38°F from 32° to 122°F)

Table 17: Data Points and Instrumentation

Within the conference room, the major internal heat gains were provided by the three seated researchers and four 75W incandescent lamps. Minor heat loads were also provided by one laptop (assumed at 10W), as well as various standalone chargers and standby losses already within the conference room (assumed at 10W). In this way, the heat loads are indicative of a seven-person meeting.

The conference room was designed to cater to a maximum of 9 people, with occupancy usually averaging around 6.

Surface temperatures were taken using an infrared camera targeted at the respective locations that had been pre-marked using masking tape from the same roll. Images were then post-processed using FLIR Tools software to account for the air temperature (measured with the Solomat MPM assembly), thermal emissivity (assumed at 0.95), and other applicable values. These values were used as inputs into the operative temperature where itself is an input into the ASHRAE 55-2017 thermal comfort outline [178].

4.1.5 Results and Discussion

4.1.5.1 Air Velocity and Thermal Comfort

The presence and operation of the ceiling fan creates an increased air velocity at the uppermost human-occupied measurement point (1.1m, 3.6 ft). As shown in Figure 67, this is especially the case for the seat closest to the exterior window. The increase drops off below the conference table height, located at 0.7 m (2.3 ft), where the air moved by the fan does not penetrate the table. Presumably this redirected air would splash across the table top, but the airspeed was not large enough to move papers on the table. For the lower elevations, especially the 0.1 m (0.3 ft) height, the airspeed was highly dependent on the location within the room. For the seated position below the chilled beam ("Near Ext Win") and with the fan off, the addition of the fan decreased the air speed at the lowermost measurement point. While at first glance this may appear to be a downside, the variation in air speed across the vertical distribution on a human subject can increase the dissatisfaction with the thermal environment [179].

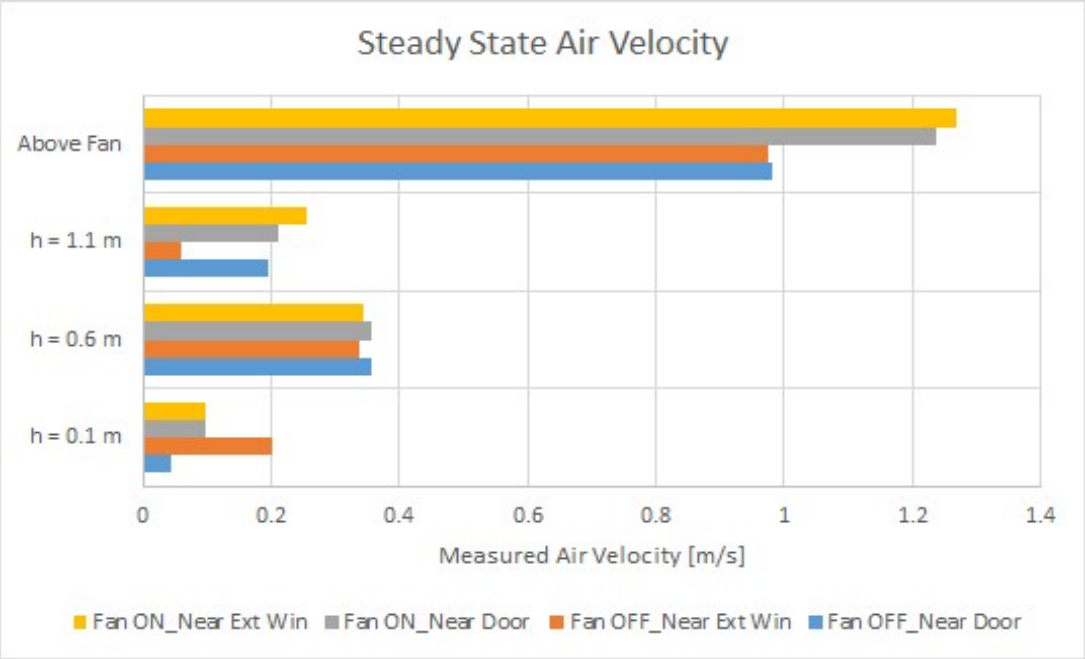

Figure 67: Steady state air velocity at various heights during testing phases.

Based on the results from Figure 67, the team took a weighted average of the air speeds with a double weighting given to the uppermost data point. This was done to account for shorter sleeves in the summer predominating the shift to shorter trousers, and since this impact is not accounted for fully by adjustments to the assembly clo values. As a result of this weighted average, the weighted average air speeds of the occupant level with the fan off was 0.18 m/s [35.4 fpm] and, with the fan on, 0.228 m/s [44.9 fpm]. While this is not the direct methodology as prescribed by ASHRAE 55, existing research from [180] called for algorithms for convective heat exchange in prediction models to be reconsidered. One such method is an exposed skin area weighted average, to which the double weighting approach may more closely approximate than a simple average.

These values, when used with the ASHRAE 55 calculator [181], and the calculated Operative Temperature of 22.46 °C (72.43 °F), 41% Relative Humidity, 1.1 Met, and 0.5 Clo produce Thermal Comfort Impacts with a roughly 0.5 °C difference in the Standard Effective Temperature (SET). The SET is a means by which it is possible to evaluate the difference in perceived temperature based on variations to the factor mentioned previously. Formally defined, the Standard Effective Temperature is set at an imaginary environment at 50% relative humidity, little to no air speed (<0.1 m/s), and where the mean radiant temperature equals the air temperature. The activity level is set at 1.0 met and the clothing at 0.6 clo. [178]

The outputs of the ASHRAE-55 calculator (16) are shown below in Table 18.

Fan Status - Air Velocity	Predicted Mean Vote	Predicted Percentage of Dissatisfied [%]	Standard Effective Temperature
Off - 0.18 m/s [35.4 fpm]	-1.21	36	21.3 °C (70.3 °F)
On - 0.228 m/s [44.9 fpm]	-1.37	44	20.8 °C (69.4 °F)

Table 18: Thermal Comfort Impacts

Using the information collected and presented in Table 18, the team sought a rough estimate of energy savings by back calculating the operative temperature assuming a heightened air velocity (Fan On case) and the existing SET (Fan Off Case), resulting in an increase of 0.5 °C (0.9 °F). Correspondingly, cooling degree days were evaluated for both Boston and Miami climates for an air temperature of 22.5 °C (72.5°F, as a proxy for the 22.4 °C air temperature observed within the testing) and 23.0 °C (73.4°F). Conceptually, these values would be the change in thermostat setpoints resulting for the increase in the use of the ceiling fan coupled with the chilled beam. The resulting reduction of cooling degree days is on the order of 10% for both climates, suggesting that the sensible cooling load on the chilled beam would reduce correspondingly.

While this is not an exhaustive attempt to quantify the energy savings of using the two systems in conjunction with one another, it does stand as a first pass to show that cooling energy savings are non-negligible. There are additional savings that can be achieved by the associated increase in the chilled water temperature, but some of those savings may be offset by the energy required for the ceiling fan. This increase of 0.5 °C (0.9 °F) falls short of the 3 °C (5.4 °F) differential that is reported by [182], and support the authors' opinions that the thermal comfort changes published in this paper are conservative estimates.

In this scenario, energy savings from a change of the chilled water temperature being sent to the chilled beams are best evaluated on a case-by-case basis, as the two predominant systems of chilled beam water supply create a substantial variation in savings estimates. For example, a system that uses blended chilled water will see a very different savings estimate than a dedicated system which can then make additional use of other energy utilization tactics such as free cooling in the cooling towers. Local weather conditions and other operational characteristics will have additional impacts to which the quantification is outside the scope of this study.

Further, it should be noted that the presence and operation of the ceiling fan decreased the overall temperature stratification in the room. Additionally, the three subjects present in the room during the experiments unanimously expressed feeling discomfort with the fan on, feeling the conditions to be on the chiller side. This discomfort supports the arguments presented above on the energy-savings potential for the hybrid system using a ceiling fan.

Another way of looking at the data supports the assertion that the baseline condition (Fan Off) is also being overcooled, as represented by the high discomfort values. Where the Fan On condition increases the nominal discomfort, it does support the concept that, had the air temperature been set to minimize the discomfort with the fan off (26.2°C, 79.2 °F), energy savings could be achieved with the fan on by relaxing the cooling setpoint to 26.7 °C (80.1 °F).

4.1.5.2 Air Mixing

Using the pre-existing building management system, the team extracted the data during the time of the study. Figure 68 shows the resultant room temperature data along with the carbon dioxide concentration levels indicating human activity in the room during the experiments.

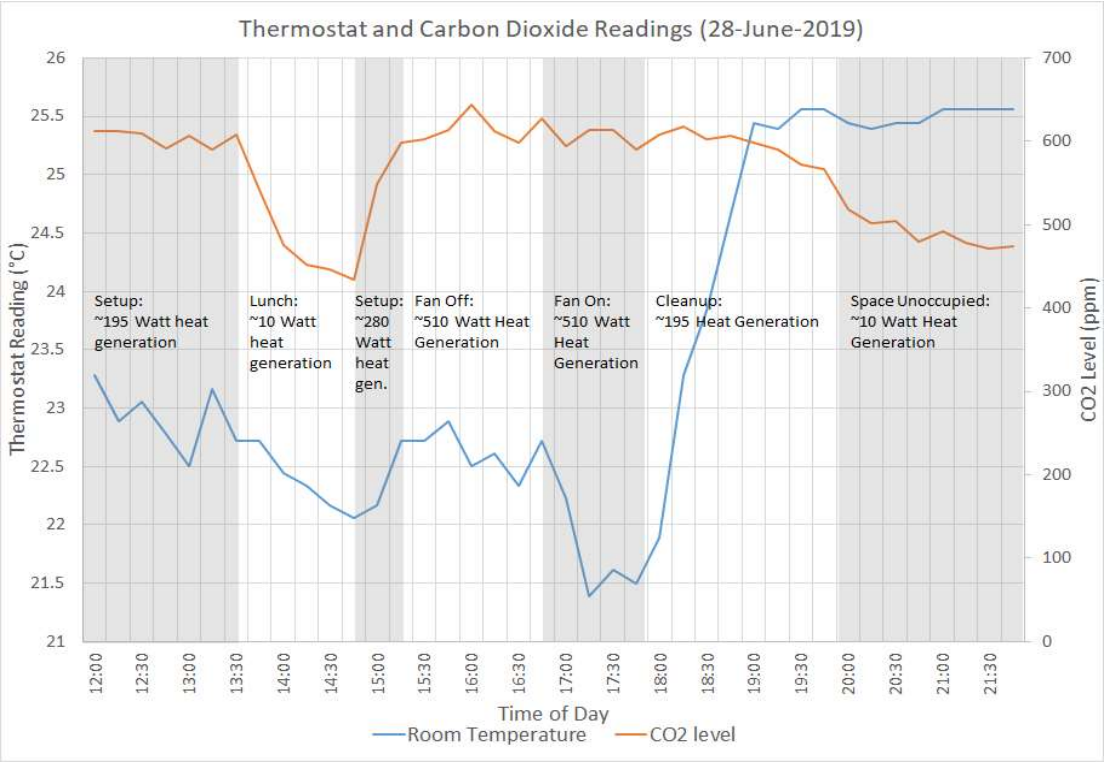

Figure 68: Thermostat temperature and CO2 readings during testing setup and execution

Using additional data from the human-occupied heights, the team observed that with the fan in the off state, the temperature difference between the simple average of the human occupied heights in the occupied zone and the building management system-derived thermostat was 1.6 °C (2.9 °F). This difference decreased substantially when the fan was turned on, to a value of only 0.7 °C (1.3 °F). Figure 68 depicts this during the 'Fan On' state and the resulting reduction in the temperature that is reported by the thermostat. The reading at 21.5 °C (70.7 °F) is more indicative of the actual air temperature during that time. During the entire testing period, the building management system reported a constant specified and resultant airflow rate for the chilled beam.

This observation has significant implications for building controls, as the ceiling fan aides in reporting an accurate value of the mean indoor air temperature of a space to the building management system. Another way to state this observation is that the assumption of well-mixed air does not always hold true, but the presence of a ceiling fan aides in enabling this assumption.

4.1.6 Conclusion

The intent of this paper was to provide an initial effort to understand the magnitude of impact on both thermal comfort and cooling energy that a ceiling fan would have on a conference room equipped with an active chilled beam. The air velocities, when weighted with a bias towards the shoulder level, show an increase from 0.18 to 0.228 m/s (35.4 to 44.9 fpm) when the fan is turned on, and a decrease in the Standard Effective Temperature of 0.5 °C (0.9 °F). Based on cooling degree days, such a decrease would be effective in reducing the sensible cooling energy that is placed on the active chilled beam by an estimated 10%. Further work is required to fully quantify the reduction in cooling energy that will result in the interaction between the two systems.

For existing installations, this paper helps to provide merit to use higher temperature setpoints during the cooling season, as well as for the inclusion of ceiling fans in an occupied space to reduce the variation in air temperature and improve data quality from building sensors. Further work is needed to understand how the inclusion of a ceiling fan may help in the transient and heating season cases.

4.2 Comfort control and improved thermostat location in conference rooms and academic working spaces

This section (4.2) was a combined effort with Nikhilesh Ghanta and Leon Glicksman. It was published in Building and Environment in November of 2021 [183].

4.2.1 Overview

The challenge of comfort control within commercial and academic spaces was explored in an attempt to determine what would be the optimum location and type of measurement over different occupancies and different seasons of the year. A computational fluid dynamic (CFD) simulation using Reynolds-averaged, RNG k – ε turbulence model was set up. It was verified by physical measurements of temperature and flow behavior within a commercial conference room containing a large external window and that was conditioned by an active chilled beam. Experimental measurements, supplemented by simulation, indicated a large, seasonal-varied deviation between the temperature measured by a wall-mounted thermostat and the average comfort conditions around occupants of the room. CFD results and post-processed predicted mean vote (PMV) values showed that having the thermostat located near the humans in the middle of the room (over a table in this case) improved the thermal comfort conditions compared to having it on a wall opposite the external window (PMV of 1.1 as compared to 1.8 for an Andover, MA summer scenario, respectively).

The major causes of the deviations were the convective and infrared heat transfer from the window surface as well as the solar gains to the room interior. The wall thermostat errors could be moderated by including temperature measurements at the window surface as an additional input in the control algorithm. This conclusion was confirmed by experiments in a dormitory room and a large shared academic workspace.

4.2.2 Introduction

One of the most commonly utilized spaces in a commercial building is the conference room. Although their variance in construction and geometry from building to building is minimal, they pose meaningful HVAC-related (Heating, Ventilation, and Air-Conditioning) questions due to the variability in occupancy and influence of external conditions. One of the most common controls for in-room conditioning is the thermostat usually placed on walls away from humans and heat sources. This is also one of the major reasons for discomfort despite thermostat setpoints set within the human comfort range, thereby leading to repeated manual adjustments of the thermostat setpoint and the resultant energy losses. The temperature stratification caused by the air conditioning system is the main reason for this discomfort, which is severely impacted by external weather fluctuations in the presence of an external window. With the increased drive for smart buildings and control systems, there is a great need to understand the human occupancy comfort conditions in a room with minimal sensor data, simulations, and manual interventions as possible. This study looks at one such system- a standard conference room with an external window and conditioned by active chilled beams. Experimental data logged using various sensors is analyzed and simulations are performed using Computational Fluid Dynamics (CFD) to understand the flows and interactions in the room. The same methodology is used in an attempt to

generalize the impact of critical variables on human thermal comfort in commercial conference rooms, quantized in terms of Fanger's Predictive Mean Vote [184]. The minimal number of sensors required to predict the occupancy comfort levels along with the optimized placement of their location is modeled from the data analysis and simulation results. This model is then tested against CFD simulations for validation.

Although chilled beams came into existence in the late 1980s, their importance grew since the early 2000s when the efficiency in decoupling the functions of the HVAC system was being studied. Mumma [185] and Roth et al [186] looked into such de-coupled HVAC systems in spaces being conditioned parallelly by air and water systems and reported a good increase in system operational efficiency when latent and sensible loads are decoupled. Such decoupling led to a rise in the popularity of chilled beams, chilled ceilings, and radiant floors. The air distribution in office spaces with chilled beams was studied by Koskela et al [172], with a primary focus on drafts and air recirculation. It was concluded that the combination of inlet jets and recirculation flows create a draft risk, which was heightened by asymmetric heat load distribution in the rooms. The study was also focused primarily on cooling using chilled beams in the summers. Air distribution was further studied in detail by Cao et al [187] and Cao et al [188], wherein they used a PIV (Particle Image Velocimetry) measurement system to determine airflow patterns surrounding the chilled beams. The interaction of ventilation airflows with convective buoyant flows from heat sources in the room was studied by Kosonen et al [189]. They utilized full-scale experimental data collection along with qualitative smoke visualization studies to understand the flow interactions and concluded that higher heat loads resulted in a significant impact on the convective flow and thereby increased the risk of draft and thermal discomfort (due to higher local airspeeds) in the occupied zones.

Conference rooms and open-plan office spaces differ quite substantially in their conditioning needs and controls. Modern open-plan office spaces have higher heat loads due to higher occupancy density and typically, higher cooling loads imply a higher risk of discomfort. However, chilled beams are better designed for higher cooling loads than other HVAC systems [189, 190]. Different configurations and arrays of chilled beams were simulated and tested for open-plan office spaces by Cehlin et al [169]. The thermal uniformity and temperature stratification in such a system were studied in detail by Rhee et al [191]. They concluded that chilled beams result in higher thermal uniformity as compared to traditional HVAC systems, especially in open-plan spaces. A detailed CFD study was performed to understand flows and energy transfers by Koskela et al [192] and Koskela et al [193]. The importance of understanding seasonal changes was also touched upon in the above-mentioned studies, with extreme load conditions only simulated. Koskela et al also discussed the risks of drafts and the impact of heat sources [192]. Kim et al [168] expanded on such studies to understand the energy savings potential of chilled beams in various US climatic zones.

One of the most commonly used thermal comfort models for human beings is the PMV (Predictive Mean Vote) model developed by Fanger [184]. This was later adopted by ASHRAE and ISO [178]. Fanger also worked on improving the model by extending it to non-air-conditioned buildings and different climate zones [194]. Later, there were multiple studies performed on the efficacy of Fanger's model, especially in the 21st century of globalization [195]. However, the extended PMV model remains one of the most common thermal comfort models for researchers and engineers to date. The other comfort models like the Adaptive comfort model, SET, etc., come with their own assumptions and limitations.

Fanger's PMV correlation is based on the identification of the sweating rate and skin temperature needed for the optimal thermal conditions. PMV is measured on a scale of -3 to 3, with positive numbers indicating hot conditions and negative indicating cold. A higher magnitude of the PMV value indicates that the condition is more uncomfortable- PMV of -3 translates to extreme cold and a PMV of +3 translates to extremely hot conditions. Ideally, a range of +0.5 to -0.5 is considered a well-conditioned space for humans to occupy.

According to Wang's study [196], the control of the indoor comfort conditions by monitoring operative temperature has a different effect on thermal comfort level and energy use by the heating/cooling system as compared to that by monitoring the air temperature. Thus, it is necessary to define what parameter is measured by thermostats available on the market. While comparisons of different thermostats can be found in the literature, for example in the work by Mylonas et al. [197], the effect of the location has not been addressed. W.Tian et al [198] proposed an optimization platform for determining the location of the thermostat in a room, based on Modeling and Fast Fluid Dynamics. However, it is just a pilot study aiming to provide a proof of concept and isn't validated to work with varied scenarios and more realistic cases. It is still an open-ended question on the ideal location of the thermostat for the best possible optimized values of thermal comfort and energy savings. Besides, the question of what variable to measure is important to be answered. Borier et al [199] researched the various types of sensors currently available in the market and experimented with different locations in the room. They concluded that for occupants sitting near external windows being influenced by the incoming solar radiation, a new generation of sensors should be developed and the currently existing ones do not satisfy the requirements for sensing thermal comfort. They also concluded that for occupants sitting in the middle of the room and away from the windows, the best possible position for thermostats without human disturbance and intervention would be on the walls and such sensors shouldn't especially be placed in front of the windows. The problem of measuring solar radiation coming through the window is compounded by the fact that radiation sensors currently available are also influenced by convective heat transfer, making it difficult to distinguish between heat transfer from radiation and convection. The research detailed in this manuscript furthers the above conclusions and extends the research on possible locations and sensors for conditioning for humans sitting next to external windows.

The research detailed in this manuscript has two components- experimental and computational. An office room in Andover, MA conditioned by chilled beams is used as a test room for conducting experiments, the results of which are later used for validating the CFD model created using Airpak and Ansys. The post-processed results from this CFD model along with the data analyzed from the experimental office room were used to understand the thermal comfort of occupants in office spaces influenced by an external window. Observations are made on the inadequacy of current thermostat technologies and temperature-control mechanisms in occupied spaces. To further investigate, quantify and highlight the magnitude of the problem and scope for improvement, additional experiments were conducted in academic office spaces and student dormitory spaces. Correlation factors were calculated to analyze and identify a better location for the thermostat along with a potential solution to improve existing thermostat systems in buildings for improved thermal comfort of occupants and optimum energy consumption.

4.2.3 Experimental Work

The conference room in study is a part of an office building occupied by Schneider Electric located in Andover, Massachusetts. The room has floor dimensions of 5.8 m x 5.5 m and has a ceiling-floor distance of 2.8 m. It has one side of the longer dimension as an external wall, facing North. The external wall has a large double-glazed window, completely covering the entire wall area from a height of 0.75 m until the ceiling. The other three walls are internal walls connected to other rooms of the building. The room has a false ceiling alongside the chilled beam ducts, rendering almost zero heat transfer through the top boundary of the room. The floor is concrete-based and is carpeted, thus acting only as a minor thermal mass. The active chilled beam is located 1 m away from the external window and parallel to it and is 2.8 m in length. The wall opposite the external window has a door with a leakage area around it. The door is 0.8 m wide and 2.5 m tall. The room has a projector mounted to the ceiling and a conference table with multiple chairs, providing occupancy for a maximum of 10 people. Apart from the incoming solar radiation through the external window, the other sources of heat generation are the projector, humans, and laptops. Artificial lighting is rarely used due to the large unshaded external window. Depending on the temperature setpoint of the thermostat located on the wall opposite the external window, the chilled beam can either heat or cool the space.

Experiments were conducted at least once in each of the major seasons, spanning six weeks every time. In addition to data logging over periodic intervals, experimental recordings were taken at steady-state conditions in the conference room. To make these recordings, the conference room containing various heat sources (occupants, laptops, and projector) was allowed to attain steady-state conditions without any additional external disturbances. The measurements of velocity were conducted using hot-wire anemometers (TSI VelociCalc Air Velocity Meter 8345; ±0.015 m/s accuracy). Temperature readings at various locations in the interior room space were recorded using multiple thermocouples (TSI VelociCalc 8345; ±0.3°C accuracy) and surface temperatures were measured using an Infrared Camera (FLIR E8 Infrared Camera; ±2% accuracy), as shown in Figure 69. Additionally, the concentration of carbon dioxide in the room was also monitored (Telaire 7001 CO2 sensor; ±50 ppm accuracy). This carbon dioxide instrumentation is crucial in the operation of the active chilled beam to ensure adequate outside air to meet ventilation requirements. However, the ventilation load could add additional conditioning load to the chilled beam.

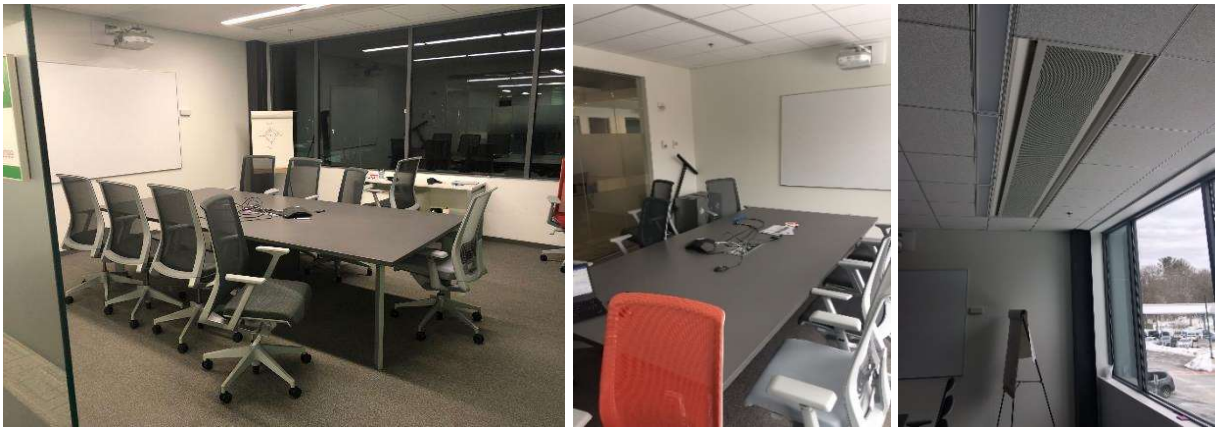

Figure 69: Photographs of the conference room used in this study (Andover, Massachusetts, USA)

Qualitative experiments were performed with smoke pencils and an infrared (IR) camera. Smoke pencils were used to understand the air flows in the room by observing the streamlines created by smoke. Infrared photography was used to understand surface heat flows in the room along with collecting temperature data from various surfaces. All the other sensors were temporarily installed to collect data and log them at fixed intervals.

Two Onset Computer Corporation (Onset) air velocity sensors were placed at the inlet and outlet of the chilled beam to measure the air temperature and velocity of incoming and outgoing air respectively. Of these, an Onset W5A3 was placed in contact with the incoming ducts that take in air from the room into the chilled beam (point 3 in Figure 70 and Figure 71) and listed in Table 1. The direction of the sensor was adjusted to ensure alignment with the air stream. An Onset W5B3 was positioned adjacent to the outlet air ducts of the chilled beam- about 2 inches away from it (point 4 in Figure 70 and Figure 71) which also coincides with the point of the entry of air into the room from the chilled beam (which is situated above the false ceiling). The direction of placement of this particular sensor is of vital importance as it is a 1-D velocity sensor. Smoke pencils were utilized to understand the angle of outlet of the air incoming from chilled beams into the room (45 degrees) and the W5B3 anemometer was positioned to match this angle. A hand-held TSI VelociCalc anemometer was used dynamically during the experiments to measure the air velocity at different points in the room- near the door inside the conference room at different vertical heights (0 m, 0.5m, 1m, 1.5m), above and below the table (0.25 meters), near the thermostat (located on the wall opposite the external window) and near the window. These recordings were primarily carried out to help validate the CFD model later on, alongside helping to understand the relative importance of air speeds and drafts in different spaces within the conference room.

Three Onset UX100-003 loggers were installed to record temperature and relative humidity at three different locations in the room. One of them was placed on the window sill next to the external window, about 5 cm away from it (point 1.1 in Figure 70 and Figure 71). This was placed at the mid-point of the length of the external window (measured in the z-direction, in Figure 71). The second logger of this series was positioned 2.5 cm below the ceiling directly above the center table (point 1.2 in Figure 70 and Figure 71). This also coincides with the geometric midpoint of the room in the x and z directions (Figure 3). The third UX100 logger was placed 2 inches away from the projector (point 1.3 in Figure 70 and Figure 71). The main purpose of this sensor was to detect the operation of the projector in the room, which contributes to heat loads in the room.

The next set of loggers installed were the Onset UX120-006 series. Each of the loggers has connections to four thermocouples that can measure individual temperature points. The first set of four thermocouples were placed above the center table in the room, taped to the four corners of the top surface of the table (point 5.1 in Figure 70 and Figure 71). The second set of four thermocouples were placed underneath the center table in the room, taped to the four corners of the bottom surface of the table (point 5.2 in Figure 70 and Figure 71). The third set of four thermocouples were placed on the surface of the door, which was made of glass. Two thermocouples were placed along the inner surface of the door and the other two along the outer surface. Each was placed at a height of 0.5 m and 1.5 meters from the floor surface. (point 5.3 in Figure 70 and Figure 71). These thermocouples were placed to measure the air temperature adjacent to the door on both the inside and outside of the surfaces. Table 1 serves as a guide to reading Figure 70 and Figure 71. All the above-described sensors were purchased new and used with fresh batteries. While there was no additional calibration performed for these sensors, a post-experiment

comparison of the temperature sensors at the melting point of gallium showed that the values were within the accuracy ranges as stated by the manufacturer.

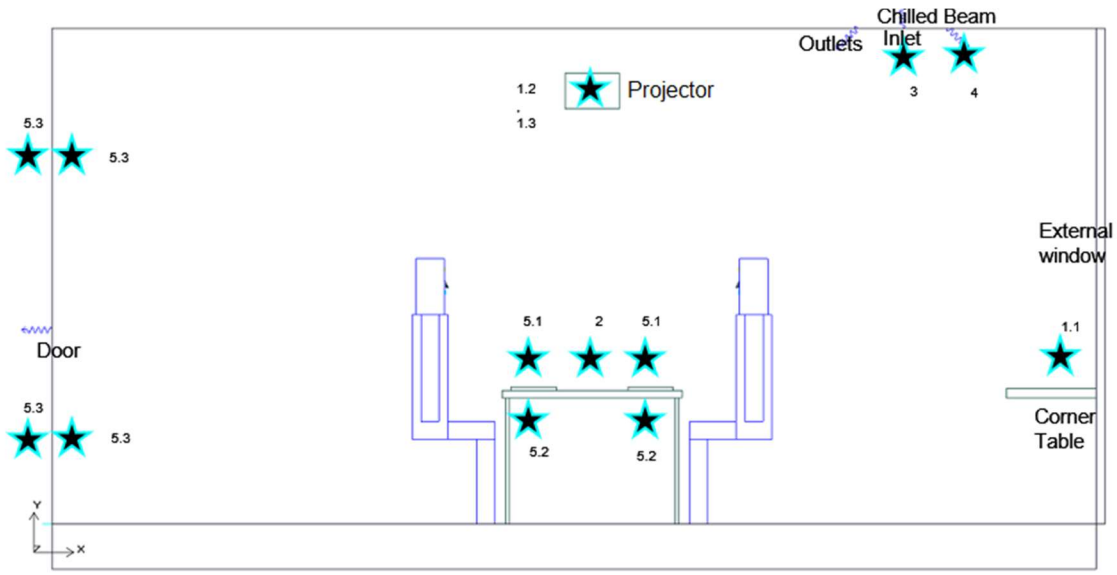

Figure 70: Side view of the sensor location in the Andover Conference room (Notation: x.y ➔ x corresponds to the sensor type referenced in Table 1 with their serial number, y corresponds to the number of such sensors)

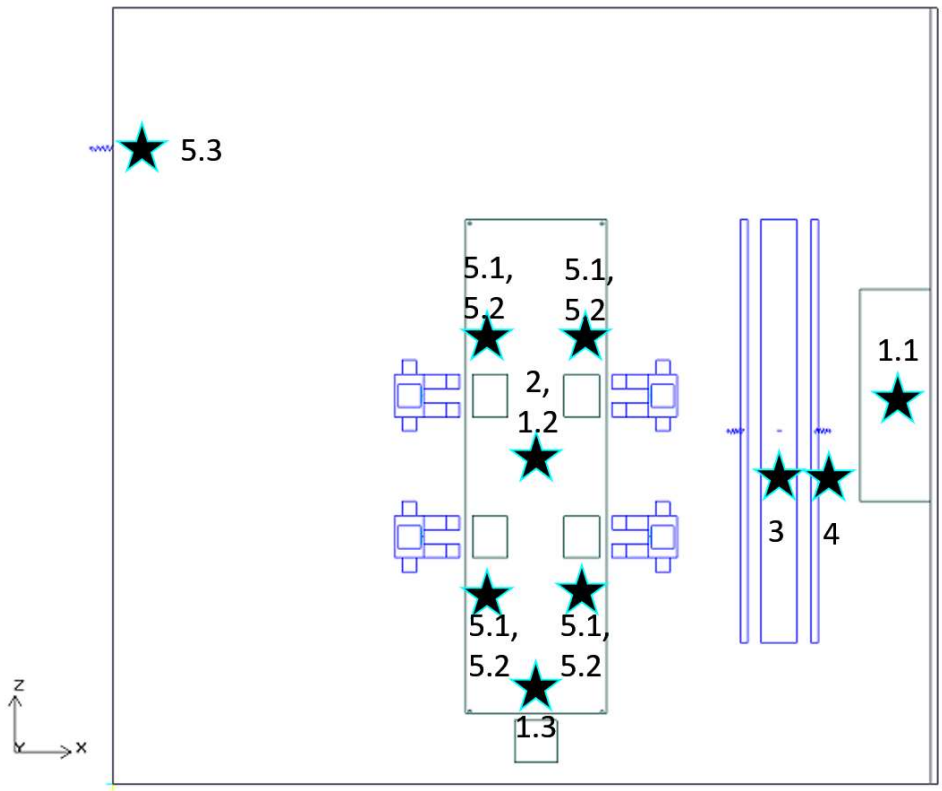

Figure 71: Plan view of the sensor location in the Andover conference room (Notation: x.y ➔ x corresponds to the sensor type referenced in Table 1 with their serial number, y corresponds to the number of such sensors)

Sl. No	Name of the sensor	No of sensors	Measurement
1	Onset UX100-003	3	Temperature, Relative Humidity
2	Onset MX1102A	1	Temperature, Relative Humidity, CO2
3	Onset T-DCI-F350-W5A3	1	Air velocity, Temperature
4	Onset T-DCI-F350-W5B3	1	Air velocity, Temperature
5	Onset UX120-006M	3	Four temperature (thermocouple) probes from each of the three loggers

Table 19: List of sensors installed, Guide to Figure 70 and Figure 71

A FLIR E8 Infrared Camera was used to capture the surface temperature profiles along with understanding the potential leaks in the room (especially to the external outdoor air). Different sections of the room were photographed using the IR camera to detect heat leakages and measure surface temperatures.

In addition to helping locate a couple of minor air leaks in the conference room, the smoke pencil also proved to be very resourceful in understanding the airflow patterns due to the chilled beam flows within the room. The direction of an airflow across the open door of the conference room was especially found to be useful as it varied significantly with varying boundary and operating conditions of the room. This helped not just in understanding the airflow patterns, but also served as a means for CFD simulation validation as discussed in the next sections.

4.2.4 Computational Work

Computational Fluid Dynamics (CFD) is utilized in this study as the computational tool to perform numerical simulations. The work presented here was conducted using ANSYS and Airpak. The Finite Volume method is utilized as the numerical discretization method. The Navier Stokes equations of continuity and conservation of momentum and energy are used as the primary set of governing equations, as shown in equations 1-3 below.

$$\frac{\partial \rho}{\partial t} + \nabla.(\rho U) = 0 \tag{56}$$

$$\frac{\partial (\rho U)}{\partial t} + \nabla.(U.\rho U) - \rho g = -\nabla p + \nabla.[\mu\,(\nabla U + (\nabla U)^T)] \tag{57}$$

$$\frac{\partial \rho c T}{\partial t} + \nabla.(\rho c U T) = \nabla.(k\,\nabla T) + P\nabla.V \tag{58}$$

Where ρ is the density, U is the velocity vector, p is the pressure, μ is the dynamic viscosity, c is the specific heat capacity, T is the temperature, and k is the thermal conductivity.

For an accurate analysis of the boundary layer and heat transfer phenomenon near the surface interface, very accurate information on the location of the interface is required. This can be done by increasing the number of grid points in the mesh generated. This requires an extremely high number of cells, leading to very high computational requirements. To avoid this trade-off, a local reconstruction of the surface interface is performed. This increases the accuracy of the location of the interface, without drastically changing the mesh resolution. The near-wall regions were meshed using very fine elements, with $y^+ < 5$ which is necessary to observe in detail the boundary phenomenon and near-wall physics. y^+ is the non-dimensional distance from the wall which is defined as below

$$y^+ = \frac{\rho u_r y}{\mu} \tag{59}$$

Where ρ and μ are the density and dynamic viscosity of air, respectively, y is the distance from the wall, and u_r is the friction velocity [200]. The friction velocity is a characteristic velocity of the flow near the wall, obtained solely by dimensional analysis arguments, and is given by

$$u_r = \sqrt{\frac{\tau_w}{\rho}} \tag{60}$$

Where, τ_w is the shear stress at the wall. Physically, y+ < 5 is the section of the flow near the wall where the viscous component of the shear stress dominates over the turbulent component [200].

The turbulence model chosen for simulations presented in this work is the RNG k – ε model. The radiation model implemented in the current work is the surface-to-surface (S2S) radiation model. Airpak software accounts for the effects of both direct and diffuse solar radiation. With specified model geometry and solar load information such as date, time, and terrestrial location, the model performs a ray tracing sharing test for all boundary surfaces. Solar illumination through this approach involves a two-bank spectral model- visible and infrared.

The 3D geometry was modeled using Airpak. The model consists of a room with the external window of flint glass material on one side, a glass wall on the opposite side comprising a door (with some leakage around it), and plywood-based interior walls on the other two sides. The roof is a false ceiling modeled for adiabatic conditions and incorporates chilled beam inlet and outlet vents. The floor is modeled as a finite thickness concrete slab with a carpet on top. There are two tables- one center table in the middle of the room and a side table next to the external window. The external window is facing North (unless specifically changed in certain simulations to simulate a variation of the original case). Humans are sitting around the table with laptops on top of the table (the number of occupants and laptops vary with simulation). The projector is next to the west-facing wall. Airpak allows humans to be modeled as both sitting or standing, with a defined head, body, and lap fraction. A default metabolic rate of 58.2 W/m^2 is considered as the thermal boundary condition for every person. The only source of exhaust from the room is the leakage area around the door if the door is closed. Artificial lighting is neglected in the CFD to match physical testing conditions. An image of the 3D model comprising of all the above-mentioned elements is shown in Figure 72. For illustration and variable definition purposes, parameters x, L, z, and W are marked in the Figure. X is the distance of the chilled beam from the wall consisting of the door and L is the length of the room, measured in the same direction. Z is the distance of the chilled beam from the wall next to the projector and W is the width of the room, measured in the same direction.

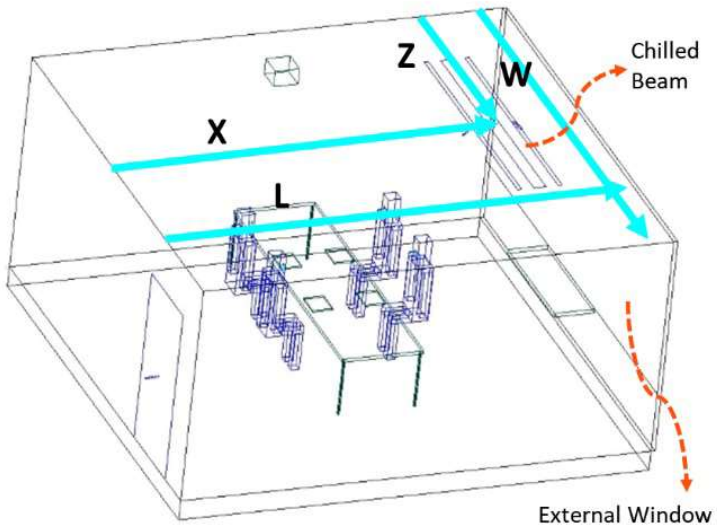

Figure 72: A 3D model of the conference room, created using Airpak

Figure 73 (Left) shows two planes marked on the geometry, that will be used for post-processing in the latter sections. The meshed plane named Plane 1 passes through the two humans seated 1.5 m away from the wall next to the projector. They would be the occupants seated farthest away from the door. The second plane marked in solid yellow color and named Plane 2 passes through the humans as well as the geometric center of the room. Plane 2 in effects bisects the width of the room. A picture showcasing the meshing involved with the modeling and simulation is represented in Figure 73 (Right).

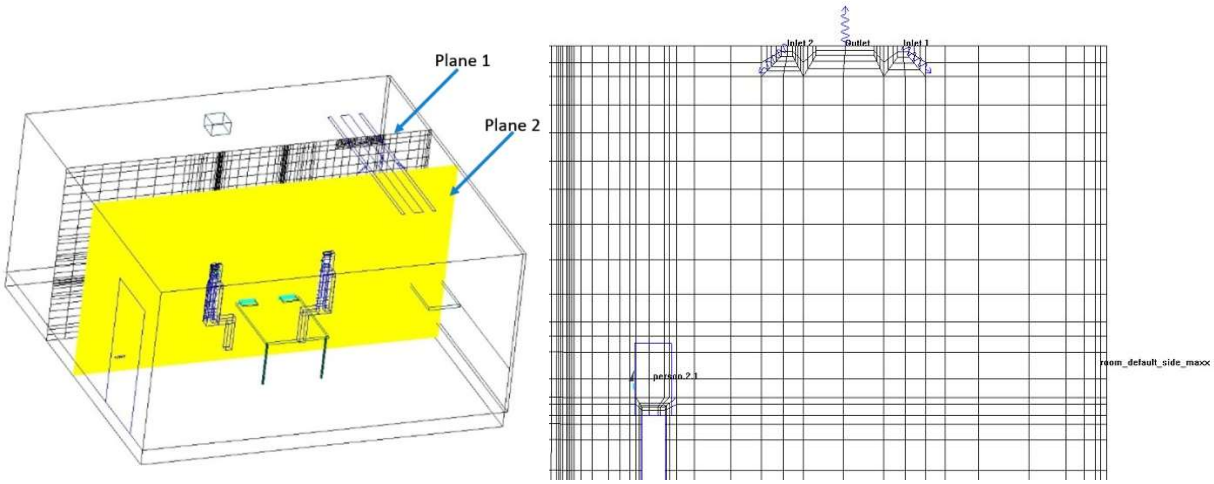

Figure 73: (Left) Planes marked on the 3D model of the conference room for post-processing and analysis. (Right) Sample meshing of the 3D geometry, showcasing the enhanced wall treatment and local reconstruction; Realized on Plane-1.

For ease of reference to initial conditions and boundary conditions, the simulation details are provided as a summary in Table 2 below. This is referenced to show results in various plots and contours for different seasons in the following sections. Several items remained unchanged throughout the simulations; including the northerly position of the exterior glazing, the projector's presence as a heat source, the location of the chilled beam, a 45° angle of air delivery from the chilled beam, and a 1.5 m/s chilled beam exit air velocity. Except for the northern wall (the external glass), the remaining five sides were modeled as adiabatic surfaces. The floor was modeled with a thermal mass (carpet covering 12.5 cm of concrete) and the wall with the door included a pressure boundary condition in place of the door when the door was in the 'Open' state. The external glass wall was modeled as a double-paned leaded glass window of 2 cm thickness and was subjected to external weather conditions. The Air Change Rate within the room was calculated to be approximately 1.8 per hour.

	External weather conditions			**Heat Sources**		**Chilled Beam Initial conditions**		
Simulation number	**Date**	**Time (24 hr)**	**Outside Temp (°C)**	**No. of Humans**	**No. of Laptops**	**CB Exit air temp (°C)**	**Steady State/ Transient**	**Door**
1	11-May	14:00	22	4	4	20	SS	Open
2	11-May	14:00	22	4	4	20	Transient	Open
3	11-April	14:00	18	6	6	20	SS	Open
4	21-Jan	14:00	-10	6	6	30	SS	Open
5	11-June	14:00	35	6	6	20	SS	Open
6	11-June	14:00	35	4	4	20	SS	Closed

Table 20: CFD Simulations reference table of initial and boundary conditions

A grid independence study was performed with decreasing mesh size (Figure 74), especially near the internal surfaces where eddy flows and turbulence are prone to occur. A nominal value of mesh size was chosen where the change in accuracy of the simulated values of temperature and velocity was found to be less than 1% when doubling the number of grid points. A sample meshing of the grid is shown in Figure 73 (Right), around the inlet and outlet areas of the chilled beams. A set total of 600,000 nodal points is considered in the mesh for the basic layout of the room, with dynamic spacing. The increased number of humans and other objects in the room increased the total number of grid points used for modeling to approximately 1-1.5 million.

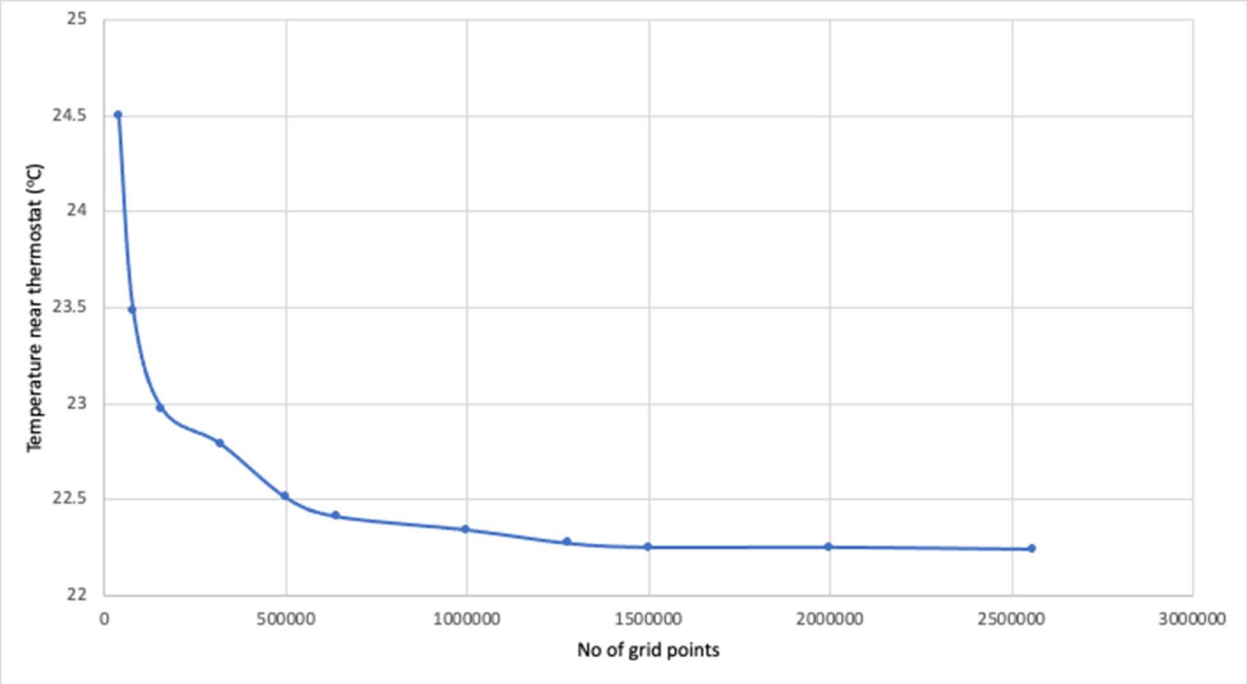

Figure 74: Grid independence study; simulation 1, Table-2

The numerical validation of the CFD simulations was done in two phases- steady-state and transient. Steady-state experimental data was gathered manually in certain conditions as detailed in the previous sub-section. Transient experimental data was recorded using data loggers along with various sensors placed strategically in the room. Qualitative validations were also performed with smoke pencil and Infrared camera testing. A qualitative and quantitative validation study was performed with the experimental readings of temperature and velocity inside various locations of the room. The vertical gradient of temperature was also checked for in the accuracy of the numerical simulations. Figure 75 shows the comparative temperature and velocity readings from experiments and CFD simulations adjacent to the door, with the door being kept open. The CFD simulations furnished a good accuracy in values and trends of temperature and velocities observed in the test room, keeping the error within 5-8%.

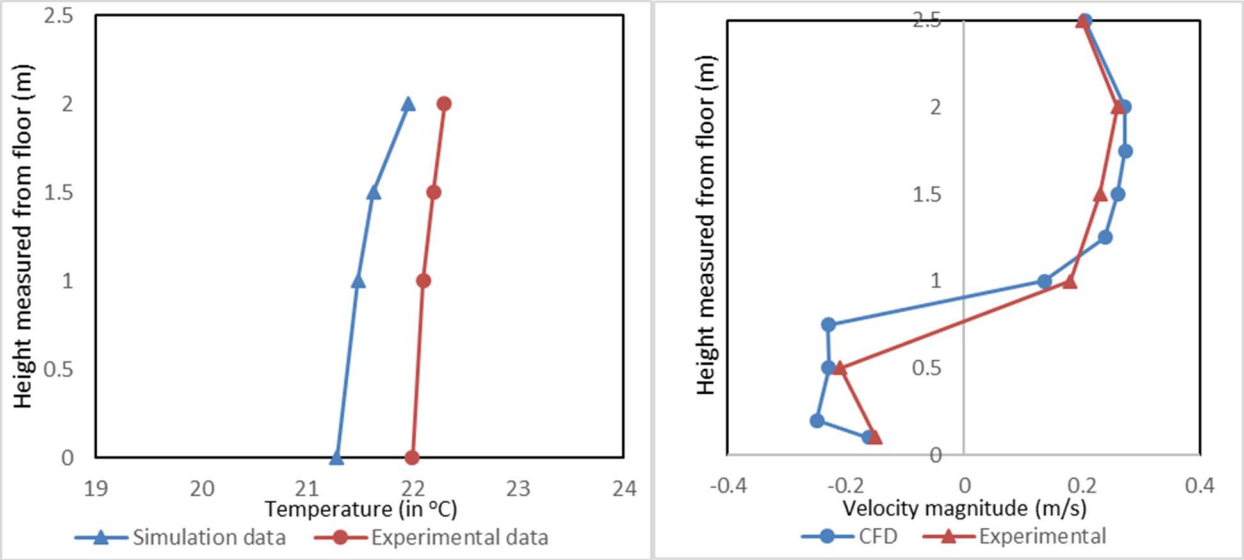

Figure 75: Validation studies of (Left) air temperature readings near the door and (Right) air velocity readings near the door, both measured at various vertical heights from the floor; Simulation 1- Table 2.

Data from sensor recordings were used to compare against transient CFD simulation results. Temperature values at several points in the room were compared, including those measured at the ceiling, near the door, on top and bottom of the central table, and near the external window. The CFD results agreed with the experimental data within the experimental uncertainty, as presented in Figure 76. The solid lines on the plot represent experimental readings of temperatures at various locations in the conference room. The dashed lines correspond to equivalent temperature values, obtained from the CFD simulations of that exact test conditions.

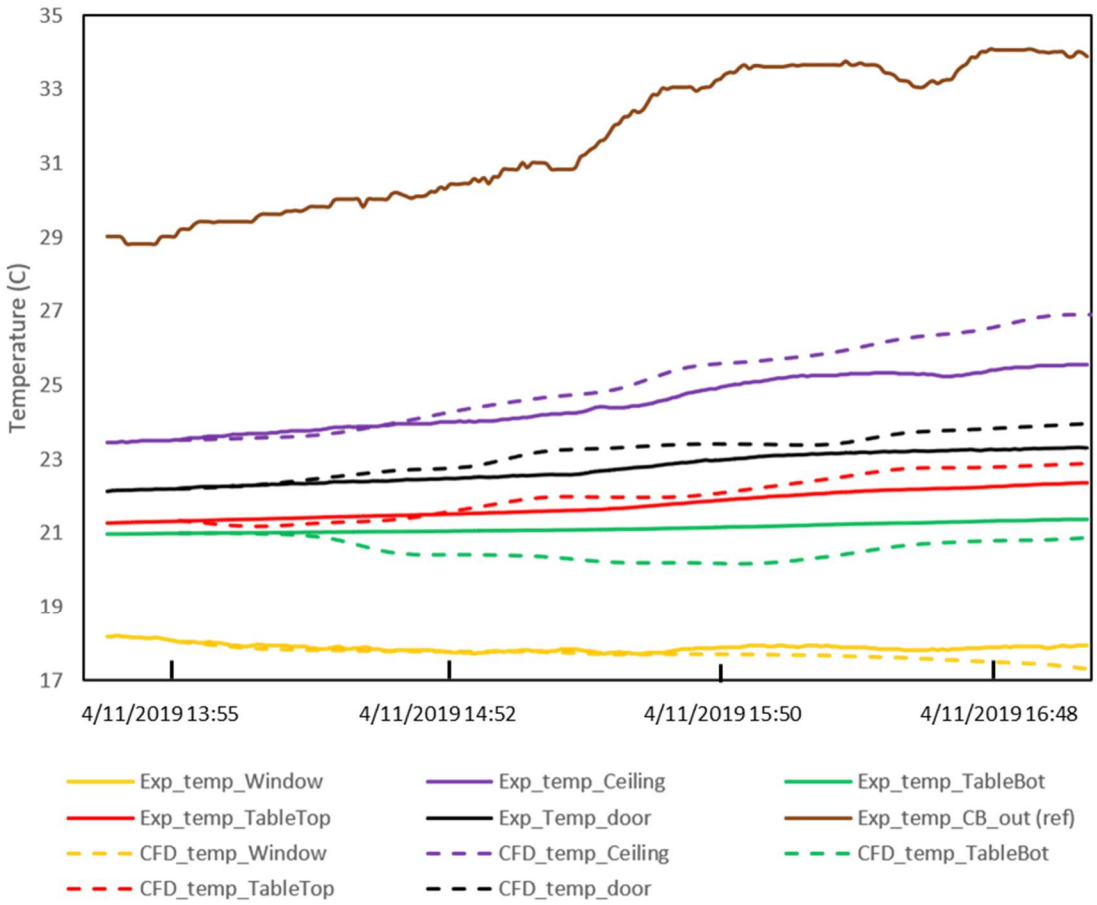

Figure 76: Validation study with air temperature readings near the door, measured at various locations within the room; Simulation 3- Table 2

A detailed parametric analysis was performed considering various critically influencing parameters [201]. The modified PMV model [194] was used as the thermal comfort model for occupants in this study. CFD simulations were performed with two and four additional people added to the room, to test the influence of the door being open versus closed. Post-processed results of PMV contours are plotted to show the impact of having 6 occupants, for varying seasons (Figure 77). The results for this case are plotted on planes that are perpendicular to planes 1 and 2 and passing through the humans sitting next to the external window. This particular change in planes is to understand the influence of external weather thought the external window and the impact of airflow through the door in the same picture. Seasonal variations were also studied to access the impact of door position on the comfort levels of people. It was observed from the resulting simulations that the door being open helps moderate the influence of the extreme external weather conditions created due to the presence of the external window.

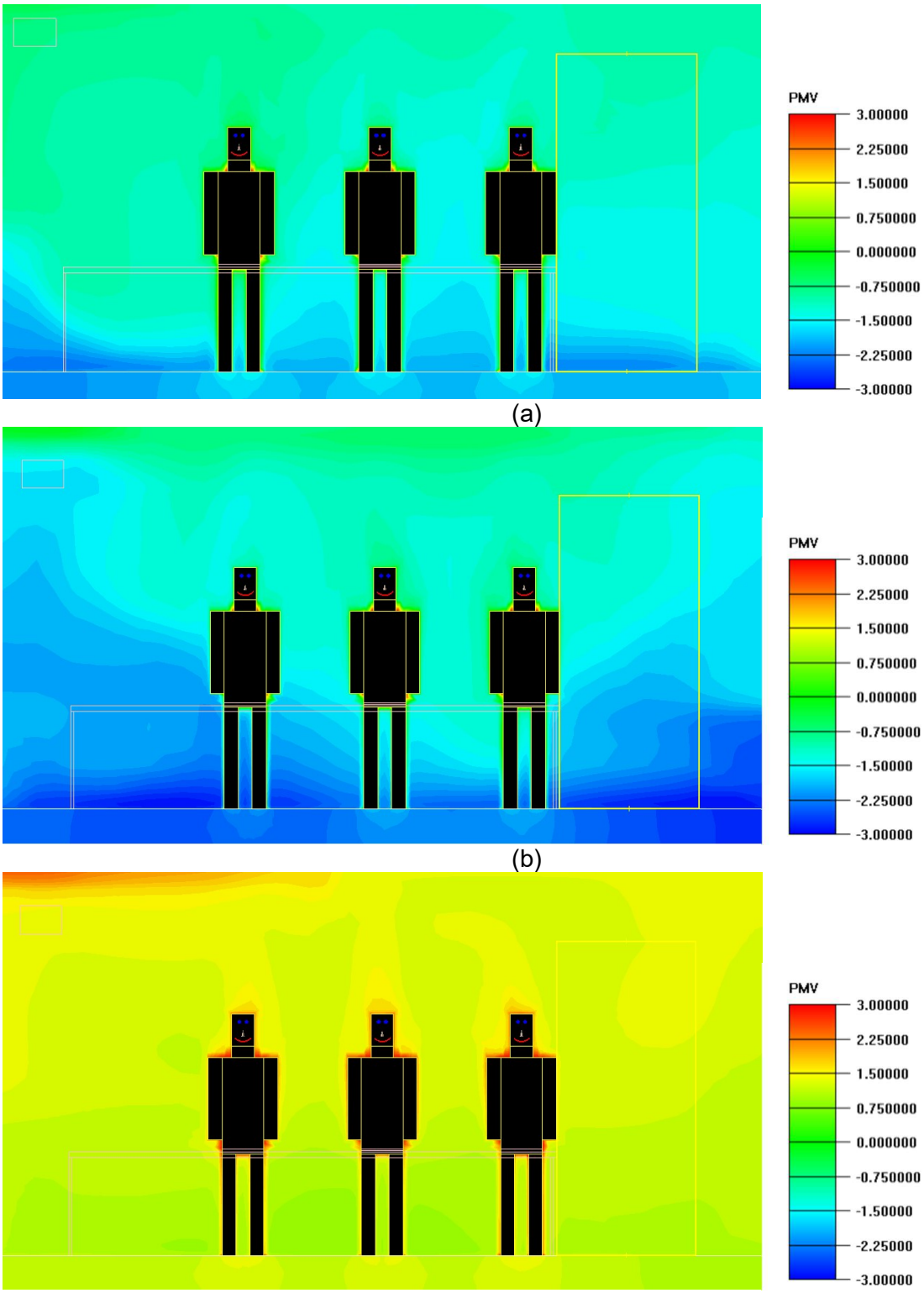

Figure 77: PMV realized on a plane perpendicular to both planes 1 and 2, with the door kept closed during (a) April for 6 occupants; Simulation 3- Table 2, (b) January for 6 occupants; Simulation 4- Table 2, and (c) June for 6 occupants; Simulation 5- Table 2.

From the data recorded using the sensors, a large number of manual setpoint changes in thermostat settings were observed in the conference workspace at Schneider Electric. These adjustments could be related to personal habits, or to unsatisfactory default settings. However, the setpoint conditions were similar to other adjacent rooms in the building (without any external window) which had few manual changes. The unusually large number of setpoint changes (as compared to other adjacent rooms in the same building) were due to a different issue and CFD simulations helped understand the underlying root cause, the external window. The external window provides a considerable heat load that impacts the thermal comfort of the occupants, especially those seated closer to the window. There is a considerable gap between the air temperature near the thermostat and that experienced by the occupants; this variation is largely dependent on the outside weather. A couple of sample extreme scenarios are shown in Figure 78. CFD simulations were performed, experimenting with various positions of the chilled beam in the room to understand this temperature stratification. It can easily be observed that there is a high stratification of temperature horizontally and vertically (depending on the season and heating/ cooling mode of the chilled beam).

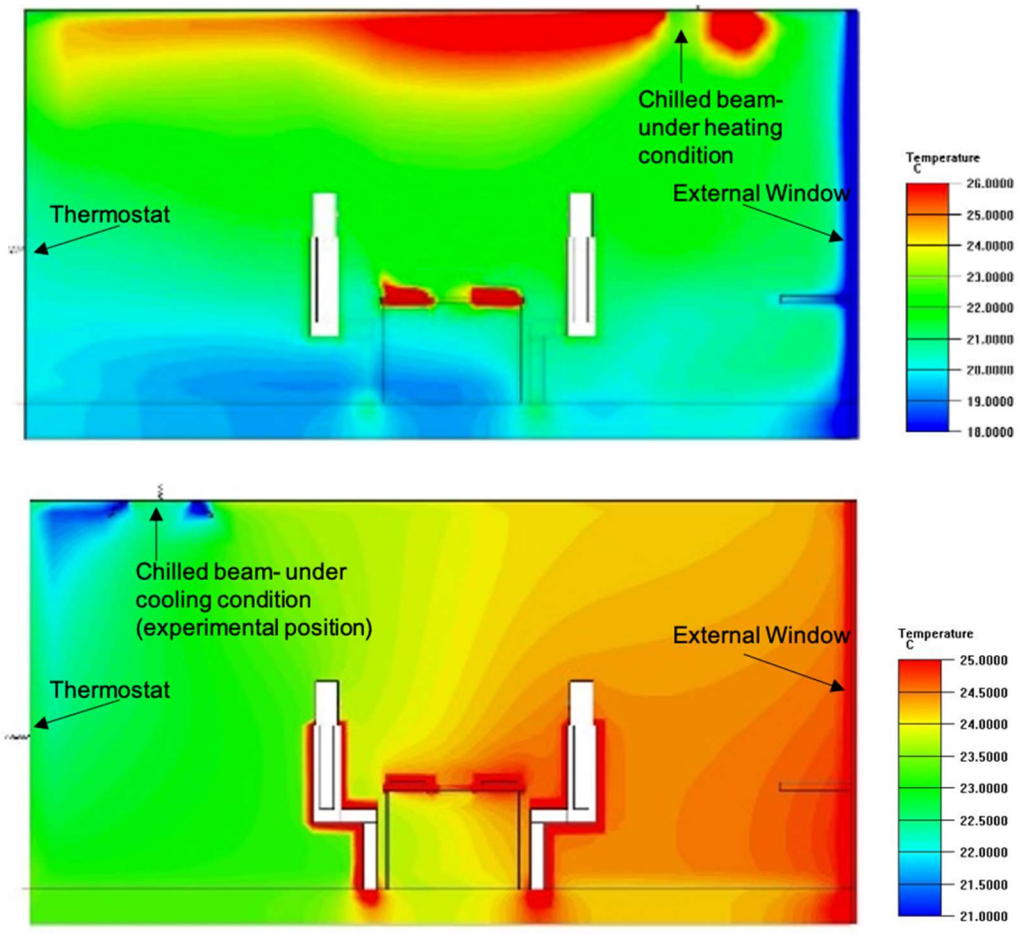

Figure 78: Temperature contours realized on plane 1 for external conditions as in Table 2-Simulation 6 showcasing the high temperature stratification in a conference room. The top figure shows the chilled beam heating condition (actual chilled beam location as in the Andover room) and the bottom figure shows chilled beam cooling condition (with experimental chilled beam location, keeping the chilled beam closer to the thermostat and humans)

For typical conference rooms with external windows (such as the one in the study), the thermostat is mounted on a wall away from the external window. CFD simulations were performed for such a conference room to understand the temperature difference created between the temperatures measured by the thermostat and that near the humans. The results are presented in Figure 79. These are results from CFD simulations, most of which are validated with the experimental data points captured. As can be seen in Figure 79, the temperature difference can go as high as 3°C (even in the most ideal and controlled circumstances- will only increase with an increase in uncertainties of operating conditions) which would mislead the control systems and conditioning of the space. The harder part is that this is not uniform throughout the occupied space. It varies as you move from the external window to spaces away from it. Hence, studies were performed to identify a better location to place the thermostat temperature sensor in the room.

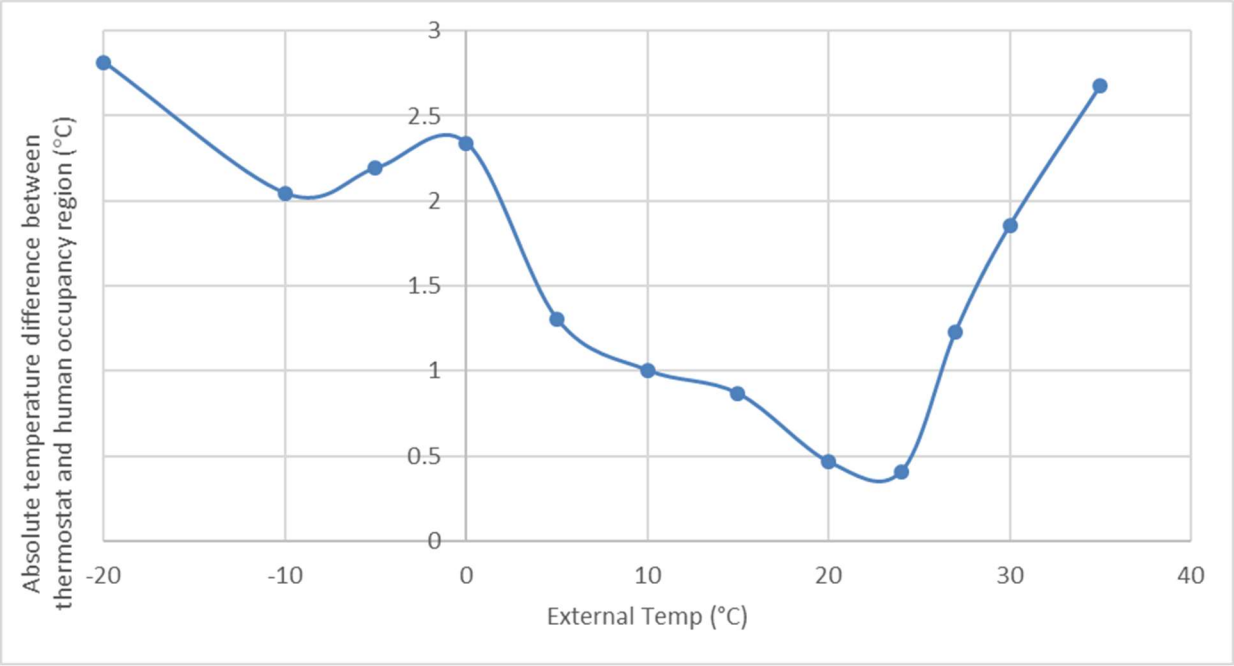

Figure 79: A plot of the temperature difference between the air near the humans and air around the thermostat

An approximate PMV calculation of the occupancy region in the Andover conference room was performed using the post-processed CFD results. The case considered was simulation 5 from Table-1, whose PMV contours using the thermostat (which was located on the wall opposite to the external window) as the controlling temperature setpoint was plotted in Figure 77 (b). The alternate position considered for controlling the comfort setpoint was the temperature measured above the central table in the middle of the room and this scenario was simulated using CFD. This position was the first logical alternate choice as it is close to the actual human occupancy region and is in the middle of the room. PMV values were considered at three different locations of varying heights (0.3m, 0.6m, 1m) for each

human model and then averaged to get the overall average occupancy PMV. The post-processed CFD showed a value of 1.8 for the case with the thermostat as the regulating temperature setpoint. The same with temperature over the center table resulted in an average occupancy PMV of 1.1. It is a simple conclusion that a thermostat placed over the table in the middle of the room caters to better thermal comfort than that which is placed on the wall opposite the external window. This indicates the poor positioning of the thermostat and a simple alternate option that improves the measurements and monitoring of the occupancy thermal comfort. Apart from air temperature, capturing more inputs for thermal comfort (like solar radiation intensity, humidity, etc) in the middle of the room over the table would further reduce the average occupancy PMV to within ideal conditions. The experiments discussed in the next sections provide further understanding on this subject.

4.2.5 Experimental investigation

CFD simulations detailed in the previous sections were used to understand the air and heat flows in the room. To understand the dependency of temperature measurement at various locations with temperature experienced by humans, experiments were conducted in two different workspaces. One of the workspaces was extremely controlled while the other one was uncontrolled with the HVAC system working with pre-determined controls and setpoints. The experiments were aimed at collecting data and analyze the correlation factors between different variables. R^2 values for appropriate variables were calculated and plotted. The various sensors used and their locations are detailed in Table 3.

Occupants in the experimental rooms were replicated using cardboard boxes 1.3 ft (0.4m) long, 1.2 ft (0.35m) wide, and 3.6 ft (1.1m) high [202]. They were heated by three 25 W lightbulbs. Two thermocouples were attached to each of the boxes, two on opposite sides. One is placed at a height of 0.8m from the base and the other at a height of 0.2m. Additionally, thermocouples were also placed on the external window and the four walls, measuring the surface temperatures. There were air temperature measurement thermocouples near the window and thermostat. The sensors near the external window were placed around 1 inch away from the glass surface and facing the glass, measuring the air temperature right adjacent to the glass. Solar irradiance was also measured for calculating heat loads through the external window. This is a common setup for both the experimental workspaces.

Sl. No	Location	Parameter Measured	Sensor Used
1	External Window	Temperature, Relative Humidity	Onset UX100-003
2	Ambient space near humans	Temperature, Relative Humidity	Onset UX100-003
3	External Window	Solar Irradiation	Onset S-LIB-M003
4	Walls, Ceiling, Floor	Surface Temperature	Onset UX120-006M
5	Human Model*	Surface Temperature	Onset UX120-006M

* Temperature was measured at four different positions of the human model: two on the side facing the external window and two away from it, at a height of 0.3 m and 0.6 meters from ground level.

Table 21: Sensor placements and models for thermostat experiments

The following list summarizes the nomenclature used for the plots in the upcoming sections for ease of identification and processing.

- Br: Bright side of the human model facing the external window
- Da: Dark side of the human model facing away from the external window
- surf: Surface measurement
- top: top sensor on the human model, at a height of 0.6 meters from the floor
- bot: bottom sensor on the human model, at a height of 0.3 meters from the floor
- A, B, C, D: Four designated walls of experimental workspace
- R sq: R^2 value for the correlation between variables indicated

4.2.5.1 Experiments in Workspace-1

The first workspace is a single-bedroom of an MIT graduate dormitory (Tang Hall) in Cambridge, USA. The room was 4.5m long, 2.8m wide, and 2.6m high, with an external single-pane clear window facing the North-East direction. The window is 2.8m wide and 1.5m tall. During the period of experimentation, semi-controlled conditions were maintained in the room with minimal human intervention. The vents from the heating system were closed to ensure no mechanical heating. There was no mechanical cooling system in place. Leakages were identified using a smoke pencil and blocked. The operable window was closed and the external glass window was the only source of external heat loads for the room. The drapes on the window were pushed to the corners to ensure maximum possible solar gain through the windows. Near-adiabatic conditions were maintained on the other three sides with walls. One human model was set up in the room, as shown in Figure 80. This model was placed 0.5 m away from the external window. The experiments lasted for five days, during which the whole setup was undisturbed and no occupants were allowed inside the room.

Figure 80: Workspace 1- A complete view of the room from near the door; also shown is a thermocouple sensor near the thermostat position on the wall to the right

It was observed that even with such controlled conditions that this experiment was performed, there is a 4 °C difference in air temperature between the external window and thermostat, and this temperature difference increases to 8 °C when you include the air temperature around the human model. These observations agree with the results from the CFD simulations shown in the previous section about horizontal temperature stratification. It was also observed that the variation of temperature near the thermostat region is quite moderate as it is at a significant distance away from the external window. However, the variation of human model temperature which is closer to the external window is much higher than the thermostat. Figure 81 shows the plots of difference in temperature measured at the human dummy to the temperatures measured at thermostat, window, and an average value of the thermostat and window.

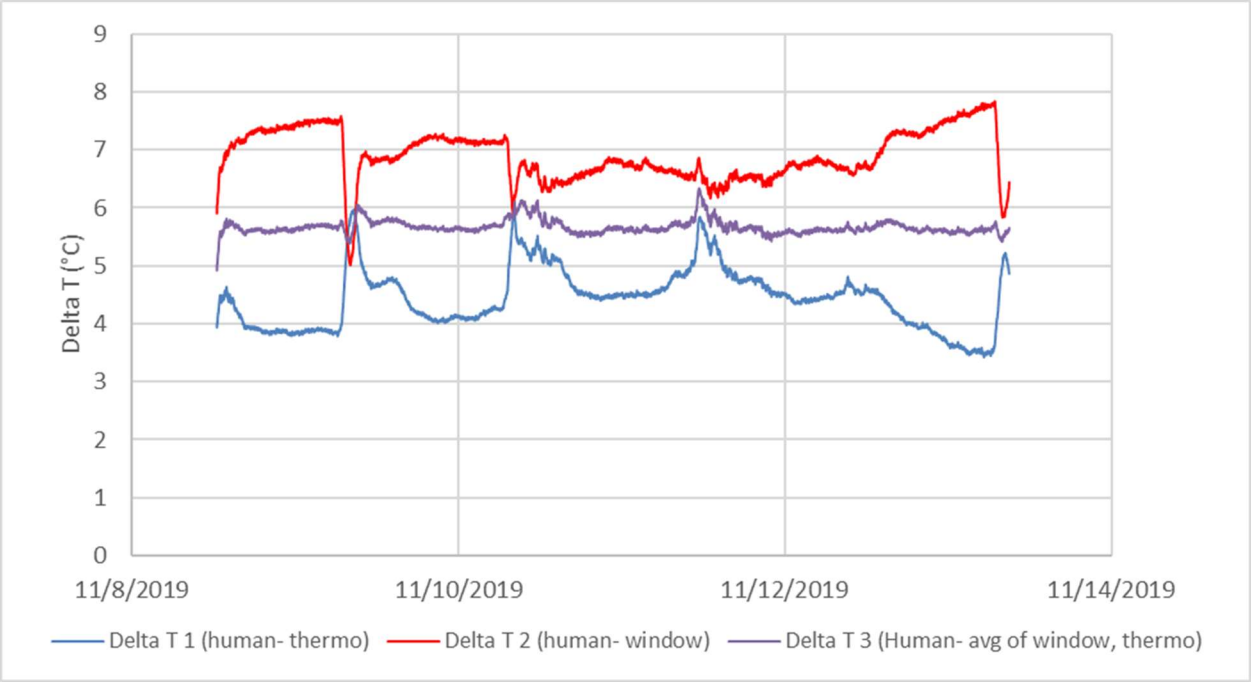

Figure 81: Difference between the temperature measured at the human dummy and that measured at thermostat (Delta T 1), between the dummy and window (Delta T 2), and between the dummy and the average of temperatures measured at window & thermostat (Delta T 3), plotted against time

It is observed from Figure 81 that both the absolute difference (up to 6 °C) and the fluctuation in the difference (up to 2.5 °C) are quite large. Overall, the R-squared value of the linear regression between the human model temperature and thermostat temperature is 0.79, and between the human model temperature and external window temperature is 0.98. Broken down by day and shown in Table 4, it can be inferred that the correlation factor of the human model temperature is better with the external window as compared to the thermostat. This is observed to be especially true on days with a higher variation in external temperatures (days 2 and 6). This clearly shows that although the thermostat temperature is closer in value to the human model temperature, the variation of the human temperature with time is better captured by the variation of temperature near the external window.

Taking both the above parameters as crucial inputs into human thermal comfort, a simple mean temperature of those measured at the thermostat and window was calculated and compared to the temperature measured at the human dummy (Delta T 3). This is plotted in Figure 81. It can be clearly observed that even with a simple average of the two temperatures, the variation in Delta T 3 is less than 1 °C as against almost 2.5 °C in Delta T 1. The variation observed in various individual thermostats placed around the human occupancy region (not plotted) is only around 1 °C, primarily affected by the air flows and distance to the external window. Hence, the average of these temperatures is an appropriate measure for comparison with the thermostat temperature measurement. A more sophisticated model than a simple average of the two temperatures would result in a better prediction for personalized human-experienced thermal comfort.

Day of experiment	R^2 value between temperature on human surface and temperature near thermostat	R^2 value between temperature on human surface and temperature near external window
1	0.96	0.97
2	0.72	0.97
3	0.77	0.99
4	0.89	0.99
5	0.87	0.96
6	0.54	0.98

Table 22: Day-by-day comparison of R-squared values between temperature on human surface and temperature recorded near the thermostat vs window adjacent air temperature

4.2.5.2 Experiments in Workspace-2

The second workspace in study is a large research office-space (MIT Building Technology Student Lab) in Cambridge, USA. The reason for this choice of academic workspace along with the previously experimented office conference space is its unique characteristic to be occupied almost completely throughout the day. Most office conference spaces are typically occupied during regular work hours between 9 am- 4 pm and occupancy is typically constrained. However, an academic workspace has students and researchers working at different times during the day. It is also observed that there is minimal to average occupancy even during the weekends and holiday seasons. In addition, the occupancy of academic workspaces seldom remains the same for a long period. They are observed to have more flux in the occupancy numbers. Hence, academic workspaces present a unique problem of maintaining thermally comfortable conditions under varying external and internal conditions.

A zone of the workspace under consideration is about 10m long, 8m wide, and 4m high. It has three large single-pane clear external windows facing North-East direction. As against workspace-1, this workspace has extremely uncontrolled boundary conditions- it has an operational HVAC with localized controls, the space is open to human movements (the room has an occupant capacity of about 20) and a large number of heat sources in the space (computers, lights, occupants, etc., as seen in Figure 82). The radiators are located right adjacent to the external windows and fan coil boxes over the occupancy spaces at a height of about 3m. For this workspace, a total of two human models were set up- at a distance of 1m and 5m from the external windows. The thermostat is located about 5.5m away from the external window. This experiment lasted for a total of 6 days in the November months of 2019. The weather in Cambridge, MA during November is cold and dry, with a maximum outdoor temperature of 11 °C and a mean outdoor temperature of 7 °C. A small section of the radiator vents near the external window was shut off to not let the heat directly affect the thermocouple sensor near the window.

Figure 82: Workspace 2- a laboratory office space with lots of heat sources (computers, occupants, lights) and uncontrolled conditions

It was observed that with uncontrolled experimental conditions, there is a 6 °C difference in temperature between the external window and thermostat and this temperature difference increases up to 10 °C when you include the human model temperature. This result is again in agreement with the results from the CFD simulations shown in the previous section about horizontal temperature stratification. It was also observed that the variation of temperature near the thermostat region is quite moderate as it is at a significant distance away from the external window. However, the variation of human model temperature which is closer to the external window is much higher than the thermostat. Figure 83 shows the plots of difference in temperature measured at the human dummy to the temperatures measured at the thermostat, window, and an average value of the thermostat and window.

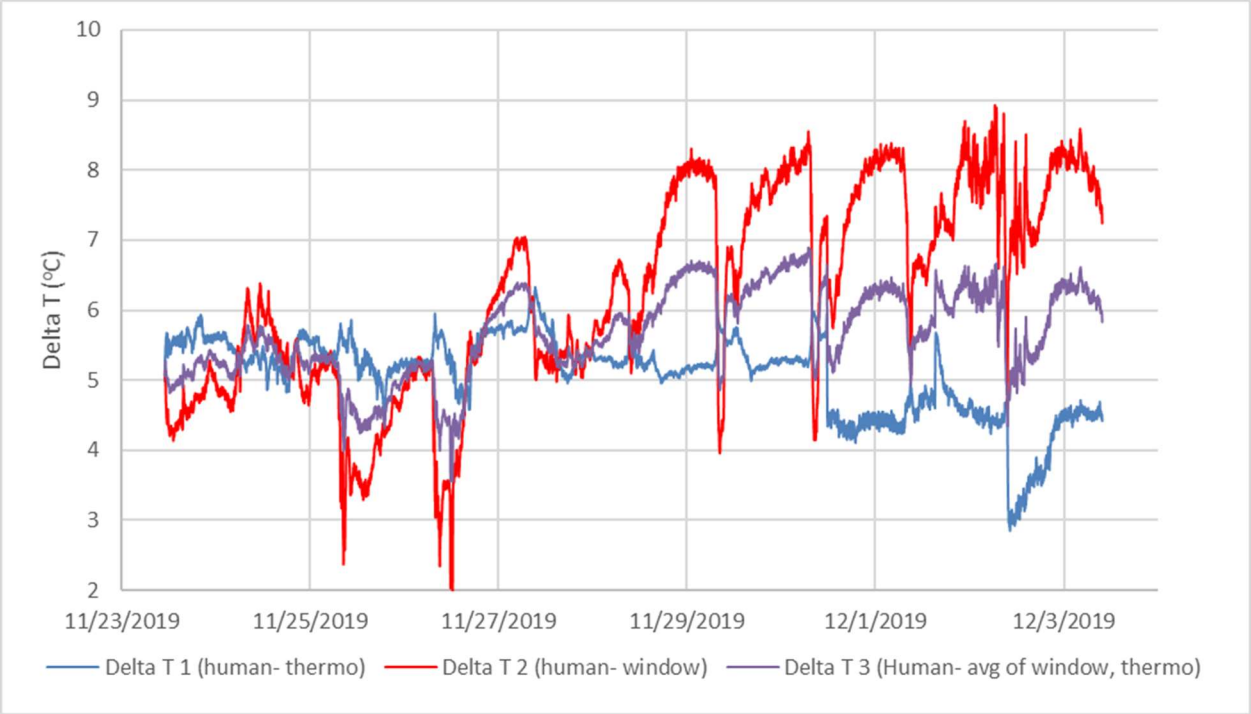

Figure 83: Difference between the temperature measured at the human dummy and that measured at thermostat (Delta T 1), between the dummy and window (Delta T 2), and between the dummy and the average of temperatures measured at window & thermostat (Delta T 3), plotted against time

From Figure 83, it is observed that both the absolute difference between the thermostat and the human dummy (up to 6.3 °C) and the fluctuation in the difference (up to 3.5 °C) is quite large. The R-squared value of the linear regression between the human model temperature and thermostat temperature is 0.49 for the human sitting far from the window, and 0.65 for the human sitting close to the window, likely due to the changes in radiative view factor between the single glazed window and the humans at different locations. The R-squared value of the linear regression between the human model temperature and external window temperature is 0.65 for the human sitting far from the window, and 0.79 for the human sitting near the window. Similar to the observations from workspace-1, the correlation factor between temperatures around the human sitting near the window and that of the external window is always much better than that of the human and thermostat. Broken down by day (not shown), on a day where the external temperature was considerably low with clear and sunny skies (day 5), the correlation factor between the human and thermostat was negative, showcasing the inconsistency in this approach and that the thermostat alone can't satisfy the comfort needs of those occupants near the external window. Although the thermostat temperature is closer in value to the human model temperature as compared to the external window temperature, the variation of the human temperature with time is better captured by the variation of temperature near the external window. Taking both the above parameters as crucial inputs into human thermal comfort, a simple mean temperature of those measured at the thermostat and window was calculated and compared to the temperature measured at the human dummy (Delta T 3). This is plotted in Figure 83. It can be clearly observed that even with a simple average of the two temperatures,

the maximum variation in Delta T 3 is around 2 °C as against 3.5 °C in Delta T 1. A more sophisticated model than a simple average of the two temperatures would result in a better prediction for human-experienced thermal comfort.

	R^2 value between temperature on human surface and temperature near thermostat		R^2 value between temperature on human surface and temperature near external window	
Human surface / Day	Human surface next to window	Human surface away from window	Human surface next to window	Human surface away from window
1	0.76	0.89	0.85	0.89
2	0.43	0.67	0.94	0.83
3	0.65	0.87	0.94	0.87
4	0.38	0.55	0.71	0.69
5	-0.08	0.16	0.65	0.65
6	0.85	0.98	0.96	0.98
7	0.75	0.86	0.80	0.74
8	0.18	0.18	0.75	0.67

Table 23: Day-by-day comparison of R-squared values between temperature on human surface and temperature recorded near the thermostat vs window adjacent air temperature

A meaningful observation from the daily breakdown of R-squared values shown in Table 5 is that even for the human sitting away from the window but closer to the thermostat, the correlation factor is better with an external window than the thermostat. This can be mostly attributed to the fact that the external windows are quite large in workspace-2 and hence there is a larger influence on solar gains on thermal comfort. On a day where the external temperature was considerably low with clear and sunny skies (day 5), the correlation factor between the human and thermostat was negative, showcasing the inconsistency in this approach and. This shows that the thermostat alone can't satisfy the comfort needs of those occupants near the external window. For either of the occupant locations, it can be concluded that measuring the variation of temperature near the external window along with a base thermostat measurement is a better means of predicting and monitoring the variation of thermal comfort for occupants, than a simple thermostat alone. Since the absolute temperature near the window is not so close to the air temperature in the occupancy region, the best course of control for thermal comfort with the present set of sensors is to have two thermocouples- one at the usual thermostat position to measure the mean air temperature of the occupancy region, while at the same time-varying with the variations detected in temperature measured by another sensor placed near the external window. Until a next-generation thermal comfort sensor is designed for practical implementation, this use of two thermocouples for sensing and comfort control seems optimum.

4.2.6 Conclusions

From the experimental results discussed in the previous sections, it was evident that the existing sensor technology and location are not the best means of monitoring human thermal comfort in occupied building spaces. The whole question of what to measure, where to measure it, and with what to measure became extremely important as the work progressed. The temperature difference between measured thermostat readings and the air temperature around the humans is dependent on the outdoor ambient temperature and the resulting temperature stratification in the room and can go to as high as 8 °C even with very controlled conditions. Simply having one thermostat in a location far away from the actual human occupancy region not only comprises of error resulting from the temperature difference between the human occupancy region and the thermostat location region but also integrates the error from not capturing the incoming solar heat loads coming from external windows. This error is realized especially in varying outdoor conditions for occupants sitting near the external window, as shown in the previous sections. CFD results and post-processed PMV values showed that having the thermostat located near the humans in the middle of the room (over a table, in this case) improved the thermal comfort conditions compared to having it on a wall opposite the external window (PMV of 1.1 as compared to 1.8 for an Andover summer scenario, respectively).

Another simple hack suggested through this work and validated with experiments performed in multiple workspaces is to incorporate a second temperature sensor placed near the external window which controls the variation of the temperature setpoint of the thermostat location on a wall far away from the external window but closer to the human occupancy region. This way, the solar loads coming in through the external window are accounted for in providing the variation and distribution of temperature and the mean average temperature is still set around the average room temperature measured by conventional thermostats. Care has to be taken in such dual-sensor modules that the second temperature sensor placed near the external window is not impacted by any heating units placed under the window. In such situations with heating units below the external window, the sensor should be placed at the edge of the window away from the updraft of heaters.

The above-described method provides a good control system to ensure a thermally comfortable workspace. A much more elegant approach is to have a single sensor in the location of the human occupancy region (for instance, on top of the central table in the Andover conference room) which can not only record the ambient air temperature but can also measure the influence of the incoming solar radiation through the external window. Such a sensor is currently unavailable in the market and one such design can greatly help simplify the controlling and monitoring system for HVAC systems to provide a thermally comfortable environment. Current thermostats and other instruments cannot accurately balance solar irradiation with convective heat transfer. A novel instrument beyond those currently available types is needed.

Future work may be performed on optimizing the location of the chilled beam (variables x, L, z and W) used in the simulations for the best comfort conditions around the occupants. Optimization can also be performed on the interior conditions of the room, including the position of the ducts, occupant quantity, and occupant seating for better thermal comfort and energy efficiency. Further optimization is feasible on the angle of incidence of the incoming cool air from the chilled beam falling onto the external window during the summer seasons to reduce the temperature stratification in the room, primarily caused by the

heat loads from the external window. In addition to ensuring more uniform comfort conditions in the room, this will also help in optimizing the energy utilization of the air conditioning system. Owing to time and space availability constraints, experiments on location of thermostat and its implications were only conducted in November. Although the methods presented in this paper can be extrapolated to other seasons and varying external temperatures, and will always be an improvement over existing single-thermostat systems in buildings, further experiments and simulations could be conducted to better optimize and further improve the thermostat location.

5 Health

5.1 Patterns of SARS-CoV-2 Aerosol Spread in Typical Classrooms

This section (5.1) was a combined effort with Gerhard Rencken, Emma Rutherford, Nikhilesh Ghanta, and Leon Glicksman. It was published in Building and Environment in October of 2021 [203].

5.1.1 Abstract

Although current industry guidelines to control the spread of aerosols such as SARS-CoV-2 (COVID-19) have adopted a six-foot (~1.8m) spacing between individuals indoors, recent evidence suggests that longer range spread is also responsible for infections in public spaces. The vehicle for long-range spread is smaller (< 5 μm) droplets or particles, termed bio-aerosols, or aerosols for short, which have a large surface area to volume ratio such that aerodynamic drag is much larger than gravity forces. The aerosols remain suspended in air for extended time periods, and they essentially move with air currents. Prediction of the danger to occupants in a closed room when exposed to an infected individual requires knowledge of the period of exposure and the concentration level of aerosols in the breathing zone of an occupant. To obtain an estimate of the concentration level, a common assumption is well-mixed conditions within an interior space. This is obtained from a mass balance between the level of aerosol produced by an infected individual along with the airflow rate into and out of the entire space. In this work, we use computational fluid dynamics, compared with experimental results in several cases, to explore the aerosol concentration distribution in a typical classroom for several common conditions and compare these results to the well-mixed assumption. We use a tracer gas to approximately simulate the flow and dispersion of the aerosol-air mixture. The two ventilation systems examined, ceiling diffusers and open windows, yield average concentrations at occupant breathing level 50% greater than the well mixed case, and some scenarios yield concentrations that are 150% greater than the well mixed concentration at specific breathing-level locations. Of particular concern are two conditions: horizontal air flow from an open window in line with a row of seating and, second, an infected individual seated near a sealed cold window. For the former, conditions are improved if a baffle is placed inside the open window to direct the air toward the floor, creating a condition similar to displacement ventilation. In the latter, the cold air flowing down along the cold window recirculates aerosols back into the breathing zone. Adding window covers or a portable heater below the window surface will moderate this condition.

5.1.2 Introduction

SARS-CoV-2 (COVID-19) has fundamentally altered many aspects of our daily lives. Despite this impact and the enormity of the research that has gone into prevention strategies, many of the industry guidelines currently in use assume a well-mixed air model [204, 205], which holds that the aerosol concentration is uniform throughout a room volume at a specific moment in time. This assumption has inherent flaws regarding both personal protection and energy consumption. Building on government guidelines and published literature, six-foot (~1.8m) spacing between individuals and the wearing of face masks are now generally accepted practices for reducing transmission rates [206, 207, 208]. However, recent evidence has suggested that longer range spread is responsible for infections in public spaces such as restaurants [209], public transit [210], hotels [211], hospitals [212], multistory buildings [213, 214], and cruise ships [215, 216, 217].

Whereas earlier studies suggested that SARS-CoV-2 spread was due to large drops dispersed within a rough ballistic trajectory of 3 to 6 feet or by surface contamination [218], more recent work has highlighted the vehicle for long-range spread as smaller droplets or particles, termed bio-aerosols, or aerosols for short, which are assumed to remain suspended in air for extended time periods [219, 220, 221, 222]. It is even possible that the aerosols are more infectious than larger particles [223]. The upper limit for the size of these bio-aerosols is 5 μm [224, 225, 218, 226], with a possibility of particles less than 100 to 200 μm becoming aerosols through evaporation [227]. As these aerosols can settle with time, an assumption of the settling velocity can be found from the Stokes equation for the drag between particles and surrounding air [228], assuming a spherical shape and density of liquid water. The Stokes equation suggests that the relative velocity between the particle and the surrounding air is less than 10^{-3} m/s, or rather, that the bio-aerosols follow the trajectory of the room air currents. Such concerns are not new [229, 230] and serve to raise questions about understanding the efficacy of ventilation systems [231, 232, 219, 233, 234].

In order to establish proper safety guidelines for interior spaces, it is important to predict the danger to occupants when exposed to an infected individual. This requires a knowledge of the period of exposure and the concentration level of aerosols in the breathing zone of an occupant. Some investigators combine this knowledge with the Wells-Riley equation [235, 236, 237] to predict the conditional probability of infection [238, 235, 207, 239]. To obtain an estimate of the concentration level, a common assumption is well-mixed conditions within an interior space [240, 236]. Given the level of aerosol produced by an infected individual along with the heating, ventilation and air conditioning (HVAC) flow rate and room geometry, a simple mass balance will yield the time resolved concentration level within the space. While the well-mixed values can lend valuable information regarding the air change rate necessary to ventilate a space, we have reason to believe that room specific conditions such as ventilation type and the locations of individuals can have large effects on the distribution of aerosol in the room.

There are several documented cases of infections of individuals seated far from the original source. The new infections are postulated to be caused by aerosol concentrations around the infected individuals well above the average for the entire room [210, 214]. Li documents the probable aerosol transmission of CoV-2 across the width of a crowded restaurant in Guangzhou due to the draft from a wall air conditioner [209, 241]. Kwon [242] presents evidence of the transmission of SARS-CoV2 across the width of a South Korean restaurant where an individual was infected from approximately 6.5 m away. Subsequent measurements of the air flow in the restaurant revealed a horizontal air stream originating from a ceiling diffuser, moving down a wall, and then being deflected by a table to form a horizontal flow with a velocity of about 1 m/s. The air stream passed close to an infected customer seated near the wall and then across the room to a second customer, who became infected. Due to this evidence of location dependent infection, we analyze both the well-mixed concentrations as well as the situation-specific hotspots of high aerosol concentration.

The challenge arises to characterize aerosol dispersion patterns for several typical interior spaces under different operating conditions. When is the well-mixed assumption valid? Under what conditions are occupants potentially exposed to unsafe high concentration and where are the unsafe locations? This, in turn, requires a generalized understanding of air flow patterns which is lacking in the current literature.

In the past, detailed studies of airflow behavior in interior spaces have been carried out, both experimentally [243] and computationally [244], to characterize natural ventilation patterns. People at rest generate about 75 watts, heating the surrounding air and creating rising plumes of warm air [111]. These plumes have a typical velocity on the order of 0.1 to 0.3 m/s. As they rise, they entrain cooler surrounding air and continue up until they encounter a layer of air at the same temperature. At this layer, the plumes will dissipate and mix with the surrounding air [245, 246]. Walls and floors heated by solar gains can also warm nearby air to create positively buoyant flows while cold windows create downflowing cold films with negative buoyancy. These buoyant flows, created by heat fluxes into and out of the room, interact with airflow from windows, vents, HVAC supply ducts, diffusers, and other heated and cooled objects in the room.

HVAC systems are designed to limit the internal air velocity around humans to reduce discomfort due to draft. Discomfort is observed generally when the air velocity reaches the range of 0.3 m/s and above [111]. Therefore, the thermal plumes and mechanical air flows have velocities that are of the same order of magnitude and together dictate the overall air flow pattern in interior spaces. The only exception is air flow from windows under high wind conditions and possibly flow created by ceiling fans that can dominate the internal flow behavior. Results from natural ventilation studies have revealed a complex pattern of air flow in buildings. In some cases, a thick heated layer of air is present below the ceiling. In others, there are downward flowing streamlines of cooler air or a series of large swirling vortices [244].

There is a dearth of systematic studies of aerosol distribution in common interior spaces, other than a limited number for spaces such as small offices [247], hospitals [248], and aircraft cabins [249]. Two recent studies have addressed safe ventilation in classrooms [250] and outdoor dining [251]. In the former, the use of ventilation from an open window above the breathing level in a typical New York classroom creates a safer condition. To broaden our understanding, we have carried out a detailed study of aerosol concentration patterns in a common space: a classroom with and without an operable exterior window supplemented by a study of streamline flow patterns in a conference room.

Our goal is to find the spatial concentration distribution produced by an infected individual under several different operating and seasonal conditions. Attention will be focused on the aerosol concentration other classroom occupants breathe. We use a tracer gas to approximately simulate the flow and dispersion of the aerosol-air mixture. The simulations assume steady state conditions. At air change rates of 4 to 6 air changes per hour, conditions are close to steady-state within one half of a normal hour-long session. We will assume that the tracer concentration levels will scale linearly with the source concentration and the tracer/aerosol moves and diffuses with the surrounding gas flow patterns. To answer the question regarding the accuracy of the well mixed assumption, the local concentration at the breathing level of the occupants will be scaled to the steady state well mixed value.

5.1.3 Computational Fluid Dynamics

Governing Equations

To computationally estimate the airflow within the space, computational fluid dynamics (CFD) was used. ANSYS Fluent software was used to simulate both airflow patterns and aerosol concentration in the conference room and classroom defined below. A steady state solver, the Reynolds Average Navier Stokes (RANS) with pseudo-transient effect was used to solve for the airflow pattern [148].

A single-phase flow with mass and momentum conservation was selected, coupled with the k-epsilon turbulence model with enhanced near-wall function to solve the effects of turbulence. No-slip boundary conditions were placed on all walls. The Species Transport model was used to solve for the differing mass concentration of different gaseous species in the space, and the Surface-to-Surface Radiation model with diffuse surfaces was used to calculate the radiation heat transfer component.

The mass conservation equation is given by:

$$\frac{\partial \rho}{\partial t} + \nabla \cdot (\rho \vec{v}) = S_m \qquad (61)$$

The right-hand term is the mass added to the continuous phase from the dispersed second phase (such as user-defined mass sources).

The solver solves the energy equation in the form below:

$$\frac{\partial}{\partial t}(\rho E) + \nabla \cdot \left(\vec{v}(\rho E + p)\right) = \nabla \cdot \left(k_{eff} \nabla T - \sum_i h_i \overrightarrow{J_i} + \left(\bar{\bar{\tau}}_{eff} \cdot \vec{v}\right)\right) + S_h \qquad (62)$$

Where k_{eff} is the effective conductivity, $\overrightarrow{J_i}$ is the diffusion flux of species i, Y_i is the mass fraction of species i, and

$$E = h - \frac{p}{\rho} + \frac{v2}{2} \qquad (63)$$

$$h = \sum_i Y_i h_i + \frac{p}{\rho} \qquad (64)$$

The momentum conservation equation is solved in the following form:

$$\frac{\partial}{\partial t}(\rho \vec{v}) + \nabla \cdot (\rho \vec{v} \vec{v}) = -\nabla p + \nabla \cdot (\bar{\bar{\tau}}) + \rho \vec{g} + \vec{F} \qquad (65)$$

$$\bar{\bar{\tau}} = \mu \left((\nabla \vec{v} + \nabla \vec{v}^T) - \frac{2}{3} \nabla \cdot \vec{v} I \right) \qquad (66)$$

Where: p is the static pressure, $\bar{\bar{\tau}}$ the stress tensor, $\rho \vec{g}$ the gravitational body force, $\vec{F}$ the external body force, μ the molecular viscosity, I the unit tensor, and $\nabla \vec{v}^T$ the effect of volume dilation.

To predict the aerosol concentration at different locations in the classroom, we make use of the species transport model, that predicts the local mass fraction of each species Y_i by obtaining the solution of a convection-diffusion equation for the i[th] species. This equation is given, in the general form, as:

$$\frac{\partial}{\partial t}(\rho Y_i) + \nabla \cdot (\rho \vec{v} Y_i) = -\nabla \cdot \vec{J}_i + S_i \qquad (67)$$

Where S_i is the rate of generation of a species at user-defined sources (diffuser inlets, windows and mouths).

This equation is solved n-1 times, where n is the total number of species. Since the mass fractions sum to unity, the final species is calculated by finding the remaining mass fraction that has not yet been solved for. To reduce numerical error, the species with the highest mass fraction is selected as the last species (in our case nitrogen).

In turbulent conditions the mass diffusion, $\vec{J}_i$, is computed as follows:

$$\vec{J}_i = -\left(\rho D_{i,m} + \frac{\mu_t}{Sc_t}\right)\nabla Y_i - D_{T,i}\frac{\nabla T}{T} \qquad (68)$$

Where Sc_t is the turbulent Schmidt number ($\frac{\mu_t}{\rho D_t}$ where μ_t is the turbulent viscosity and D_t is the turbulent diffusivity).

To model the effects of turbulence in the simulation, we utilize the standard k-epsilon model. This two-equation model allows the solver to compute for both a turbulent length as well as time scale. The equations provide a reasonably robust and economic accuracy for a variety of turbulent flows.

The Surface-to-Surface (S2S) model was used to account for the radiative heat transfer between surfaces in the room. This model takes into consideration the size, separation distance, and orientation of surfaces, through a calculated view factor. All surfaces are assumed to be diffuse emitters and reflectors by use of radiosity.

5.1.4 Geometry

Our base classroom geometry was abstracted from a classroom at MIT which is 12 meters long, 6 meters wide, and 3.5 meters tall, as shown in Figure 84. Under the assumption that precautions for safety during COVID-19 would be considered when setting up a classroom, we placed ten students into two rows, all at least six feet apart (~1.8m). In some simulations, we considered a large single glazed window behind the back row of students, in others, open windows on one end wall.

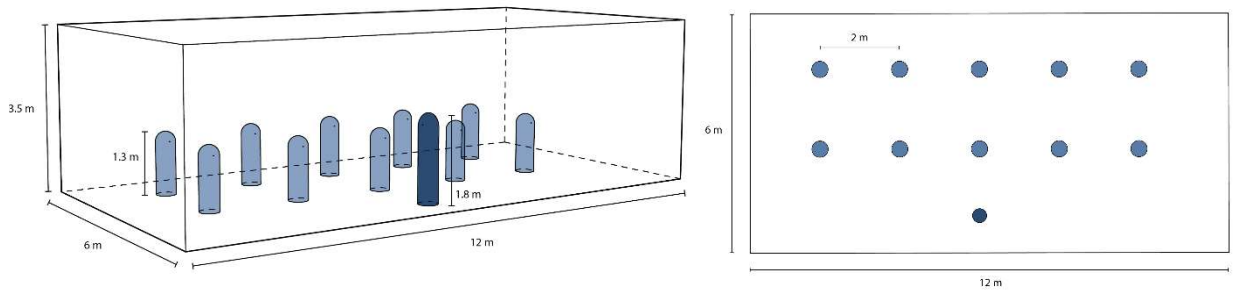

Figure 84: Classroom geometry for simulations. People are modelled by 1.3 m tall cylinders with hemispheres on top. They are placed in two rows so that all students are six feet apart.

We used a simplified human geometry of a cylinder with a half sphere on top due to this form's accuracy in modeling plumes, as shown in section 2.5. Students were modeled to be seated at a height of 1.3 meters with a standing teacher at the front of the classroom at a height of 1.8 meters. The students had a surface area of 1.7 m^2 and the teacher a surface area of 1.9 m^2. Each person has a circular mouth of variable area based on the exhalation velocity in order to maintain a constant air exhalation rate of 0.42 m^3/hour.

5.1.4.1 Boundary Conditions

All walls, the floor, and the ceiling were assumed to be adiabatic unless otherwise stated. The humans were given a heat transfer rate of 44 Watts/m^2 (convection plus radiation) which provides 75 Watts from each student, a typical heat generation rate for a resting person, and 84 Watts from the teacher, corresponding to a standing, more active person.

To track the mixture of aerosols and air exhaled by an "infected" individual, we chose to use carbon monoxide (CO) as a tracer gas due to its similar density and viscosity to air. It has been shown that tracer gases are accurate as a substitute for simulating individual particles since aerodynamic drag is much larger than gravity forces, making them behave similarly to a gas. One main difference between gas and particle simulations is that deposition of droplets on surfaces is not present when using a tracer gas. However, for particles between 200 nm and 1 µm in diameter, deposition is minimal [252, 213]. Another difference between particle and gas models is that gas models neglect evaporation. Experimental analysis of exhaled aerosols by Morawska et al showed that non-equilibrium particle evaporation was not detectable for aerosols between 0.5 and 20 µm in diameter [234]. Thus, evaporation was neglected in our models. Further, the similarity of results between particle simulations and tracer gas simulations has been confirmed experimentally and computationally through many studies [213, 252]. We also ran our own confirmation test by comparing a simulation using discrete water droplet particles the size of aerosols with a simulation using carbon monoxide as a tracer gas.

In our tracer gas simulations, as shown throughout the paper, each mouth was simulated as a constant velocity source of either 0.35 m/s or 1.0 m/s normal to the surface, resulting in a mass flow rate of 0.42 m^3/hour, which corresponds to an average human exhalation rate. The infected individual's exhaled air was 100% CO and the uninfected individuals' exhaled air was 16% oxygen (O_2), 4% carbon dioxide (CO_2), and 80% nitrogen (N_2). This enabled us to visualize the possible spread of virus-infected

aerosols throughout the room and measure the concentrations at various locations to compare between models. Previous studies have shown that droplets measured around a human model were similar whether or not normal inhales and exhales were modeled, so we neglected to model inhales but made sure to have the proper amount of air exiting the mouth to correspond to normal breathing [253]. The temperature of the exhaled air is set at human body temperature of 310 K.

The results of our comparative study are shown in Figure 85. For the comparative particle simulation, 40 droplets with diameters distributed between 0.5 and 5 μm with a mean of 1 μm were placed at the face of the mouth with air being exhaled at 1 m/s from the mouth surface to carry the particles. This case is a natural ventilation case with air entering at 1 m/s through the two bottom windows at the left of the room, and the windows are in line with the rows of students. Two upper windows act as a pressure outlet. The geometry of this simulation and boundary conditions of the people are the same as the rest of our simulations and the setup is the same as Simulation A. The paths taken by the gas and particles were very similar, and the locations of high density of particles also resembled the areas of high CO mass fraction in the air. The velocities of the particles and the gas clouds were also very similar. Thus, we elected to use a tracer gas in order to reduce computational complexity and allow us to examine numerous scenarios quickly.

(a)

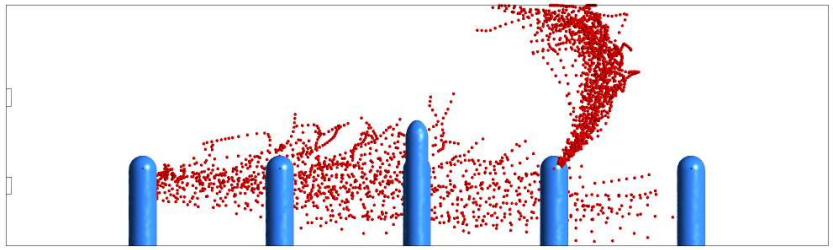

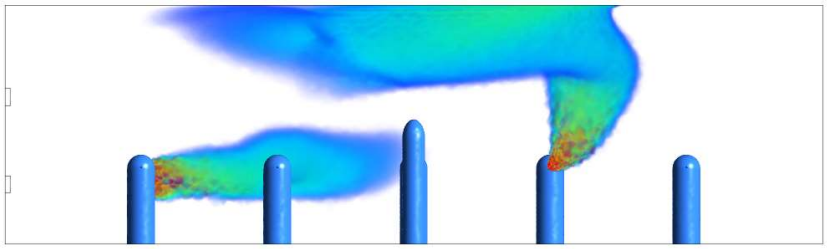

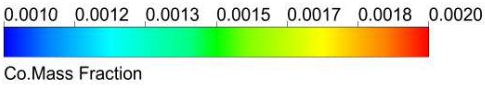

(b)

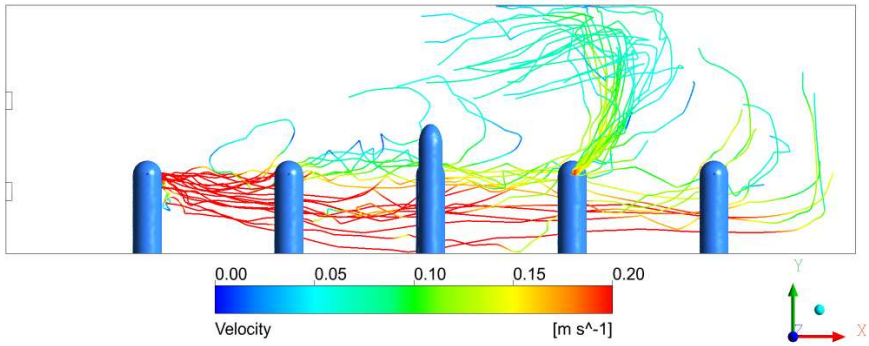

(c)

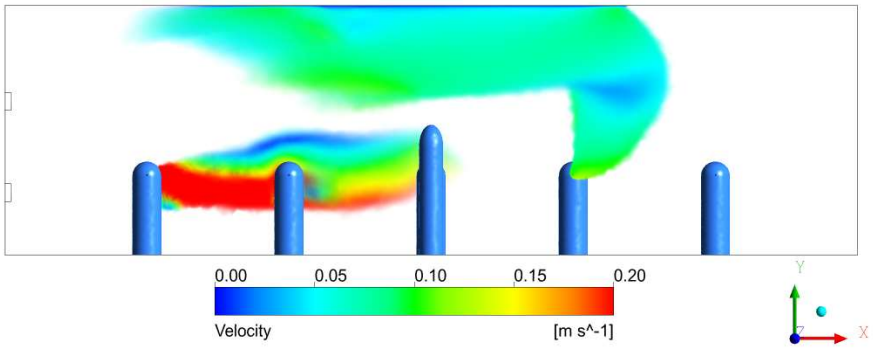

(d)

Figure 85: Visual comparison between discrete particle simulation and tracer gas simulation. (a) Paths of water droplets with diameters between 0.5 and 5 μm and turbulent dispersion modelled by discrete random walks. (b) Volume rendering of CO mass fraction with transparent being 0.0010 and below, which is approximately twice the well-mixed concentration of CO in the room, and red being 0.0020 and above, which is approximately four times the well-mixed concentration. (c) Paths of water droplet particles with color showing velocity of the particles on a scale from 0 m/s to 0.2 m/s. (d) Same volume rendering of CO as in (b) except colored to show velocity of the gas on the same scale as (c).

In this paper, we look at various combinations of ventilation methods and room conditions, including HVAC through ceiling diffusers, opening windows and doors, and non-adiabatic closed windows with temperature differences across them. It is assumed that all supply air does not contain any infected aerosols. In some simulations, a negative or positive heat flux is introduced to the rear wall of the classroom to model a single-glazed window during either hot or cold seasonal conditions. In natural ventilation simulations, windows are introduced on the left (-X direction) wall, which are modeled by rectangular cutouts on the left wall.

5.1.4.2 Meshing and Grid Independence Test

The space in the classroom is divided into small tetrahedral mesh elements, for each of which the air parameters are calculated by the solver. The mesh size is varied throughout the space, to ensure that smaller detail can be captured in areas where it is important. The mesh along the walls, human surfaces, mouth area and inlet surfaces is refined as is visualized in Figure 86, resulting in an average Y-plus value of 4.1 at the surface of the people. The size of the mesh elements was determined by running a grid independence test. The number of mesh elements was increased by a factor of two until the patterns of the air paths and the tracer gas concentrations converged within a 10% error bound.

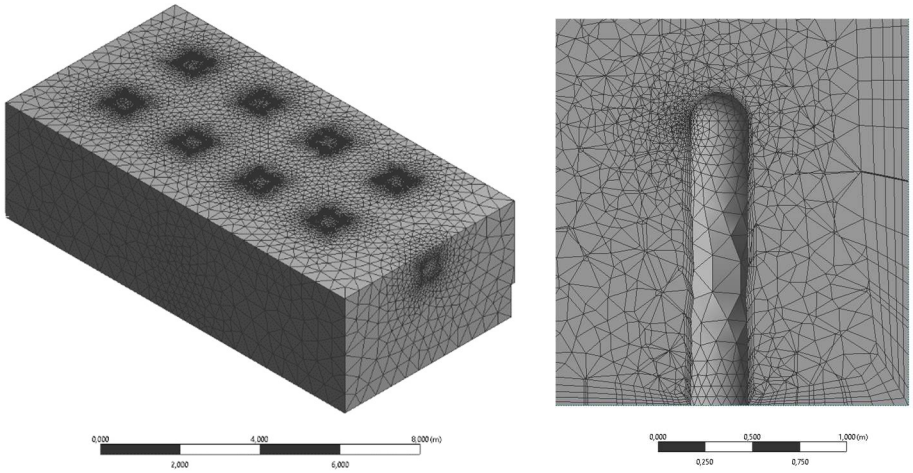

(a) (b)

Figure 86: Visualization of meshing for all simulations. (a) View of classroom from outside. Smaller mesh elements can be seen around the HVAC diffusers and return vent. (b) Slice to view mesh around human model.

5.1.4.3 Experimental Confirmation

To verify that the models and boundary conditions used in the CFD simulations resembled the real world, a case of a single person in a room and a case of people in a conference room with experimental results were considered.

In the single person room case, the goal was to verify the plumes created by the boundary conditions of our human models. Our sitting human model of a cylinder with a half sphere on top is positioned alone in a cylindrically shaped room. Due to symmetry along the X and Z planes through the center of the room, only a quarter of the room was simulated. The ceiling of the room was held at a constant 295.5 K and the floor at 293 K. The curved outer wall had a negative heat flux of -1.286 W/m^2.

The human model was given a heat flux of 44 W/m^2, as is used in all of our simulations. The results were compared to experimental measurements for a very similar real-life case [254] and are illustrated in Figure 87. The close agreement between the plume velocity at different distances above the head and the vertical temperature distribution in the room help to establish confidence in the computational results.

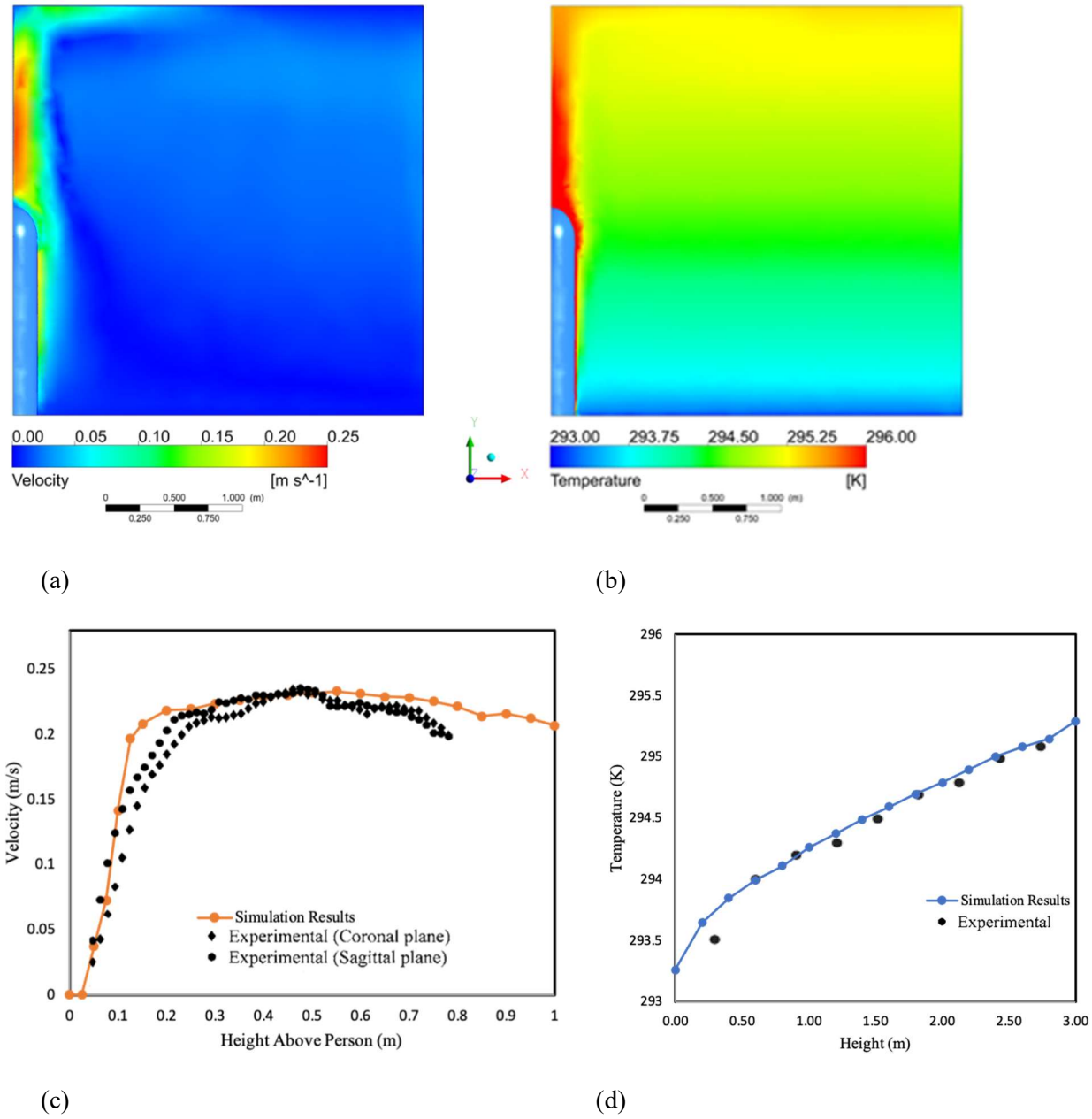

Figure 87: Experimental Confirmation of CFD Accuracy through comparison of plume rise velocity and temperature data from an experiment with single human subject with the results of our simulation modelling the same situation. Simulation results of (a) velocity distribution and (b) temperature distribution. Graphs of (c) plume velocity vs height compared with experimental data [111] above the head of a person and (d) temperature versus the height above the floor in the room, measured a meter away from the person.

A related study of air flow patterns in a conference room near MIT provides further confirmation of the accuracy of the CFD model used. The room studied in this related experiment had seating for six

around a central table, a chilled beam conditioning system, a larger double-glazed window, and exhaust through the doorway. Both the conference room [201] and classroom studies were modeled in Ansys Fluent with similar boundary conditions to the ones we used. Experimental measurements of the conference room were able to be taken to gain confidence in the results. Near the doorway the experimental velocity varied by as much as 0.5 m/s from floor to ceiling. The simulated velocity values at this location agreed with the experimental ones within six percent on average, while the simulated vertical temperature profile agreed within 0.5 °K with measurements.

5.1.5 Results

5.1.5.1 Effects of Exhale Speed on Direction of Expelled Aerosols and Importance of Masks

When researching the spread of virus containing aerosols in an indoor environment, the importance of human plumes is often understated. We argue, however, that warm air plumes drastically affect the movement of air in rooms with stationary people. Exhaled air is immediately affected by the warm air plume rising around a human, and the speed of the exhalation determines whether or not the aerosols within a breath rise with the plume towards the ceiling or escape the plume and follow other air currents in the room. We assume in our simulations that air leaves the mouth horizontally at human body temperature with a mass flow rate comparable to that of a resting person (0.42 m^3/hour). While this mass flow rate is always maintained with normal breathing, the horizontal velocity of the infected air escaping from the mouth can vary greatly depending on the presence and fit of masks. The size of the mouth opening on the human models was adjusted as velocity of exhaled breath changed in order to maintain this mass flow rate.

Without masks, human exhales have an initial velocity of around 1 m/s [255]. However, stronger exhales can have an initial velocity around 2 m/s, and talking or coughing can result in even faster speeds. When individuals are wearing a mask, air escapes mainly around the sides and out the top. Thus, an exhale speed of 0.35 m/s was chosen to represent a poorly fitted mask case. We argue that exhale speed has a large impact on spread of aerosols throughout the room since air that remains close to the body for extended periods rises relatively quickly with the human plume to the ceiling, whereas air that escapes the plume remains at breathing level for much longer and is likely to be pulled by other air currents in the room.

To examine the effects a mask might have in diverting infected air away from other individuals, a simulation involving discrete water droplets of varying initial velocities was run. It is assumed that mass flow rate across the mouth, corresponding to the amount of exhaled air, remains constant with and without a mask. In this setup, there is a single individual in a room, without any flow generated by the HVAC system. To reach steady state, the ceiling, floor, and walls in front of and behind the manikin have a negative heat flux of 2.1 W/m^2 such that the total heat generated by the human is removed by the walls. The side wall act as a pressure boundary condition at gauge pressure, allowing air to pass out of the room. Backflow is allowed across these walls at 295 K. Discrete water droplets with a range of diameters from 0.5 µm to 5 µm with an average diameter of 1 µm were injected into the room from the mouth so that they could be carried by exhaled air of varying speeds. Figure 88 shows three paths of water droplets with exhale speeds of 0.35 m/s, 1.0 m/s, and 2.0 m/s, colored by velocity as they leave the mouth and rise, along with the temperature profile for each case.

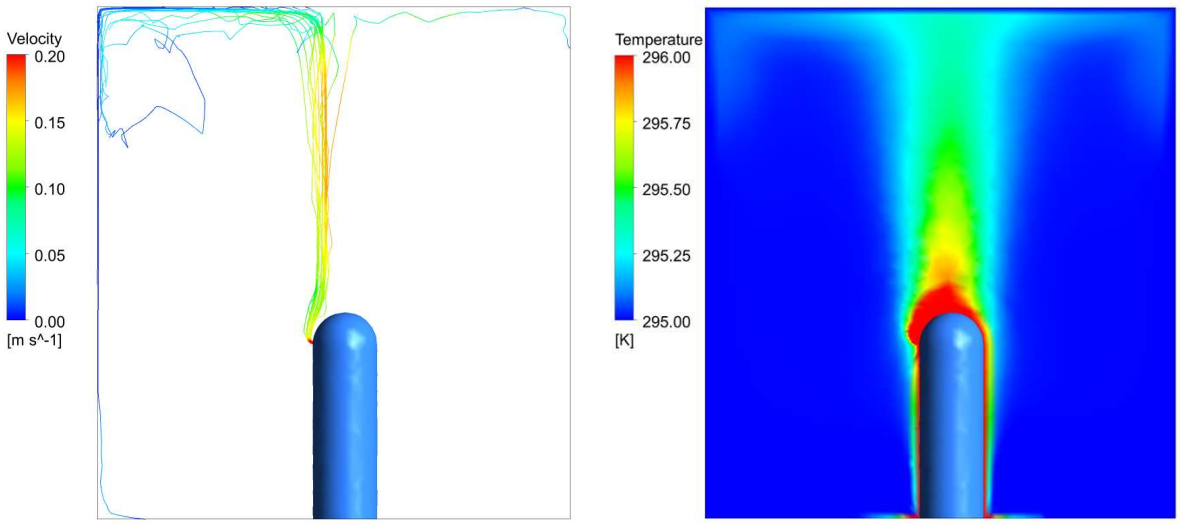
Velocity
0.20
0.15
0.10
0.05
0.00
[m s^-1]
Temperature
296.00
295.75
295.50
295.25
295.00
[K]

(a)

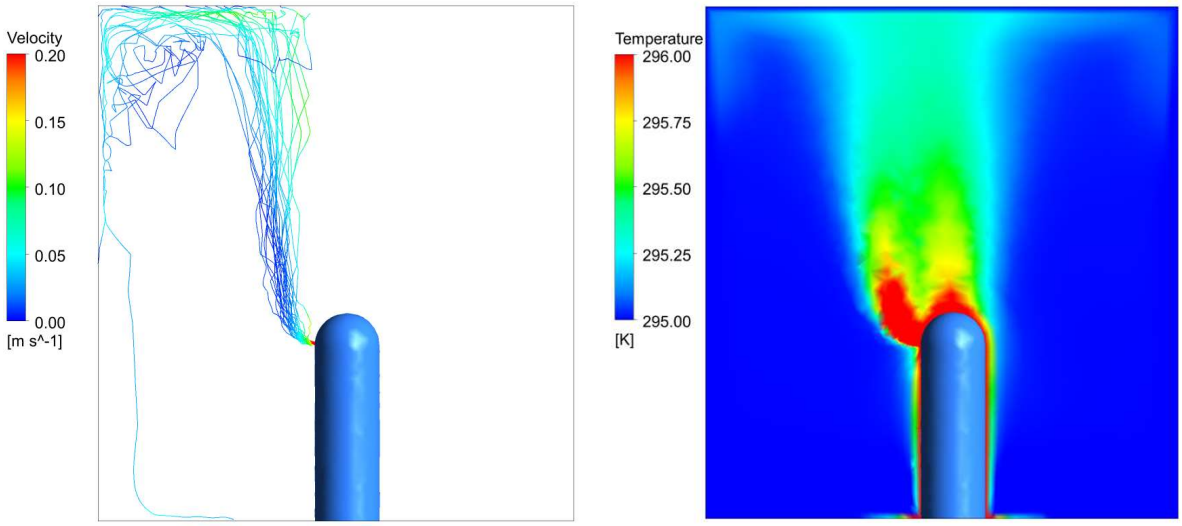
Velocity
0.20
0.15
0.10
0.05
0.00
[m s^-1]
Temperature
296.00
295.75
295.50
295.25
295.00
[K]

(b)

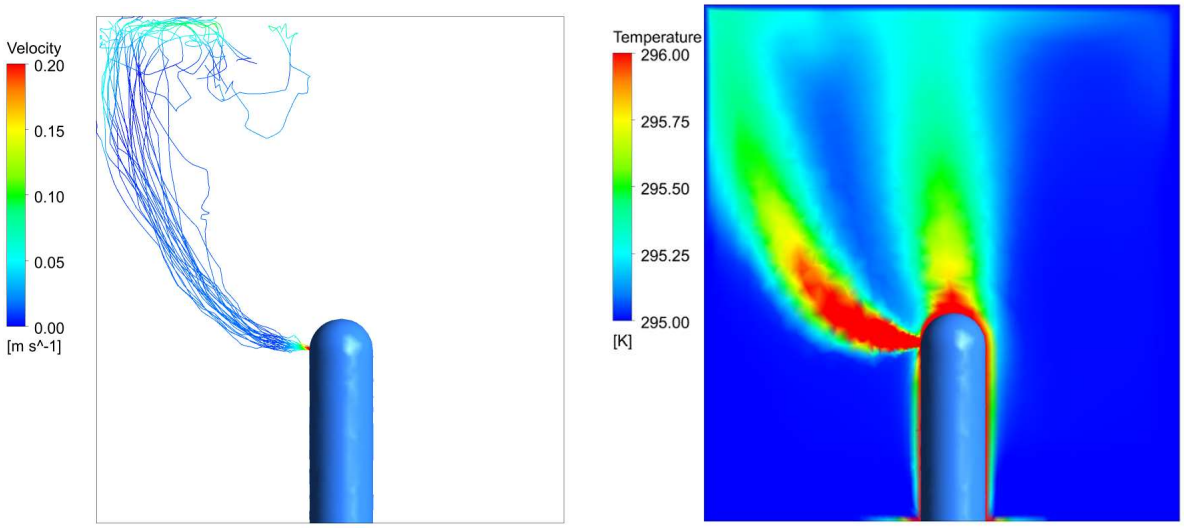

(c)

Figure 88: Trajectories of water droplets exhaled at various speeds and the accompanying temperature profiles. (a) Exhale velocity of 0.35 m/s, which corresponds to a poorly fitted mask case. (b) Exhale velocity of 1 m/s, which corresponds to normal breathing case. (c) Exhale velocity of 2 m/s which corresponds to stronger exhales.

We found that only air leaving the mouth area at a very low speed, comparable to the speed of air being exhaled through or around a mask, rises with the human plume. All greater exhalation speeds have a high enough velocity to escape the plume. The exhaled air is hotter than the surrounding air, so it will rise, although at a very low velocity of approximately 0.01 m/s. The particles in the plume rise to the ceiling at a velocity of about 0.15 m/s. Therefore, the aerosols that escape the plume have a high chance of interacting with other air circulation in the room and spending more time at the breathing level or below rather than rising to the ceiling, creating a more infectious environment. These results further emphasize the importance of wearing a mask in indoor environments.

The CFD model for the conference room [201] illustrates this same phenomenon. In this simulation, exhaust from the individual mouths was omitted. Figure 89(a) shows streamlines of air originating in the thermal plumes right above the head of the two individuals sitting on the left of the table. Figure 89(b) depicts a streamline starting 5 cm away from the seated individual's head. The distinction between these flow paths despite relatively close starting locations shows the importance of the plume in redirecting air. It also shows how thin the thermal boundary layer producing the plume is to the body since air only 5 cm away did not experience the buoyant effects. This supports the idea that a low exhale velocity is needed for infected breath to be captured by the human plume. Therefore, aerosols emitted around a face mask that stay within the buoyant plume have a different trajectory than aerosols expelled with a horizontal velocity that takes them outside the human plume.

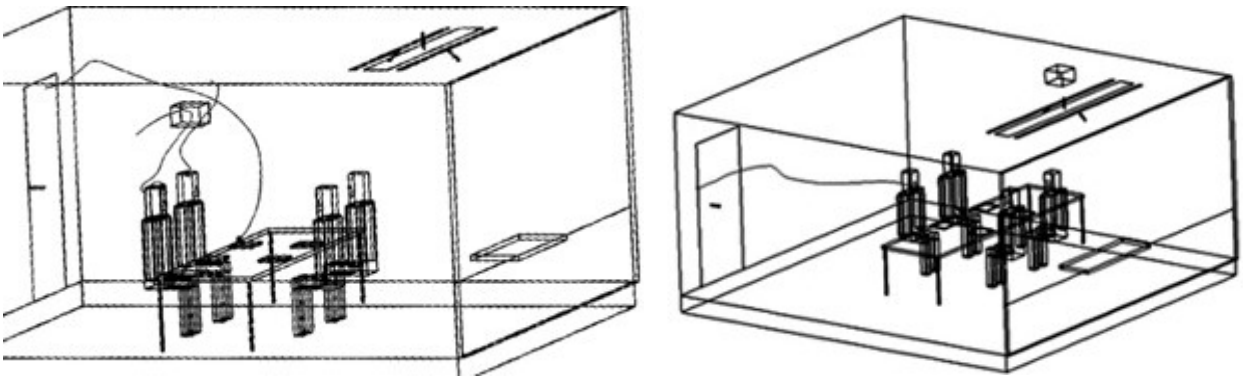

(a) (b)

Figure 89: Streamlines originating (left) within the thermal plumes and from a computer, and (right) 5 cm from the face [201].

As a comparison to these thermal plume effects, we also ran a simulation of the ceiling diffusers running in a classroom with adiabatic walls and no people in the room. In this case, streamlines originating from the inlets show a random pathway of air throughout the space, compared to the streamlines present in a classroom with people, where air is warmed and rises around the people and then falls again as it cools. The significance of the thermal plumes on the overall airflow pattern in the room is further supported by these results.

5.1.5.2 Display of Results

Both qualitative and quantitative displays are used to illustrate the results. Methods to compare the simulations include volume renders and color-coded planes of temperature and CO mass fraction, as well as streamlines showing air paths from the infected individuals. To easily compare results between simulations, we will use a scale relative to the calculated well-mixed concentrations of the room with the given boundary conditions. For the Natural Ventilation Simulations, volume renderings are displayed with transparency representing twice the well-mixed concentration and red representing four times the well-mixed concentration. Plane views of the seated and standing breathing planes are colored with blue representing areas at or below the well mixed concentration and red representing four times the well-mixed concentration. For HVAC ventilation, the transparent limit for volume renderings is set at well-mixed concentration, and the opaque scale at four and a half times well-mixed concentration. Any point that has a mass fraction value below the transparent bound, is shown as transparent, enabling a 3D visual. This allows us to visually distinguish areas in the room with elevated aerosol concentrations.

5.1.5.3 Natural Ventilation Results

Although most modern buildings are equipped with HVAC systems, many older buildings and schools rely on opening windows and doors for ventilation. Furthermore, many classrooms with mediocre ventilation systems are opening windows in hopes of increasing airflow and reducing the spread of COVID-19. For these reasons, it is important to consider the various scenarios that may arise when windows are opened and to analyze possible risk factors. Multiple setups with different window and door conditions were considered.

In the following natural ventilation simulations, we assume an exit velocity of 1 m/s for air breathed out by the students, corresponding to a normal breathing case. We placed two infected individuals in the room, one close to the windows in the back row, and one far from the windows in the front row, so that we can compare the differing situations of being seated near or far from the inlet windows. The total area of window inlets is 0.46 m^2 and the velocity of incoming air is 1 m/s. This yields an air change rate of 6.5 changes per hour and a well-mixed, steady state concentration of 0.00052 total mass fraction of CO. The different situations modeled are described in Table 24 below.

Simulation A	Double Hung Windows Aligned with Rows of Students
Simulation B	Double Hung Windows Between Rows of Students
Simulation C	Baffles on Double Hung Windows Aligned with Rows of Students
Simulation D	Door Open and Bottom Windows as Inlets Between Rows of Students
Simulation E	Door Open and Top Windows as Inlets Between Rows of Students

Table 24: Descriptions of simulation variations with operable windows

5.1.5.3.1 Simulation A: Double Hung Windows Aligned with Rows of Students

In Simulation A, the windows are double hung and in line with the two rows of students, with an air speed of 1 m/s across each, normal to the boundary. Based on the nature of double hung windows, we assume a constant inflow of air through the bottom pair of windows at 1 m/s and set the top windows to be pressure outlets. There is no other exhaust vent. This situation would be similar to placing a fan near the lower windows or a breezy day with an overhang blocking the wind approaching the upper windows. There is no other outlet in the room. The results are pictured in Figure 90, with infected individuals indicated with a red arrow.

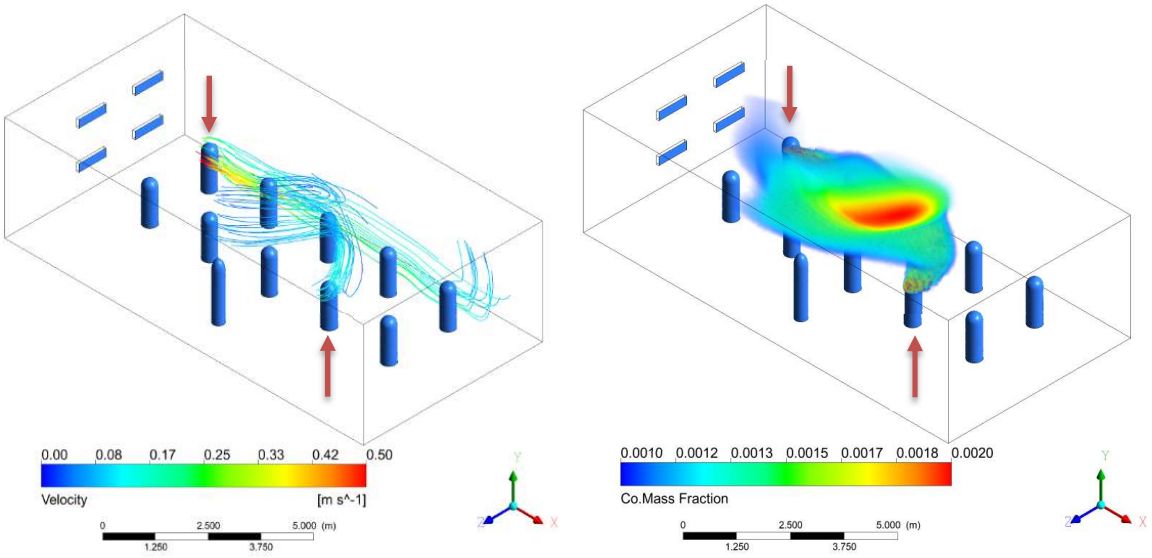

(a) (b)

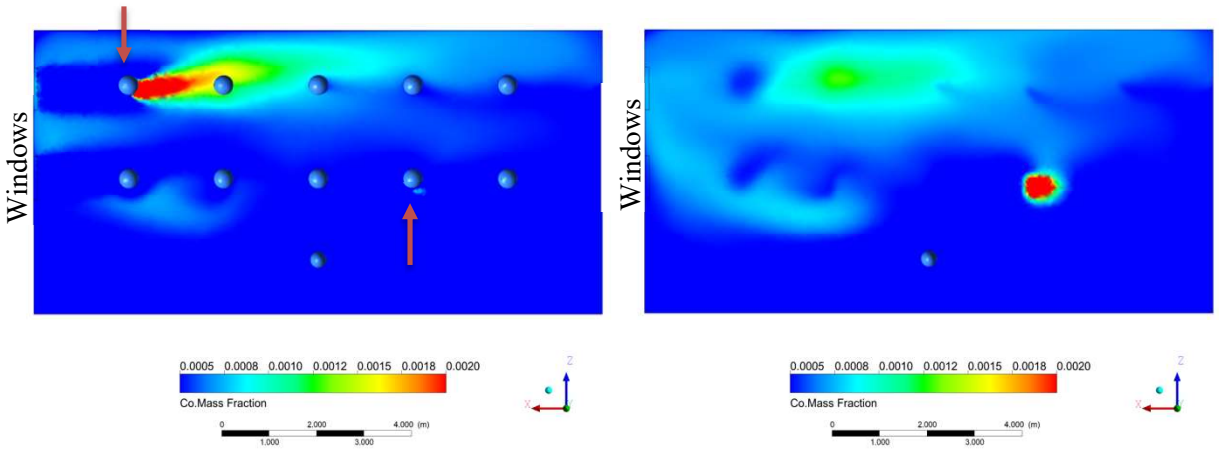

Sitting Breathing Level Standing Breathing Level

(c) (d)

Figure 90: Results of Simulation A with double hung windows aligned with the rows of students. (a) Streamlines originating around the heads of the two infected individuals from 0 to 60 seconds and colored according to velocity. (b) Volume rendering of CO mass fraction. The transparent limit is set at 2x well mixed, and the opaque scale at 4x well mixed. (c) Colored rendering of CO mass fraction right below mouth level of seated students. (d) Colored rendering of CO mass fraction right below mouth level of standing teacher. The lower limit is set at 1x well mixed, and the upper limit at 4x well mixed.

In this simulation, a circular airflow pattern arises as cool air enters through the windows and sinks due to buoyancy effects while maintaining a horizontal velocity. As the air is warmed by the students and teacher, it rises and is pulled back toward the upper outlet window due to the positive pressure difference created by the incoming air. As seen in Figure 90(a) and Figure 90(c), this creates a dangerous situation when an infected student is seated next to the window, as infected aerosols are pushed directly into the next student by horizontal currents. Since the incoming air is cooler, the airstream drops as it moves toward the next student. If the open window was slightly higher, the concentration around the next student might be higher since the incoming air will blow rising aerosols from the infected individual's plume and reach the next student at breathing level. The infected student farther away from the window does not create a hazardous environment for the person sitting next to them, and we mainly see the infected aerosols they breathed out rise to the ceiling.

5.1.5.3.2 Simulation B: Double Hung Windows Between Rows of Students

We hypothesized that this problem of horizontal breezes pushing infected air directly into other students could be mitigated by positioning the students so that they are not directly in line with the windows. We studied this case in Simulation B, which has the same setup as Simulation A, however, the windows were moved to be in the gaps between the two rows of students.

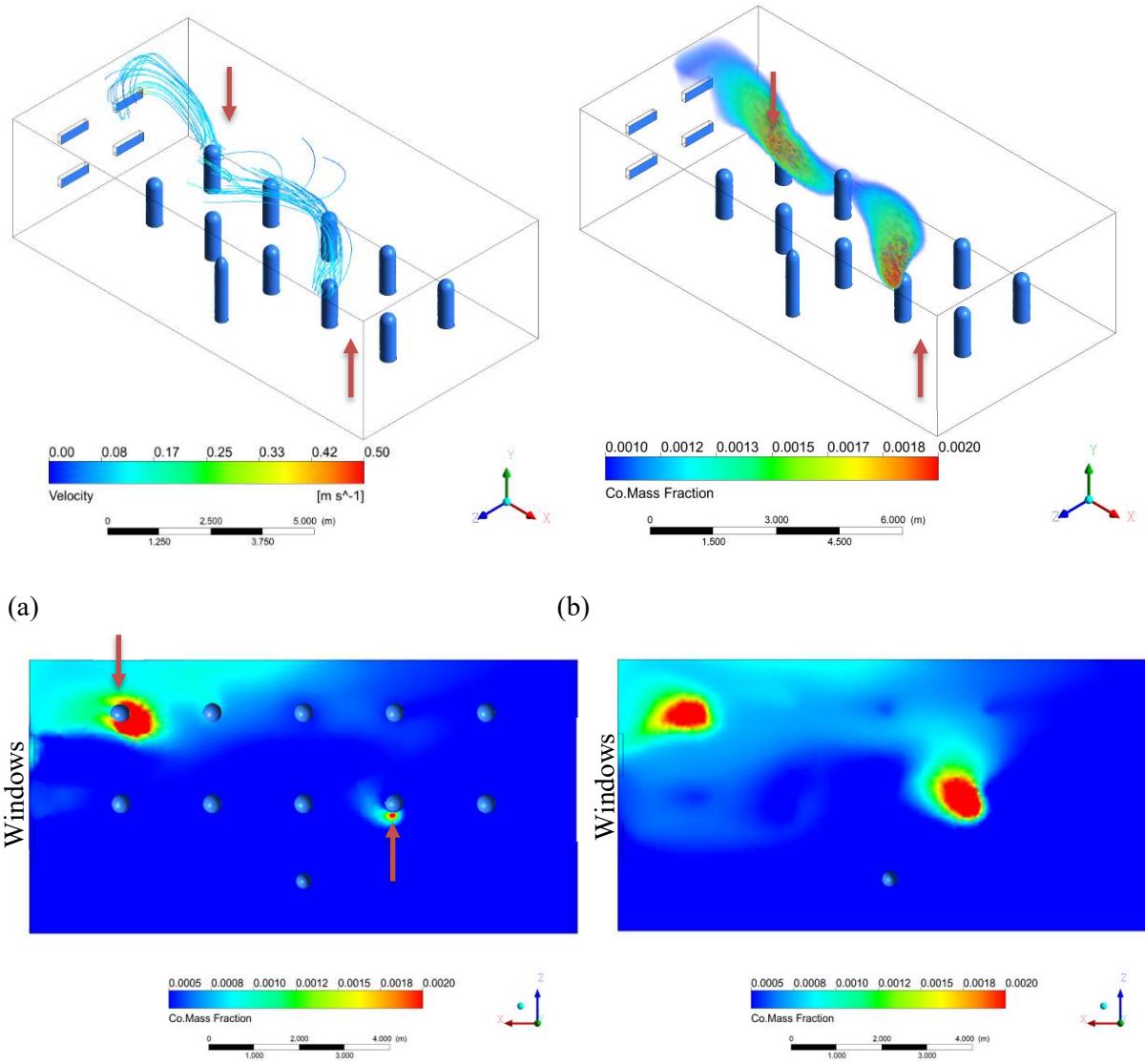

Figure 91: Results of Simulation B with double hung windows placed in between the rows of students. (a) Streamlines originating around the heads of the two infected individuals from 0 to 60 seconds and colored according to velocity. (b) Volume rendering of CO mass fraction. The transparent limit is set at 2x well mixed, and the opaque scale at 4x well mixed. (c) Colored rendering of CO mass fraction right below mouth level of seated students. (d) Colored rendering of CO mass fraction right below mouth level of standing teacher. The lower limit is set at 1x well mixed, and the upper limit at 4x well mixed.

The resulting streamlines are very similar to in Simulation A, exhibiting a strong circular pattern of circulation in the XY plane, with the cool incoming air less disturbed by immediate interaction with the human plumes. In contrast to Simulation A, however, the plumes coming off the students in Simulation B are being largely pulled back towards the windows, whereas the plumes were being largely pushed directly toward the next student in Simulation A. In this case, the students sitting next to the infected individuals are more protected than those in Simulation A, as seen by comparing Figure 90(c) to Figure 91(c). This suggests that seating students away from strong horizontal air currents is preferable.

5.1.5.3.3 Simulation C: Baffles on Double Hung Windows Aligned with Rows of Students

Another possible way to avoid strong horizontal air currents interacting with exhaled air would be to place a baffle inside the windows that directs the air downwards. We simulated this by maintaining the same mass flow rate but directing the incoming air from the windows downwards at a 45 degree angle. In Simulation C, the windows are again aligned with the rows of students as in Simulation A.

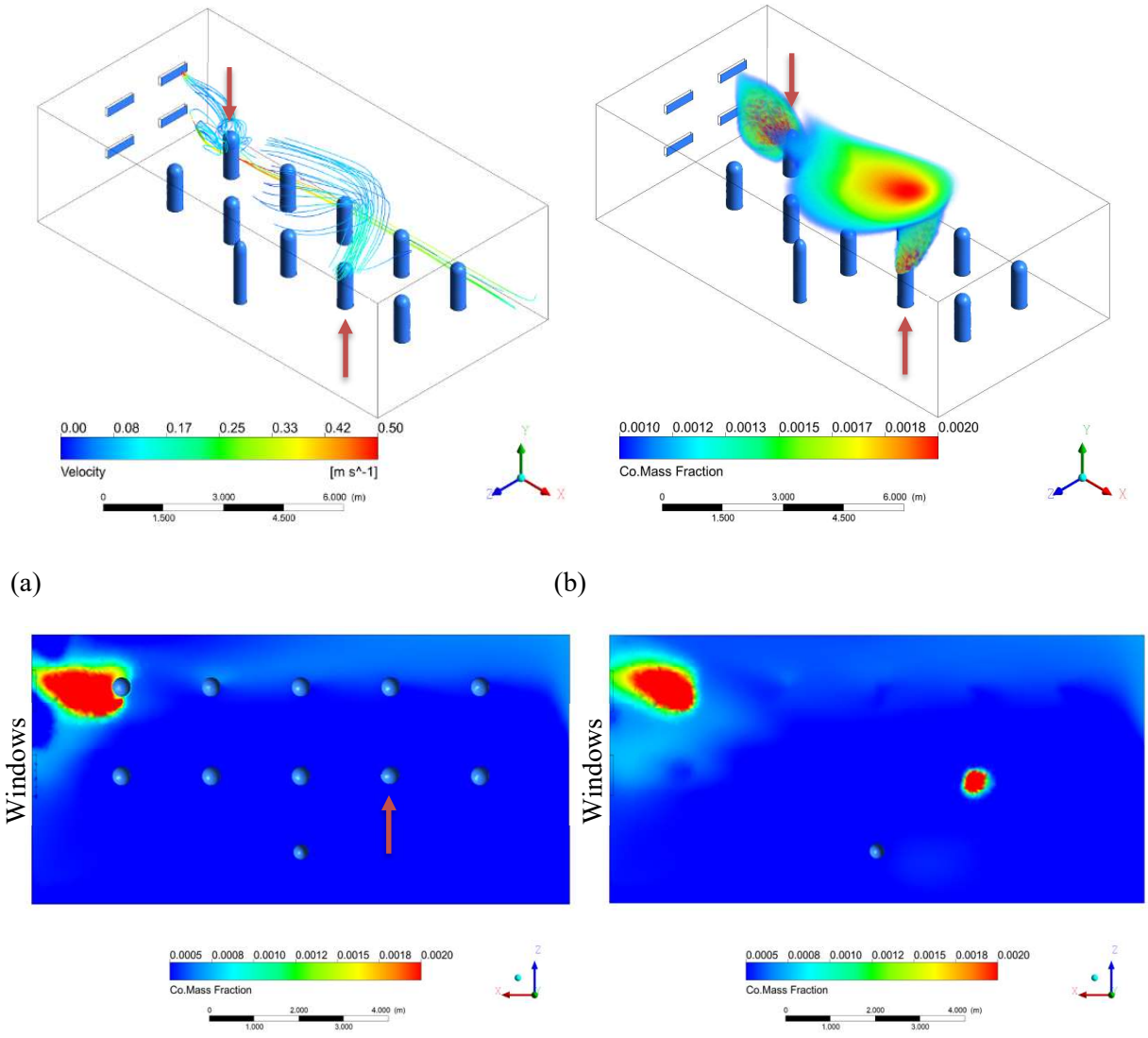

(a) (b)

Sitting Breathing Level Standing Breathing Level

(c) (d)

Figure 92: Results of Simulation C with double hung windows aligned with the rows of students and the air flow directed downwards to prevent strong horizontal drafts. (a) Streamlines originating around the heads of the two infected individuals from 0 to 60 seconds and colored according to velocity. (b) Volume rendering of CO mass fraction. The transparent limit is set at 2x well mixed, and the opaque scale at 4x well mixed. (c) Colored rendering of CO mass fraction right below mouth level of seated students. (d) Colored rendering of CO mass fraction right below mouth level of standing teacher. The lower limit is set at 1x well mixed, and the upper limit at 4x well mixed.

Compared with the results of Simulation A, where the air entered the room normal to the windows, the CO concentration at the breathing planes is lower for Simulation C, where the air from the windows is directed downwards. A cool layer of air near the floor seems to create a strong buoyancy effect so that most of the infected aerosols rise and are suspended above breathing level until they exit the room through the outlet windows. This starts to approach displacement ventilation although the air entering the room in this case has a high momentum causing recirculation and higher aerosol concentration at breathing level. These results suggest that baffles to direct air downwards could be an effective measure in classrooms with windows spanning an entire wall where the staggered alignment of Simulation B is not possible.

Simulation D: Door Open and Bottom Windows as Inlets Between Rows of Students

A strategy schools may employ to improve ventilation is to open the door along with the windows. In general, this would allow greater air flow into the room through the windows, since any positive pressure built up in the room can exit through the door. In Simulation D, we added an open door opposite of the windows. For this simulation, the windows are between the rows since we have established the risks of having them aligned with the students. The results are nearly identical regardless of if the windows are double hung since most of the air exits through the door. In this simulation, the upper window is closed.

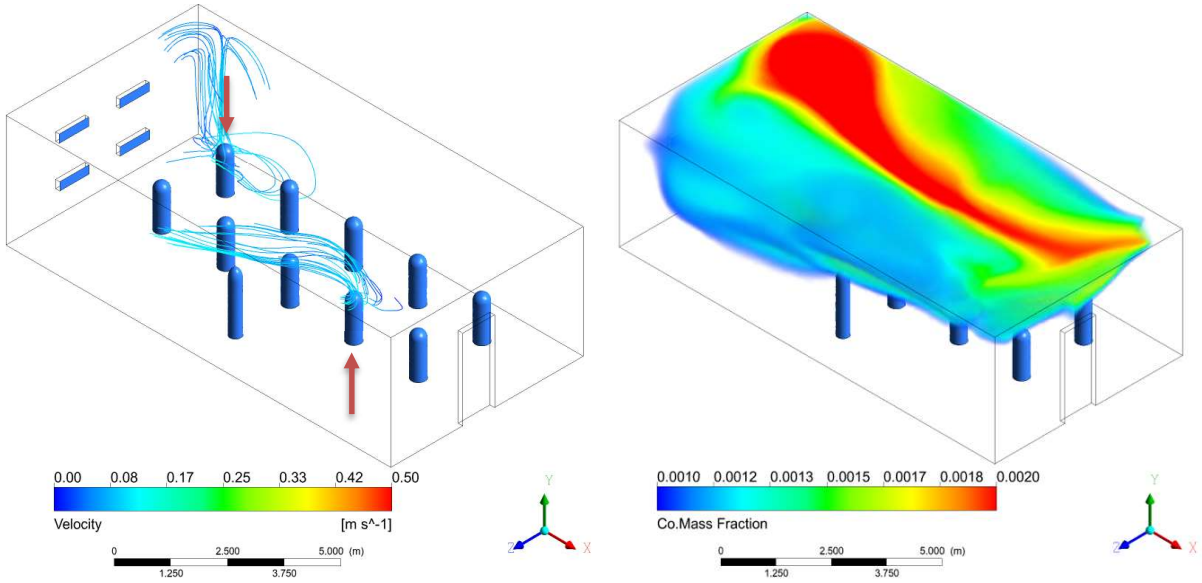

(a) (b)

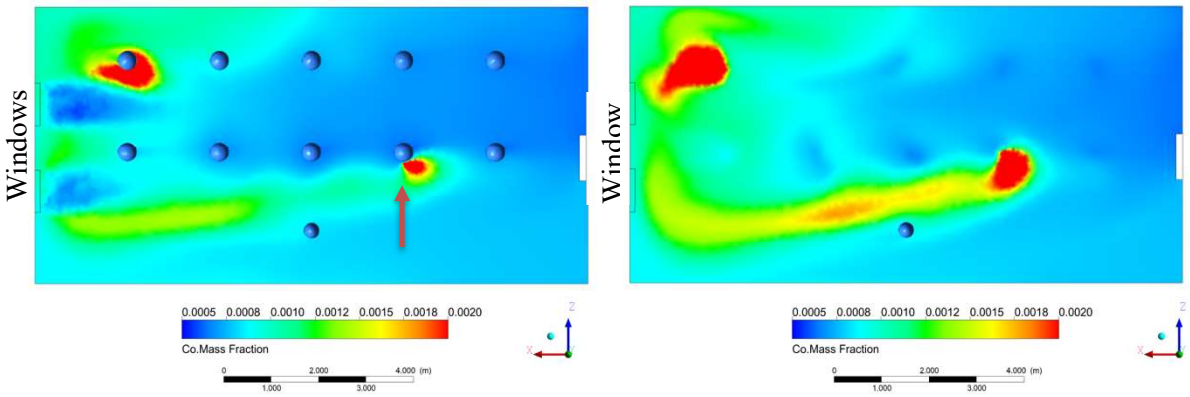

Sitting Breathing Level

Standing Breathing Level

(c)

(d)

Figure 93: Results of Simulation D with a pair of windows between the rows of students and an open door on the opposite wall. Air flows in from the lower window. (a) Streamlines originating around the heads of the two infected individuals from 0 to 60 seconds and colored according to velocity. (b) Volume rendering of CO mass fraction. The transparent limit is set at 2x well mixed, and the opaque scale at 4x well mixed. (c) Colored rendering of CO mass fraction right below mouth level of seated students. (d) Colored rendering of CO mass fraction right below mouth level of standing teacher. The lower limit is set at 1x well mixed, and the upper limit at 4x well mixed.

Since the outlet is now on the opposite wall from the inlet and air can exit lower to the ground, a vertical temperature stratification occurs in the room with warm air accumulating above the top of the doorway, especially on the side of the room with the windows. Infected air rises with the human plumes and then becomes trapped in the warm layers as cool air continues to enter through the windows and creates buoyant effects. This situation is not ideal since the concentration is increased in the upper part of the room and the concentration of aerosols is elevated at the breathing level. If the windows were higher on the wall, the dangers of this situation may be reduced. This hypothesis is investigated in the next simulation.

5.1.5.3.4 Simulation E: Door Open and Top Windows as Inlets Between Rows of Students

In Simulation E, we again have a single open window with an open door on the opposite wall, however, the upper windows are now open, and the bottom windows are closed, creating a situation where the inlet is above breathing level.

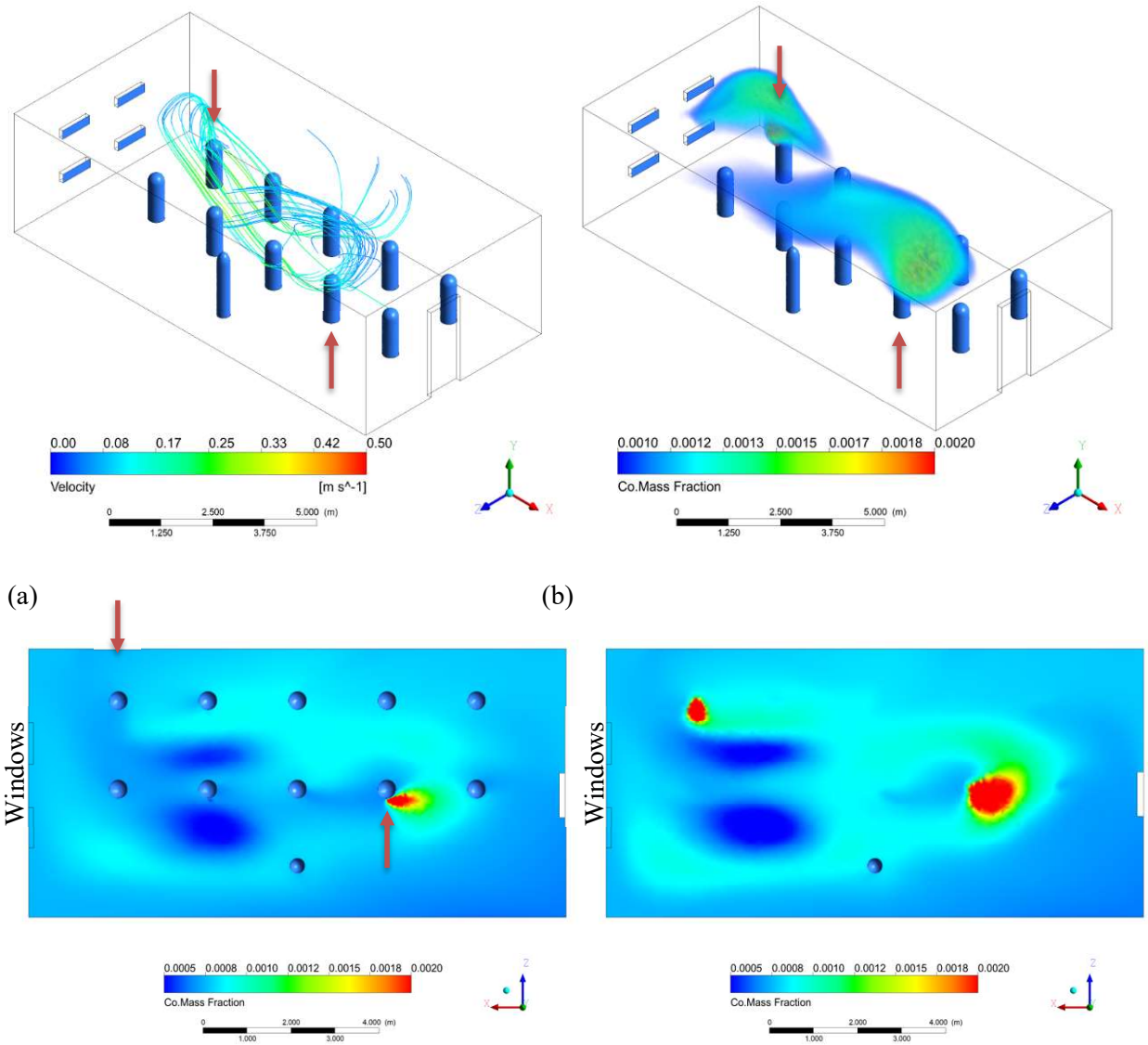

Figure 94: Results of Simulation E with a pair of windows between the rows of students and an open door on the opposite wall. Air flows in from the upper windows. (a) Streamlines originating around the heads of the two infected individuals from 0 to 60 seconds and colored according to velocity. (b) Volume rendering of CO mass fraction. The transparent limit is set at 2x well mixed, and the opaque scale at 4x well mixed. (c) Colored rendering of CO mass fraction right below mouth level of seated students. (d) Colored rendering of CO mass fraction right below mouth level of standing teacher. The lower limit is set at 1x well mixed, and the upper limit at 4x well mixed.

The stratification seen in Simulation D was still prevalent in Simulation E, however the beginning of this warm layer was closer to the ceiling. The air flow entering from a higher elevated acted as a mixing force in the room, and more of the room was closer to the well-mixed CO mass fraction, as opposed to the large cloud of infected aerosols seen in Simulation D.

5.1.5.4 HVAC Results

In the HVAC scenarios, the windows are sealed, and the room is ventilated from eight diffusers on the ceiling, as shown in Figure 95. There is single return outlet, located just below the ceiling at the center of the left wall (when facing to the front of the classroom). The outlet has a surface area of 0.36 m^2, and is modelled as a constant pressure boundary, at atmospheric pressure, considering hydrostatic pressure effect, labeled in Figure 96(a). The air enters along the ceiling from the diffusers with a speed of 0.5 m/s and temperature varying based on the simulation. The size of the diffusers is shown in Figure 95, with a cross sectional area of 0.06906 m^2 per diffuser. The wall opposite the instructor is treated as a single glazed window, and several different outdoor temperatures are investigated. A radiator is also present at the base of the window, but is only used in one simulation. The radiator is also labeled in Figure 96(a). The results of the ceiling diffuser HVAC simulations are presented below. Table 25 shows different simulation conditions and their names. Table 26 contains their respective boundary conditions.

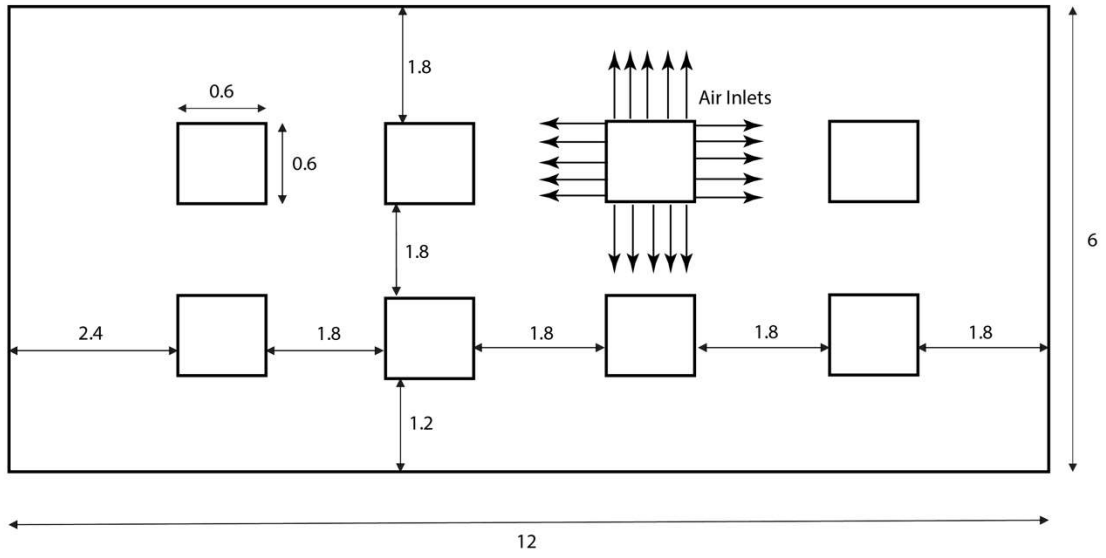

Figure 95: Top view of ceiling diffusers in HVAC cases. Air enters parallel to the ceiling from the sides of each square diffuser. There are eight diffusers in total, spaced 1.8 m apart. The initial velocity of air across the inlets is 0.5 m/, resulting in 0.343 kg/sec of fresh air entering the room. A square return vent is present on one side wall, which acts as a pressure boundary at gauge pressure.

Simulation F	Heating with Moderate Heat Loss to a Window
Simulation G	Heating, Cold Windows
Simulation H	Heating, Coldest Windows
Simulation I	Heating with Radiator
Simulation J	Cooling with Warm Windows
Simulation K	Cooling with Hot Windows
Simulation L	No Mask, Infected Person in Back Row
Simulation M	No Mask, Infected Person in Front Row
Simulation N	Adiabatic Window

Table 25: Descriptions of simulation variations without operable windows

Simulation	**F**	**G**	**H**	**I**	**J**	**K**	**L**	**M**	**N**
Inlet Temperature	301 K (28 C)	302 K (29 C)	303 K (30 C)	298 K (25 C)	288 K (15 C)	287 K (14 C)	301 K (28 C)	301 K (28 C)	292 K (19 C)
Rear Window Heat Flux [W/m^2]	-50	-75	-100	-75	35	70	-50	-50	0
Mouth Velocity [m/s]	0.35	0.35	0.35	0.35	0.35	0.35	1	1	0.35
Infected Person Location	Back Center	Back Center	Back Center	Back Center	Back Center	Back Center	Back Center	Front Right	Back Center

Table 26: Boundary conditions for simulations F-N, inclusive

For the HVAC case, the total carbon monoxide injection was 0.0001544 kg/sec and the fresh air inlet was 0.343 kg/sec across the total interior air volume of 252 m^3 yielding 4.4 air changes per hour. Based on this, the resulting well-mixed carbon monoxide concentration is 0.00045 total mass fraction of CO. The temperature of the inlet was adjusted to maintain comfortable temperature conditions in the room at steady state as the heat flux across the window changes. In these simulations, we assume an exhale velocity from the mouths of 0.35 m/s (people wearing poorly fitted masks) while maintaining the same mass flow rate as in the natural ventilation cases.

5.1.5.4.1 Simulation F: Heating with Moderate Heat Loss to a Window

This case represents the base heating case, with a moderate temperature gradient between the inside and outside. A negative heat flux of 50 W/m^2 is present at the window along the back wall, corresponding to an outside air temperature roughly 10 K below the inside air temperature. Warm air enters the room from the ceiling diffusers at 301 K (28 C). Figure 95(a) below shows the presence of the thermal plumes around the individuals, which is key to the general airflow patterns in the room since there are no dominating horizontal air currents from windows. A similar visual, using CO mass fraction as the display variable, is shown in Figure 96(b). For the CO volume renders, the transparent boundary is set at 0.0005, which is 1.11 x the well-mixed concentration, and the red upper limit is set at 0.002, 4.44x well-mixed. From this visual we see that the effect of the thermal plumes has a significant effect on the spread of the exhaled gas, which rises around the infected individual, identified with an arrow.

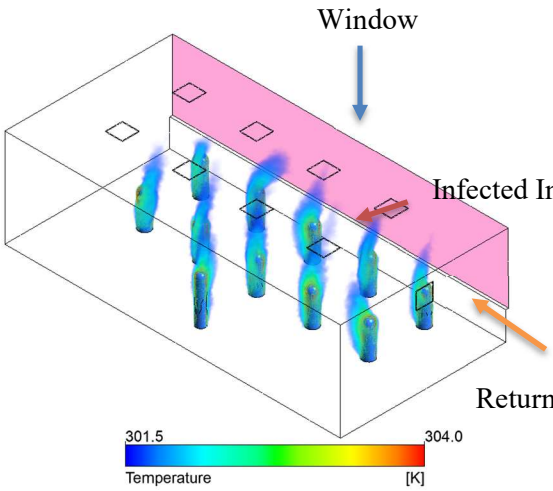

(a)

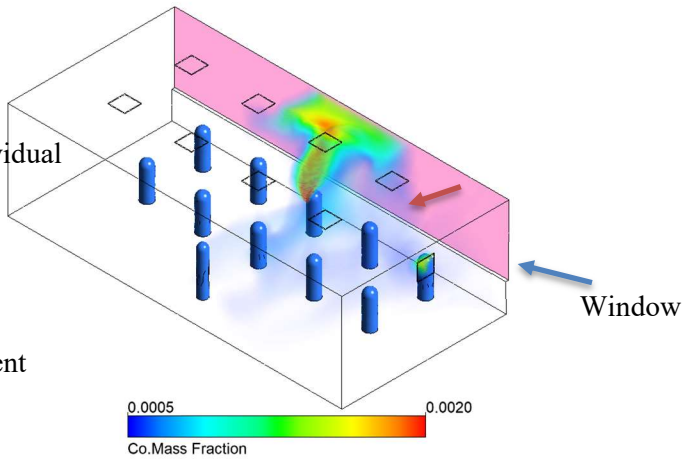

(b)

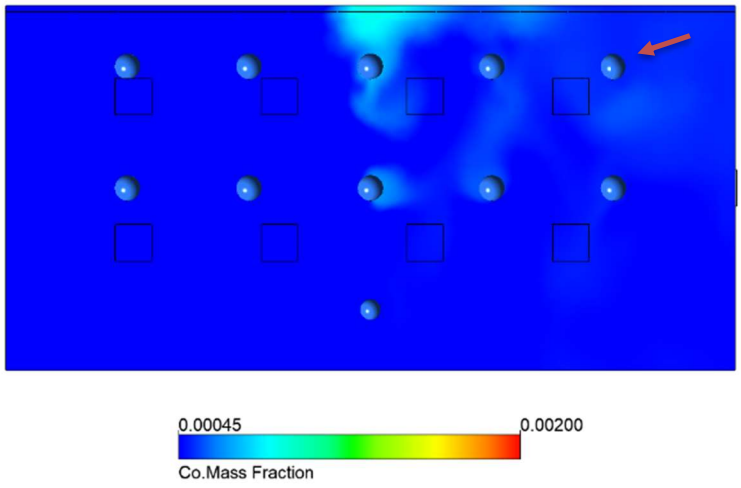

(c)

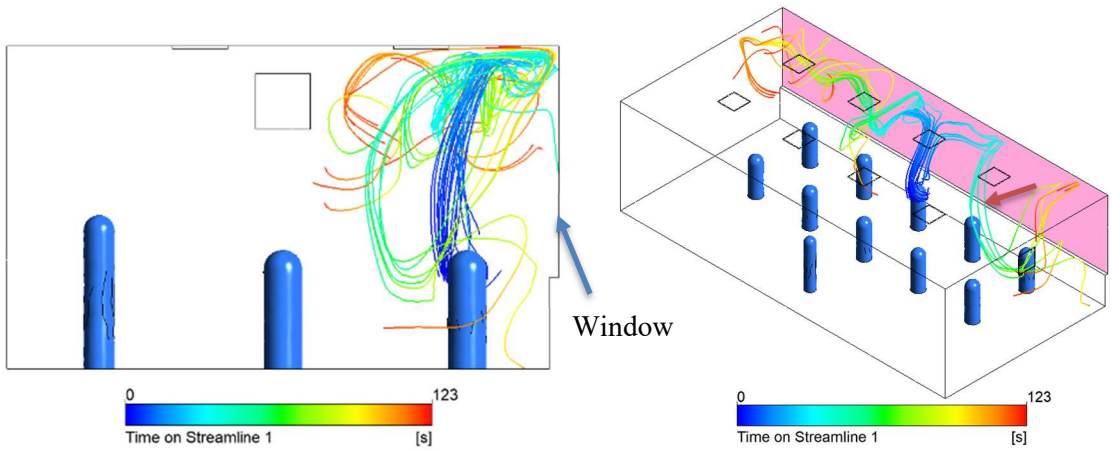

(d) (e)

Figure 96: In Simulation F, warm air at 301 K (28 C) enters through the ceiling diffusers and a cold window at the back of the classroom creates a negative heat flux against that wall of -50 W/m^2. (a) Temperature Volume Render of Simulation F, clearly showing the thermal plumes in the room. (b) Volume Render of the CO mass fraction of Simulation F. (c) Horizontal Plane at breathing level, showing the CO mass fraction. (d, e) Steady state streamlines from infected individual for Simulation F.

We can see from these initial results that horizontal air flows are not as prevalent as in the natural ventilation cases, and the thermal plumes and cool air from the ceiling play a large role in the movement of air instead. The color scale on the streamlines in Figure 96(d, e) is representative of the time that has passed since that air passed by the infected individual. The streamlines clearly rise with the human plume before spreading throughout the room. The remaining sets of simulations will explore how changes in different variables impact the resulting steady-state conditions in the room.

5.1.5.5 Simulation G and H: Heating Cases, Cold and Colder Windows

In Simulations G and H, the total heat flux at the window to the outside was increased to 75 W/m^2 and 100 W/m^2 to simulate larger temperature gradients across the single-glazed windows, analogous to a wintertime condition. The approximate outside temperatures for Simulations G and H are 10°C and 0°C respectively. From Figure 97, which shows the results of simulation H, we can see that the increase of the temperature gradient resulted in much larger values of CO mass fraction throughout the room, indicating a more dangerous situation when an infected individual is seated next to a cool window with heating from above. The colder temperature at the window cools the adjacent air, which sinks to the floor from where it is picked up again by the plumes, carrying infected aerosols. The two simulations, suggest that the effect is magnified proportionally to the temperature gradient. This increase is also displayed in the box-and-whisker plot in Figure 101.

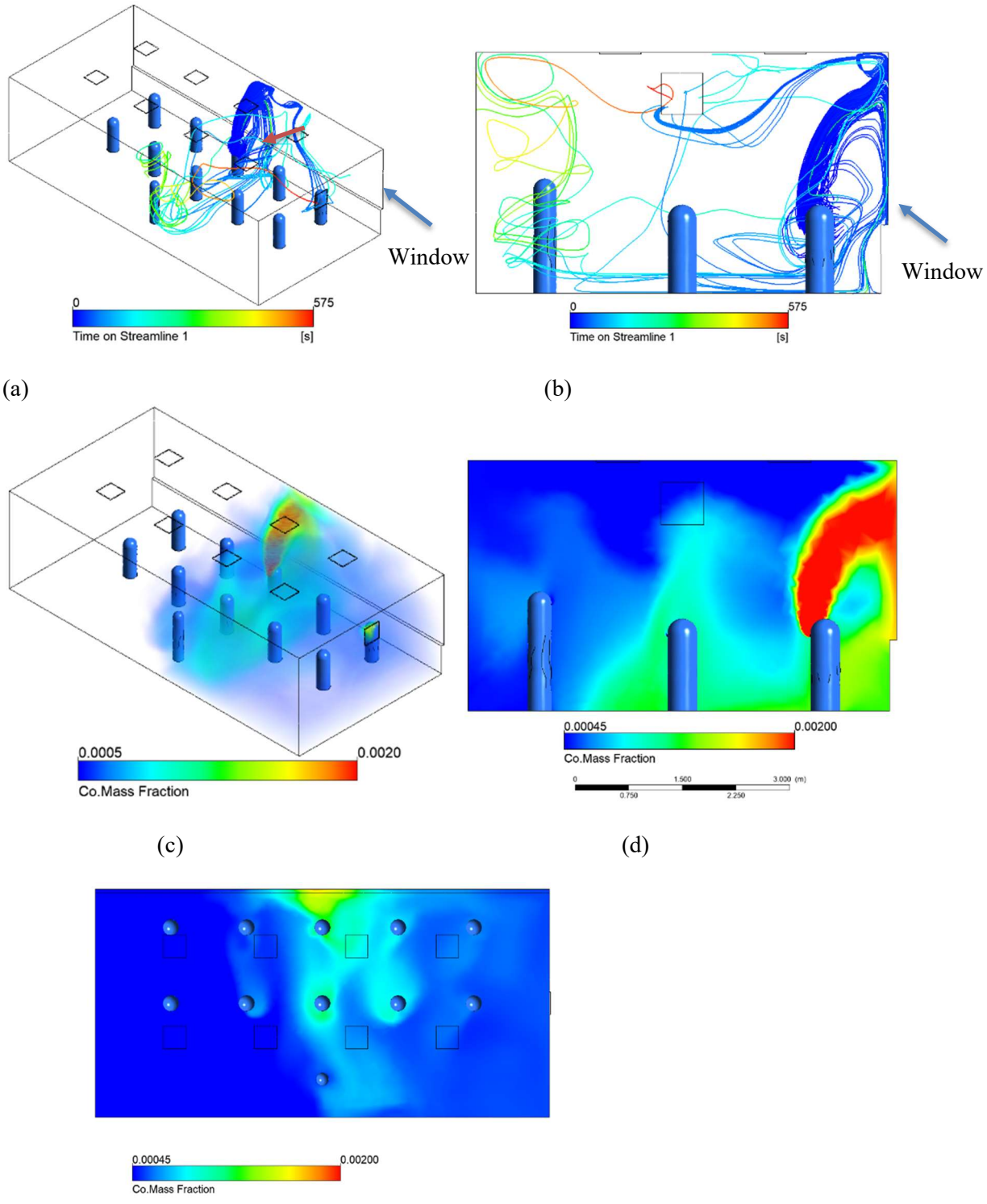

Figure 97: Simulation H is a heating case with outside temperature of 0°C respectively, represented by a negative heat flux across the back wall -100 W/m^2. Simulation H results. (a) Streamlines for Simulation H. (b) Side view of streamlines for Simulation H. (c) Volume rendering of CO mass fraction for Simulation H. (d) Side view of CO mass fraction for Simulation H.. (e) CO mass fraction at sitting breathing level for Simulation H.

With the colder case, the higher aerosol concentration rises in the plume, is drawn down near the cold window, and then contacts the student in the next row. This effect of colder outside temperatures can be counteracted by implementing better thermal insulation at the window, such as double-glazing or using a radiator to heat the window surface. This last claim is supported by Simulation I.

5.1.5.6 Simulation I: Heating with Radiator

Simulation I considers the short wall below the window, to be a radiator. The two exposed surfaces act as a recirculation inlet and outlet, respectively. The air is drawn in on the vertical face and released with a temperature increase of 5 Kelvin from the horizontal face, onto the window. The CO mass fraction plots below clearly show the extreme reduction of the spread of the tracer gas. The effects of the cold window are for all practical purposes, cancelled out.

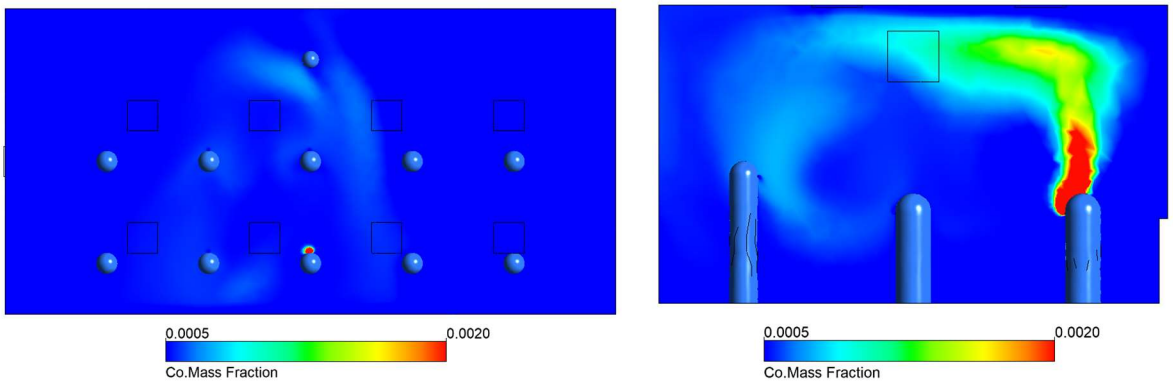

(a) (b)

Figure 98: Simulation I considers the same boundary conditions as Simulation G, with the addition of a radiator below the window. (a) CO Mass fraction at breathing level. (b) CO Mass fraction in the vertical plane, at the center of the room. For both images, the colour scale ranges from 1-4.4 x well mixed mass fraction.

5.1.5.7 Simulations J and K: Cooling Cases, Warm and Hot Windows

In Simulation J the opposite season to Simulation F was considered, where the outside temperature is warmer than comfortable room temperature. From these simulation results, it was seen that there is no large difference between the mild heating in Figure 96(c) and mild cooling case, but as soon as the net heat flux increases across the window, there are greater temperature gradients throughout the room, intensifying airflow patterns, and increasing airflow velocities. When the HVAC system compensates for a higher outside temperature, without adjusting the flow rate, the inlet temperature is decreased. This colder air, causes the air around the diffusers to sink down, including air which has risen in the infected plume. So as the inlet temperature decreases, the temperature gradient increases, causing more air to sink to the floor. This pattern is displayed in Figure 99, which shows the streamlines for the more extreme cooling case, Simulation K.

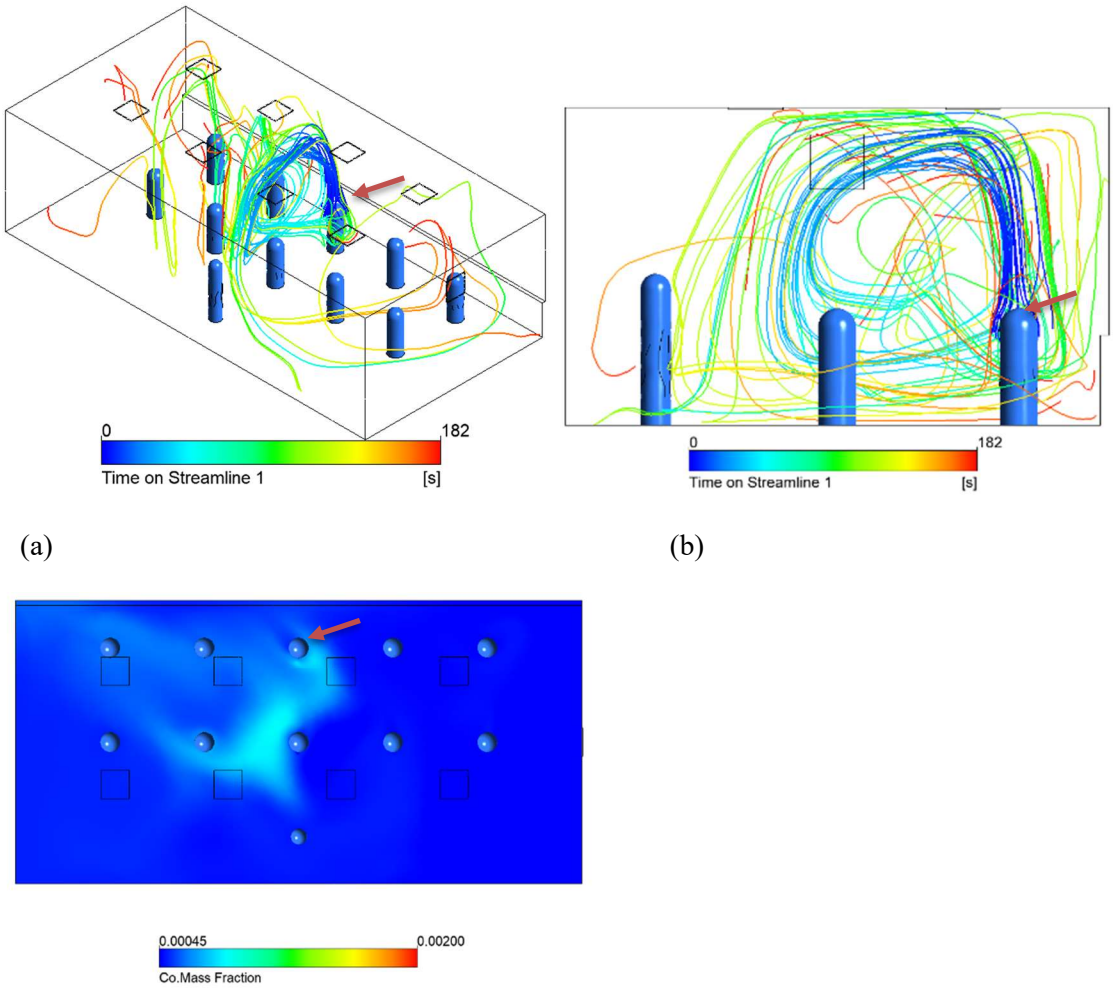

Figure 99: Simulation K is a more extreme cooling case with a hot window. Air enters from the diffusers at 287 K (14 C) and a heat flux of and 70 W/m^2 across the window. (a) Streamlines for Simulation J. (b) Side view of streamlines for Simulation J. (c) CO mass fraction at sitting breathing level for Simulation K.

5.1.5.8 Simulations L and M: No Mask

In Simulations L and M, we investigate the effect that the velocity of exhaled air has on the CO mass fraction profile in the room. In these simulations, the velocity of the air exhaled by people was increased to 1 m/s, corresponding to people not wearing a face mask at all. The infected individual in Simulation M is moved to the front row, to investigate dependence on location with respect to the window. In the CO mass fraction planes in Figure 100, the values are much higher than the other simulations, because the mouth velocity was increased without changing the geometry, the total CO volume introduced into the space increases proportionally. To provide adequate comparison between simulations, the scales for simulations L and M have been adjusted accordingly with respect to the well-mixed concentration. From the box and whisker plot in Figure 101, we can see that the normalized mass fraction values are higher for Simulations L and M than the lower velocity case in Simulation F. This further confirms our previous study on the effects of varied exhale speed in Figure 88. We can see that

when the exhalation velocity is high enough, the exhaled air travels fast enough to escape the entraining effects of the thermal plume and spreads more by diffusion in the breathing plane.

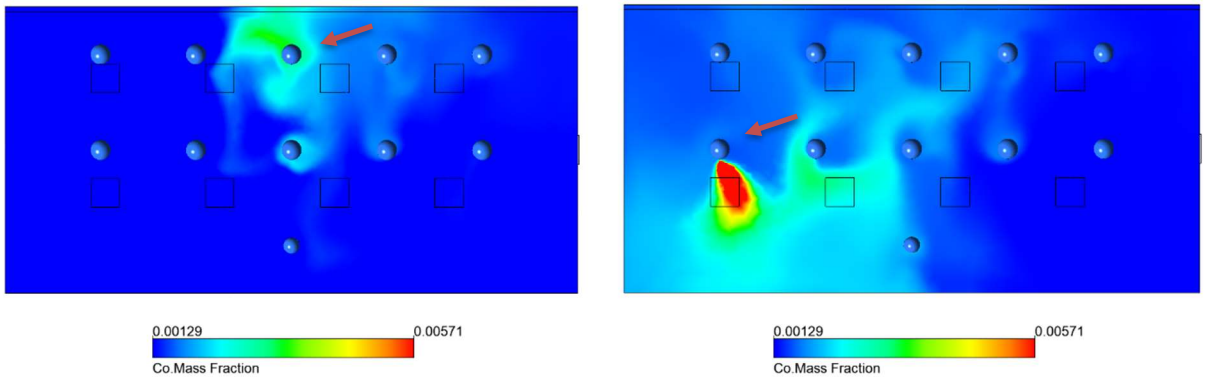

(a) (b)

Figure 100: Simulations L and M have the same boundary conditions as Simulation F, heating with moderate heat loss to a window (Figure 94), but for these cases, the people have a higher breathing velocity of 1m/s opposed to 0.35m/s to represent unmasked breathing. (a) CO mass fraction at sitting level for Simulation L with infected student in back row. (b) CO mass fraction at sitting level for Simulation M with infected student in front row on the far right. The upper limit of the color scale is 4.44x well mixed, and the lower limit is 1.11x well-mixed.

5.1.5.9 Simulation N: No Window, Adiabatic Room

In Simulation N, the thermal effects introduced by the window are removed to simulate a classroom with no windows. For these conditions, the CO tracer gas rises from the infected individual without much lateral motion. This further reinforces the theory of cold windows/walls creating worse conditions. From the comparison of all simulations shown in the following section, we see the adiabatic wall case performing well. This suggests that better insulation on windows and walls leads to safer conditions inside the room.

5.1.6 Simulation Comparisons

The colored volume and plane results give a good qualitative picture of the aerosol dispersion. To obtain a quantitative comparison, a different method of comparison between situations was selected. By using CO as a tracer gas for exhaled air and monitoring the mass fraction throughout the space, we are able to gain some numeric basis for comparison. Samples of the average CO mass fraction near the breathing zone of all non-infected individuals in a sphere of radius 0.33 m centered around the head were taken in each natural ventilation and HVAC simulation. The results of these samples are shown in the box-and-whisker graph in Figure 101. The values are normalized with respect to the well-mixed CO mass fraction for each simulation. The distribution of CO mass fraction values can then be used as an indicator of infection risk for each of the situations. Cases A through E have ventilation through open windows while the rest of the cases use a standard HVAC ventilation design. The individuals with the highest and lowest concentration are shown as the extremes. Some cases resulted in an average local CO mass fraction value near the well-mixed value, whereas some averaged much higher. In some cases, the concentration reaches 2.5 times the well mixed value at certain locations.

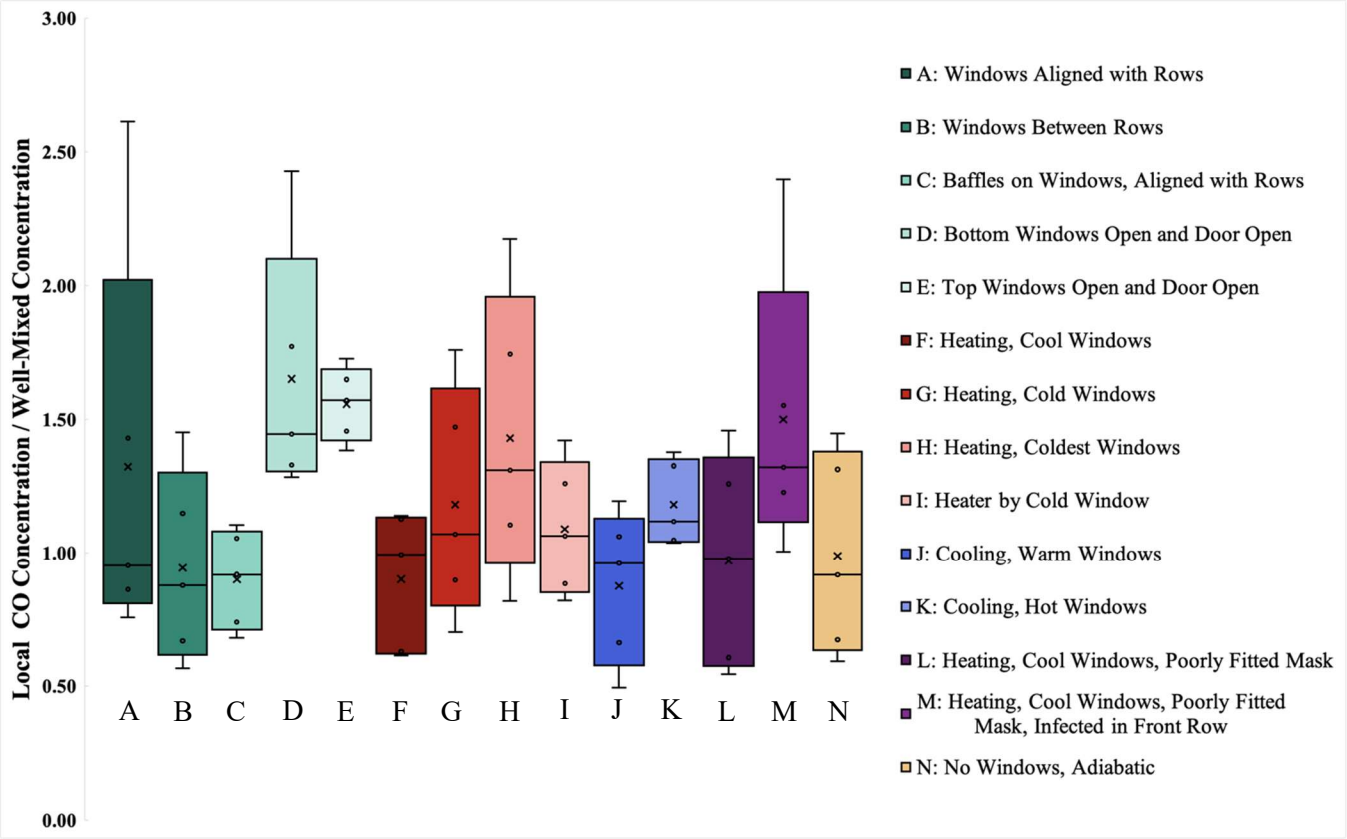

Figure 101: Box and whisker diagram of normalized CO mass fraction compared to well-mixed concentration at breathing plane for different simulations. 'X' represents the volume average concentration for the entirety of the room volume. The subset of values represented by the box and whisker plot represent individual spheres of 0.33 m radius surrounding the head of the non-infected occupants within the space.

In some cases, with open windows, the concentration reaches 2.5 times the well mixed value. The worst cases occur with lower windows in line with student seating and with exhaust through a modest door height. Directing the air immediately downward from the windows (mimicking displacement ventilation) gives the lowest level of exposure for all occupants. Opening the upper windows and the door results in a uniform exposure but at a higher average concentration.

For the HVAC cases with ceiling diffusers, concentration levels are highest when an infected individual is close to a very cold widow and when individuals wear a loosely fitted mask in a classroom with a cold window.

5.1.7 Flushing Simulation

A flushing simulation was completed on a transient solver to determine how accurate the well-mixed assumption is in an empty room with only clean air entering. The same HVAC geometry with ceiling diffusers was modeled with adiabatic walls and an initial condition of the well mixed concentration at time zero. Occupants were intentionally not modeled during this simulation. This case is representative of a space being flushed out by the clean inlet air, overnight or between classes. If we assume large disturbances when the occupants leave the room, the well-mixed initial assumption is not far off. From the transient simulation, we found the average, maximum, and minimum volumetric mass

fraction at 60 second intervals, and compared them to the corresponding theoretical, well-mixed values. There was a very close correlation between the two data sets. This suggests that a well-mixed assumption is an accurate representation of flushing an empty room.

5.1.8 Energy implications and reduced occupancy

Based on this work, air change rate increases above the current recommendations are necessary to maintain exposure limits equivalent to the current well-mixed assumption for all occupants. Such an increase in air change rate will require a commensurate increase in energy requirements, to which local and zonal air filtration may be helpful in reducing contaminant levels near the source. In the simulations modeled above, the occupancy level has remained constant at eleven persons except for the flushing transient simulation. As shown in Figure 91(d), a wall-mounted CO_2 sensor may also misrepresent the carbon dioxide levels in a space if the well-mixed assumption is invalid based on the airflow within same said space. The well-mixed assumption is particularly dangerous if the sensor location is used to control ventilation for the space itself.

As outside air is brought into a building for contaminant control, it is conditioned for both temperature and humidity limits, which requires energy to be spent in achieving those limits. A common control algorithm for the room HVAC system, demand control ventilation, maintains a prescribed CO_2 level by varying the proportion of outside air in the ventilation airflow. The algorithm assumes a well-mixed steady state condition for the room, where the concentration of a pollutant, CO_2 or aerosol, will be a function of the rate of pollutant mass generation and the mass flow rate of outside air.

With reduced occupancy, the total CO_2 generation is reduced and the probabilistic chance of a non-infected individual encountering an infected individual is lower. However, with demand control ventilation and a reduced occupancy level, although the CO_2 remains within prescribed limits, the resultant reduction of the outside air ventilation will result in a higher average concentration of aerosol in the room produced from an infected occupant (if present) than the same occupant in a room at full occupancy. Therefore, with reduced room occupancy, the chance of encountering an infected individual decreases. Yet if an individual is infected, the infection risk for other occupants increases with reduced room occupancy when demand control ventilation based on CO_2 feedback is used. To address these scenarios, the safest operation requires a constant flow of outside air irrespective of occupancy level. To alleviate the energy impact of this strategy, an alternative approach may include a high-performance filtration system. Further work is needed to address this filtration question, as well as additional simulations of airflow to identify safe seating configurations with low occupancy and reduced airflow rates.

5.1.9 Conclusions

COVID-19 is an aerosolized virus. With such small particle sizes, the established six-foot (~1.8 m) spacing guidelines and heightened air change rates are an incomplete picture. The results from this paper help reinforce the concept that exhaled particles of modest velocity (such as a person with a mask or face shield) are entrained in the thermal plume of the body heat and rise toward the ceiling. However, higher horizontal velocities (such as a person without a mask or face shield) can escape the thermal plume and can linger within the breathing plane of others. These thermal plumes from people and heated objects continue to have an impact on air flow within the room, along with influences from cold or heated surfaces, mechanical HVAC systems, and outside air ventilation.

Two HVAC systems have been examined to show that, even with industry standard air change rates, the well-mixed assumption as applied to a conventional HVAC system made up of ceiling diffusers may underpredict the contaminant levels inhaled by the occupants by half. Even with the window open, the perceived safety of the well-mixed assumption is too conservative and underpredicts the potential exposure by 60%.

Aside from air change rate changes, other strategies can be employed to limit potential exposure of non-infected individuals. For situations where a cold outside surface (i.e. an uninsulated window) may exist, contaminant levels can be reduced by an order of 20% by the addition of a convective heater below the window, the use of curtains or blinds, or replacement of the windows to improve their insulative value. Care should be taken as a similar case is presented by exterior spaces with plastic enclosures used by many eateries where cold outside surfaces allow for recirculation of contaminants.

While open windows may give the impression of ventilation, they also create their own problems as the influx of air near the breathing plane carries contaminants horizontally from an infected person near the window to other occupants. Staggering seating arrangements and redirecting window air to the ground may remove this issue as it allows for the buoyant plumes to redevelop and bring contaminants out of the breathing plane.

Regarding flushing out contaminants in the absence of any occupants, the well-mixed assumption is valid for this application and a generalized air change model may be used.

Future work should include other HVAC systems such as displacement ventilation for improvements. For properly operated displacement ventilation systems with low speed floor inlets and ceiling exhaust, concentration at breathing levels should be below well mixed values. However, if occupants have loosely fitted masks, the performance could degrade if breathing exhaust escapes the thermal plumes around the individual. Cold windows could also degrade performance

Based on this work, air change rate increases above the current recommendations are necessary to maintain exposure limits equivalent to the current well-mixed assumption for all occupants. Such an increase in air change rate will require a commensurate increase in energy requirements, to which local and zonal air filtration may be helpful in reducing contaminant levels near the source. More work is necessary to determine the impact of increased ventilation on air flow patterns, the threshold for infection by aerosols, and to enhance the removal of aerosols through the design of the airflow within an occupied

space. This work does not assess the impact of reducing occupancy levels further while occupied and represents an opportunity for further work to answer.

6 Conclusions

This work has covered a variety of topics, from inclined and double-layer roofing, impacts of interior convection coefficients in low-income Indian housing, thermostat and chilled beam interactions, and aerosol dispersion. Fundamentally, these are all connected through airflow in interior spaces and seek to answer the question of how to improve thermal comfort, reduce negative health impacts, and present methods to decrease energy use.

In Bhuj, India, where extreme heat is an immediate risk for survival, existing housing typologies fail to protect low-income populations. As seen through recent events in May 2022, climate change is exacerbating heatwaves and adding risk not only for lower-income families that cannot afford air-conditioning, but is straining the grid for those that now rely exclusively on air-conditioning and have no fallback options. Double-layer inclined roofing, when used with a radiant barrier on the lower surface of the upper layer and coupled with a moderate thermal mass as the lower layer, has the potential to reduce inside air temperatures by roughly 10.9 °C as compared to an informal home on the hottest days of the year. At a linearized excess mortality rate of 3.2 percentage points per 1 °C during a heat wave, this can help reduce the excess mortality possibility by 34 percentage points as compared to an informal home, or by 26 percentage points from the ambient environment. Critically, most of the performance of the system comes from the presence of the radiant barrier. The color (solar absorptivity) of the exterior layer, thickness of the mudroll, and powered ventilation of the cavity have little impact on the performance of the roof as a whole. Double-layer inclined roofing may also be conceptualized as a means of air-conditioning avoidance; where the reduction of heat to the inside surface of roof system as compared to the Mangalore tile along is roughly equivalent to a 7,750 BTU/h air conditioning unit.

For single-layer horizontal roofing where the external surface cannot be modified or for apartment dwellers with an exposed concrete slab roof, adopting a targeted nighttime flushing strategy focused on directing incoming air towards the ceiling has the potential to conservatively decrease the next-day peak temperature by half a degree, reducing excess mortality by 1.6 percentage points during a heat wave. External solar absorptivity changes remain the best method to improve comfort and reduce the next-day peak temperature of the slab. Both strategies can be employed concurrently. For those living in multi-story housing, even modest increases in the convective heat transfer coefficient have the capacity to make meaningful reductions in the slab temperature possible.

Both the double-layer inclined roofing and the single-layer flat roofing convection techniques are universally applicable to hot climates. Notably, outside of India and neighboring Pakistan, immediate adoption is possible in the Middle East, Western Africa, and the Caribbean. For applications in these regions, the Mangalore tiles may be replaced with locally-available options so long as the radiant-barrier and air gap are retained. For cost-constrained building construction, both of these techniques represent solutions that are tangible, easily conceptualized, and have recognizable impacts. While there are benefits of the systems for heat reduction within moderate climates, further research is needed to understand the implications of the system on heat loss during cooler temperatures and on possible control of ventilation within the cavity.

For offices with chilled beams, the addition of a ceiling fan can reduce the reactive nature of the thermal response of a chilled beam to a sudden load and maintain thermal comfort for new occupants. Further, the presence of large differentially heated surface (i.e. an outside window) has a negative impact

on a room thermostat's ability to read the air temperature of a space. Relocating thermostat sensors within the room to central locations improves the representativeness of the data and can also reduce energy usage through reducing overheating and overcooling. Relocation can also benefit the thermal comfort of a building through reduced thermostat setpoint changes.

For classrooms seeking to minimize bioaerosol exposure, the well-mixed assumption has the potential to underpredict the aerosol concentration at the breathing layer by 60%, especially when risk factors are present. Locating potentially bioaerosol sources near air inlets increases the risk to others within the space, as does a disruption of the thermal stratification. Mitigation measures applicable to airborne viruses, include drawing blinds to reduce the thermal impact of outside windows, masking to entrain bio-effluent in an individual's thermal plume, and directing inlet air towards the floor.

This work contributes to the academic body of knowledge through a triad of socially-conscious field work, thermal modeling, and lab experiments. Novel contributions from long-term monitoring present insights into both the benefits of codesign and early integration of stakeholders to achieve thermally preferable solutions. Efforts to elevate the discussion on airflow within conference and classroom spaces as applied to thermal comfort and health are broadly applicable to provide insight for operators and occupants alike.

Future work is needed to implement and field validate the ventilation strategies within the single-layer slab roofing, as well as to investigate the possibility of coupling ventilation strategies with movable radiant barrier systems. Other options include the evaluation of different air dispersion methodologies and fan styles (i.e. centrifugal fans) to improve performance and reduce conflicts during implementation.

7 References

[1] T. Stocker, D. Qin, G.-K. Plattner, M. Tignor, S. K. Allen, J. Boschung, A. Nauels, Y. Xia, V. Bex and P. Midgley, "IPCC, 2013: Climate Change 2013: The Physical Science Basis. Contribution of Working Group I to the Fifth Assessment Report of the Intergovernmental Panel on Climate Change," Cambridge University Press, Cambridge, 2013.

[2] J. Hansen, M. Sato and R. Ruedy, "Perception of climate change," *Proceedings of the National Academy of Sciences,* vol. 109, no. 37, pp. E2415-E2423, 2012.

[3] G. A. Meehl and C. Tebaldi, "More intense, more frequent, and longer lasting heat waves in the 21st century," *Science,* vol. 305, no. 5686, pp. 994-997, 13 August 2004.

[4] C. Mora, B. Dousset, I. R. Caldwell, F. E. Powell, R. C. Geronimo, C. R. Bielecki, C. W. W. Counsell, B. S. Dietrich, E. T. Johnston, L. V. Louis, M. P. Lucas, M. M. McKenzie, A. G. Shea, H. Tseng, T. W. Giambelluca, L. R. Leon, E. Hawkins and C. Trauernicht, "Global risk of deadly heat," *Nature Climate Change,* vol. 7, pp. 501-506, 2017.

[5] O. Mazdiyasni, A. AghaKouchak, S. J. Davis, S. Madadgar, A. Mehran, E. Ragno, M. Sadegh, A. Sengupta, S. Ghosh, C. T. Dhanya and M. Niknejad, "Increasing probability of mortality during Indian heat waves," *Science advances,* vol. 3, no. 6, p. e1700066, 2017.

[6] Y. Shuang, X. Jiangjiang, Y. Zhongwei, Z. Anzhi, X. Yang, G. Dabo, H. Jiaru, W. Jun, C. Liang and K. Yakun, "Loss of work productivity in a warming world: Differences between developed and developing countries," *Journal of Cleaner Production,* vol. 208, pp. 1219-1225, 2019.

[7] S. Ehsan, F. Abbas, M. Ibrahim, B. Ahmad and A. A. Farooque, "Thermal Discomfort Levels, Building Design Concepts, and Some Heat Mitigation Strategies in Low-Income Communities of a South Asian City," *International Journal of Environmental Research and Public Health,* vol. 18, no. 5, 2021.

[8] R. Banerjee and R. Maharaj, "Heat, infant mortality, and adaptation: Evidence from India," *Journal of Development Economics,* vol. 143, 2020.

[9] J. C. Alberdi, J. Diaz, J. C. Montero and I. Miron, "Daily mortality in Madrid community 1986–1992: relationship with meteorological variables," *European journal of epidemiology,* vol. 14, no. 6, pp. 571-578, 1998.

[10] H. Eng and J. B. Mercer, "Seasonal variations in mortality caused by cardiovascular diseases in Norway and Ireland," *Journal of cardiovascular risk,* vol. 5, no. 2, pp. 89-95, 1998.

[11] M. Hashizume, Y. Wagatsuma, T. Hay, S. Saha, K. Streatfield and M. Yunus, "The effect of temperature on mortality in rural Bangladesh—a population-based time-series study," *International Journal of Epidemiology,* vol. 38, no. 6, pp. 1689-1697, 2009.

[12] G. S. Azhar, D. Mavalankar, A. Nori-Sarma, A. Rajiva, P. Dutta, A. Jaiswal, P. Sheffield, K. Knowlton and J. Hess, "Heat-Related Mortality in India: Excess All-Cause Mortality Associated with the 2010 Ahmedabad Heat Wave," *PLOS ONE,* vol. 9, no. 3, pp. 1-8, March 2014.

[13] Indian Census 2011, "Ahmedabad City Population 2011," Census Population 2022 Data, [Online]. Available: https://www.census2011.co.in/census/city/314-ahmedabad.html. [Accessed 4 May 2022].

[14] Ahmedabad Municipal Corporation, "Ahmedabad Heat Action Plan 2016," 9 March 2018. [Online]. Available: https://www.nrdc.org/sites/default/files/ahmedabad-heat-action-plan-2016.pdf.

[15] World Population Review, "Ahmedabad Population 2022," World Population Review, [Online]. Available: https://worldpopulationreview.com/world-cities/ahmedabad-population. [Accessed 4 May 2022].

[16] Reuters, "Extreme heat kills at least 25 in India's Maharashtra state," Al Jazeera Media Network, 3 May 2022. [Online]. Available: https://www.aljazeera.com/news/2022/5/3/extreme-heat-kills-at-least-25-in-indias-maharashtra-state. [Accessed 4 May 2022].

[17] S. Mehrotra, R. Bardhan and K. Ramamritham, "Urban Informal Housing and Surface Urban Heat Island Intensity: Exploring Spatial Association in the City of Mumbai," *Environment and Urbanization ASIA,* vol. 9, no. 2, pp. 158-177, 2018.

[18] A. Binazzi, M. Levi, M. Bonafede, M. Bugani, A. Messeri, M. Morabito, A. Marinaccio and A. Baldasseroni, "Evaluation of the impact of heat stress on the occurrence of occupational injuries: Meta-analysis of observational studies," *American Journal of Industrial Medicine,* vol. 62, no. 3, pp. 233-243, 2019.

[19] H. Yingdong, W. Chen, Z. Wang and H. Zhang, "Review of fan-use rates in field studies and their effects on thermal comfort, energy conservation, and human productivity," *Energy and Buildings,* vol. 194, pp. 140-162, 2019.

[20] A. Orlov, J. Sillmann, K. Aunan, T. Kjellstrom and A. Aaheim, "Economic costs of heat-induced reductions in worker productivity due to global warming," *Global Environmental Change,* vol. 63, p. 102087, 2020.

[21] S. Das, "Temperature Increase, Labor Supply and Cost of Adaptation in Developing Economies: Evidence on Urban Workers in Informal Sectors," *Climate Change Economics,* vol. 6, no. 2, p. 1550007, 2015.

[22] PTI, "AC sales hit record high of 17.5 lakh units in April; to touch 90 lakh in 2022: CEMA," *The Times of India,* 3 May 2022.

[23] S. Sun, "Air conditioner market size in India from financial year 2010 to 2020 with estimates up to 2023," Statista, 21 October 2021. [Online]. Available: https://www.statista.com/statistics/1232397/india-ac-market-size/. [Accessed 5 May 2022].

[24] M. Santamouris, Advances in Passive Cooling, London, UK: Earthscan, 2007.

[25] A. Phadke, N. Abhyankar and N. Shah, "Avoiding 100 New Power Plants by Increasing Efficiency of Room Air Conditioners in India: Opportunities and Challenges," Lawrence Berkeley National Laboratory, Berkeley, 2014.

[26] D. Mahadevia, M. Pathak, N. Bhatia and S. Patel, "Climate Change, Heat Waves and Thermal Comfort—Reflections on Housing Policy in India," *Environment and Urbanization ASIA,* vol. 11, no. 1, pp. 29-50, 2020.

[27] D. Satterhwaite, D. Archer, S. Colenbrander and D. Dodman, "Responding to climate change in cities and in their informal," International Institute for Environment and Development, Edmonton, 2018.

[28] U.S. Energy Information Administration, "Country Analysis Executive Summary: India," U.S. Energy Information Administration, Washington, 2020.

[29] J. Dzieza, "The Race Against Heat," The Verge, 14 September 2017. [Online]. Available: https://www.theverge.com/2017/9/14/16290934/india-air-conditioner-cooler-design-climate-change-cept-symphony. [Accessed 4 May 2022].

[30] K. Thiagarajan, "The World's Most Polluted Capital City," *BBC: Future Planet,* 4 April 2022.

[31] UN-Habitat, "Energy efficient housing: Improvement of thermal performance of RC slab roofs," UN-Housing, Pakistan, 2010.

[32] M. Rawat and R. N. Singh, "A study on the comparative review of cool roof thermal performance in various regions," *Energy and Built Environment,* 2021.

[33] Q. Zhao, J. Yang, Z.-H. Wang and E. A. Wentz, "Assessing the Cooling Benefits of Tree Shade by an Outdoor Urban Physical Scale Model at Tempe, AZ," *Urban Science,* vol. 2, no. 1, 2018.

[34] H. B. Cheikh and A. Bouchair, "Experimental studies of a passive cooling roof in hot arid areas," *The Open Fuels Energy Science Journal,* vol. 1, no. 1, 2008.

[35] E. Nelson, "Demonstration and Implementation of Thermally Passive Low-Income Housing: A Case Study in Bhuj," Massachusetts Institute of Technology, Cambridge, MA, 2017.

[36] M. S. Gradillas, "Analysis and design for thermally autonomous housing in resource-constrained communities: A Case Study in Bhuj, India," Massachusetts Institute of Technology, Cambridge, MA, 2015.

[37] J. Lueker, "Exploring mechanisms for improved air quality in Mumbai resettlement dwellings : evidence from fieldwork and simulation," Massachusetts Institute of Technology, Cambridge, 2019.

[38] ASHRAE, "Bhuj, India Weather Data WMO# 426340," ASHRAE, Atlanta, 2017.

[39] J. Kongoletos, "Implementation and evaluation of thermal avoidance strategies in arid, cost-constrained climates aimed at improving indoor thermal comfort : a case study in Bhuj, India," Massachusetts Institute of Technology, Cambridge, 2018.

[40] R. S. Priya, M. C. Sundarraja, S. Radhakrishman and L. Vijayalakshmi, "Solar passive techniques in the vernacular buildings of coastal regions in Nagapattinam, TamilNadu-India – a qualitative and quantitative analysis," *Energy and Buildings,* vol. 49, pp. 50-61, 2012.

[41] M. K. Singh, S. Mahapatra and S. K. Atreya, "Bioclimatism and vernacular architecture of north-east India," *Building and Environment,* vol. 44, no. 55, pp. 878-888, 2009.

[42] V. Garg, R. Kotharkar, J. Sathaye, H. Rallapalli, N. Kulkarni, N. Reddy, P. Rao and A. Sarkar, "Assessment of the impact of cool roofs in rural buildings in India," *Energy and Buildings,* vol. 114, pp. 156-163, 2016.

[43] H. L. Macintyre and C. Heaviside, "Potential benefits of cool roofs in reducing heat-related mortality during heat waves in a European city," *Environment International,* vol. 127, pp. 430-441, 2019.

[44] K. T. Zingre, E.-H. Yang and M. P. Wan, "Dynamic thermal performance of inclined double-skin roof: Modeling and experimental investigation," *Energy,* vol. 133, pp. 900-9112, 2017.

[45] D. Beal and S. Chandra, "The Measured Summer Performance of Tile Roof Systems and Attic Ventilation Strategies in Hot, Humid Climates," in *Proceedings of the Thermal Performance of the Exterior Envelopes of Buildings VI*, Clearwater, 1995.

[46] W. A. Miller, E. Herman and R. Graves, "The Tradeoff Between Solar Reflectance and Above-Sheathing Ventilation for Metal Roofs on Residential and Commercial Buildings," ORNL, Oak Ridge, 2012.

[47] W. Miller, J. Wilson and A. Karagiozis, "The Impact of Above-Sheathing Ventilation on the Thermal and Moisture Performance of Steep-Slove Residential Roofs and Attics," in *Fifteenth Symposium on Improving Building Systems in Hot and Humid Climates*, Orlando, 2006.

[48] E. Di Giuseppe, S. Sabbatini, N. Cozzolino, P. Stipa and M. D'Orazio, "Optical properties of traditional clay tiles for ventilated roofs and implication on roof thermal performance," *Journal of Building Physics,* vol. 42, no. 4, pp. 484-505, 2018.

[49] M. D'Orazio, C. Di Perna and E. Di Giuseppe, "The effects of roof covering on the thermal performance of highly insulated roofs in Mediterranean climates," *Energy and Buildings,* vol. 42, no. 10, pp. 1619-1627, 2010.

[50] M. Bottarelli, M. Bortoloni, G. Zannoni, R. Allen and N. Cherry, "CFD analysis of roof tile coverings," *Energy,* pp. 391-398, 2017.

[51] Government of India Ministry of Housing and Urban Poverty Alleviation National Buildings Organization, "Slums in India: A Statistical Compendium," Government of India, New Delhi, India, 2015.

[52] Office of the Prime Minister of India, "News Updates," 17 June 2015. [Online]. Available: http://www.pmindia.gov.in/en/news_updates/housing-for-all-by-2022-mission-national-mission-for-urban-housing/.

[53] W. Elenbaas, "Heat dissipation of parallel plates by free convection," *Physica,* vol. 9, no. 1, pp. 1-28, 1942.

[54] L. F. A. Azevedo and E. M. Sparrow, "Natural Convection in Open-Ended Inclined Channels," *Journal of Heat Transfer,* vol. 107, no. 4, pp. 893-901, 1985.

[55] G. V. Fracastoro, L. Giai and M. Perino, "Ventilation and Cooling," in *18th AIVE Conference*, Athens, 1997.

[56] F. Miranville, H. Boyer, T. Mara and F. Garde, "On the thermal behaviour of roof-mounted radiant barriers under tropical and humid climatic conditions: modelling and empirical validation," *Energy and Buildings,* vol. 35, no. 10, pp. 997-1008, 2003.

[57] W. Miller, J. Wilson and A. Karagiozis, "The impact of above-sheathing ventilation on the thermal and moisture performance of steep-slope residential roofs and attics," in *Fifteenth Symposium on Improving Building Systems in Hot and Humid Climates*, Orlando, 2006.

[58] P. H. Biwole, M. Woloszyn and C. Pompeo, "Heat transfers in a double-skin roof ventilated by natural convection in summer time," *Energy and Buildings,* vol. 40, pp. 1487-1497, 2008.

[59] Ludowici, "French lwo profile interlocking clay tile," Ludowici, [Online]. Available: https://ludowici.com/product/french/. [Accessed 27 March 2022].

[60] M. Chari, "Mangalore's age-old tiles survive the shift towards cement," Scroll.in, 3 July 2014. [Online]. Available: https://scroll.in/article/668853/mangalores-age-old-tiles-survive-the-shift-towards-cement. [Accessed 27 March 2022].

[61] I. J. S. Shet, "Ruined Glory," Mangalore Today, 17 September 2010. [Online]. Available: https://www.mangaloretoday.com/opinion/Ruined-Glory.html. [Accessed 27 March 2022].

[62] D. Sateesh, "Tile Colonialism," 2017.

[63] J. M. Hughes and H. Weill, "Asbestos Exposure —Quantitative Assessment of Risk," *American Review of Respiratory Disease,* vol. 1, 1985.

[64] A. L. Frank and T. K. Joshi, "The Global Spread of Asbestos," *Annals of Global Health,* vol. 80, no. 4, pp. 257-262, 2014.

[65] E. Goswami, V. Craven, D. L. Dahlstrom, D. Alexander and F. Mowat, "Domestic Asbestos Exposure: A Review of Epidemiologic and Exposure Data," *International Journal of Environmental Research and Public Health,* vol. 10, no. 11, pp. 5629-5670, 2013.

[66] Bureau of Indian Standards, Civil Engineering Division Council, Clay Products for Buildings Sectional Committee, "Clay Roofing Tiles, Managalore Pattern -- Specification (Third Revision)," Bureau of Indian Standards, New Delhi, 2002.

[67] No Broker Times, "All You Need to Know About Mangalore Tiles," The No Broker Times, [Online]. Available: https://www.nobroker.in/blog/all-you-need-to-know-about-mangalore-tiles/. [Accessed 27 March 2022].

[68] I. M. Cook, "Mud Marine: The Rise and Fall of Mangalore Tiles," *Sharpening the Haze: Visual Essays on Imperial History and Memory,* pp. 111-122, 2020.

[69] Havells, "I Cool Personal Fan," Havells India Ltd., [Online]. Available: https://www.havells.com/en/consumer/fans/personal-fan/personal/i-cool-(3).html#specification. [Accessed 21 March 2022].

[70] G. Clark and C. Allen, "The Estimation of Atmospheric Radiation for Clear and Cloudy Skies," in *2nd National Passive Solar Conference (AS/ISES)*, 1978.

[71] Big Ladder Software, "Engineering Reference - EnergyPlus 9.5," Big Ladder Software, LLC., 20 December 2021. [Online]. Available: https://bigladdersoftware.com/epx/docs/9-5/engineering-reference/. [Accessed 19 February 2022].

[72] G. N. Walton, "Thermal Analysis Research Program Reference Manual. NBSSIR 83-2655," National Bureau of Standards, 1983.

[73] W. H. McAdams, Heaty Transmission: 3rd Edition, New York: McGraw-Hill, 1954.

[74] E. W. Lemmon, M. O. McLinden and M. L. Huber, "NIST STANDARD REFERENCE DATABASE 23: Nist Reference Fluid Thermodynammic and Transport Properties - REFPROP," National Institute of Standard and Technology, Gaithersburg, 2002.

[75] E. G. Cravalho, J. L. Smith, Jr., J. B. Brisson and G. McKinley, 2.006 Property Data Tables, Cambridge: MIT CopyTech, 2013.

[76] K. Stephan and A. Laesecke, "The Thermal Conductivity of Fluid Air," *Journal of Physical and Chemical Reference Data,* vol. 14, pp. 227-234, 1985.

[77] J. R. Hottel, "A Catalog of Radiation Heat Transfer Configuration Factors: 3rd Edition: Section C-14: Two finitie rectangles of same length, having one common edge, and at an angle of 90 degrees to each other.," The University of Texas at Austin, [Online]. Available: http://www.thermalradiation.net/sectionc/C-14.html. [Accessed 25 March 2022].

[78] M. D'Orazio, C. Di Perna and E. Di Giuseppe, "The effects of roof covering on the thermal performance of highly insulated roofs," *Energy and Buildings,* vol. 42, pp. 1619-1627, 2010.

[79] R. Paolini, G. Terraneo, C. Ferrari, M. Sleiman, A. Muscio, P. Metrangolo, T. Poli, H. Destaillats, M. Zinzi and R. Levinson, "Effects of soiling and weathering on the albedo of building envelope materials: lessons learned from natural exposure in two European cities and tuning of a laboratory simulation practice," *Solar Energy Materials and Solar Cells,* vol. 205, 2020.

[80] G. Y. Goswami, Principles of Solar Engineering: Third Edition, Boca Ration: CRC Press/Taylor and Francis Group, 2015.

[81] B. Anderson, Solar energy: fundamentals in building design, New York: McGraw Hill, 1977.

[82] M. F. Modest, Radiation Heat Transfer: Third Edition, Oxford: Academic Press, 2013.

[83] D. K. Edwards, A. F. Mills and V. E. Denny, Transfer Processes: Second Edition, New York: Hemisphere/McGraw-Hill, 1979.

[84] T. Kubota, R. Watanabe and H. Miyashita, "Effects of thermal radiation and insolation on passenger compartments of an automobile," in *IEEE International Conference on Control Applications*, Yokohama, 2010.

[85] S. Watanabe, T. Horikoshi, J. Ishii and A. Tomita, "The measurement of the solar absorptance of the clothed human body – The case of Japanese, college-aged male subjects," *Building and Environment,* vol. 59, pp. 492-500, 2013.

[86] C. Martin, "Thermal Adjustment of Man and Animals to External Conditions," *The Lancet,* vol. 216, no. 5587, pp. 673-678, 1930.

[87] B. Nielsen, "Solar heat load, heat balance during exercise in clothed subjects," *European Journal of Applied Physiology and Occupational Physiology,* vol. 60, pp. 452-456, 1990.

[88] J. A. Clark and K. Cena, "Net Radiation and Heat Transfer through Clothing: The Effects of Insulation and Colour," *Ergonomics,* vol. 21, no. 9, pp. 691-696, 1978.

[89] G. A. Abanto, M. Karkri, G. Lefebvre, M. Horn, J. L. Solia and M. M. Gómez, "Thermal properties of adobe employed in Peruvian rural areas: Experimental results and numerical simulation of a traditional bio-composite material," *Case Studies in Construction Materials,* vol. 6, pp. 177-191, 2017.

[90] Y. Wang, Y. Lu, R. Horton and T. Ren, "Specific Heat Capacity of Soil Solids: Influences of Clay Content, Organic Matter, and Tightly Bound Water," *Soil Science Society of America Journal,* vol. 83, pp. 1062-1066, 2019.

[91] B. Evstatiev, "Heat flow through green and tile roofs under winter conditions," University of Ruse, Ruse, 2013.

[92] A. Ekinci, A. Abki and M. Mirzababaei, "Parameters Controlling Strength, Stiffness and Durability of a Fibre-Reinforced Clay," *International Journal of Geosynthetics and Ground Engineering,* vol. 8, no. 6, 2022.

[93] F. Kreith, Principles of Heat Transfer, Boston: PWS Publishing Co., 1997.

[94] Weather Underground: VABJ, "Bhuj, India Weather History," The Weather Channel (IBM), [Online]. Available: https://www.wunderground.com/history/daily/in/bhuj/VABJ. [Accessed 19 November 2021].

[95] J. Cano, "Photovoltaic modules: Effect of tilt angle on soling," Arizona State University, Tempe, 2011.

[96] G. Salvalai, M. Imperadori, F. Lumina, E. Mutti and I. Polese, "Architecture for refugees, resilience shelter project: A case study using recycled skis," *Procedia Engineering,* vol. 180, pp. 1110-1120, 2017.

[97] T. Scott-Smith, "A Slightly Better Shelter?," Limn, [Online]. Available: https://limn.it/articles/a-slightly-better-shelter/. [Accessed 6 March 2022].

[98] R. Kronenburg, "1 - Introduction: The development of fabric structures in architecture," in *Fabric Structures in Architecture*, Cambridge, Woodhead Publishing, 2015, pp. 1-21.

[99] R. A. Shareef and H. A. S. Al-Alwan, "Sustainable textile architecture: history and," in *IOP Conf. Series: Materials Science and Engineering: 4th International Conference on Engineering Sciences (ICES 2020)*, 2021.

[100] E. Hasgül and A. Özsoy, "A living solution for refugees: Transient, modular and flexible sheltering systems," in *ENHR Conference: Affordable Housing for All! Redefining the role of public and private sectors*, Tirana, 2017.

[101] United Nations HCR, "Shelter Design Catalogue," UNHCR, Geneva, 2016.

[102] United Nations High Commissioner for Refugees, "UNHCR Family Tent: UNHCR Item No 05353," UNHCR, Geneva, 2014.

[103] L. R. Glicksman and J. H. Lienhard V, Modeling and Approximation in Heat Transfer, New York: Cambridge University Press, 2016.

[104] M. K. Howlader, M. H. Rashid, D. Mallick and T. Haque, "Effects of Aggeregate Types on Thermal Properties of Concrete," *ARPN Journal of Engineering and Applied Sciences,* vol. 7, no. 7, pp. 900-907, 2012.

[105] M. Owczarek, S. Owczarek, A. Barylka and A. Grzebielec, "Measurement Method of Thermal Diffusivity of the Building Wall for Summer and Winter Seasons in Poland," *Energies,* vol. 14, no. 3836, 2021.

[106] A. P. Carman and R. A. Nelson, "The Thermal Conductivity and Diffusivity of Concrete," *University of Illinois Bulletin,* vol. XVIII, no. 34, pp. 1-39, 25 April 1921.

[107] F. P. Incropera, D. P. Dewitt, T. L. Bergman and A. S. Lavine, Fundamentals of Heat and Mass Transfer: Sixth Edition, Hoboken: John Wiley & Sons, 2007.

[108] A. G. Ostrogorsky, "Simple explicit equations for transient heat conduction in finite solids," *Journal of Heat Transfer,* vol. 131, no. 1, p. 011303, 2009.

[109] A. Zukauskas and A. Slanciauskas, Heat transfer in turbulent fluid flows, Washington: Hemisphere Publishing Corp., 1987.

[110] J. H. Lienhard V, "Heat transfer in flat-plate boundary layers: a correlation for laminar, transitional, and turbulent flow," *ASME Journal of Heat Transfer,* vol. 142, no. 6, 2020.

[111] American Society of Heating, Refrigerating, and Air-Conditioning Engineers, ASHRAE Handbook - Fundamentals, Atlanta: ASHRAE, 2017.

[112] Vaisala, "HM70 Handheld Humidity and Temperature Meter: Datasheet," Vaisala, Vantaa, 2020.

[113] Owens Corning, "Foamular & Foamular NGX 250: Publication 43522-P," Owens Corning Foam Insulation, LLC, Toledo, 2020.

[114] Johns Manville, "AP Foil-Faced Polyisocyanurate continuous insulation: Technical Data Sheet," Johns Manville, Denver, 2022.

[115] NETZSCH-Gerätebau GmbH, "Smart Solutions," Selb, 2014.

[116] NETZSCH-Gerätebau GmbH, "Operating Instructions: HFM 436/3 Lambda," Selb, 2014.

[117] R. R. Zarr and S. D. Leigh, "Standard Reference Material 1450d, Fibrous Glass Board, for Thermal Insulation Measurements," *ASTM Selected Technical Papers,* vol. STP1574, pp. 39-52, 4 February 2014.

[118] R. R. Zarr, A. C. Harris, J. F. Roller and S. D. Leigh, "NIST Special Publication 260-173. Standard Reference Materials: SRM 1450d, Fibrous-Glass Board, for Thermal Conductivity from 280 K to 340 K," Gaithersburg, 2011.

[119] K. Y. Li, C. M. Fleischmann and M. J. Spearpoint, "Determining thermal physical properties of pyrolyzing New Zealand medium density fibreboard (MDF)," *Chemical Engineering Science,* vol. 95, pp. 211-220, 2013.

[120] K. Y. Li, C. M. Fleischmann and M. J. Spearpoint, "Determining thermal physical properties of pyroliyzing New Zealand medium density fibreboard (MDF)," *Chemical Engineering Science,* vol. 95, pp. 211-220, 2013.

[121] D. Ustaomer and U. E. Baser, "Thermal and Fire Properties of Medium-density Fiberboard Prepared with Huntite/hydromagnesite and Zinc Borate," *BioResources,* vol. 15, no. 3, pp. 5940-5950, 2020.

[122] J. Zhou, H. Zhou, C. Hu and S. Hu, "Measurements of Thermal and Dielectric Properties of Medium Density Fiberboard with Different Moisture Contents," *BioResources,* vol. 8, no. 3, pp. 4185-4192, 2013.

[123] F. A. Kamke and S. C. Zylkowski, "Effects of wood-based panel characteristics on thermal conductivty," *Forest products journal,* vol. 39, no. 5, pp. 19-24, 1989.

[124] A. Gustavsen and P. Berdahl, "Spectral Emissivity of Anodized Aluminum and the Thermal Transmittance of Aluminum Window Frames," *Nordic Journal of Building Physics,* vol. 3, no. 1970, pp. 1-12, 2003.

[125] Suncourt, "Product Data Sheet: DB204C (DB204C-DS-1215)," Suncourt, Durant, 2015.

[126] FLIR Systems, "FLIR Ex Series Data Sheet," FLIR Systems, Inc., Boston, 2013.

[127] M-D Building Products, Inc., "SmartTool Technical Specs," 2015. [Online]. Available: https://smarttoollevels.com/technical-specs/. [Accessed 7 April 2022].

[128] National Fire Protection Association, "Section 210.19 (A): Conductors - Minimum Ampacity and Size, Branch Circuits Not More Than 600 Volts," in *National Electical Code*, Quincy, National Fire Protection Association, 2019, p. 69.

[129] BESTEK, "MRI5011BU Tech Specs," 14 October 2019. [Online]. Available: https://www.bestekdirect.com/system/storage/download/MRI5011BU-500w-power-inverter.pdf. [Accessed 22 January 2022].

[130] B. Hughey, Interviewee, *Gas velocity vs Anemometer voltage.* [Interview]. 28 May 2021.

[131] Testo North America, "Testo 425 Data Sheet," Testo North America, West Chester, 2020.

[132] TSI Incorporated, "Model 8345/8346/8347/8347A VELOCICALC Air Velocity Meters: Operation and Service Manual, Rev. E," TSI Incorporated, Shoreview, 2002.

[133] Onset Computer Corporation, "HOBO T-DCI-F350-W5x3 Sensor Specifications," Onset Computer Corporation, Bourne, 2022.

[134] Degree Controls, Inc., "F350 Remote Head Datasheet," Degree Controls, Inc., Milford, 2021.

[135] Campbell Scientific, Inc., "AM25T Solid State Multiplexer (Revision: 1/10)," Campbell Scientific, Inc., Logan, 2010.

[136] Campbell Scientific, Inc., "CR10X Measurement and Control Module Operator's Manual. Revision: 2/03," Campbell Scientific, Inc., 2003, 2003.

[137] B. Nef, "Web Rqst #108130," Campbell Scientific, Inc., Logan, 2018.

[138] OMEGA: A Spectris Company, "Thermocouple types," Omega, 17 April 2019. [Online]. Available: https://www.omega.com/en-us/resources/thermocouple-types. [Accessed 14 February 2022].

[139] G. F. Strouse, "NIST Special Publication 260-157. Standard Reference Material 1751: Gallium Melting-Point Standard," Nationals Institute of Standards and Technology, Gaithersburg, 2004.

[140] J. Figueroa, Y. Cao, T. Wang, D. Torres and N. Sepulveda, "Programming emissivity on fully integrated VO2 windows," *Advanced Materials Letters,* vol. 9, no. 6, pp. 406-410, 2018.

[141] N. Ogasawara, C. Kobayashi and H. Yamada, "Image Processing for Reduction of Background Reflection from Thermal Image," *Advanced Experimental Mechanics,* vol. 3, pp. 173-179, 2018.

[142] H. Emteborg, R. Zeleny, J. Charoud-Got, G. Martos, J. Luddeke, H. Schellin and K. Teipei, "Infrared Thermography for Monitoring of Freeze-Drying Processes: Instrumental Developments and Preliminary Results," *Journal of Pharmaceutical Sciences,* vol. 103, no. 7, pp. 2088-2097, 2014.

[143] N. Kostic, N. Hadziefendic, D. Tasic and M. Kostic, "Improved measurement accuracy of industrial-commercial thermal imagers when inspecting low-voltage electrical installations," *Measurement,* vol. 185, p. 109934, 2021.

[144] C. Resch and M. Pecht, "Validation of a Thermal Model Using Infrared Thermography (SRC TR 88-18)," Institute for Systems Research, 1988.

[145] Omega: A Spectris Company, "T Type Thermocouple Duplex Extension Wire," 20 August 2012. [Online]. Available: https://assets.omega.com/pdf/cable-and-wire/thermocouple-and-rtd-wire-and-cable/EXTT_TX_WIRE.pdf. [Accessed 7 April 2022].

[146] GlobalTestSupply.com, "Watts Up Pro Portable Power Meter - 99333," PowerMeterStore.com, [Online]. Available: https://www.powermeterstore.com/p1206/watts_up_pro.php. [Accessed 8 April 2022].

[147] Onset Computer Corporation, "HOBO UX120-018 Data Logger," Onset Computer Corporation, Bourne, 2022.

[148] ANSYS, Inc., "ANSYS Fluent User's Guide: 2020 R1," ANSYS, Inc., Canonsburg, 2020.

[149] K. Ražnjević, Handbook of thermodynamic tables, New York: Begell House, 1995.

[150] J. R. Howell, A Catalog of Radiation Configuration Factors, New York: McGraw-Hill, 1982.

[151] J. D. Spitler, C. O. Pedersen and D. E. Fisher, "Interior Convective Heat Transfer in Buildings with Large Ventilative Flow Rates," *ASHRAE Transactions,* vol. 97, no. 1, pp. 505-515, 1991.

[152] Orient Electric, "Tornado II Stand Fan," Orient Electric, [Online]. Available: https://www.orientelectric.com/fan/stand-fans/tornado-ii. [Accessed 18 April 2022].

[153] GlobalPetrolPrices, "India electricity prices," GlobalPetrolPrices.com, September 2021. [Online]. Available: https://www.globalpetrolprices.com/India/electricity_prices/#hl193. [Accessed 18 April 2022].

[154] International Energy Agency, "Fuels and Technologies: Electricity," [Online]. Available: https://www.iea.org/fuels-and-technologies/electricity. [Accessed 20 March 2022].

[155] M. L. Mittal, C. Sharma and R. Singh, "Estimates of emissions from coal fired thermal power plants in India.".

[156] S. Bhawan and R. K. Puram, "CO2 Baseline Database for the Indian Power Sector," Government of India: Ministry of Power: Central Electricity Authority, New Delhi, 2018.

[157] Central Electricity Authority, "Carbon Emissions from Power Sector in 2021-22 and 2026-27," Central Electricity Authority, New Delhi, 2018.

[158] International Energy Agency, "Average CO2 emissions intensity of hourly electricity supply in India, 2018 and 2040 by scenario and average electricity demand in 2018," IEA, Paris, 2020.

[159] Carbon Footprint, "2019 Grid Electricity Emissions Factors v1.0 - June 2019," Carbon Footprint, 2019.

[160] S. Doshi, P. Roy, M. Iyer and G. Mishra, "The need and rise of secondary smart cities: a case of Bhuj," in *2020 IOP Conference Series: Earth and Environmental Science; The 5th PlanoCosmo International Conference*, 2020.

[161] Knoema, "Gujarat - Crude death rate," Knoema, [Online]. Available: https://knoema.com/atlas/India/Gujarat/Death-rate. [Accessed 25 April 2022].

[162] J. Kongoletos, N. Ghanta and L. Glicksman, "Hybrid Chilled Beam and Ceiling Fan System for Space Conditioning: Impact on Thermal Comfort & Energy Efficiency," in *CIBSE ASHRAE Technical Sympposium*, Glasgow (Online), 2020.

[163] G. Brager, "Mixed-mode cooling," *ASHRAE Journal,* vol. 48, pp. 30-7, 2006.

[164] P. Karava, A. K. Athienitis, T. Stathopoulos and E. Mouriki, "Experimental study of the thermal performance of a large institutional building with mixed-mode cooling and hybrid ventilation," *Building and Environment,* vol. 57, pp. 313-26, 2012.

[165] H. C. Spindler, "System identification and optimal control for mixed-mode cooling," *PhD Thesis,* September 2004.

[166] J. Kim, A. Tzempelikos, W. T. Horton and J. E. Braun, "Experimental investigation and data-driven regression models for performance characterization of single and multiple passive chilled beam systems," *Energy and Buildings,* vol. 158, pp. 1736-50, 2018.

[167] B. Wu, W. Cai and K. Ji, "Heat source effects on thermal comfort for active chilled beam systems," *Buildings and Environment,* vol. 141, pp. 91-102, 2018.

[168] J. Kim, A. Tzempelikos and J. E. Braun, "Energy savings potential of passive chilled beams vs air systems in various US climatic zones with different system configurations," *Energy and Buildings,* vol. 186, pp. 244-60, 2019.

[169] M. Cehlin, T. Karimipanah, U. Larsson and A. Ameen, "Comparing thermal comfort and air quality performance of two active chilled beam systems in an open-plan office," *Journal of Building Engineering,* vol. 22, pp. 56-65, 2019.

[170] C. Sekhar and L. Zheng, "Study of an integrated personalized ventilation and local fan-induced active chilled beam air conditioning system in hot and humid climate," *Building Simulation,* vol. 11, no. 4, pp. 787-801, 2018.

[171] P. Filipsson, A. Trüschel, J. Gräslund and J. O. Dalenbäck, "A thermal model of an active chilled beam," *Energy and Buildings,* vol. 149, pp. 89-90, 2016.

[172] H. Koskela, H. Häggblom, R. Kosonen and M. Ruponen, "Air distribution in office environment with asymmetric workstation layout using chilled beams," *Building and Environment,* vol. 45, no. 9, pp. 1923-1931, 2010.

[173] R. Upadhyay and R. Mora, "Performance Evaluation of Active Chilled Beam in Real Office Conditions in a High-Performance Building in Heating," *ASHRAE Transactions,* vol. 125, no. 1, pp. 238-46, 2019.

[174] B. Wu, W. Cai, H. Chen and K. Ji, "Experimental investigation on airflow pattern for active chilled beam system," *Energy and Buildings,* vol. 166, pp. 438-449, 2018.

[175] A. S. Azad, D. Rakshit, M. P. Wan, S. Babu, J. N. Sarvaiya, D. Kumar, Z. Zhang, A. S. Lamano, K. Krishnasayee, C. P. Gao, S. Valliappan, A. Goh and A. Seoh, "Evaluation of thermal comfort criteria of an active chilled beam system in tropical climate: A comparative study," *Building and Environment,* vol. 145, pp. 196-212, 2018.

[176] Y. H. Yau and J. H. Tam, "A Comparison Study for Active Chilled Beam and Variable Air Volume Systems for an Office Building," *Energy Procedia,* vol. 152, pp. 378-83, 2018.

[177] N. Ghanta, B. Coflan and L. Glicksman, "Interaction of Chilled Beam Flows and its Impact on Air Circulation and Thermal Comfort in Buildings," in *Prometheus Journal-Proceddings of the 3rd International Graduate Student Symposium, "Buildings Cities and Performance"*, IIT Chicago, 2019.

[178] ASHRAE, ANSI/ASHRAE Standard 55-2017: Thermal Environmental Conditions for Human Occupancy, Atlanta: ASHRAE, 2017.

[179] B. W. Olesen and K. C. Parsons, "Introduction to thermal comfort standards and to the proposed new version of EN ISO 7730," *Energy and Buildings,* vol. 34, no. 6, pp. 537-48, 2002.

[180] G. Havenith, I. Holmér and K. Parsons, "Personal factors in thermal comfort assessment: clothing properties and metabolic heat production," *Energy and Buildings,* vol. 34, pp. 581-91, 2002.

[181] T. Hoyt, S. Schiavon, F. Tartarini, T. Cheung, K. Steinfeld, A. Piccoli and D. Moon, "CBE Thermal Comfort Tool," University of California, Berkeley, Center for the Built Environment, 2019.

[182] A. Lipczynska, S. Schiavon and L. T. Graham, "Thermal comfort and self-reported productivity in an office with ceiling fans in the tropics," *Building and Environment,* vol. 135, pp. 202-12, 2018.

[183] N. Ghanta, J. Kongoletos and L. Glicksman, "Comfort control and improved thermostat location in conference rooms and academic working spaces," *Building and Environment,* vol. 205, p. 108192, 2021.

[184] P. O. Fanger, Thermal Comfort: Analysis and Applications in Environmental Engineering, Copenhagen: Danish Technical Press, 1970.

[185] S. A. Mumma, "Overview of Integrating Dedicated Outdoor Air Systems with Parallel Terminal," *ASHRAE Transactions,* vol. 107, p. 545, 2001.

[186] K. Roth, J. Dieckmann, R. Zogg and J. Brodrick, "Chilled beam cooling," *ASHRAE Journal,* vol. 49, no. 9, p. 84, 2007.

[187] G. Cao, J. Kurnitski, M. Ruponen, P. Mustakallio and O. Seppänen, "Plane-air-jet corner zone," *International Journal of Ventilation,* vol. 7, no. 4, pp. 287-297, 2008.

[188] G. Cao, M. Sivukari, J. Kurnitski, M. Ruponen and O. Seppänen, "Particle Image Velocimetry," *Building and Environment,* vol. 45, no. 9, pp. 1932-1940, 2010.

[189] R. Kosonen, M. Virta and H. Oy, "Taking flexibity into account in designing beam," in *WellBeing Indoors Clima: Proceedings of Clima*, Helsinki, 2007.

[190] J. Woollett and J. Rimmer, Active and Passive Beam Application Design Guide: REHVA-ASHRAE Guidebook No. 21, Atlanta: American Society of Heating Refrigeration and Air Conditioning Engineers, 2015.

[191] K.-N. Rhee, M.-S. Shin and S.-H. Choi, "Thermal uniformity in an open plan room with an active chilled beam system and conventional air distribution systems," *Energy and Buildings,* vol. 93, pp. 236-248, 2015.

[192] H. Koskela, H. Häggblom, R. Kosonen and M. Ruponen, "Flow pattern and thermal comfort in office environment with active chilled beams," *HVAC&R Research,* vol. 18, no. 4, pp. 723-736, 2012.

[193] H. Koskela, P. Saarinen, H. Freitag, M. Schmidt, D. Müller and P. Mustakallio, "LES simulation of the active chilled beam flow pattern," in *Roomvent 2014: 13th SCANVAC international conference on air distribution in rooms*, 2014.

[194] T. Goto, J. Toftum, R. de Dear and P. Fanger, "Thermal Sensation and Comfort with Transient Metabolic Rates," in *Indoor Air 2002*, 2002.

[195] J. v. Hoof, H. S. M. Kort, J. L. M. Hensen, M. S. H. Duijnstee and P. G. S. Rutten, "Thermal comfort and HVAC design for people with dementia," in *9th International Healthy Buildings Conference and Exhibition (Healthy Buildings 2009)*, Syracuse, 2009.

[196] W. Wang, R. Zmeureanu and H. Rivard, "Applying multi-objective genetic algorithms in green building design optimization," *Building and Environment,* vol. 40, no. 11, pp. 1512-1525, 2005.

[197] A. Mylonas, O. B. Kazanci, R. K. Andersen and B. W. Olesen, "Capabilities and limitations of wireless CO2, temperature and relative humidity sensors," *Building and Environment,* vol. 154, pp. 362-374, 2019.

[198] W. Tian, Y. Fu, Q. Wang, T. A. Sevilla and W. Zuo, "Optimization on thermostat location in an office room using the coupled simulation platform in modelica buildings library: a pilot study," in *4th International Conference on Building Energy and Environment (COBEE2018)*, 2018.

[199] O. M. Borier, O. B. Kazanci, B. W. Olesen and D. Khovalyg, "Which sensor type at which location should offices with south orientated window choose to improve comfort and reduce energy consumption?," *Journal of Physics: Conference Series,* vol. 1343, pp. 1-6, 2019.

[200] F. M. White, Fluid mechanics, Boston: Tata McGraw-Hill Education, 1999.

[201] N. Ghanta, "Meta-modeling and Optimization of Computational Fluid Dynamics (CFD) analysis in thermal comfort for energy-efficient Chilled Beams-based Heating, Ventilation and Air-Conditioning (HVAC) systems," Massachusetts Institute of Technology, Cambridge, 2020.

[202] X. Yuan, Q. Chen, L. R. Glicksman, Y. Hy and X. Yang, "Measurements and computations of room airflow with displacement ventilation," *ASHRAE Transactions,* vol. 105, 1999.

[203] G. K. Rencken, E. K. Rutherford, N. Ghanta, J. Kongoletos and L. Glicksman, "Patterns of SARS-CoV-2 aerosol spread in typical classrooms," *Building and Environment,* vol. 204, 2021.

[204] ASHRAE, "ASHRAE Position Document on Airborne Infectious Diseases," The American Society of Heating, Refrigeration, and Air-Conditioning Engineers, Atlanta, 2020.

[205] R. L. Riley and E. A. Nardell, "Clearing the Air: The Theory and Application of Ultraviolet Air Disinfection," *American Review of Respiratory Diseases,* vol. 139, no. 5, pp. 1286-1294, 1989.

[206] J. Howard, A. Huang, Z. Li, Z. Tufekci, V. Zdimal, H.-M. v. d. Westhuizen, A. v. Delft, A. Price, L. Fridman, L.-H. Tang, V. Tang, G. L. Watson, C. E. Bax, R. Shaikh, F. Questier, D. Hernandez, L. F. Chu, C. M. Ramirez and A. W. Rimoin, "An evidence review of face masks against COVID-19," *Proceedings of the National Academy of Sciences,* vol. 118, no. 4, 2021.

[207] The Association of Energy Engineers: Utah Chapter, "The Wells-Riley Equation and COVID-19: Reducing Risk in Indoor Environments," AEE Utah, Salt Lake City, 2020.

[208] Centers for Disease Control and Prevention, "Social Distancing: Keep a Safe Distance to Slow the Spread," CDC, 17 November 2020. [Online]. Available: https://www.cdc.gov/coronavirus/2019-ncov/prevent-getting-sick/social-distancing.html. [Accessed 22 April 2021].

[209] Y. Li, H. Qian, J. Hang, X. Chen, P. Cheng, H. Ling, S. Wang, P. Liang, J. Li, S. Xiao, J. Wei, L. Liu, B. J. Cowling and M. Kang, "Probable airborne transmission of SARS-CoV-2 in a poorly ventilated restaurant," *Building and Environment,* vol. 196, 2021.

[210] Y. Shen, C. Li, H. Dong, Z. Wang, L. Martinez, Z. Sun, A. Handel, Z. Chen, E. Chen, M. H. Ebell, F. Wang, B. Yi, H. Wang, x. Wang, A. Wang, B. Chen, Y. Qi, L. Liang, Y. Li, F. Ling, J. Chen and G. Xu, "Community Outbreak Investigation of SARS-CoV-2 Transmission Among Bus Riders in Eastern China," *JAMA Internal Medicine,* vol. 180, no. 12, pp. 1665-1671, 2020.

[211] D. Normile, "The Metropole, Superspreaders, and Other Mysteries," *Science,* vol. 339, no. 6125, pp. 1272-1273, 2013.

[212] Z. Ding, H. Qian, B. Xu, Y. Huang, T. Miao, H.-L. Yen, S. Xiao, L. Cui, X. Wu, W. Shao, Y. Song, L. Sha, L. Zhou, Y. Xu, B. Zhu and Y. Li, "Toilets dominate environmental detection of severe acute respiratory syndrome coronavirus 2 in a hospital," *Science of The Total Environment,* vol. 753, 2021.

[213] Z. T. Ai and C. M. Mak, "Large eddy simulation of wind-induced interunit dispersion around multistory buildings," *International Journal of Indoor Environment and Health,* vol. 26, no. 2, pp. 259-273, 2015.

[214] Y. Li, S. Duan, I. T. S. Yu and T. W. Wong, "Multi-zone modeling of probable SARS virus transmission by airflow between flats in Block E, Amoy Gardens," *International Journal of Indoor Environment and Health,* pp. 96-111, 2004.

[215] P. Azimi, Z. Keshavarz, J. G. C. Laurent, B. Stephens and J. G. Allen, "Mechanistic transmission modeling of COVID-19 on the Diamond Princess cruise ship demonstrates the importance of aerosol transmission," *Proceedings of the National Academy of Sciences,* vol. 118, no. 8, 2021.

[216] G. Kampf, Y. Brüggemann, H. Kaba, J. Steinman, S. Pfaender, S. Scheithauer and E. Steinmann, "Potential sources, modes of transmission and effectiveness of prevention measures against SARS-CoV-2," *Journal of Hospital Infection,* vol. 106, no. 4, pp. 678-697, 2020.

[217] I. F.-N. Hung, V. C.-C. Cheng, X. Li, A. R. Tam, D. L.-L. Hung, K. H.-Y. Chiu, C. C.-Y. Yip, J.-P. Cai, D. T.-Y. Ho, S.-C. Wong, S. S.-M. Leung, M.-Y. Chu, M. O.-Y. Tang, J. H.-K. Chen, R. W.-S. Poon, A. Y.-F. Fung, R. R. Zhang, E. Y.-W. Yan, L.-L. Chen, C. Y.-K. Choi, K.-H. Leung, T. W.-H. Chung, S. H.-Y. Lim, T. P.-W. Lam, J. F.-W. Chan, K.-H. Chan, T.-C. Wu, P.-L. Ho, J. W.-M. Chan, C.-S. Lau, K. K.-W. To and K.-Y. Yuen, "SARS-CoV-2 shedding and seroconversion among passengers quarantined after disembarking a cruise ship: a case series," *The Lancet Infectious Diseases,* vol. 10, no. 9, pp. 1051-1060, 2020.

[218] J. S. Kutter, M. I. Spronken, P. L. Fraaij, R. A. Fouchier and S. Hersft, "Transmission routes of respiratory viruses among humans," *Current Opinion in Virology,* vol. 28, pp. 142-151, 2018.

[219] E. C. Cole and C. E. Cook, "Characterization of infectious aerosols in health care facilities: An aid to effective engineering controls and preventive strategies," *American Journal of Infection Control,* vol. 26, no. 4, pp. 453-464, 1998.

[220] S. Asadi, N. Bouvier, A. S. Wexler and W. D. Ristenpart, "The coronavirus pandemic and aerosols: Does COVID-19 transmit via expiratory particles?," *Aerosol Science and Technology,* vol. 54, no. 6, pp. 635-638, 2020.

[221] W. E. Bischoff, K. Swett, I. Leng and T. R. Peters, "Exposure to Influenza Virus Aerosols During Routine Patient Care," *The Journal of Infectious Diseases,* vol. 7, no. 7, pp. 1037-1046, 2013.

[222] B. Blocken, F. Malizia, T. v. Druenen and T. Marchal, "Towards aerodynamically equivalent COVID19 1.5 m social distancing for walking and running," *preprint,* 2020.

[223] L. S. Sonkin, "The Role of Particle Size in Experimental Air-Borne Infection," *American Journal of Epidemiology,* vol. 53, no. 3, pp. 337-354, 1951.

[224] K. P. Fennelly, J. W. Martyny, K. E. Fulton, I. M. Orme, D. M. Cave and L. B. Heifets, "Cough-generated Aerosols of Mycobacterium tuberculosis: A New Method to Study Infectiousness," *American Journal of Respiratory and Critical Care Medicine,* vol. 169, no. 5, pp. 604-609, 2003.

[225] C. E. Wainwright, M. W. France, P. O'Rourke, S. Anuj, T. J. Kidd, M. D. Nissen, T. P. Sloots, C. Coulter, Z. Ristovski, M. Hargreaves, B. R. Rose, C. Harbour, S. C. Bell and K. P. Fennelly, "Cough-generated aerosols of Pseudomonas aeruginosa and other Gram-negative bacteria from patients with cystic fibrosis," *Thorax,* vol. 64, no. 11, pp. 926-931, 2009.

[226] W. F. Wells, Airborne Contagion and Air Hygiene, Cambridge: Cambridge University Press, 1955.

[227] W. F. Wells, "On Air-Borne Infection: Study II. Droplets and Droplet Nuclei.," *American Journal of Epidemiology,* vol. 20, no. 3, pp. 611-618, 1934.

[228] W. C. Hinds, Aerosol technology: properties, behavior, and measurement of airborne particles, New York: Wiley, 1999.

[229] O. Lidwell and A. Towers, "Protection from microbial contamination in a room ventilated by a uni-directional air flow," *Journal of Hygiene,* vol. 67, no. 1, pp. 95-106, 1969.

[230] M. Mitman, "Aerial Infection," *The British Medical Journal,* vol. 1, no. 4385, pp. 71-74, 1945.

[231] C. P. Yaglou and U. Wilson, "Disinfection of Air by Air Conditioning Processes," *Aerobiology,* pp. 129-132, 1942.

[232] W. F. Wells, M. W. Wells and T. S. Wilder, "The Environmental Control of Epidemic Contagion," *American Journal of Epidemiology,* vol. 35, no. 1, pp. 97-121, 1942.

[233] M. Yamakawa, N. Hosotani, K. Matsuno, S. Asao, T. Inomoto and S. Ishihara, "Viral Infection Simulation in an Indoor Environment," in *The Asian Symposium on Computational Heat Transfer and Fluid Flow 2015*, Busan, 2015.

[234] L. Morawska, J. W. Tang, W. Bahnfleth, P. M. Bluyssen, A. Boerstra, G. Buonanno, J. Cao, S. Dancer, A. Floto, F. Franchimon, C. Haworth, J. Hogeling, C. Isaxon, J. L. Jimenez, J. Kurnitski, Y. Li, M. Loomans, G. Marks, L. C. Marr, L. Mazzarella, A. K. Melikov, S. Miller, D. K. Milton, W. Nazaroff, P. V. Nielsen, C. Noakes, J. Peccia, X. Querol, C. Sekhar, O. Seppänen, S.-i. Tanabe, K. Wai, K. W. Tham, P. Wargocki, A. Wierzbicka and M. Yao, "How can airborne transmission of COVID-19 indoors be minimised?," *Environmental International,* vol. 142, 2020.

[235] M. Nicas, W. W. Nazaroff and A. Hubbard, "Toward Understanding the Risk of Secondary Airborne Infection: Emission of Respirable Pathogens," *Journal of Occupational and Environmental Hygiene,* vol. 2, no. 3, pp. 143-154, 2005.

[236] E. C. Riley, G. Murphy and R. L. Riley, "Airborne Spread of Measles in a Suburban Elementary School," *American Journal of Epidemiology,* vol. 107, no. 5, pp. 421-432, 1978.

[237] D. A. Rothamer, S. Sanders, D. Reindl and T. H. Bertram, "Strategies to minimize SARS-CoV-2 transmission in classroom settings: Combined impacts of ventilation and mask effective filtration efficiency," *medRxiv preprint,* 2021.

[238] REHVA, "REHVA COVID-19 guidance document v4.0," Federation of European Heating, Ventilation and Air Conditioing Associates, Brussels, 2020.

[239] B. Stephens, "HVAC filtration and the Wells-Riley approach to assessing risks of infectious airborne diseases," NAFA, Virginia Beach, 2012.

[240] M. Evans, "Avoiding COVID-19: Aerosol Guidelines," *arXiv preprint,* 2020.

[241] J. Lu, J. Gu, K. Li, C. Xu, W. Su, Z. Lai, D. Zhou, C. Yu, B. Xu and Z. Yang, "COVID-19 Outbreak Associated with Air Conditioning in Restaurant, Guangzhou, China, 2020," *Emerging Infectious Diseases,* vol. 26, no. 7, pp. 1628-1631, 2020.

[242] K.-S. Kwon, J.-I. Park, Y. J. Park, D.-M. Jung, K.-W. Ryu and J.-H. Lee, "Evidence of Long-Distance Droplet Transmission of SARS-CoV-2 by Direct Air Flow in a Restaurant in Korea," *Journal of Korean Medical Science,* vol. 35, no. 46, 2020.

[243] C. E. Walker, L. K. Norford and L. R. Glicksman, "Assessing the Performance of a Naturally Ventilated Office Building," *ASHRAE Transactions,* vol. 112, no. 1, pp. 281-294, 2006.

[244] F. D. Espinosa and L. R. Glicksman, "Determining thermal stratification in rooms with high supply momentum," *Building and Environment,* pp. 99-114, 2017.

[245] R. K. Bhagat, M. S. D. Wykes, S. B. Dalziel and P. F. Linden, "Effects of ventilation on the indoor spread of COVID-19," *Journal of Fluid Mechanics,* vol. 903, 2020.

[246] J. Srebric, V. Vukovic, G. He and X. Yang, "CFD boundary conditions for contaminant dispersion, heat transfer and airflow simulations around human occupants in indoor environments," *Building and Environment,* vol. 43, no. 3, pp. 294-303, 2008.

[247] Q. He, J. Niu, N. Gao, T. Zhu and J. Wu, "CFD study of exhaled droplet transmission between occupants under different ventilation strategies in a typical office room," *Building and Environment,* vol. 46, no. 2, pp. 397-408, 2011.

[248] M. P. Wan, C. Y. H. Chao, Y. D. Ng, G. N. Sze To and W. C. Yu, "Dispersion of Expiratory Droplets in a General Hospital Ward with Ceiling Mixing Type Mechanical Ventilation System," *Aerosol Science and Technology,* vol. 41, no. 3, pp. 244-258, 2007.

[249] M. P. Wan, G. N. Sze To, C. Y. H. Chao, L. Fang and A. Melikov, "Modeling the Fate of Expiratory Aerosols and the Associated Infection Risk in an Aircraft Cabin Environment," *Aerosol Science and Technology,* vol. 43, no. 4, pp. 322-343, 2009.

[250] N. Bartzokas, M. Gröndahl, K. Patanjali, M. Peyton, B. Saget and U. Syam, "Why Opening Windows Is a Key to Reopening Schools," New York City, 2021.

[251] R. Padilla and S. J. Beard, "Seating in outdoor structures isn't always safer than indoor dining. Here's why.," McLean, 2021.

[252] M. Bivolarova, J. Ondráček, A. Melikov and V. Ždímal, "A comparison between tracer gas and aerosol particles distribution indoors: The impact of ventilation rate, interation of airflows, and presence of objects," *Indoor Air,* vol. 27, no. 6, pp. 1-12, 2017.

[253] D. Rim and A. Novoselac, "Transport of particulate and gaseous pollutants in the vicinity of a human body," *Building and Environment,* vol. 44, pp. 1840-1849, 2009.

[254] B. A. Craven and G. S. Settles, "A Computational and Experimental Investigation of the Human Thermal Plume," *Journal of Fluids Engineering,* vol. 128, no. 6, pp. 1251-1258, 2006.

[255] C. Xu, P. V. Nielsen, G. Gong, L. Liu and R. L. Jensen, "Measuring the exhaled breath of a manikin and human subjects," *Indoor Air,* vol. 25, pp. 188-197, 2015.

[256] Pacer Instruments, Inc., "DA30 User Manual," Pacer Instruments, Inc., Chippewa Falls, 2007.

Appendix A: Campbell Scientific CR10X/AM25T temperature measurement program

1 reading every 10 seconds, averaged during each minute and recorded at the top of the minute.

```
;{CR10X}
;
*Table 1 Program
  01: 10.0000   Execution Interval (seconds)   ;sample every 10 seconds

1:  Batt Voltage (P10)       ;record DC power supply/battery voltage on line 1
 1: 1        Loc [ BattVolt  ]

2:  Internal Temperature (P17)  ;record internal temperature on line 2
 1: 2        Loc [ CR10XTmpC ]

3:  Set Port(s) (P20) ;Configure Control Ports for 1 millisecond pulse    ;Configuration prep for AM25T
 1: 9999     C8..C5 = nc/nc/nc/nc
 2: 9933     C4..C1 = nc/nc/1ms/1ms

4:  Do (P86) ;Turn On AM25T
 1: 42       Set Port 2 High

5:  Full Bridge (P6) ;Measure the output of the reference temp. full bridge
 1: 1        Reps
 2: 23       25 mV 60 Hz Rejection Range
 3: 1        DIFF Channel
 4: 1        Excite all reps w/Exchan 1
 5: 1200     mV Excitation
 6: 4        Loc [ RefTemp_C ]
 7: -0.001   Multiplier
 8: 0.09707  Offset

6:  BR Transform Rf[X/(1-X)] (P59) ;Calculate RTD resistance R/R0 (RTD temp spec of +- 0.02 deg C)
 1: 1        Reps
 2: 4        Loc [ RefTemp_C ]
 3: 10.025   Multiplier (Rf)

7:  Temperature RTD (P16) ;Calculate Reference Temperature
 1: 1        Reps
 2: 4        R/R0 Loc [ RefTemp_C ]
 3: 4        Loc [ RefTemp_C ]
 4: 1        Multiplier
 5: 0        Offset

8:  Beginning of Loop (P87) ;Loop through thermocouple channels
 1: 0        Delay
 2: 25       Loop Count

    9:  Do (P86) ;Clock AM25T twice
     1: 71       Pulse Port 1
```

```
   10:  Do (P86)
    1: 71       Pulse Port 1

   11:  Thermocouple Temp (DIFF) (P14) ;Measure the connected thermocouple
    1: 1        Reps
    2: 21       2.5 mV 60 Hz Rejection Range
    3: 1        DIFF Channel
    4: 1        Type T (Copper-Constantan)
    5: 4        Ref Temp (Deg. C) Loc [ RefTemp_C ]
    6: 5     -- Loc [ Ch1       ]
    7: 1        Multiplier
    8: 0        Offset

12:  End (P95) ;End Loop

13:  Do (P86) ;Turn off AM25T
 1: 52       Set Port 2 Low

14:  If time is (P92) ;Output data 1x Minute
 1: 0        Minutes (Seconds --) into a
 2: 1        Interval (same units as above)
 3: 10       Set Output Flag High (Flag 0)

15:  Set Active Storage Area (P80)^4919
 1: 1        Final Storage Area 1
 2: 100      Array ID

16:  Real Time (P77)^26908  ;Output with timestamp  (Year, Day of year (previous day as midnight), 2400 at
midnight)
 1: 1220     Year,Day,Hour/Minute (midnight = 2400)

17:  Average (P71)^8395
 1: 26       Reps
 2: 4        Loc [ RefTemp_C ]

18:  Sample (P70)^8438
 1: 2        Reps
 2: 1        Loc [ BattVolt  ]

19:  Serial Out (P96)
 1: 52       Printer Comma/9600 Baud

*Table 2 Program
  02: 0.0000    Execution Interval (seconds)

*Table 3 Subroutines

End Program
```

Appendix B: Catalog of Thermogram Results

Note that the color scales vary based on the testing conditions.

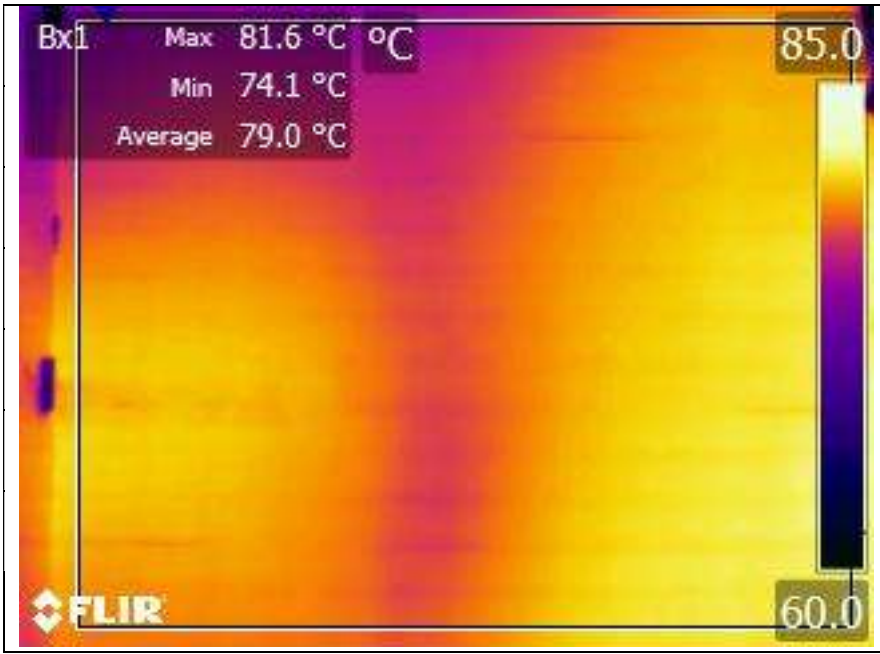

T_{inlet}	22.2 °C
$T_{Upper\ T/C}$	38.4 °C
$\Delta T_{ceiling}$	56.8 °C
$\Delta T_{inside\ air}$	13.6 °C
$\dot{Q}_{cond}$	152.4 W
Re_{inlet}	7,019
h_{inlet}	2.2 W/(m²·K)
$h_{upper\ T/C}$	3.1 W/(m²·K)

Figure 102: Thermogram from 1" offset jet, 0.91 m/s jet from bottom of image

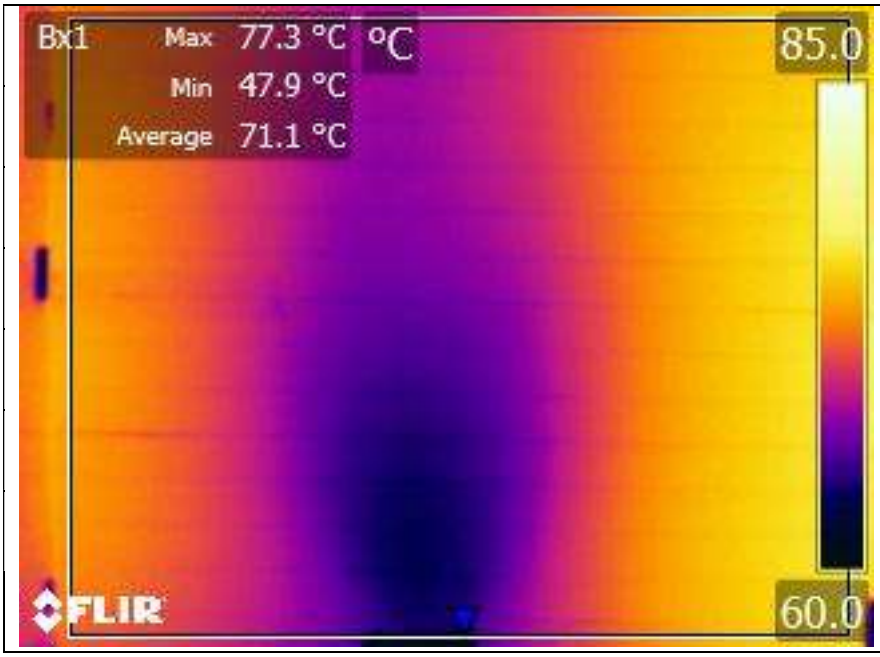

T_{inlet}	22.3 °C
$T_{Upper\ T/C}$	44.0 °C
$\Delta T_{ceiling}$	48.8 °C
$\Delta T_{inside\ air}$	12.9 °C
$\dot{Q}_{cond}$	154.0 W
Re_{inlet}	7,011
h_{inlet}	3.0 W/(m²·K)
$h_{upper\ T/C}$	5.5 W/(m²·K)

Figure 103: Thermogram from 1" offset jet, 0.91 m/s jet from bottom of image angled 20 degrees towards ceiling

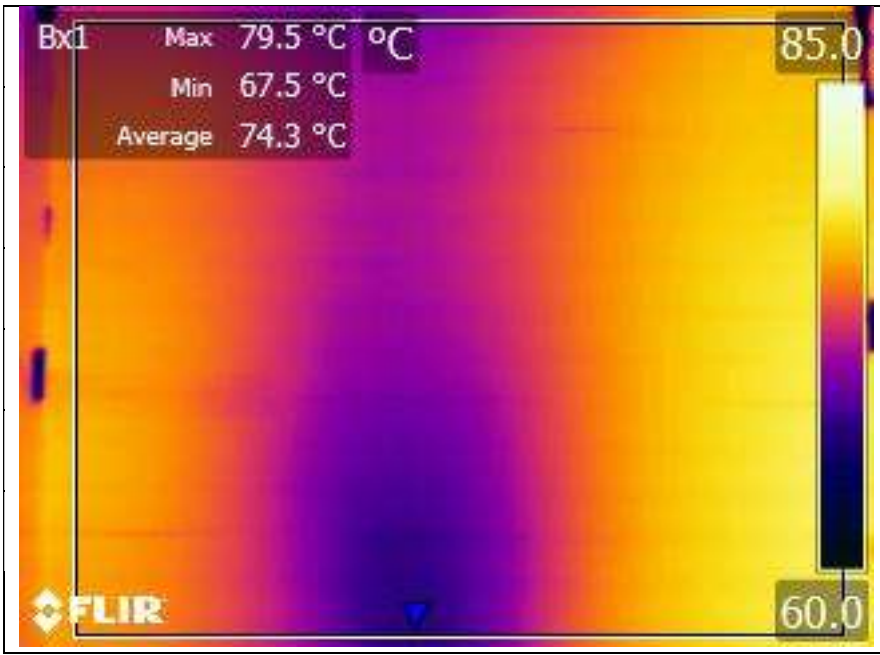

T_{inlet}	22.2 °C
$T_{Upper\ T/C}$	42.4 °C
$\Delta T_{ceiling}$	52.1 °C
$\Delta T_{inside\ air}$	12.6 °C
$\dot{Q}_{cond}$	153.3 W
Re_{inlet}	7,016
h_{inlet}	2.7 W/(m^2·K)
$h_{upper\ T/C}$	4.4 W/(m^2·K)

Figure 104: Thermogram from 1" offset jet, 0.91 m/s jet from bottom of image angled both 20 degrees towards ceiling and 20 degrees horizontal spread, with a compound louver

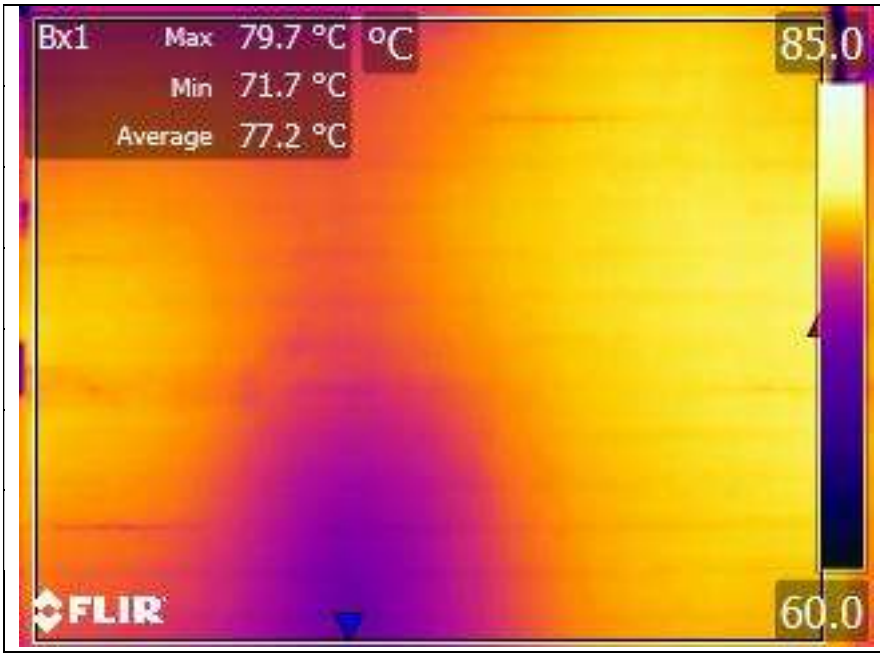

T_{inlet}	21.4 °C
$T_{Upper\ T/C}$	32.4 °C
$\Delta T_{ceiling}$	55.8 °C
$\Delta T_{inside\ air}$	13.7 °C
$\dot{Q}_{cond}$	152.3 W
Re_{inlet}	7,067
h_{inlet}	2.3 W/(m^2·K)
$h_{upper\ T/C}$	2.8 W/(m^2·K)

Figure 105: Thermogram from 1" offset jet, 0.91 m/s jet from bottom of image, 20 degree horizontal spread

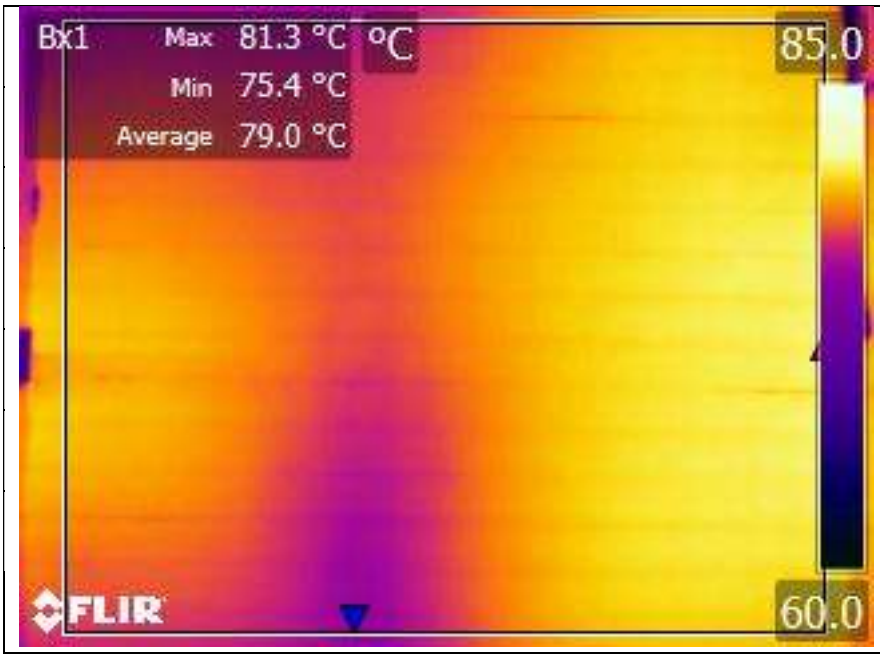

T_{inlet}	22.1 °C
$T_{Upper\ T/C}$	32.0 °C
$\Delta T_{ceiling}$	56.9 °C
$\Delta T_{inside\ air}$	13.8 °C
$\dot{Q}_{cond}$	152.1 W
Re_{inlet}	7,027
h_{inlet}	2.2 W/(m^2·K)
$h_{upper\ T/C}$	2.7 W/(m^2·K)

Figure 106: Thermogram from 1" offset jet, 0.91 m/s jet from bottom of image, 10 degrees horizontal spread

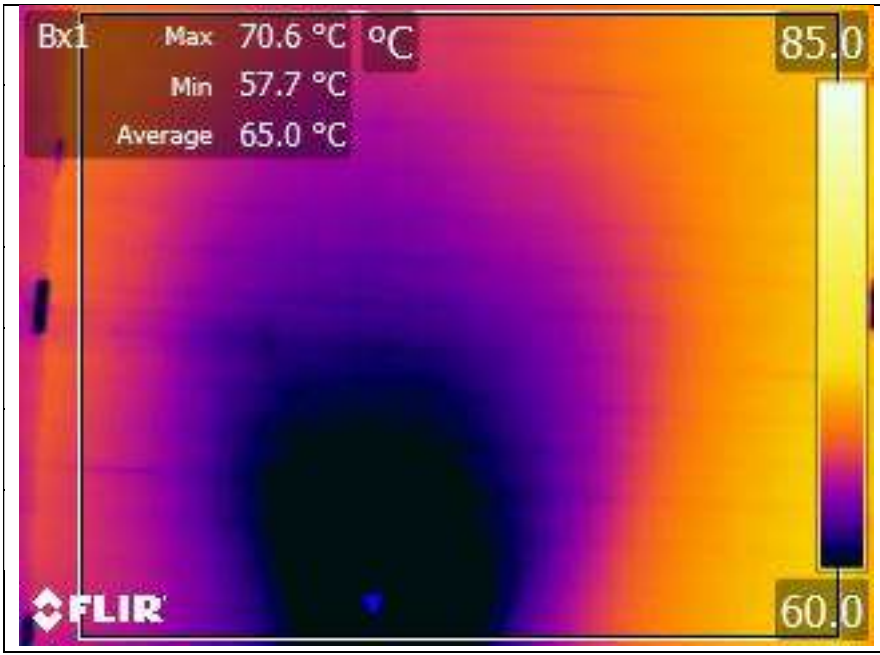

T_{inlet}	22.0 °C
$T_{Upper\ T/C}$	36.9 °C
$\Delta T_{ceiling}$	42.9 °C
$\Delta T_{inside\ air}$	14.4 °C
$\dot{Q}_{cond}$	154.3 W
Re_{inlet}	7,028
h_{inlet}	3.7 W/(m^2·K)
$h_{upper\ T/C}$	5.6 W/(m^2·K)

Figure 107: Thermogram from 1" offset jet, 0.91 m/s jet from bottom of image angled 20 degrees towards ceiling and 20 degrees horizontally

T_{inlet}	21.7 °C
$T_{Upper\ T/C}$	29.8 °C
$\Delta T_{ceiling}$	64.8 °C
$\Delta T_{inside\ air}$	12.3 °C
$\dot{Q}_{cond}$	151.4 W
Re_{inlet}	7,052
h_{inlet}	1.7 W/(m^2·K)
$h_{upper\ T/C}$	1.9 W/(m^2·K)

Figure 108: Thermogram from 4.2" offset jet, 0.91 m/s jet normal to wall

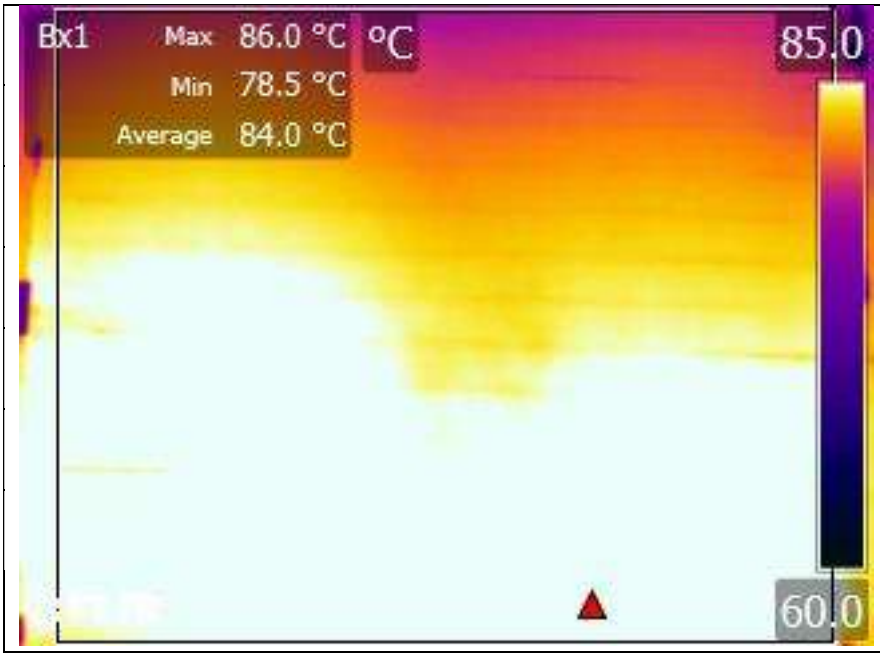

T_{inlet}	21.4 °C
$T_{Upper\ T/C}$	31.7 °C
$\Delta T_{ceiling}$	62.6 °C
$\Delta T_{inside\ air}$	12.0 °C
$\dot{Q}_{cond}$	151.5 W
Re_{inlet}	7,068
h_{inlet}	1.8 W/(m^2·K)
$h_{upper\ T/C}$	2.2 W/(m^2·K)

Figure 109: Thermogram from 4.2" offset jet, 0.91 m/s jet from bottom of image angled 10 degrees towards ceiling

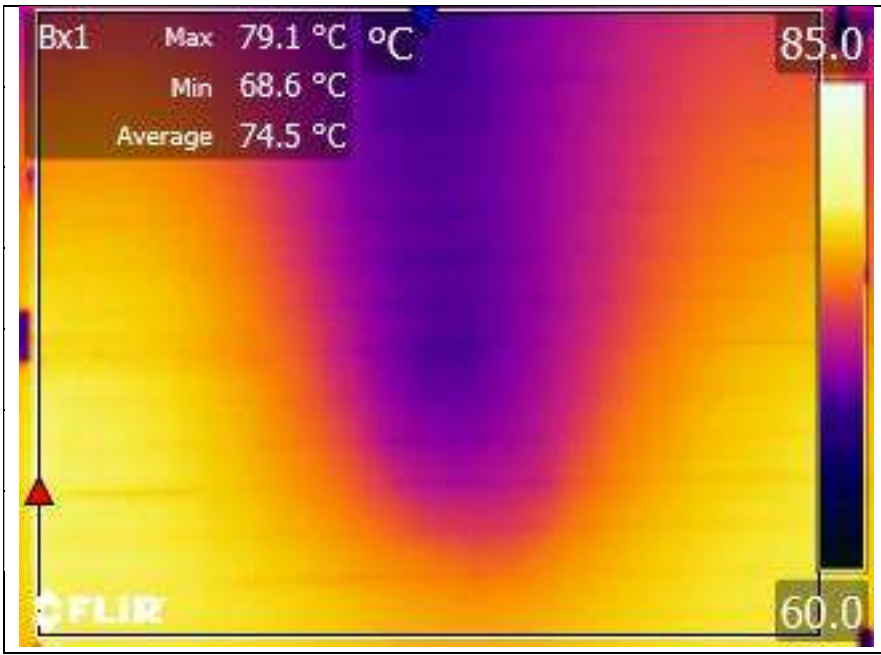

T_{inlet}	21.5 °C
$T_{Upper\ T/C}$	37.9 °C
$\Delta T_{ceiling}$	53.0 °C
$\Delta T_{inside\ air}$	11.5 °C
$\dot{Q}_{cond}$	153.6 W
Re_{inlet}	7,061
h_{inlet}	2.7 W/(m^2·K)
$h_{upper\ T/C}$	3.8 W/(m^2·K)

Figure 110: Thermogram from 4.2" offset jet, 0.91 m/s jet from bottom of image angled 20 degrees towards ceiling

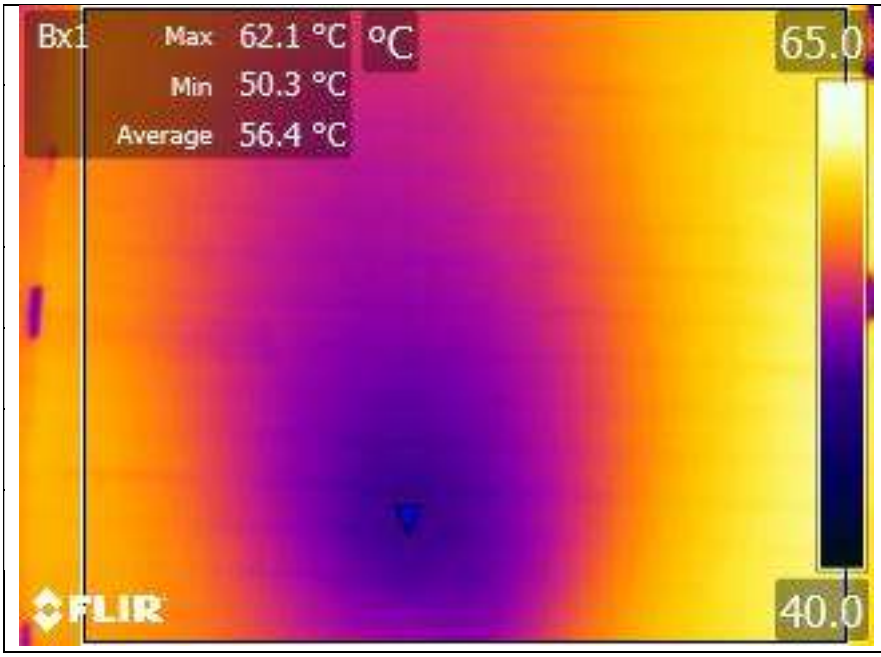

T_{inlet}	21.5 °C
$T_{Upper\ T/C}$	38.6 °C
$\Delta T_{ceiling}$	34.9 °C
$\Delta T_{inside\ air}$	11.6 °C
$\dot{Q}_{cond}$	155.6 W
Re_{inlet}	7,060
h_{inlet}	5.0 W/(m^2·K)
$h_{upper\ T/C}$	9.8 W/(m^2·K)

Figure 111: Thermogram from 4.2" offset jet, 0.91 m/s jet from bottom of image angled 30 degrees towards ceiling

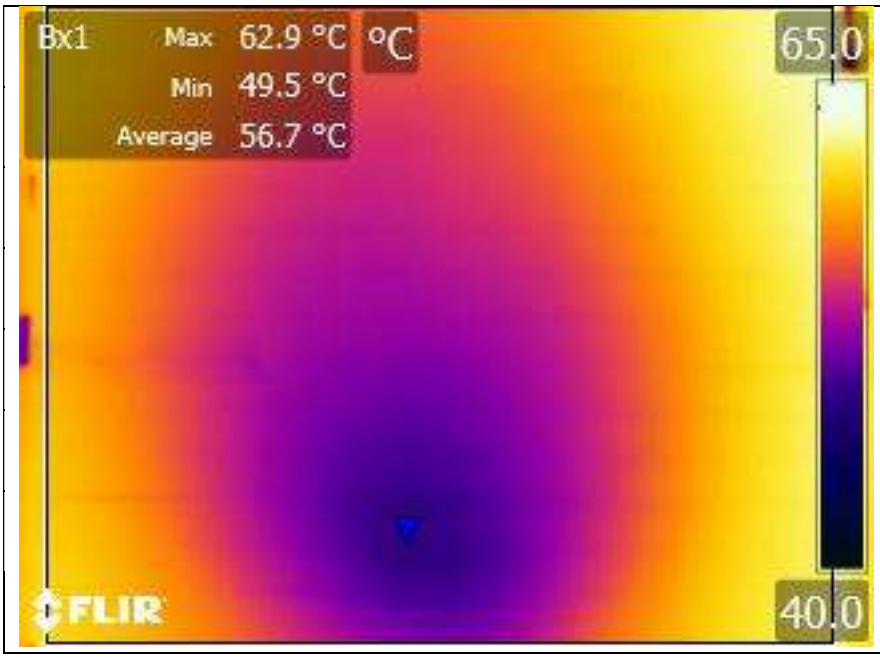

T_{inlet}	21.7 °C
$T_{Upper\ T/C}$	37.9 °C
$\Delta T_{ceiling}$	35.0 °C
$\Delta T_{inside\ air}$	11.2 °C
$\dot{Q}_{cond}$	156.5 W
Re_{inlet}	7,052
h_{inlet}	5.0 W/(m²·K)
$h_{upper\ T/C}$	9.4 W/(m²·K)

Figure 112: Thermogram from 4.2" offset jet, 0.91 m/s jet from bottom of image angled 30 degrees towards ceiling with a 20 degree spread

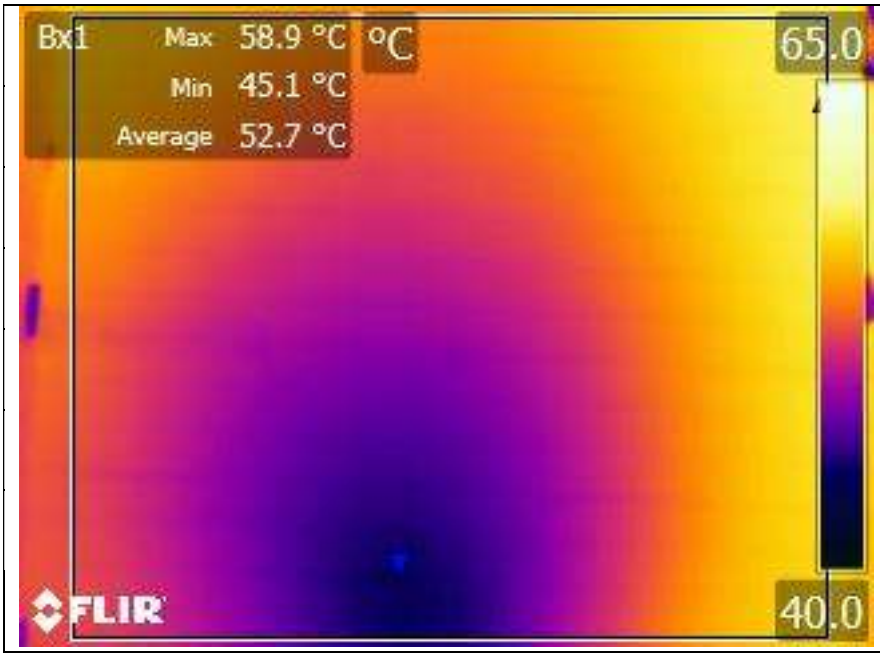

T_{inlet}	21.6 °C
$T_{Upper\ T/C}$	37.7 °C
$\Delta T_{ceiling}$	31.1 °C
$\Delta T_{inside\ air}$	12.0 °C
$\dot{Q}_{cond}$	156.1 W
Re_{inlet}	7,056
h_{inlet}	5.9 W/(m²·K)
$h_{upper\ T/C}$	12.1 W/(m²·K)

Figure 113: Thermogram from 4.2" offset jet, 0.91 m/s jet from bottom of image angled 40 degrees towards ceiling

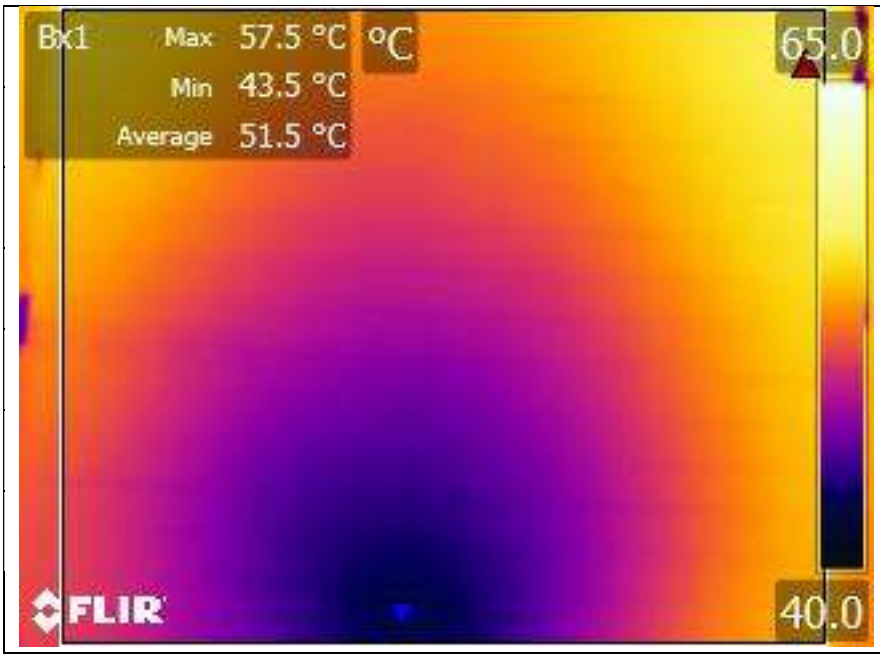

T_{inlet}	21.3 °C
$T_{Upper\ T/C}$	38.3 °C
$\Delta T_{ceiling}$	30.2 °C
$\Delta T_{inside\ air}$	12.0 °C
$\dot{Q}_{cond}$	156.4 W
Re_{inlet}	7,078
h_{inlet}	6.1 W/(m²·K)
$h_{upper\ T/C}$	13.9 W/(m²·K)

Figure 114: Thermogram from 4.2" offset jet, 0.91 m/s jet from bottom of image angled 40 degrees towards ceiling with a 20 degree horizontal spread

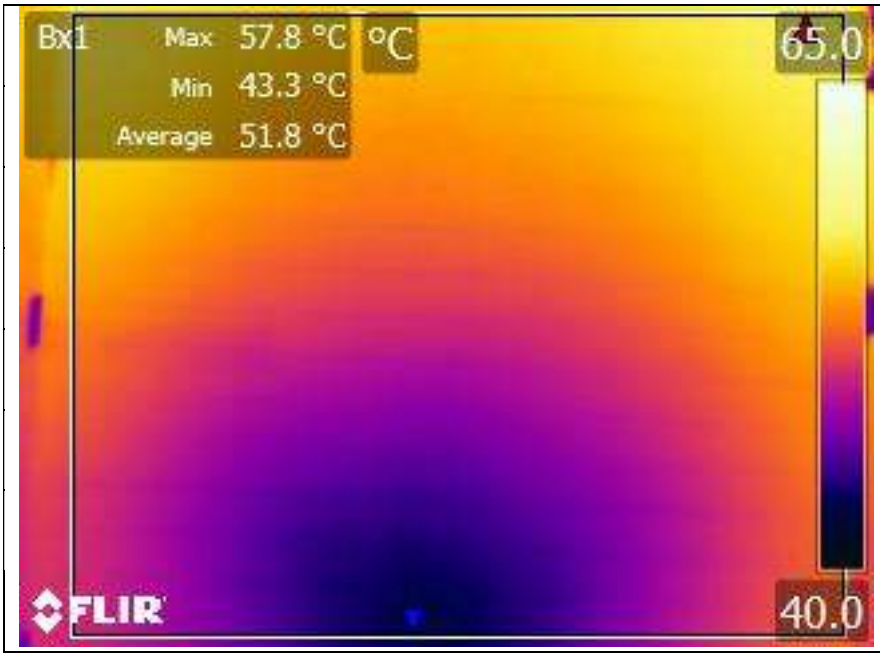

T_{inlet}	21.3 °C
$T_{Upper\ T/C}$	36.1 °C
$\Delta T_{ceiling}$	30.0 °C
$\Delta T_{inside\ air}$	13.0 °C
$\dot{Q}_{cond}$	156.2 W
Re_{inlet}	7,079
h_{inlet}	6.1 W/(m²·K)
$h_{upper\ T/C}$	12.0 W/(m²·K)

Figure 115: Thermogram from 4.2" offset jet, 0.91 m/s jet from bottom of image angled 40 degrees towards ceiling with a 40 degree horizontal spread

T_{inlet}	21.5 °C
$T_{Upper\ T/C}$	37.8 °C
$\Delta T_{ceiling}$	30.7 °C
$\Delta T_{inside\ air}$	12.6 °C
$\dot{Q}_{cond}$	156.4 W
Re_{inlet}	7,063
h_{inlet}	5.9 W/(m^2·K)
$h_{upper\ T/C}$	12.6 W/(m^2·K)

Figure 116: Thermogram from 4.2" offset jet, 0.91 m/s jet from bottom of image angled 50 degrees towards the ceiling

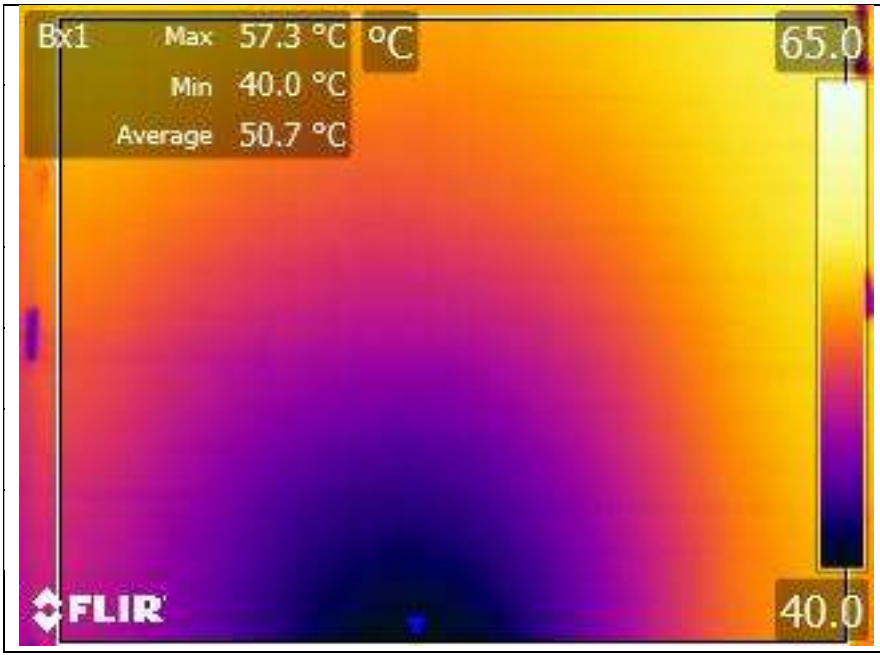

T_{inlet}	19.4 °C
$T_{Upper\ T/C}$	37.9 °C
$\Delta T_{ceiling}$	36.6 °C
$\Delta T_{inside\ air}$	12.6 °C
$\dot{Q}_{cond}$	156.1 W
Re_{inlet}	7,200
h_{inlet}	4.7 W/(m^2·K)
$h_{upper\ T/C}$	8.3 W/(m^2·K)

Figure 117: Thermogram from 4.2" offset jet, 0.91 m/s jet from bottom of image angled 50 degrees towards the ceiling with half as many louvers as Figure 116

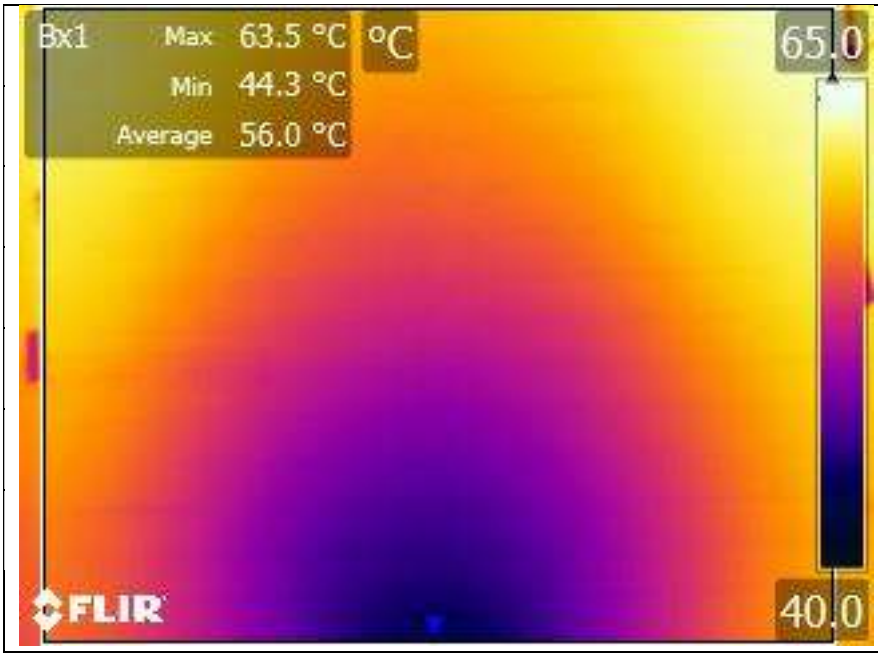

T_{inlet}	21.6 °C
$T_{Upper\ T/C}$	35.2 °C
$\Delta T_{ceiling}$	34.4 °C
$\Delta T_{inside\ air}$	13.6 °C
$\dot{Q}_{cond}$	156.2 W
Re_{inlet}	7,055
h_{inlet}	5.1 W/(m^2·K)
$h_{upper\ T/C}$	9.8 W/(m^2·K)

Figure 118: Thermogram from 4.2" offset jet, 0.91 m/s jet from bottom of image angled 50 degrees towards the ceiling with 20 degree spread

T_{inlet}	19.7 °C
$T_{Upper\ T/C}$	36.2 °C
$\Delta T_{ceiling}$	32.6 °C
$\Delta T_{inside\ air}$	13.6 °C
$\dot{Q}_{cond}$	155.8 W
Re_{inlet}	7,186
h_{inlet}	5.5 W/(m^2·K)
$h_{upper\ T/C}$	11.1 W/(m^2·K)

Figure 119: Thermogram from 4.2" offset jet, 0.91 m/s jet from bottom of image angled 60 degrees towards the ceiling with half as many louvers as Figure 116

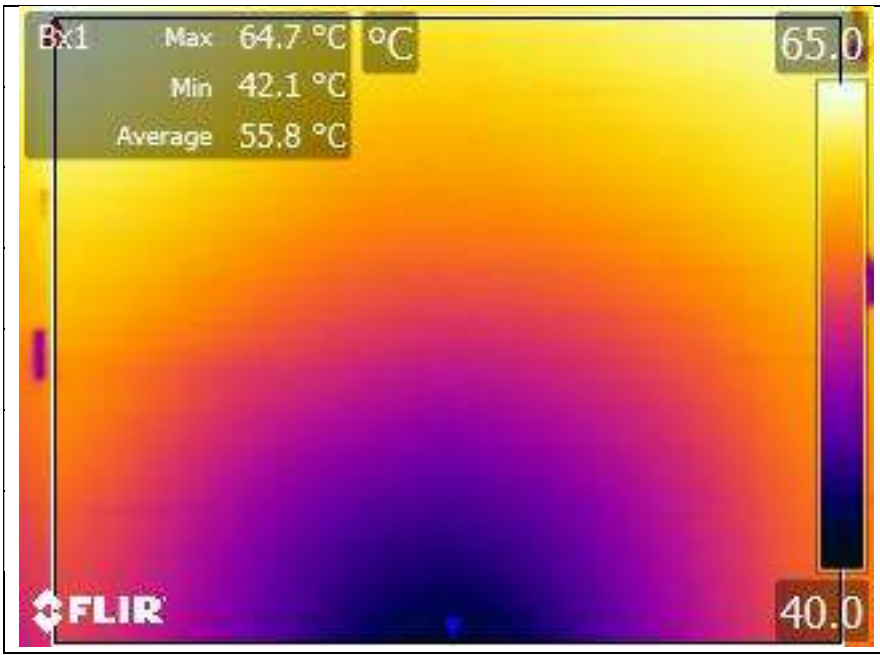

T_{inlet}	20.8 °C
$T_{Upper\ T/C}$	35.9 °C
$\Delta T_{ceiling}$	35.0 °C
$\Delta T_{inside\ air}$	14.1 °C
$\dot{Q}_{cond}$	155.9 W
Re_{inlet}	7,111
h_{inlet}	4.9 W/(m^2·K)
$h_{upper\ T/C}$	8.7 W/(m^2·K)

Figure 120: Thermogram from 4.2" offset jet, 0.91 m/s jet from bottom of image angled 60 degrees towards the ceiling with a 20 degree horizontal spread

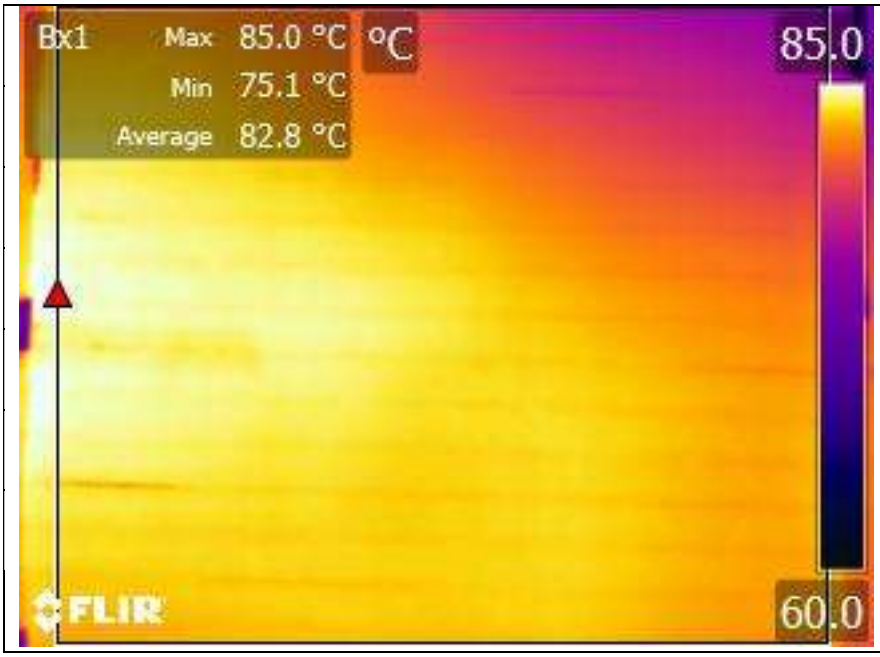

T_{inlet}	21.5 °C
$T_{Upper\ T/C}$	30.8 °C
$\Delta T_{ceiling}$	61.3 °C
$\Delta T_{inside\ air}$	10.3 °C
$\dot{Q}_{cond}$	151.7 W
Re_{inlet}	7,064
h_{inlet}	1.9 W/(m^2·K)
$h_{upper\ T/C}$	2.2 W/(m^2·K)

Figure 121: Thermogram from 4.2" offset jet, 0.91 m/s jet from bottom of image angled with a 20 degree clockwise swirl

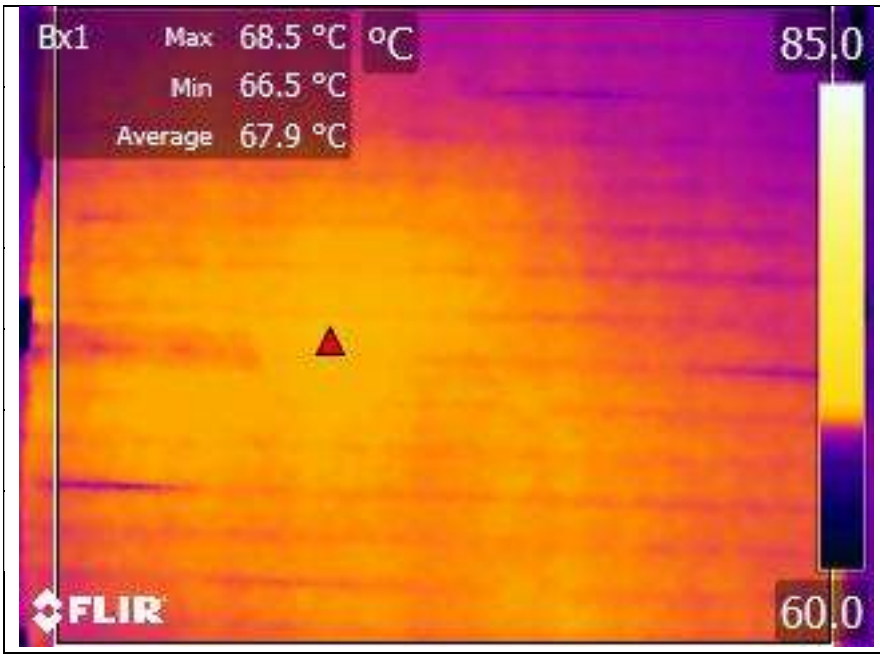

T_{inlet}	19.7 °C
$T_{Upper\ T/C}$	34.7 °C
$\Delta T_{ceiling}$	48.2 °C
$\Delta T_{inside\ air}$	12.9 °C
$\dot{Q}_{cond}$	73.2 W
Re_{inlet}	3,948
h_{inlet}	0.7 W/(m^2·K)
$h_{upper\ T/C}$	1.1 W/(m^2·K)

Figure 122: Thermogram from 4.2" offset jet, 0.50 m/s jet from bottom of image normal to the wall

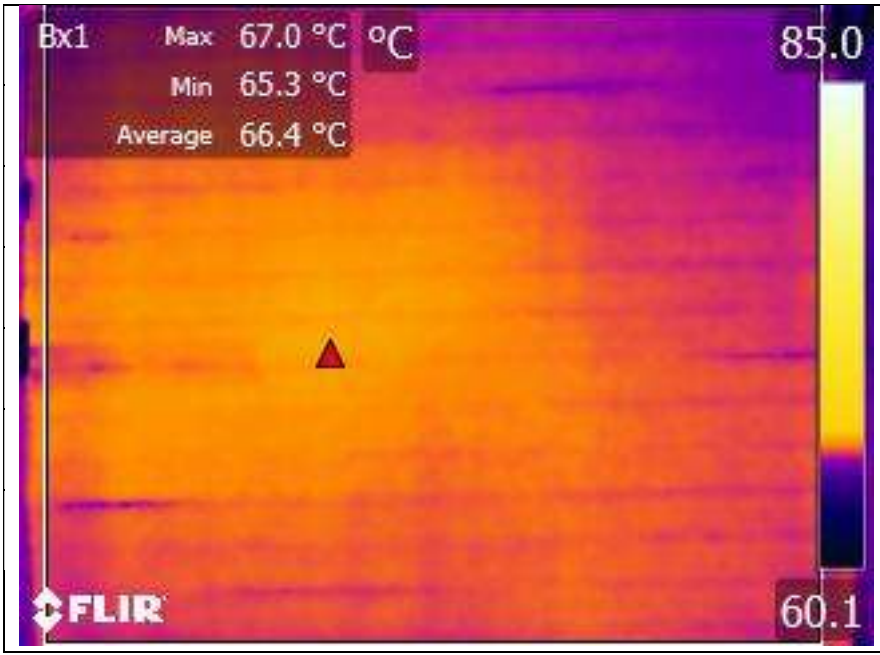

T_{inlet}	19.2 °C
$T_{Upper\ T/C}$	33.5 °C
$\Delta T_{ceiling}$	47.2 °C
$\Delta T_{inside\ air}$	11.0 °C
$\dot{Q}_{cond}$	73.3 W
Re_{inlet}	3,967
h_{inlet}	0.8 W/(m^2·K)
$h_{upper\ T/C}$	1.2 W/(m^2·K)

Figure 123: Thermogram from 4.2" offset jet, 0.50 m/s jet from bottom of image angled 20 degrees towards the ceiling

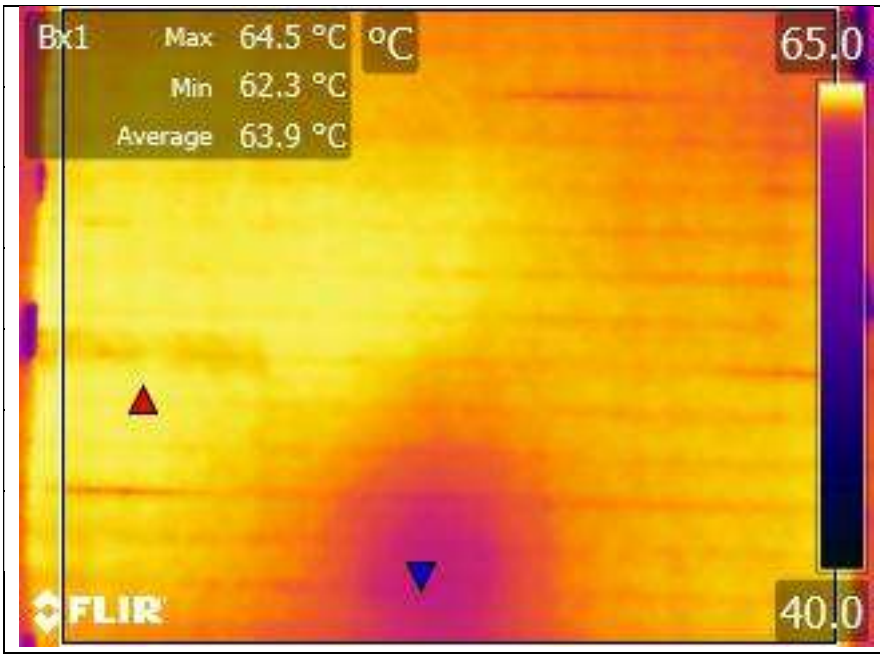

T_{inlet}	19.9 °C
$T_{Upper\ T/C}$	33.1 °C
$\Delta T_{ceiling}$	44.0 °C
$\Delta T_{inside\ air}$	11.2 °C
$\dot{Q}_{cond}$	73.9 W
Re_{inlet}	3,941
h_{inlet}	1.1 W/(m^2·K)
$h_{upper\ T/C}$	1.6 W/(m^2·K)

Figure 124: Thermogram from 4.2" offset jet, 0.50 m/s jet from bottom of image angled 40 degrees towards the ceiling

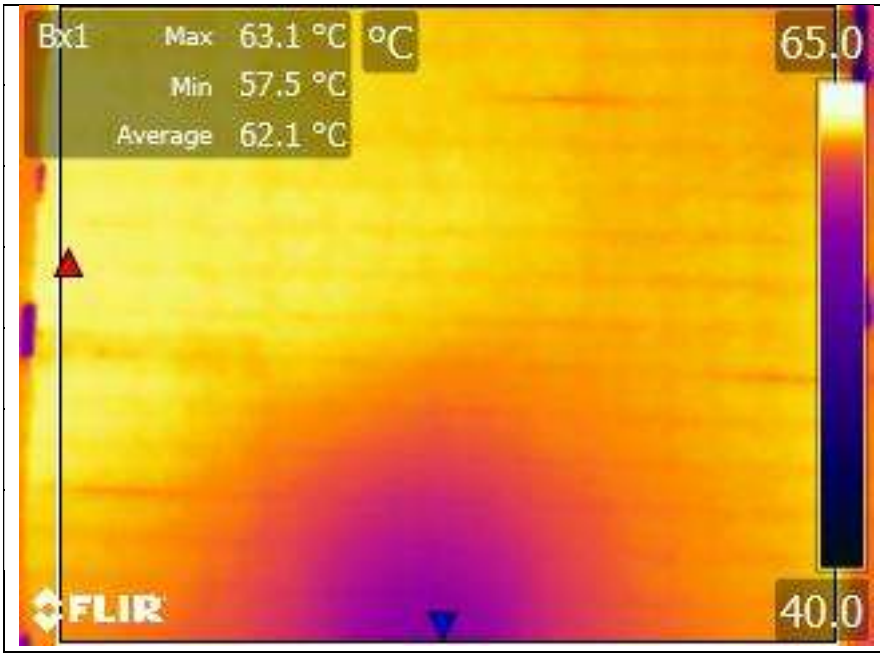

T_{inlet}	20.0 °C
$T_{Upper\ T/C}$	37.3 °C
$\Delta T_{ceiling}$	42.1 °C
$\Delta T_{inside\ air}$	11.7 °C
$\dot{Q}_{cond}$	74.2 W
Re_{inlet}	3,936
h_{inlet}	1.3 W/(m^2·K)
$h_{upper\ T/C}$	2.1 W/(m^2·K)

Figure 125: Thermogram from 4.2" offset jet, 0.50 m/s jet from bottom of image angled 50 degrees towards the ceiling

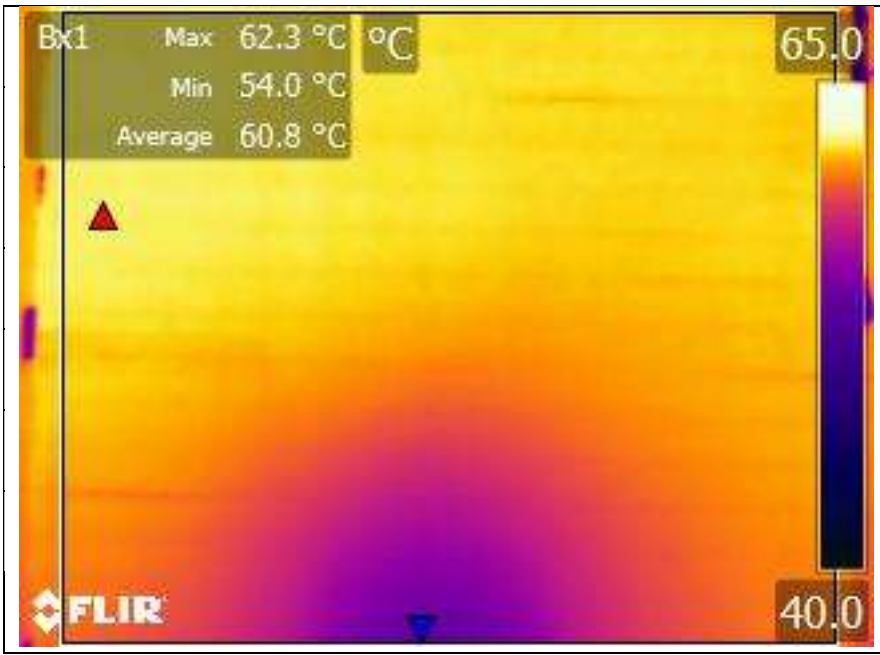

T_{inlet}	19.9 °C
$T_{Upper\ T/C}$	36.9 °C
$\Delta T_{ceiling}$	40.9 °C
$\Delta T_{inside\ air}$	12.0 °C
$\dot{Q}_{cond}$	74.3 W
Re_{inlet}	3,941
h_{inlet}	1.3 W/(m^2·K)
$h_{upper\ T/C}$	2.3 W/(m^2·K)

Figure 126: Thermogram from 4.2" offset jet, 0.50 m/s jet from bottom of image angled 60 degrees towards the ceiling, with half the louvers as Figure 125.

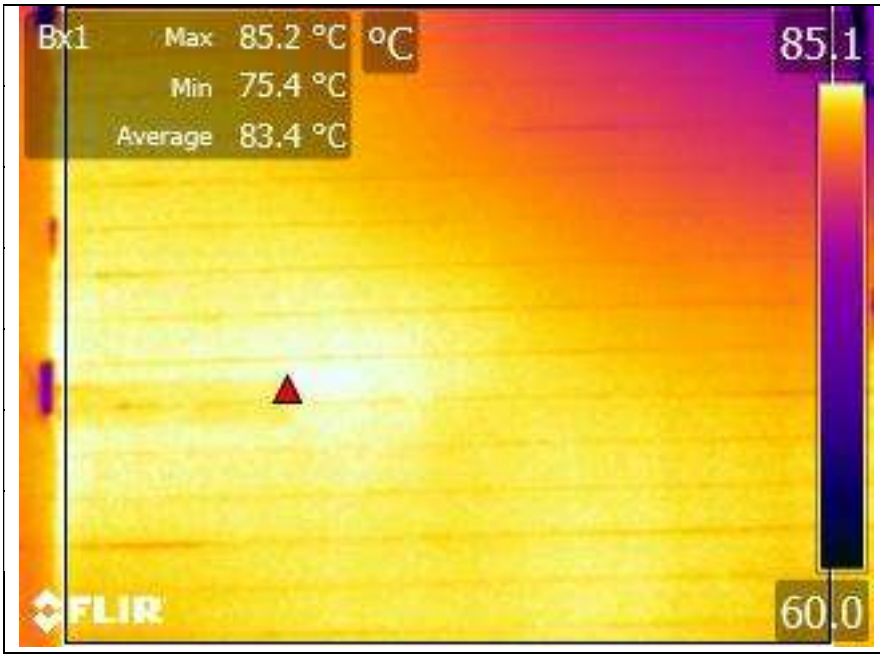

T_{inlet}	20.5 °C
$T_{Upper\ T/C}$	31.9 °C
$\Delta T_{ceiling}$	62.9 °C
$\Delta T_{inside\ air}$	12.4 °C
$\dot{Q}_{cond}$	141.5 W
Re_{inlet}	6,657
h_{inlet}	1.6 W/(m^2·K)
$h_{upper\ T/C}$	1.9 W/(m^2·K)

Figure 127: Thermogram from 4.2" offset jet, 0.85 m/s jet from bottom of image normal to inlet wall

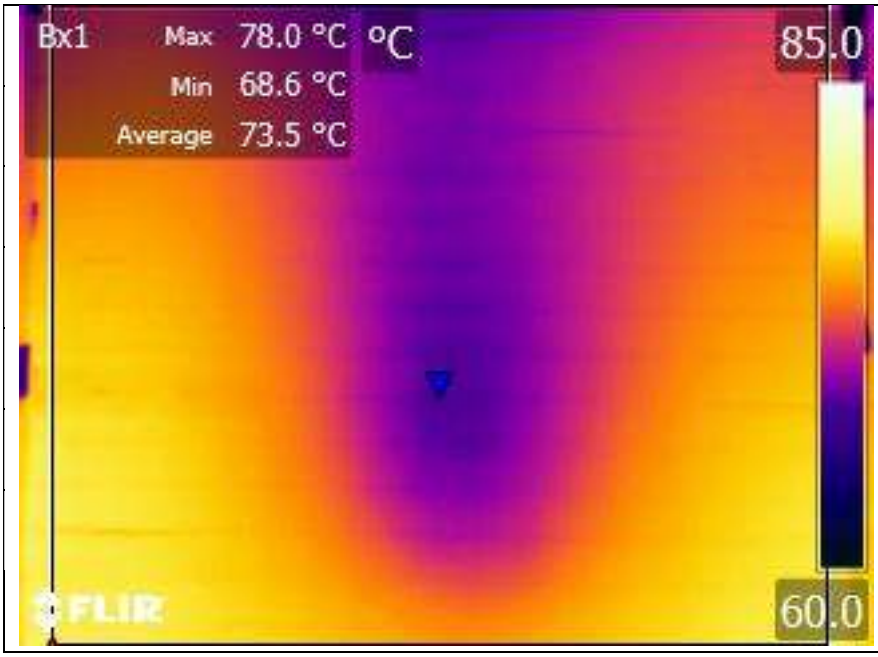

T_{inlet}	20.5 °C
$T_{Upper\ T/C}$	39.3 °C
$\Delta T_{ceiling}$	53.0 °C
$\Delta T_{inside\ air}$	12.9 °C
$\dot{Q}_{cond}$	143.6 W
Re_{inlet}	6,658
h_{inlet}	2.4 W/(m^2·K)
$h_{upper\ T/C}$	3.7 W/(m^2·K)

Figure 128: Thermogram from 4.2" offset jet, 0.85 m/s jet from bottom of image angled 20 degrees towards the ceiling

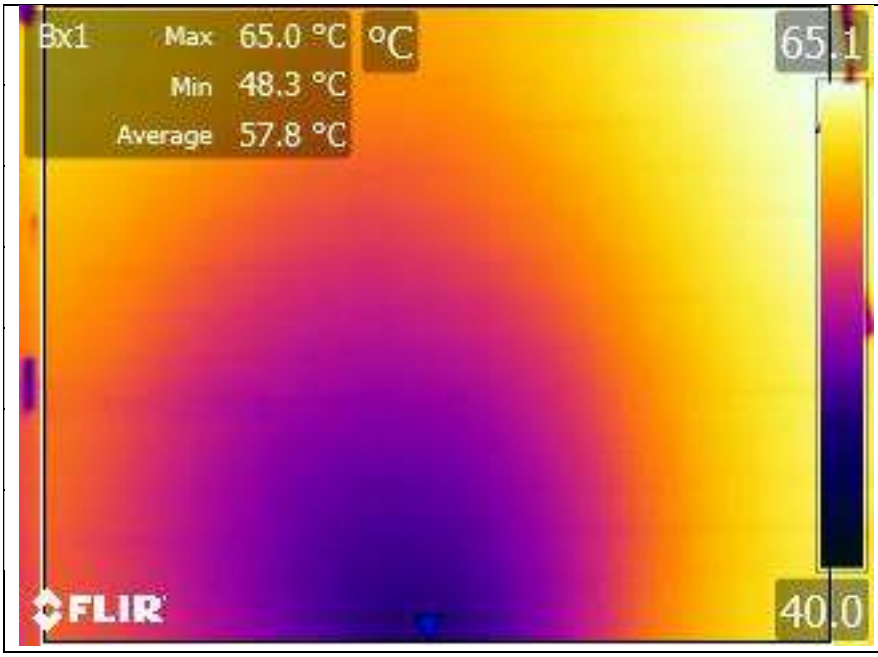

T_{inlet}	20.6 °C
$T_{Upper\ T/C}$	38.2 °C
$\Delta T_{ceiling}$	37.2 °C
$\Delta T_{inside\ air}$	14.3 °C
$\dot{Q}_{cond}$	146.0 W
Re_{inlet}	6,654
h_{inlet}	4.3 W/(m^2·K)
$h_{upper\ T/C}$	8.2 W/(m^2·K)

Figure 129: Thermogram from 4.2" offset jet, 0.85 m/s jet from bottom of image angled 40 degrees towards the ceiling

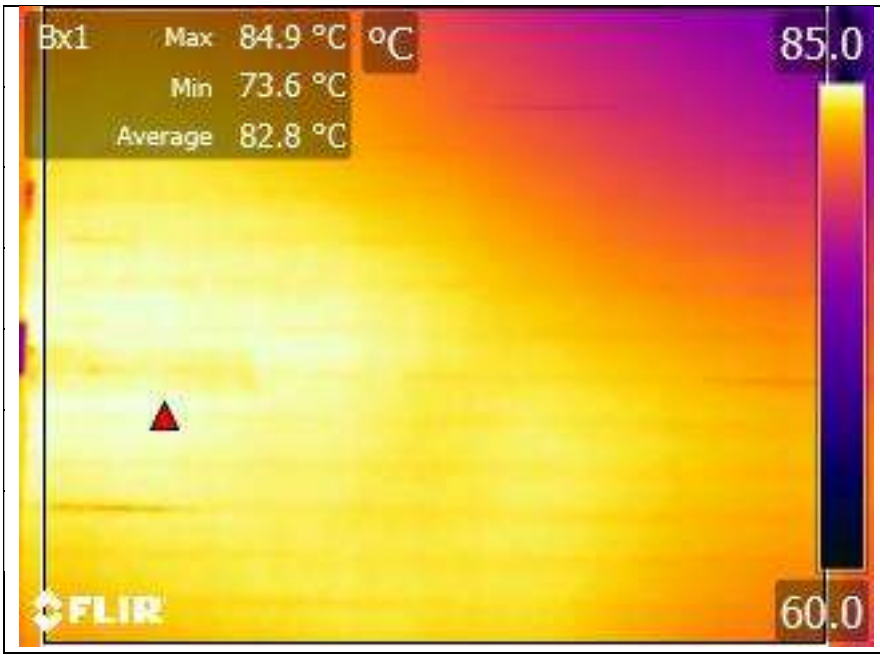

T_{inlet}	22.2 °C
$T_{Upper\ T/C}$	31.6 °C
$\Delta T_{ceiling}$	60.6 °C
$\Delta T_{inside\ air}$	11.3 °C
$\dot{Q}_{cond}$	152.7 W
Re_{inlet}	7,791
h_{inlet}	2.0 W/(m^2·K)
$h_{upper\ T/C}$	2.3 W/(m^2·K)

Figure 130: Thermogram from 4.2" offset jet, 1.01 m/s jet from bottom of image normal to inlet wall

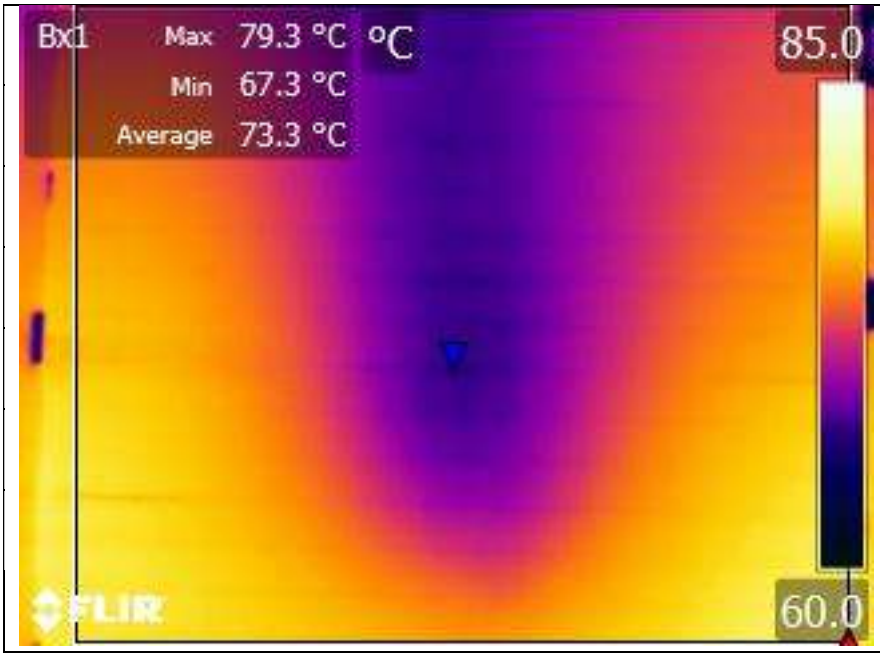

T_{inlet}	22.3 °C
$T_{Upper\ T/C}$	40.2 °C
$\Delta T_{ceiling}$	51.0 °C
$\Delta T_{inside\ air}$	11.8 °C
$\dot{Q}_{cond}$	154.6 W
Re_{inlet}	7,784
h_{inlet}	2.8 W/(m^2·K)
$h_{upper\ T/C}$	4.3 W/(m^2·K)

Figure 131: Thermogram from 4.2" offset jet, 1.01 m/s jet from bottom of image angled 20 degrees towards the ceiling

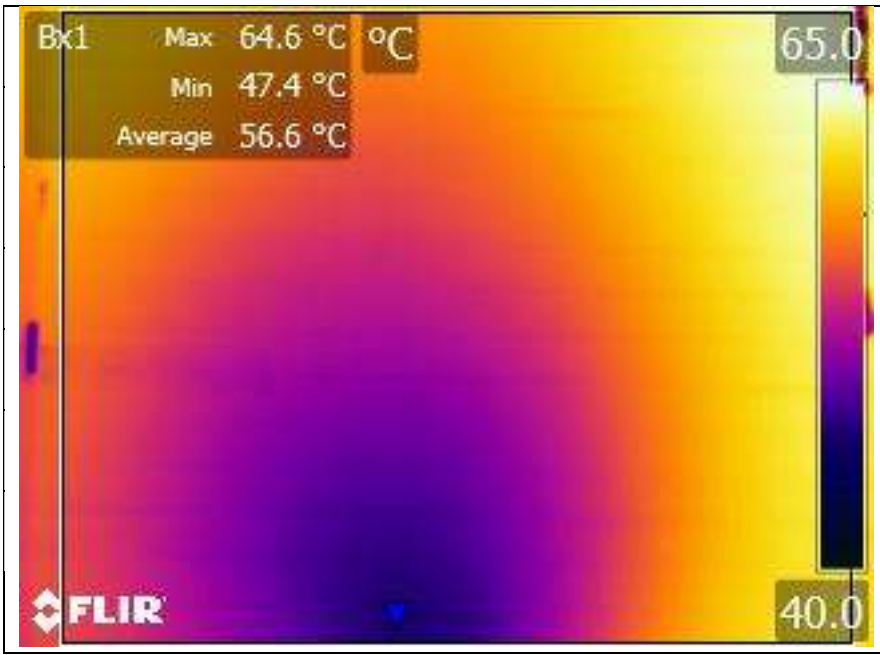

T_{inlet}	22.0 °C
$T_{Upper\ T/C}$	35.8 °C
$\Delta T_{ceiling}$	34.6 °C
$\Delta T_{inside\ air}$	12.3 °C
$\dot{Q}_{cond}$	157.0 W
Re_{inlet}	7,806
h_{inlet}	5.0 W/(m^2·K)
$h_{upper\ T/C}$	8.4 W/(m^2·K)

Figure 132: Thermogram from 4.2" offset jet, 1.01 m/s jet from bottom of image angled 40 degrees towards the ceiling

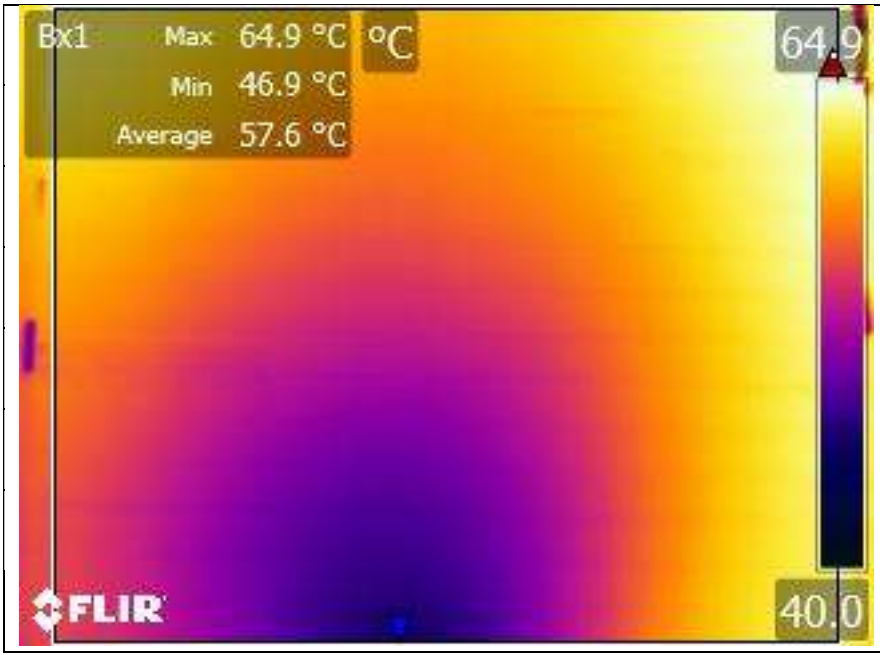

T_{inlet}	22.6 °C
$T_{Upper\ T/C}$	38.7 °C
$\Delta T_{ceiling}$	35.0 °C
$\Delta T_{inside\ air}$	13.1 °C
$\dot{Q}_{cond}$	157.2 W
Re_{inlet}	7,757
h_{inlet}	5.0 W/(m^2·K)
$h_{upper\ T/C}$	9.4 W/(m^2·K)

Figure 133: Thermogram from 4.2" offset jet, 1.01 m/s jet from bottom of image angled 50 degrees towards the ceiling

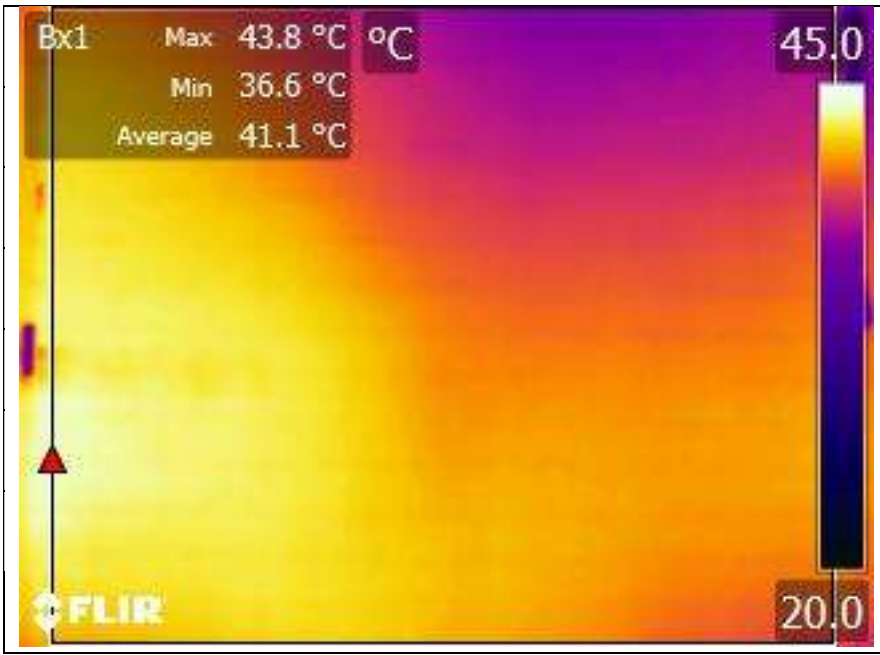

T_{inlet}	20.2 °C
$T_{Upper\ T/C}$	24.2 °C
$\Delta T_{ceiling}$	20.9 °C
$\Delta T_{inside\ air}$	4.2 °C
$\dot{Q}_{cond}$	170.3 W
Re_{inlet}	44,801
h_{inlet}	9.8 W/(m^2·K)
$h_{upper\ T/C}$	12.2 W/(m^2·K)

Figure 134: Thermogram from 4.2" offset jet, 5.7 m/s jet from bottom of image, normal to inlet wall

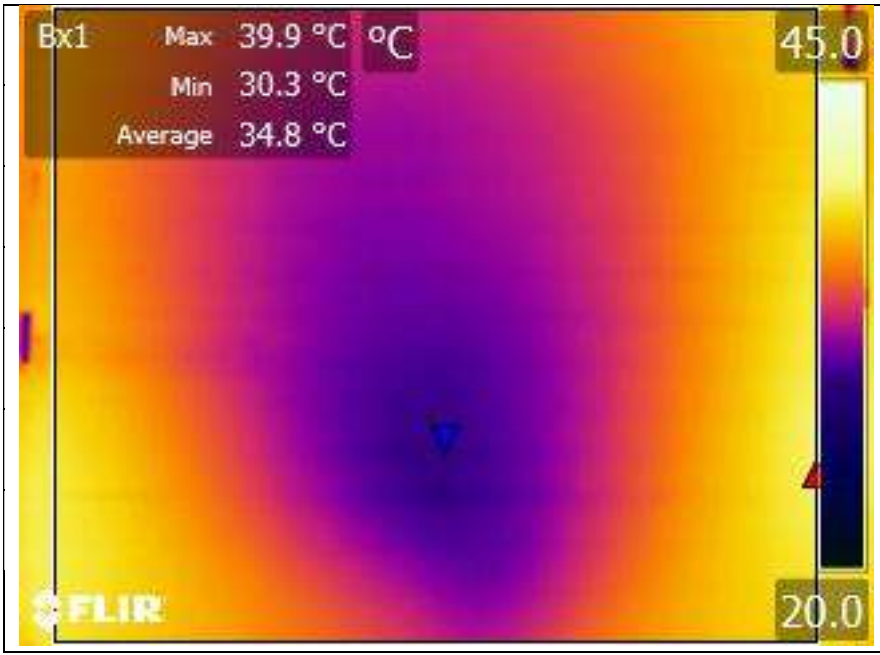

T_{inlet}	19.3 °C
$T_{Upper\ T/C}$	24.5 °C
$\Delta T_{ceiling}$	15.5 °C
$\Delta T_{inside\ air}$	4.0 °C
$\dot{Q}_{cond}$	171.4 W
Re_{inlet}	45,148
h_{inlet}	14.0 W/(m^2·K)
$h_{upper\ T/C}$	21.0 W/(m^2·K)

Figure 135: Thermogram from 4.2" offset jet, 5.7 m/s jet from bottom of image, angled 20 degrees towards ceiling

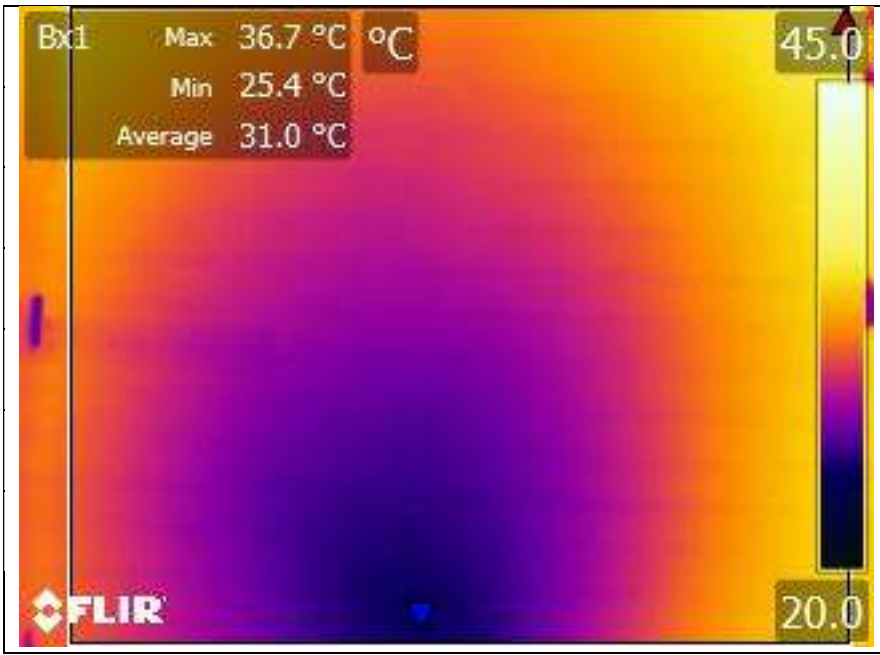

T_{inlet}	18.0 °C
$T_{Upper\ T/C}$	23.0 °C
$\Delta T_{ceiling}$	13.0 °C
$\Delta T_{inside\ air}$	4.4 °C
$\dot{Q}_{cond}$	171.9 W
Re_{inlet}	45,710
h_{inlet}	16.9 W/(m²·K)
$h_{upper\ T/C}$	27.5 W/(m²·K)

Figure 136: Thermogram from 4.2" offset jet, 5.7 m/s jet from bottom of image, angled 40 degrees towards ceiling

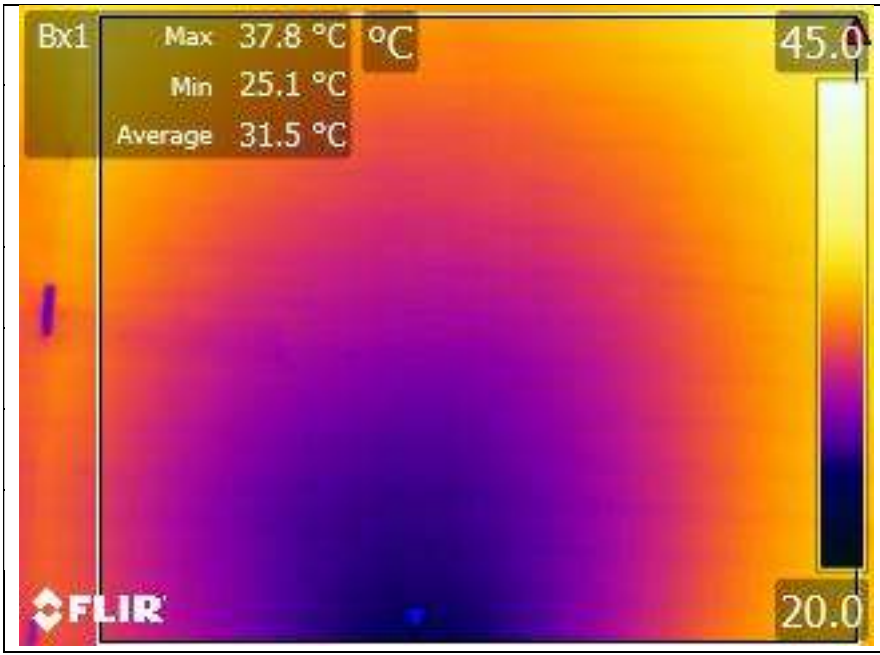

T_{inlet}	21.7 °C
$T_{Upper\ T/C}$	24.0 °C
$\Delta T_{ceiling}$	9.8 °C
$\Delta T_{inside\ air}$	2.0 °C
$\dot{Q}_{cond}$	175.6 W
Re_{inlet}	44,170
h_{inlet}	22.8 W/(m²·K)
$h_{upper\ T/C}$	29.7 W/(m²·K)

Figure 137: Thermogram from 4.2" offset jet, 5.7 m/s jet from bottom of image, angled 50 degrees towards ceiling

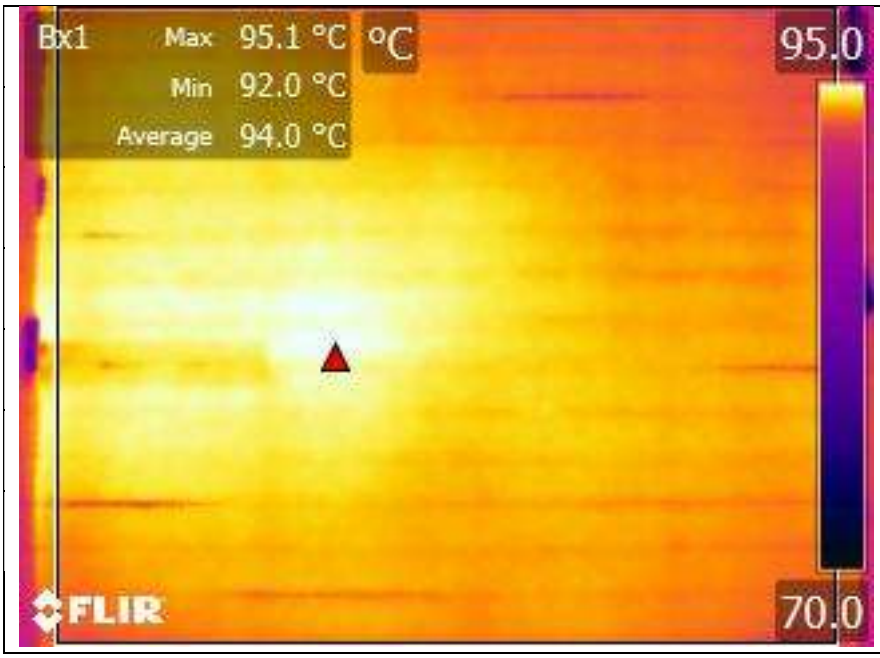

T_{inlet}	21.3 °C
$T_{Upper\ T/C}$	43.9 °C
$\Delta T_{ceiling}$	72.7 °C
$\Delta T_{inside\ air}$	16.0 °C
$\dot{Q}_{cond}$	151.4 W
Re_{inlet}	6,845
h_{inlet}	1.3 W/(m^2·K)
$h_{upper\ T/C}$	1.8 W/(m^2·K)

Figure 138: Thermogram from 4.2" offset jet, 0.88 m/s jet from bottom of image, normal to inlet wall

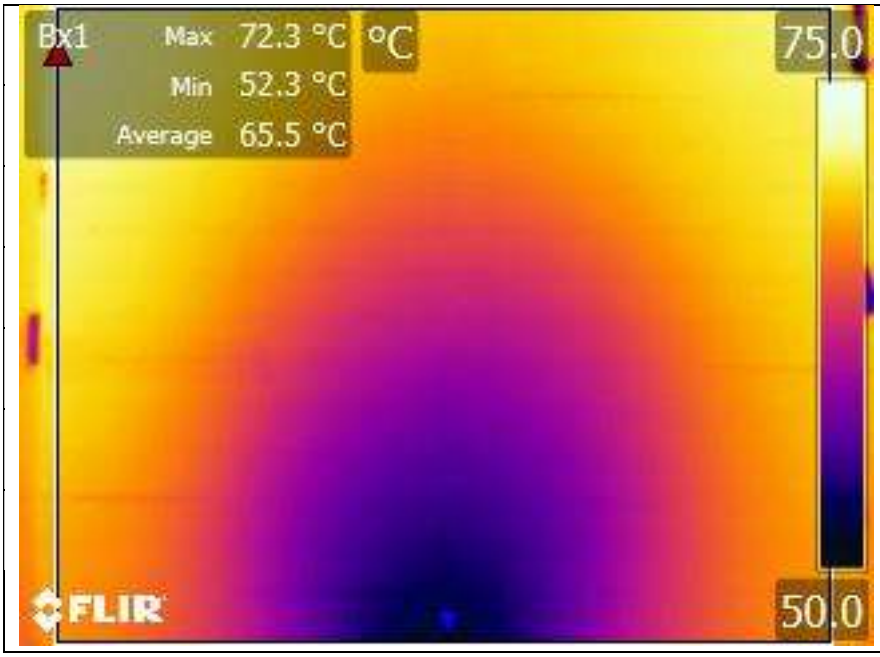

T_{inlet}	18.1 °C
$T_{Upper\ T/C}$	36.0 °C
$\Delta T_{ceiling}$	69.1 °C
$\Delta T_{inside\ air}$	16.2 °C
$\dot{Q}_{cond}$	152.5 W
Re_{inlet}	7,051
h_{inlet}	1.6 W/(m^2·K)
$h_{upper\ T/C}$	2.1 W/(m^2·K)

Figure 139: Thermogram from 4.2" offset jet, 0.88 m/s jet from bottom of image, angled 20 degrees towards the ceiling

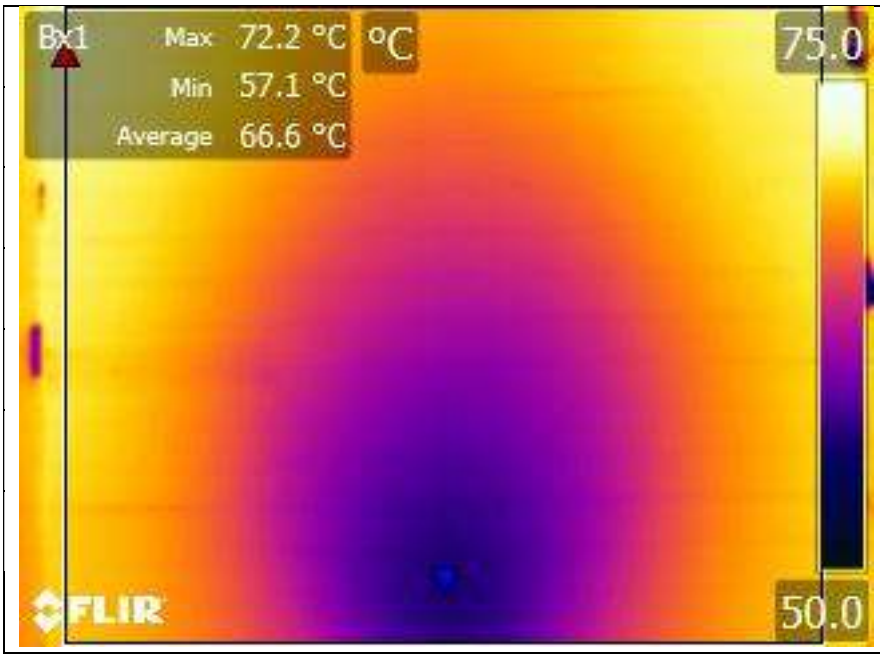

T_{inlet}	17.9 °C
$T_{Upper\ T/C}$	39.6 °C
$\Delta T_{ceiling}$	48.7 °C
$\Delta T_{inside\ air}$	18.1 °C
$\dot{Q}_{cond}$	155.7 W
Re_{inlet}	7,064
h_{inlet}	3.2 W/(m^2·K)
$h_{upper\ T/C}$	5.8 W/(m^2·K)

Figure 140: Thermogram from 4.2" offset jet, 0.88 m/s jet from bottom of image, angled 40 degrees towards the ceiling

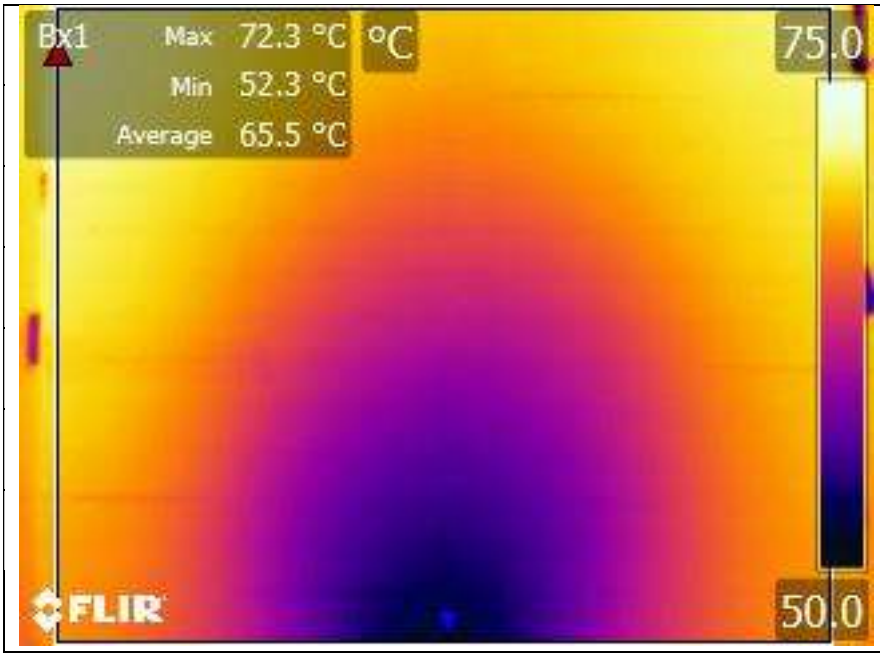

T_{inlet}	17.2 °C
$T_{Upper\ T/C}$	41.9 °C
$\Delta T_{ceiling}$	48.3 °C
$\Delta T_{inside\ air}$	19.0 °C
$\dot{Q}_{cond}$	155.9 W
Re_{inlet}	7,115
h_{inlet}	3.2 W/(m^2·K)
$h_{upper\ T/C}$	6.7 W/(m^2·K)

Figure 141: Thermogram from 4.2" offset jet, 0.88 m/s jet from bottom of image, angled 50 degrees towards the ceiling

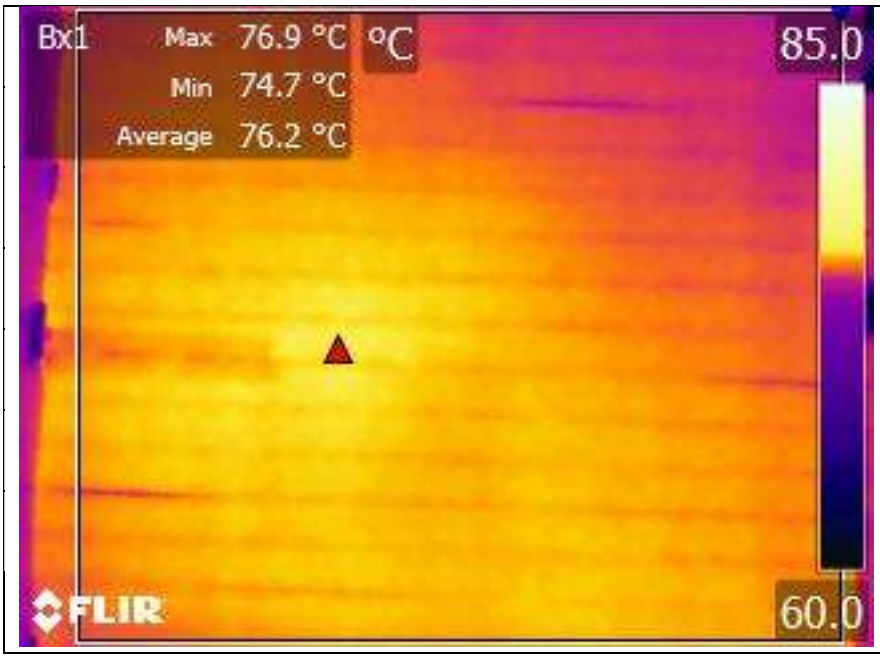

T_{inlet}	20.6 °C
$T_{Upper\ T/C}$	40.0 °C
$\Delta T_{ceiling}$	55.6 °C
$\Delta T_{inside\ air}$	14.9 °C
$\dot{Q}_{cond}$	94.0 W
Re_{inlet}	4,461
h_{inlet}	0.9 W/(m^2·K)
$h_{upper\ T/C}$	1.4 W/(m^2·K)

Figure 142: Thermogram from 4.2" offset jet, 0.57 m/s jet from bottom of image, normal to the inlet wall

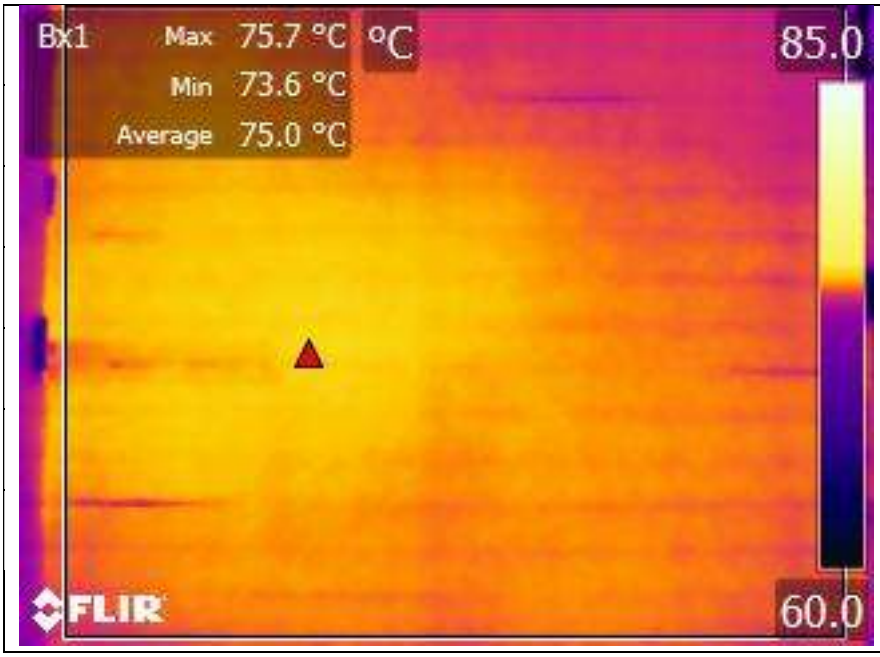

T_{inlet}	20.7 °C
$T_{Upper\ T/C}$	30.4°C
$\Delta T_{ceiling}$	54.3 °C
$\Delta T_{inside\ air}$	13.5 °C
$\dot{Q}_{cond}$	95.3 W
Re_{inlet}	4,457
h_{inlet}	1.0 W/(m^2·K)
$h_{upper\ T/C}$	1.2 W/(m^2·K)

Figure 143: Thermogram from 4.2" offset jet, 0.57 m/s jet from bottom of image, angled 20 degrees towards ceiling

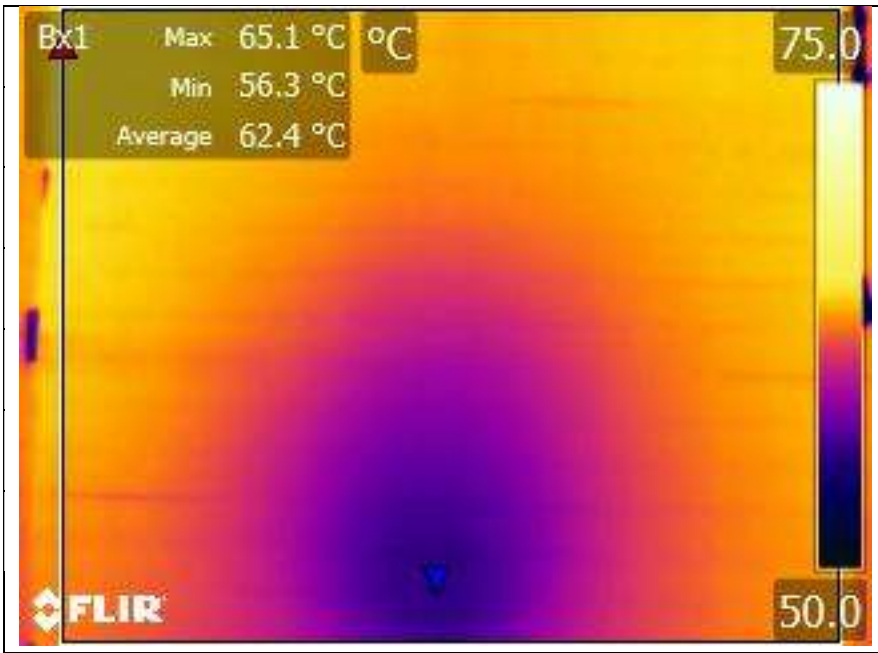

T_{inlet}	20.5 °C
$T_{Upper\ T/C}$	37.6 °C
$\Delta T_{ceiling}$	41.9 °C
$\Delta T_{inside\ air}$	14.0 °C
$\dot{Q}_{cond}$	96.2 W
Re_{inlet}	4,465
h_{inlet}	2.0 W/(m^2·K)
$h_{upper\ T/C}$	3.4 W/(m^2·K)

Figure 144: Thermogram from 4.2" offset jet, 0.57 m/s jet from bottom of image, angled 40 degrees towards ceiling

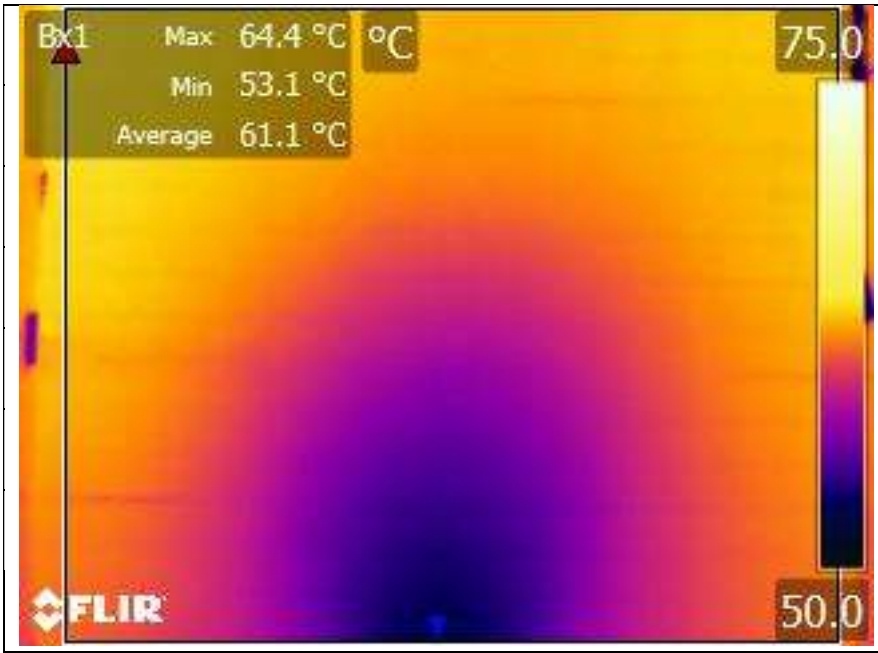

T_{inlet}	20.5 °C
$T_{Upper\ T/C}$	38.8 °C
$\Delta T_{ceiling}$	40.6 °C
$\Delta T_{inside\ air}$	14.7 °C
$\dot{Q}_{cond}$	96.5 W
Re_{inlet}	4,465
h_{inlet}	2.1 W/(m^2·K)
$h_{upper\ T/C}$	3.9 W/(m^2·K)

Figure 145: Thermogram from 4.2" offset jet, 0.57 m/s jet from bottom of image, angled 50 degrees towards ceiling